

**REDUCING CO₂ AND CORROSION: INSIGHTS
FROM THERMODYNAMIC DESCRIPTORS
CALCULATED WITH DENSITY FUNCTIONAL
THEORY**

by

Mitchell C. Groenenboom

Bachelor of Science in Engineering, Calvin College, 2013

Submitted to the Graduate Faculty of
the Swanson School of Engineering in partial fulfillment
of the requirements for the degree of

Doctor of Philosophy

University of Pittsburgh

2018

UNIVERSITY OF PITTSBURGH
SWANSON SCHOOL OF ENGINEERING

This dissertation was presented

by

Mitchell C. Groenenboom

It was defended on

March 15, 2018

and approved by

John A. Keith, Ph.D., Assistant Professor, Department of Chemical and Petroleum
Engineering

Giannis Mpourmpakis, Ph.D., Assistant Professor, Department of Chemical and Petroleum
Engineering

Guofeng Wang, Ph.D., Associate Professor, Department of Mechanical Engineering and
Materials Science

James R. Mckone, Ph.D., Assistant Professor, Department of Chemical and Petroleum
Engineering

Dissertation Director: John A. Keith, Ph.D., Assistant Professor, Department of Chemical
and Petroleum Engineering

**REDUCING CO₂ AND CORROSION: INSIGHTS FROM
THERMODYNAMIC DESCRIPTORS CALCULATED WITH DENSITY
FUNCTIONAL THEORY**

Mitchell C. Groenenboom, PhD

University of Pittsburgh, 2018

Catalytic reaction mechanisms can be extremely complex, and it is difficult to determine all the factors that control reaction rates. Fortunately, complex chemical phenomena can frequently be described by thermodynamic properties (such as molecular pK_a s and reaction overpotentials) that correlate with catalytic reaction rates. While these properties can be difficult or time intensive to measure experimentally, they can be easily computed using Kohn-Sham density functional theory (KS-DFT).

We have developed a thermodynamic descriptor-based model that uses molecular pK_a s and redox potentials calculated with KS-DFT to predict the electrochemical conditions at which aromatic N-heterocycle (ANH) molecules could facilitate multi-proton and multi-electron reduction reactions. By automating this procedure using the ADF modeling suite, we can rapidly screen through potential catalysts with minimal user input. To establish a baseline procedure for studying the chemical reduction of CO₂ via hydride transfers from ANH molecules, we characterized the chemical reduction of CO₂ by hydride transfers from sodium borohydride. We located hydride transfer pathways with nudged elastic band calculations and obtained free energy barriers from potentials of mean force derived from constrained molecular dynamics simulations along the reaction pathways. These simulations provided reaction energetics at realistic operating conditions and highlighted the potential pitfalls of only studying reaction pathways at 0 K.

Cathodic reduction reactions can limit galvanic corrosion rates in atmospheric environments. To help guide the design of titanium alloys that resist galvanic corrosion, we used density functional theory to predict dopants that inhibit cathodic reduction reaction kinetics on oxide surfaces. We calculated overpotentials for the oxygen reduction reaction (ORR) occurring on metal dopants in an amorphous TiO_2 surface. These overpotential trends successfully predicted six dopants that have been experimentally verified to inhibit ORR activity by up to 77% (Sn, Cr, Co, Al, Mn, and V). Next, we used this approach to study the native oxides of Ti-6Al-4V, a Ti alloy with improved corrosion resistance. We used Behler-Parrinello neural networks to create defective and amorphous surface models for TiAl_2O_5 (the oxide that forms on Ti-6Al-4V surfaces in addition to TiO_2) and predicted how ORR activity was altered by different complex oxide surface morphologies.

Keywords: Computational Chemistry, Density Functional Theory, Oxygen Reduction Reaction, Oxide, Carbon Dioxide Reduction, Aromatic N-Heterocycles, Neural Networks.

TABLE OF CONTENTS

PREFACE	xxiv
1.0 INTRODUCTION	1
1.1 Electrocatalytic Carbon Dioxide Reduction	1
1.1.1 Chemically Reducing Carbon Dioxide	1
1.1.2 Aromatic N-Heterocycle Promoted Carbon Dioxide Reduction Pro- cesses	4
1.1.3 Studies of Homogeneous ANH Reaction Mechanisms	6
1.1.4 Studies of Surface Catalyzed ANH Reaction Mechanisms	10
1.2 Modeling the Atomistic reactions that drive Corrosion	12
1.2.1 Corrosion Chemistry	13
1.2.2 Anti-Corrosion Technology	15
1.2.3 Electrochemical Reaction Overpotentials	16
1.2.4 Modeling Reactions on Amorphous Oxide Surfaces	17
1.3 Dissertation Overview	20
2.0 STRUCTURAL AND SUBSTITUENT GROUP EFFECTS ON MUL- TIELECTRON STANDARD REDUCTION POTENTIALS OF ARO- MATIC N-HETEROCYCLES	21
2.1 Introduction	21
2.2 Experimental methods	23
2.2.1 pK_a Measurements	23
2.2.2 COMPUTATIONAL METHODS	23
2.3 Results	25

2.4	Conclusions	35
3.0	EXPLICITLY UNRAVELING THE ROLES OF COUNTER IONS, SOLVENT MOLECULES, AND ELECTRON CORRELATION IN SOLUTION PHASE REACTION PATHWAYS	36
3.1	Introduction	36
3.2	Computational Methods	40
3.3	Results and Discussion	43
3.3.1	Model 1: Cluster models of reacting atoms with explicit water molecules and continuum solvation	44
3.3.2	Model 2: Explicit solvent models with pathways determined from gSS-NEB calculations within periodic boundary conditions	46
3.3.3	Model 3: Fully microsolvated clusters obtained from gSS-NEB reaction pathways embedded within continuum solvation models	51
3.3.4	Other reactions: BH_3OH^- as a reducing agent	55
3.4	Conclusions	60
4.0	QUANTUM CHEMICAL ANALYSES OF BH_4^- AND BH_3OH^- HYDRIDE TRANSFERS TO CO_2 IN AQUEOUS SOLUTION WITH POTENTIALS OF MEAN FORCE	62
4.1	Introduction	62
4.2	Computational Methods	64
4.3	Results and Discussion	65
4.4	Conclusions	73
5.0	DOPED AMORPHOUS TI OXIDES TO DEOPTIMIZE OXYGEN REDUCTION REACTION CATALYSIS	74
5.1	Introduction	74
5.2	Computational Methods	75
5.3	Experimental Methods	76
5.4	Results and Discussion	77
5.4.1	Amorphous TiO_2 Model	77
5.4.2	Calculating ORR Overpotentials	79

5.4.3 Dopant Screening	81
5.4.4 Cathodic Polarization Scans	84
5.4.5 Comparison to Experiment	85
5.5 Conclusions	87
6.0 INHIBITING THE OXYGEN REDUCTION REACTION ACTIVITY ON THE OXIDES OF TI-6AL-4V	89
6.1 Introduction	89
6.2 Computational Methods	91
6.3 Results and Discussion	93
6.3.1 Training Neural Networks	93
6.3.2 Creating Surface Models	95
6.3.3 Calculating ORR Overpotentials	98
6.3.4 Dopant Screening	100
6.4 Conclusions	103
7.0 SUMMARY AND FUTURE WORK	104
7.1 Aromatic N-heterocycle Co-catalyzed Carbon Dioxide Reduction	104
7.2 Inhibiting Surface Oxygen Reduction Reactivity	105
APPENDIX A. SUPPORTING INFORMATION FOR STRUCTURAL AND SUBSTITUENT GROUP EFFECTS ON MULTIELECTRON STAND- DARD REDUCTION POTENTIALS OF AROMATIC N-HETEROCYCLES	107
APPENDIX B. POURBAIX DIAGRAM GENERATION PROCEDURE .	123
B.1 Pourbaix Diagram Screening Procedure	123
B.2 Pourbaix Diagram Generator Keywords	125
B.3 Pourbaix Diagram Generator Keywords	129
B.4 Pourbaix Diagram Data Generation	130
B.5 Generating Pourbaix Diagrams	135
APPENDIX C. SUPPORTING INFORMATION FOR EXPLICITLY UN- RAVELING THE ROLES OF COUNTER IONS, SOLVENT MOLECULES, AND ELECTRON CORRELATION IN SOLUTION PHASE REAC- TION PATHWAYS	138

APPENDIX D. SUPPORTING INFORMATION FOR QUANTUM CHEMICAL ANALYSES OF BH_4^- AND BH_3OH^- HYDRIDE TRANSFERS TO CO_2 IN AQUEOUS SOLUTION WITH POTENTIALS OF MEAN FORCE	141
D.1 Umbrella Sampling Constraints for Reaction 1 ($\text{BH}_4^- + \text{CO}_2 \rightleftharpoons [\text{BH}_3\text{-H-CO}_2]^-$)	141
D.2 Umbrella Sampling Simulation Overlap for Reaction 1 ($\text{BH}_4^- + \text{CO}_2 \rightleftharpoons [\text{BH}_3\text{-H-CO}_2]^-$)	141
D.3 Umbrella Sampling Constraints for Reaction 2 ($\text{H}_2\text{O} + [\text{BH}_3\text{-H-CO}_2]^- \rightleftharpoons \text{BH}_3\text{OH}^- + \text{HCOOH}$)	144
D.4 Umbrella Sampling Simulation Overlap for Reaction 2 ($\text{H}_2\text{O} + [\text{BH}_3\text{-H-CO}_2]^- \rightleftharpoons \text{BH}_3\text{OH}^- + \text{HCOOH}$)	144
D.5 Umbrella Sampling Constraints for Reaction 3 ($\text{BH}_3\text{OH}^- + \text{CO}_2 \rightleftharpoons \text{BH}_2\text{OH} + \text{HCOO}^-$)	144
D.6 Umbrella Sampling Simulation Overlap for Reaction 3 ($\text{BH}_3\text{OH}^- + \text{CO}_2 \rightleftharpoons \text{BH}_2\text{OH} + \text{HCOO}^-$)	148
D.7 Comparing Reaction Energies against Average Potential Energies	148
D.8 Umbrella Sampling Simulation Timestep Comparison	148
APPENDIX E. SUPPORTING INFORMATION FOR DOPED TI OXIDES TO DEOPTIMIZE OXYGEN REDUCTION REACTION CATALYSIS	151
E.1 Creating Doped Ti Alloys	151
E.2 Metal Oxide X-ray Photoelectron Spectroscopy Data	151
E.3 XPS Characterization of Sn Doped Ti Oxide	153
E.4 ReaxFF Annealing Simulations	153
E.5 Determining Dopant Oxidation States	156
E.6 ORR Intermediate Scaling Relationships	157
E.7 Effect of Solvation on ORR Overpotentials	157
E.8 ORR Intermediates Adsorbed to Dopants	159

APPENDIX F. SUPPLEMENTARY ANALYSIS OF AVERAGE OXY-	
GEN REDUCTION REACTION OVERPOTENTIALS	166
F.1 Calculating ORR Overpotentials of the Two Electron ORR Mechanism . . .	166
F.2 Computing Average Overpotential increase from a metal dopant	168
APPENDIX G. SUPPORTING INFORMATION FOR INHIBITING THE	
OXYGEN REDUCTION REACTION ACTIVITY ON THE OXIDES	
OF TI-6AL-4V	171
G.1 Training and Validation of Neural Networks	171
G.2 Creating Accurate Surface Models	178
G.3 Calculating ORR Overpotentials	182
G.4 Determining Dopant Oxidation States	187
BIBLIOGRAPHY	189

LIST OF TABLES

2.1	Experimental and calculated pK_a s for ANH molecules in this work.	27
3.1	Bond lengths for the relevant bonds in the gSS-NEB determined reaction pathway.	50
5.1	Percent Change and standard deviation in current at $-0.8 V_{SCE}$ of alloy samples versus the undoped Ti.	86
6.1	TiAl ₂ O ₅ surface formation energies	96
A.1	Comparing energies calculated at different levels of QC theory	108
A.2	Substituent group effects on absolute pK_a s and redox potentials	109
C.1	Bond lengths for Figure 3.10	140
D.1	The bond lengths and force constants used to harmonically restrain bonds for Reaction 1.	142
D.2	The bond lengths and force constants used to harmonically restrain bonds for Reaction 2.	145
D.3	The bond lengths and force constants used to harmonically restrain bonds for Reaction 3.	147
E.1	Alloy and Oxide Compositions	153
E.2	Determining the oxidation state of metal dopants embedded in our amorphous TiO ₂ surface by comparing their Bader charges to those of the dopants in metal oxides where the oxidation state is known.	158
F.1	Computing average surface ORR inhibition for an Al ³⁺ dopant in amorphous TiO ₂	170

G.1	The combinations nodes in each hidden layer that were used to train neural networks	173
G.2	The average error, mean unsigned error (μe), and standard deviation for portions of the training and validation sets.	174
G.3	Determining the oxidation states of metal dopants by comparing Bader charges.	188

LIST OF FIGURES

1.1	Standard redox potentials referenced to the standard hydrogen electrode (SHE) in aqueous electrolyte solutions (pH = 7) at 25°C; taken from references [26] and [32].	4
1.2	Example ANH-CO ₂ complexes studied by Tossell. A) a neutral pyridine and CO ₂ complex. CO ₂ remains linear, and the complex has N-C length bond of 2.79 Å. B) a negatively charged pyridine and CO ₂ complex. CO ₂ becomes bent, and the N-C bond length decreases to 1.46 Å.	7
1.3	The reduction of pyridine into para-dihydropyridine, a pyridine derivative that Keith and Carter suggested as responsible for CO ₂ reduction.	8
1.4	Relative electrochemical energies referenced to the energy of pyridine at an SCE potential of (a) 0 V and (b) -0.58 V vs. the SCE for pyridine species in solution at different pH. (c) Pourbaix diagram depicting the most thermodynamically stable species at a given pH and electrode potential. Calculation data here used high level (U)CCSD(T)-F12/aug-cc-pVTZ-F12 calculations. Reproduced from ref. [54] with permission from The Royal Society of Chemistry	9
1.5	Combined experimental and DFT results showing that by spatially resolving the LUMO, the STM images predict the sites susceptible to nucleophilic attack[69] on adsorbed pyridine by adsorbed hydrides and protons from solution to produce 1,2- and 1,4- dihydropyridine, as described in ref [65]. Reprinted with permission from [70]. Copyright (2015) American Chemical Society.	12

1.6	Illustration of galvanic corrosion in an atmospheric environment. The junction of the two plates of metal 1 with a noble metal fastener establishes the galvanic junction of dissimilar metals that can cause corrosion once a droplet of water forms on the surface. The high surface area-to-volume ratio of the droplet allows a high dissolved oxygen concentration even once the reduction reaction begins consuming oxygen.	14
1.7	a) The associative ORR mechanism. * denotes a surface site. b) ORR reaction energies calculated on an amorphous TiO ₂ surface plotted at an applied potential of 0, 0.73, and 1.23 V _{RHE} . The blue arrows show the scaling relationship between reaction energies and the number of electrons involved.	18
1.8	Two possible types of oxide growth that can occur on a binary component, two-phase alloy. A) The α and β phases oxidize independently to form oxides enriched in the components of each phase. B) The α and β phases oxidize cooperatively to form an oxide with uniform composition.	19
2.1	Aromatic N-heterocycles (ANH) molecules considered in this work.	26
2.2	Redox reactions reported in Figure 2.3.	28
2.3	Redox potentials for 20 ANH molecules calculated at 0 pH. Lines correspond to redox processes shown in Figure 2.2. DMAP corresponds to N,N dimethylaminopyridine.	29
2.4	Electron density difference plots for transferring 1-e ⁻ to pyridine (left) and quinoline (right). Yellow areas correspond to higher electron density density in the radicals after 1-e ⁻ addition while gray areas correspond to lower electron density. Isovalue = 0.004 for both cases.	30
2.5	a) quinoline and b) 1,8-naphthyridine Pourbaix diagrams. The gray lines represent equilibrium between H ₂ CO ₃ , HCO ₃ ⁻ , and their potential reduction products (formic acid/formate). The red dashed line represents the hydrogen evolution reaction.	33

2.6	Compiled Pourbaix diagram triple point conditions for all considered molecules. The red dashed line corresponds to the hydrogen evolution reaction. Gray lines correspond to the CO ₂ equilibrium products and standard redox potentials in an aqueous environment.	34
3.1	Continuum solvated clusters created from gSS-NEB optimized coordinates containing a) only the reacting atoms, and b) the reacting atoms and the first solvation shell. Calculations without the counter ion use clusters that omit atoms in the shaded regions.	42
3.2	Reduction of CO ₂ to formate by BH ₄ ⁻	44
3.3	Model 1 transition state structures for BH ₄ ⁻ + CO ₂ being converted to formate and BH ₃ OH ₂ with a) zero, b) one, and c) three explicit H ₂ O molecules to stabilize the product (BH ₃ OH ₂).	45
3.4	Relative reactant, intermediate, and product energies from ORCA optimized structures using Model 1.	46
3.5	The relative energies of the gSS-NEB for BH ₄ ⁻ reacting with CO ₂ to produce formate. This reaction is qualitatively different from that identified using Model 1.	48
3.6	The gSS-NEB determines a) reactant, b) metastable intermediate, and c) product geometries for Figure 3.2. The dashed lines denote key interatomic distances (see Table 3.1).	49
3.7	Bader charge analysis on reacting fragments. The charge transfers from BH ₃ and the transferred hydride to CO ₂ over the course of the reaction. Na ⁺ (not shown here) has a consistent +0.85 charge over the course of the reaction.	51
3.8	Single point energy (SP) calculations on clusters from gSS-NEB optimized pathways for the reaction given in Figure 3.2. Energies were calculated with several different exchange correlation functionals as well as RI-MP2 (labeled as MP2) and DLPNO-CCSD (labeled as CCSD) in figures a) and c). See the main text for more details.	53

3.9	Electron density different plots showing the effect of a) continuum solvation on the isolated intermediate, b) the explicit waters in the first solvation shell interaction with the intermediate, c) a comparison of the NEB energy profile in Fig. 3.5 compared to different calculations using the reacting atoms, the counter ion, and the nine explicit waters that appeared active from Fig. 3.9b, d) a comparison of the NEB energy profiles using COSMO or SMD-embedded molecular clusters containing the counter ion and the explicit solvation shell. Single point energies were performed at the PBE0/def2-TZVP level.	56
3.10	CO ₂ reduction with BH ₃ OH ⁻ to produce formate.	57
3.11	A) The transition state structure for the hydride transfer from BH ₃ OH ⁻ to CO ₂ to produce formate. B) The reaction pathway energies for the reaction in Figure 3.10 calculated using ORCA (B3LYP/def2-TZVP embedded in COSMO solvation).	58
3.12	A) The transition state structure for the hydride transfer from BH ₃ OH ⁻ to CO ₂ to produce formate. B) The reaction pathway energies for the reaction in Figure 3.10 calculated using ORCA (B3LYP/def2-TZVP embedded in COSMO solvation).	59
3.13	Single point energy (SP) calculations on clusters from gSS-NEB optimized pathways for the reaction given in Figure 3.10. Energies were calculated with several different types of KS-DFT as well as RI-MP2 (labeled as MP2) and DLPNO-CCSD (labeled as CCSD) for all of the clusters described in the computational methods on a) only the reacting atoms without Na ⁺ , b) the reacting atoms with Na ⁺ , and c/d) the geometries from a) and b) with the first solvation shell.	60
4.1	Three pathways characterized with umbrella sampling. Reactions 1 and 2 are parts of a sequential, two-step hydride transfer reaction. Reaction 3 is a different one-step hydride transfer from a partially oxidized borohydride species (BH ₃ OH ⁻). These reaction pathways all involve explicit solvation and a Na ⁺ counter ion and were obtained with G-SSNEB calculations in previous work.[216]	66

4.2	Reaction pathway analyses of Reaction 1 (Figure 4.1) using C-H bond distance as the reaction coordinate. A) Plot of B-H distance vs. C-H distance over the course of Reaction 1. Transition states are marked with a triangle. B) Minimum free energy reaction pathways determined from WHAM analysis (labelled PMF), G-SSNEB reaction pathway optimizations at 0 K (labelled NEB[216]).	67
4.3	Analysis of Reaction 2 in Figure 4.1. A) Minimum energy reaction pathways determined from WHAM analysis (labelled PMF) or obtained from G-SSNEB reaction pathway optimizations (labelled NEB). Transition states are marked with a triangle. B) Reaction energies determined from WHAM analysis or obtained from G-SSNEB reaction pathway optimizations.[216] .	69
4.4	Analysis of Reaction 3 in Figure 4.1. A) Minimum energy reaction pathways determined from WHAM analysis (labelled PMF) or obtained from G-SSNEB reaction pathway optimizations (labelled NEB). Transition states are marked with a triangle. B) Reaction energies determined from WHAM analysis or obtained from G-SSNEB reaction pathway optimizations.[216] .	71
5.1	The radial distribution functions for the Ti-Ti, Ti-O, and O-O pairs from the ReaxFF annealed structure, the annealed structure after being optimized with density functional theory in VASP, and experimental data.[243] The QM optimized structure agrees with experimental data.	78
5.2	a) The associative ORR mechanism modeled in this work. * denotes an empty surface site on the material. b) ORR reaction energies calculated with PBE for four different surface sites in the undoped TiO ₂ surface (labeled 1-4) plotted at an applied potential of 0 and 1.23 V _{SHE} . The intermediates correspond to the reactions in Figure 5.2a.	80

5.3	Sabatier volcano plots of computationally predicted dopant overpotentials. Dopants that were predicted and tested in this work are labeled in red, and dopants not yet experimentally verified are labeled in black. a) overpotentials calculated with PBE without solvation effects, b) overpotentials calculated with HSE06 and including solvation energies. HSE06 calculations were only performed for dopants with available experimental data. The effect of solvation is discussed further in Figure E.6.	83
5.4	Cathodic polarizations scans of the undoped titanium and the 1 at% doped titanium samples in air-saturated 0.6 M NaCl at pH 12 with a scan rate of 0.167 mV/s. Each scan began after an 18-hour OC hold.	85
6.1	An illustration of galvanic corrosion in an atmospheric environment. The contact between metal 1 and the noble metal fastener forms a galvanic junction that can corrode metal 1 when a water droplet is present on the surface.	90
6.2	Parity plots of neural network (NN) and DFT absolute energies for surface structures that were a) annealed and b) annealed and quenched with neural network one (NN1) and two (NN2). All DFT energies were calculated with PBE. c) The Ti/Al/O-Ti/Al/O and Ti-Ti/Al radial distribution functions for an amorphous TiAl_2O_5 slab after being quenched with NN2 and fully relaxed with DFT.	94
6.3	a) A comparison of neural network (NN) and DFT absolute energies for defective and amorphous surface structures annealed and quenched with neural network two. b) The energy of defective surfaces compared against the energy of the crystalline surface in the gas phase and solvated with VASPsol. The 200, 300, 400, and 600 K lines correspond to the kinetic energy present at each temperature added to the energy of the relaxed (010) crystalline surface ($E = -1134.97$ eV).	97
6.4	a) The associative ORR mechanism modeled in this work. The minimum gas and solvent phase ORR overpotentials for each surface calculated using b) PBE and c) HSE06.	99

6.5	The gas and solvent phase ORR overpotentials for dopants embedded in an amorphous surface calculated with a) PBE and b) HSE06 as well as a crystalline surface calculated with c) PBE and d) HSE06. "A" = the most active amorphous surface site, "Swap" = the most active crystalline surface site when a surface Ti and Al are swapped, and "Cryst" = the most active crystalline surface site.	102
A.1	Quinoline Pourbaix diagram	109
A.2	2-quinoline Pourbaix diagram	110
A.3	1,2-diazine Pourbaix diagram	110
A.4	1,3-diazine Pourbaix diagram	111
A.5	1,4-diazine Pourbaix diagram	111
A.6	1,4-naphthyridine Pourbaix diagram	112
A.7	1,6-naphthyridine Pourbaix diagram	112
A.8	1,8-naphthyridine Pourbaix diagram	113
A.9	Phenanthroline Pourbaix diagram	113
A.10	2,2'-bipyridine Pourbaix diagram	114
A.11	4,4'-bipyridine Pourbaix diagram	114
A.12	4-Cl-quinoline Pourbaix diagram	115
A.13	Pteridine Pourbaix diagram	115
A.14	Adenine Pourbaix diagram	116
A.15	Purine Pourbaix diagram	116
A.16	Benzimidazole Pourbaix diagram	117
A.17	4-CN-quinoline Pourbaix diagram	117
A.18	Mercaptopteridine Pourbaix diagram	118
A.19	2-picoline Pourbaix diagram	118
A.20	3-picoline Pourbaix diagram	119
A.21	4-picoline Pourbaix diagram	119
A.22	2,6-lutadine Pourbaix diagram	120
A.23	2,5-lutadine Pourbaix diagram	120
A.24	4-aminopyridine Pourbaix diagram	121

A.25	N,N-dimethyl-4-aminopyridine Pourbaix diagram	121
A.26	Nicotinamide Pourbaix diagram	122
A.27	4-acetylquinoline Pourbaix diagram	122
B.1	The basic connectivity for the molecules produced by adding protons to pyridine. This demonstrates the exponential growth of unique molecular structures with additional protons.	124
B.2	The screening procedure used to calculate molecular Pourbaix diagrams. . .	126
C.1	Additional energetics for Model 1 at the B3LYP/PBE/PBE0/MP2/DLPNO-CCSD (def2-TZVP) level. The energetics correspond to the coordinates shown in a) Figure 3.3a (1 H ₂ O molecule) in the main text, b) figure 3.3b (2 H ₂ O molecules) in the main text, and c) figure 3.3c (4 H ₂ O molecules) in the main text. The transition state and product energies vary by up to 0.2 eV, but the overall trend is the same for every level of theory considered. . .	139
C.2	Additional energetics for Figure 3.10 using Model 1 at the B3LYP, PBE, PBE0, MP2, DLPNO-CCSD (def2-TZVP) level. The energetics correspond to the coordinates shown in Figure 3.11a.	140
D.1	The umbrella sampling simulation overlap between umbrella sampling windows. Gray B-H and C-H bond length distributions correspond to reaction coordinates from G-SSNEB calculations, while red B-H and C-H bond distributions correspond to reaction coordinates interpolated between G-SSNEB images.	143
D.2	The umbrella sampling simulation overlap between umbrella sampling windows. Gray B-H and C-H bond length distributions correspond to reaction coordinates from G-SSNEB calculations, while red B-H and C-H bond distributions correspond to reaction coordinates interpolated between G-SSNEB images.	146

D.3	The umbrella sampling simulation overlap between umbrella sampling windows. Gray B-H and C-H bond length distributions correspond to reaction coordinates from G-SSNEB calculations, while red B-H and C-H bond distributions correspond to reaction coordinates interpolated between G-SSNEB images.	149
D.4	The NEB energy profile, PMF free energy profile, and average unbiased potential energies from umbrella sampling windows containing the reactant, transition state, and product for reaction three.	150
D.5	Umbrella sampling energetics for Reaction 1 using an 0.5 and 0.25 fs timestep	150
E.1	X-ray diffraction spectra for each alloy after casting and machining processing.	152
E.2	Representative sample of chemical characterization of the oxides by XPS. Plot of counts per second as a function of binding energy for the oxide formed from the $\text{Ti}_{99}\text{Sn}_1$ alloy after 96 hours exposure to air.	154
E.3	The Ti-Ti pair radial distribution function for rutile TiO_2 annealed with ReaxFF in LAMMPS. The initial surfaces were supercells composed of 1x1, 3x3, 7x7, and 15x15 rutile TiO_2 unit cells. The average features of the material converge by the 3x3 simulation cell.	155
E.4	Comparing Mn Bader charges in materials where Mn's oxidation state is well known. Benchmarking bader charges helps determine the oxidation state of Mn in our amorphous surface.	156
E.5	The scaling relationship between the energy of OH and OOH adsorbed to dopant atoms in the amorphous surface. This correlation is used to create the volcano in the Sabatier activity volcano plots in the main text.	159
E.6	Sabatier volcano plots of computationally predicted dopant overpotentials. Dopants that were predicted and tested in this work are labeled in red, and dopants not yet experimentally verified are labeled in black. Overpotentials calculated with a) PBE, b) PBE + VASPsol solvation, c) HSE06, and d) HSE06 + VASPsol solvation. Although already shown in the main text, a) and d) are shown here as a comparison.	160

E.7	Reaction intermediates adsorbed to the 4 different sites on the undoped surface. Pink spheres denote Ti atoms, red spheres atoms denote O atoms, and white spheres denote H atoms.	161
E.8	ORR intermediates adsorbed to Ag^+ , Al^{3+} , Co^{2+} , and Cr^{3+} . Pink spheres denote Ti atoms, red spheres atoms denote O atoms, white spheres denote H atoms, and other colored spheres denote dopant atoms.	162
E.9	ORR intermediates adsorbed to Cu^{2+} , Ga^{3+} , Ge^{4+} , and Mn^{2+} . Pink spheres denote Ti atoms, red spheres atoms denote O atoms, white spheres denote H atoms, and other colored spheres denote dopants atoms.	163
E.10	ORR intermediates adsorbed to Nb^{5+} , Ni^{2+} , Sc^{3+} , and Si^{4+} . Pink spheres denote Ti atoms, red spheres atoms denote O atoms, white spheres denote H atoms, and other colored spheres denote dopant atoms.	164
E.11	ORR intermediates adsorbed to Sn^{4+} , V^{3+} , V^{5+} , and Zn^{2+} . Pink spheres denote Ti atoms, red spheres atoms denote O atoms, white spheres denote H atoms, and other colored spheres denote dopant atoms.	165
F.1	a) The two electron ORR mechanism and four electron ORR mechanism. b) Comparing the four electron (left) and two electron ORR (right) mechanism thermodynamic onset potentials. "A" = the most active amorphous surface site. All energetics computed with PBE.	167
G.1	The error in the training and validation set for neural network one for a) and b) all equation of state data, c) and d) independent stresses on each unit cell vector, and e) and f) moving individual Ti, Al, and O atoms in the x, y, and z directions within a crystalline supercell. All energies are referenced against that of the crystalline material.	175
G.2	The error in the training and validation set for neural network two for a) and b) all equation of state data, c) and d) independent stresses on each unit cell vector, and e) and f) moving individual Ti, Al, and O atoms in the x, y, and z directions within a crystalline supercell. All energies are referenced against that of the crystalline material.	176

G.3	The error in the training and validation set for annealed bulk structures computed with a) neural network one and b) neural network two. All energies are referenced against that of the crystalline material.	177
G.4	A comparison of neural network and DFT energies for surface structures annealed and quenched with NN1. Zone I = crystalline surfaces with swapped Ti/Al atoms, II = surface defects, III = amorphous surface structures. The 300, 400, and 600 K lines correspond to the kinetic energy present at each temperature added to the energy of the relaxed (010) crystalline surface ($E = -1134.97$ eV).	178
G.5	The Ti/Al/O-Ti/Al/O and Ti-Al/Ti RDFs for four different annealed structures. Each structure was fully relaxed with DFT (PBE) after being annealed and quenched using a neural network. The Ti-Ti/Al radial distribution function shows the variety of different structures that can be observed with annealing simulations.	180
G.6	a) and c) The neural network and DFT energies computed during on structures obtained from MD simulations using neural network two. b) and d) The neural network and DFT energies computed on fully quenched structures obtained from MD simulations using neural network two.	181
G.7	The low energy (010) crystalline surface, two (010) crystalline surfaces with swapped Ti/Al atoms, two defective surfaces produced by annealing simulations, and the lowest energy amorphous surface located from an annealing simulation.	183
G.8	The scaling relationship between *OOH and *OH on the doped TiAl_2O_5 surfaces.	184
G.9	The ORR overpotentials for all potential reaction sites on the a) Amorphous, b) Defect B, c) Defect A, d) Swap B, e) Swap A, and f) Crystalline TiAl_2O_5 surfaces. All overpotentials are computed from HSE06 energy calculations on structures optimized with PBE.	185

G.10 The ORR overpotentials for all potential reaction sites on the a) Amorphous, b) Defect B, c) Defect A, d) Swap B, e) Swap A, and f) Crystalline TiAl_2O_5 surfaces. All overpotentials are computed from PBE energies. 186

PREFACE

I am extremely grateful to all of those who have supported me through this research. I would especially like to thank my advisor Dr. John Keith for his help, guidance, and continuous ability to provide new ideas. I am also grateful to the other members of the Keith lab for their advice and for forcing me to think critically about my research. I thank Dr. Aude Marjolin and Dr. Victor Oyeyemi for helping me learn the ropes when I first started as a graduate student. I would also like to thank Karthikeyan Saravanan and Yasemin Basdogan for many great conversations about research and for putting up with my jokes.

I am grateful to all of my friends for providing relief from the occasional monotony of research. Thanks to my Michigan friends, especially Mckenzie, Matt and Aj, for always wanting to hangout when I'm visiting Grand Rapids. Travis and Zach, thanks for being available to talk (and trying to hangout when we are in the same area). Tim, thanks for flying out to Pittsburgh to visit whenever you had time, your visits were always appreciated. Brandon, thanks for helping me resist becoming a fan of the Pittsburgh Penguins. Thanks to Kyle (the 2018 curling bracket champion), Dan, and Andrew for helping me relax by playing video games online. I would also like to thank all of the friends I have made at the Pittsburgh Theological Seminary for many great games of ultimate frisbee and incredibly late boardgame nights. There are too many of you to list by name, but I am incredibly thankful for your support.

Finally, I would like to thank my siblings for their support and my parents for helping me appreciate the value of dedication and hard work. Most importantly, I thank my wife Annamarie for being a constant source of motivation and encouragement throughout this process. Your kind words and patience have helped provide me with the motivation required to successfully complete this research.

1.0 INTRODUCTION

This chapter is divided into two distinct sections. Section 1.1 summarizes the recent advances towards using aromatic N-heterocycles to promote electrocatalytic CO₂ reduction. This section provides the background and motivation for chapters 2, 3, and 4. Section 1.2 provides details about galvanic corrosion processes, modeling the oxygen reduction reaction with computational techniques, and building oxide surface models that are relevant to Chapters 5 and 6.

1.1 ELECTROCATALYTIC CARBON DIOXIDE REDUCTION

The content of this section was previously published as part of M. C. Groenenboom, K. Saravanan, and J. A. Keith, "Homogeneous M(bpy)(CO)₃X and aromatic N-heterocycle catalysts for CO₂ reduction" in *Electrochemical Reduction of Carbon Dioxide Overcoming the Limitations of Photosynthesis*, D. Fermin, F. Marken (Eds.), Royal Society of Chemistry, ISBN: 9781782620426.

1.1.1 Chemically Reducing Carbon Dioxide

Sustainable, efficient and economical CO₂ utilization as a chemical feedstock addresses two potentially catastrophic problems facing humanity.[1, 2, 3] First, it would stem the accumulation of anthropogenic CO₂, which is correlated with severe weather patterns[4] and global climate change[5] that bring severe economic consequences. Second, it would alleviate the global dependence on petroleum for transportation fuels and petrochemical feedstocks while

allowing greater flexibility with how finite petroleum reserves are used. Industrially-scalable routes to convert CO₂ to liquid fuels (e.g. methanol) are greatly desired but not yet available. The U.S. Energy Information Administration projects that more 32% of the energy used by OECD nations will come from liquid fuels until 2040.[6] There is a massive barrier for completely abandoning petroleum based liquid fuels for other energy sources, so chemical processes that regenerate fuels and petrochemicals from post-combustion CO₂ are greatly desired.

Regenerating petroleum via carbon-neutral[7] CO₂ recycling processes requires that anthropogenic CO₂ be captured[8] and then converted.[3, 9] Synthesizing chemicals and fuels from coal, natural gas, or renewable forms of carbon inevitably requires H₂ which is most economically generated by steam reforming fossil fuels like coal or natural gas. Unfortunately, these processes release CO₂. Producing H₂ from water electrolysis itself does not release CO₂, but this requires electricity that is typically generated from burning coal or natural gas. Entirely solar-driven processes[10] may hopefully soon bring sustainable and economical carbon-neutral solar fuels, but doing so requires improved fundamental understanding for how to activate and convert CO₂.

Converting CO₂ into useful products requires substantial amounts of energy. Possible schemes to do so range from utilizing bacterial microorganisms,[11] molten salts,[12, 13] formate and CO dehydrogenase enzymes[14, 15] enzyme surrogate models,[16, 17] molecular homogeneous catalysts,[18, 19, 20, 21, 22, 23, 15] industrial thermal processes,[24] solar-powered metal oxide reactors,[25] and electrochemical methods in traditional[26] or solid oxide[27] devices as well as continuous flow electrolyzers.[28] Though these processes are diverse, at an atomic level, CO₂ conversion fundamentally requires energetically efficient hydrogenations under different chemical environments. An atomic-level understanding of how different H-transfer steps occur would likely provide fundamental insight into how such processes can be better engineered.

Many consider electrochemical CO₂ reduction a promising avenue to investigate. Unfortunately, the electricity consumed by these processes is often generated by burning fossil fuels. To design more sustainable and environmentally friendly processes, we can utilize photovoltaic devices to generate carbon-neutral electricity from sunlight that can in turn

be used to drive CO₂ reduction.[29] A common concept in electrochemistry is the standard redox potential, E , defined as the free energy change in an electrochemical reaction, ΔG , divided by the number of electrons transferred, n , and Faraday’s constant, F :

$$E = -\Delta G/nF \tag{1.1}$$

Figure 1.1.1 lists several relevant standard redox potentials involved in CO₂ reduction and exemplifies why such processes are challenging. First, Eq. 1.2a shows that adding one electron to CO₂ requires more than 1.9 eV (43.8 kcal/mol, since the redox potential corresponds to the lower limit of the actual reaction barrier). Second, while less-negative redox potentials are associated with simultaneously transferring multiple electrons and protons, such reactions carry an unfavorable entropy penalty, necessitating higher overpotentials. (Note that electrochemical reaction barriers govern activation overpotentials defined within the Butler-Volmer equation.) However, activation overpotentials nowadays are also often referred to as the extra thermodynamic energy, relative to the thermodynamic equilibrium potential, required to make all sequential reaction intermediates downhill in energy. Though less-rigorous, this approximation is often heuristically valid.[30, 31, 32] Lastly, since electrochemical reduction involves proton and electron transfers, CO₂ reduction must compete with the hydrogen evolution reaction (HER, Eq. 1.2i). To maximize their efficiency, CO₂ electro-reduction catalysts must have the lowest possible overpotential while also inhibiting pathways that result in H₂ generation.

Another consideration is the energy required to convert CO₂ relative to the energy that is stored within the final reduced products. Often times the sunlight driven processes are energetically efficient, but they also have small thermodynamic driving forces to form products, and thus reaction rates are slow. High overpotential processes on the other hand have much higher driving forces for product formation but require much more energy. In each case, there is knowledge that can be gained by studying catalytic reaction pathways, particularly by using first principles quantum chemistry. With these tools, reaction energies and barrier heights for elementary reactions can be predicted with reasonable degrees of accuracy. By linking together elementary pathways, we can better understand full reaction mechanisms, and obtain insights into how to make slow reaction steps occur faster and with less energy.

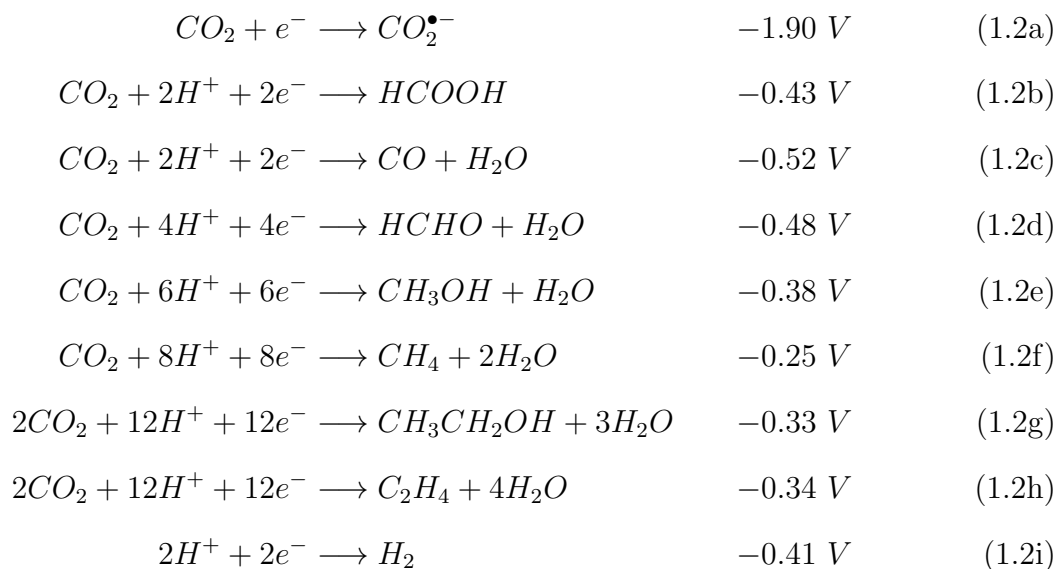


Figure 1.1: Standard redox potentials referenced to the standard hydrogen electrode (SHE) in aqueous electrolyte solutions (pH = 7) at 25°C; taken from references [26] and [32].

1.1.2 Aromatic N-Heterocycle Promoted Carbon Dioxide Reduction Processes

Many CO₂ conversion processes only operate with high overpotentials. Again, this is usually attributed to the high reduction potential to form CO₂^{•-} from CO₂ (Eq. 1.2a) or the energy required to regenerate reaction sites on the catalyst by removing reaction intermediates (i.e., CO or CHO).[33] Brønsted acids are often included in these systems to provide protons for proton-coupled electron transfers (PCET). PCET mechanisms are less endoergic,[34, 35, 36] and thus can be expected to operate at lower reaction overpotentials. Unfortunately, these protons also increase hydrogen evolution reaction activity and thus lower the overall selectivity and efficiency for CO₂ reduction. An ideal process would have a low overpotential and a high selectivity for CO₂ reduction.

The past decade has seen numerous experimental reports of CO₂ reduction occurring at low overpotentials with high faradiac efficiencies using aromatic N-heterocycles (ANHs) in aqueous solutions. Bocarsly and co-workers first reported this chemistry using electrolytes

containing pyridinium with hydrogenated Pd electrodes.[37] Later, the chemistry was revisited using pyridinium[38, 39], and imidazolium[37] to promote CO₂ reduction on several types of metal electrodes. While some reports have claimed not to see products,[40, 41] others have,[42, 43] raising the question of what the mechanism for these processes might be. There has been a significant amount of research towards using pyridine and other ANH containing molecules to improve electrochemical CO₂ reduction with metal electrodes.

It has been argued that this chemistry must have a surface dependence because ANH-promoted CO₂ reduction was reported to occur on Pt but not glassy carbon electrodes.[44] However, MacDonnell and co-workers[45] used a homogeneous photochemical cells containing[Ru(phen = phenanthroline)₃]²⁺ chromophores to reduce CO₂ to methanol in the presence of pyridinium. Furthermore, Dyer has reported ¹³C-labeled experiments resulting in methanol using mercaptopteridine ANH molecules,[46] though interpretations of these results have recently been questioned by Tard and Saveant.[40]

Portenkichner et. al. observed CO₂ reduction to methanol in the presence of pyridine and pyridazine on platinum electrodes.[42] They also note that no methanol was formed when only acetic acid was present, suggesting that pyridine plays an integral role in the reaction and serves as more than a proton source. Similar studies by Rybchenko,[43] Yang,[47] Chernyshova,[48] and Lee[49] have also reported CO₂ reduction to formate or methanol in the presence of pyridine, pyridine embedded into platinum electrodes, pyridine based polymers wrapped around copper electrodes, and pyridoxine (vitamin B-6, also an ANH molecule) at various faradaic efficiencies and overpotentials. However a number attempts to obtain similar results with analogous studies have found that these ANH molecules appear to only increase the rate of the hydrogen evolution.[50, 44, 41, 40] Currently, there is no consensus on how ANH molecules serve in these reactions, but on the basis of work by Portenkirchner et al., it appears the ANH molecules are playing a role beyond that of simply being a Brønsted acid. Understanding why ANH molecules might cause lower overpotentials and higher faradic efficiencies would provide helpful design principles for improved renewable energy catalysts.

1.1.3 Studies of Homogeneous ANH Reaction Mechanisms

Several computational groups have attempted to elucidate the role of ANH molecules in CO₂ electroreduction reactions with quantum chemistry calculations. This section discusses homogeneous reaction mechanism studies that do not explicitly account for reactions taking place at electrode surfaces. The impact of the electrode surface will be discussed later.

The first computational study related to ANH chemistry utilized DFT to calculate reaction energetics and HOMO orbitals of several proposed intermediate states.[38] Later, Tossell calculated additional thermodynamic energetics including p*K*_as and standard redox potentials which showed that the one electron reduction potential of pyridine and protonated pyridine were both significantly more negative (-2.90 and -1.44 V vs SCE, respectively) than the reported experimental conditions (-0.58 V vs SCE).[51] Tossell also calculated a series of ANH-CO₂ complexes, an example of two such complexes is shown in Figure 1.2. Binding CO₂ in this complex is energetically uphill for pyridine (complex a in Figure 1.2), but it is energetically more favorable with other ANH molecules (such as imidazole and 1,5,7-triazabicyclo[4.4.0]dec-5-ene (TBD)). The complexes also form spontaneously if either pyridine or CO₂ has been reduced by one electron (complex b in Figure 1.2). By calculating one electron reduction potentials for these ANH-CO₂ complexes (-1.44 to -1.76 V vs. SHE) he showed that they were easier to reduce than CO₂ alone (-2.16 V vs SCE). While imidazole and TBD more readily formed complexes with CO₂, the redox potentials of those complexes were significantly more negative (and less favorable) than that of the pyridine-CO₂ complexes. These calculations supported the claim that ANH molecules could potentially serve as CO₂ reduction catalysts.

Other mechanisms, such as those proposed by the Carter group and the Musgrave group considered pyridinium as a CO₂ reducing agent. The conclusions of these studies from the two groups differed in the extent to which the ANH molecule reduces CO₂. In 2012, calculations by Keith and Carter[52] reiterated that the one electron reduction potential of pyridinium (-1.37 V vs SCE) to form the pyridinyl radical (PyH[•]) as well as the ANH-CO₂ complexes calculated by Tossell were significantly more negative than the experimental reduction potential (-0.58 V vs SCE) reported by Bocarsly.[38] This extremely negative reduction potential

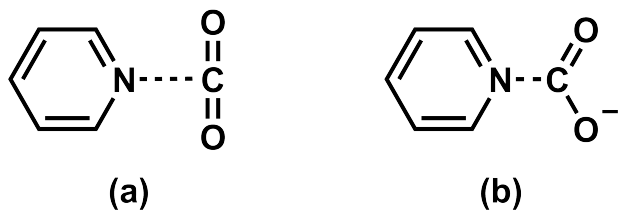


Figure 1.2: Example ANH-CO₂ complexes studied by Tossell. A) a neutral pyridine and CO₂ complex. CO₂ remains linear, and the complex has N-C length bond of 2.79 Å. B) a negatively charged pyridine and CO₂ complex. CO₂ becomes bent, and the N-C bond length decreases to 1.46 Å.

means that it is very unlikely that PyH• would participate in CO₂ reduction unless at very high applied potentials or in the presence of photolysis conditions.[52, 53] However, other ANH molecules, such as doubly protonated 4,4'-bipyridine, have less negative one electron reduction potentials (-0.37 V vs SCE) and could be more active reduction catalysts.

Keith and Carter later predicted that the reduction event observed at -0.58 V vs SCE on Pt electrodes may actually correspond to the two electron reduction of pyridine to dihydropyridine, see Figure 1.3.[54] By calculating the energy of various protonated and reduced states of pyridine they created a molecular Pourbaix diagram, as shown in Figure 1.4. Pourbaix diagrams are electrochemical phase diagrams that show the most stable state for a molecule (or material) at different applied potentials and pH values. These can be used to predict which form of reduced pyridine would be most stable near the reaction conditions. The Pourbaix diagram revealed that Py, PyH⁺, and 1,4-dihydropyridine all have similar chemical potentials near the experimental conditions for CO₂ reduction. 1,4-dihydropyridine closely resembles the active moiety in NADH, one of nature's most active redox catalysts. This suggests that these Py species might reduce CO₂ through some type of coupled proton-electron transfer, or a biomimetic proton-hydride transfer reaction. These Pourbaix diagram triple-points may also serve as descriptors of the electrochemical conditions where ANH molecules are most active as proton/hydride transfer agents. Marjolin and Keith later continued in this direction to show that several different ANH molecules also have two-electron reduced species

with standard redox potentials close to those for CO₂ reduction.[55] While this methodology produces useful thermodynamic descriptors, accurate reaction barriers would still be needed to fully understand this proposed mechanism.

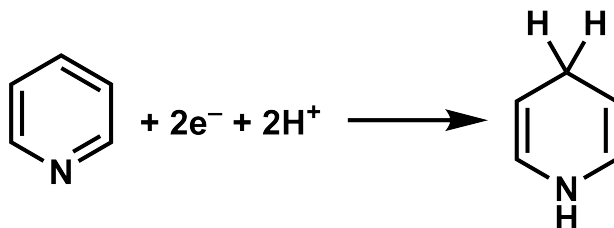


Figure 1.3: The reduction of pyridine into para-dihydropyridine, a pyridine derivative that Keith and Carter suggested as responsible for CO₂ reduction.

Musgrave and coworkers presented data supporting a one-electron pyridine assisted CO₂ reduction mechanism in 2013.[56] Calculations on a Pt surface proposed that PyH• can be formed, and that this radical can react with CO₂ to form PyCOOH• through an inner-sphere electron transfer as was originally proposed by Bocarsly.[38] While the reaction to form PyCOOH• is energetically uphill, they report that the reaction barrier is substantially lower when the electron transfer is accompanied by a proton transfer across a water chain from the aqueous solvent. Because PyH• has a very high p*K*_a (approximately 29 as reported by Keith and Carter[57]), the proton transfer must likely be coupled with the electron transfer if it is to occur. Similar proton relay mechanisms were reported by Siegbahn.[58] This proton relay can be significantly more energetically favorable than the direct reaction of PyH• and CO₂ to produce PyH⁺ and CO₂^{•-}. While the formation of PyCOOH• is energetically favorable, their mechanism does not account for the high energetic cost to form PyH•.

In 2014 Musgrave and coworkers[59] presented another pyridine assisted CO₂ reduction mechanism that utilizes 1,2-dihydropyridine to reduce CO₂. The argument was that although 1,2-dihydropyridine was less stable than then 1,4-dihydropyridine species proposed by Keith and Carter, the sequential proton and electron transfer steps to make it were more energetically accessible. Again, their reaction mechanism assumes the facile formation of PyH•, which has a very negative calculated redox potential as previously mentioned and very short lifetime in solutions.[52] They stress that there are several routes to generate PyH•, such as

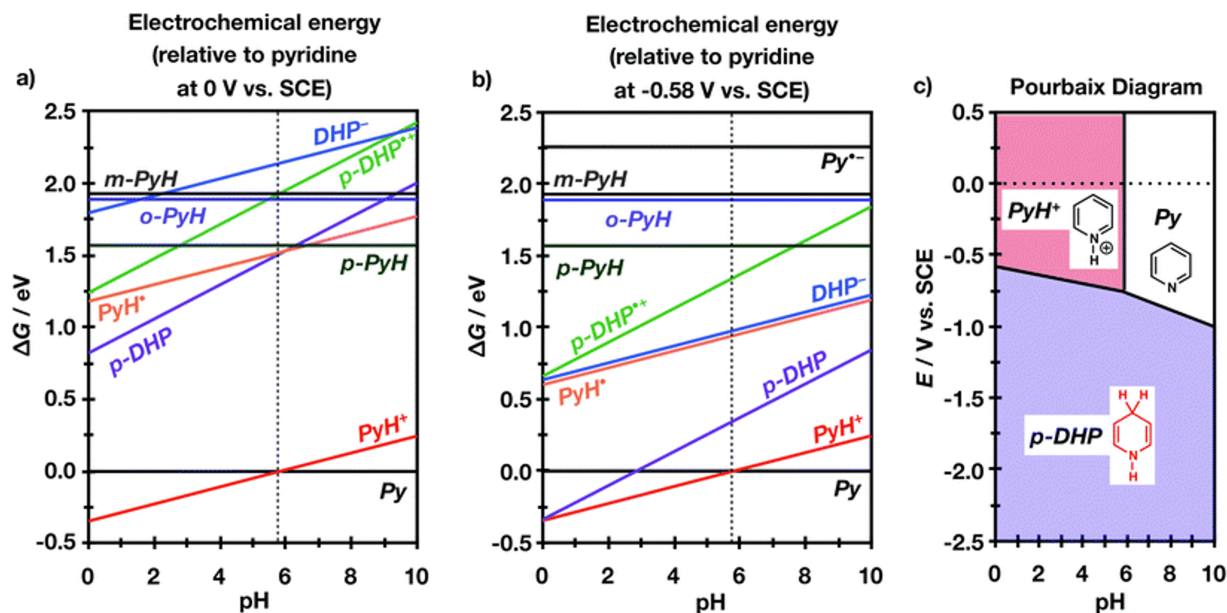


Figure 1.4: Relative electrochemical energies referenced to the energy of pyridine at an SCE potential of (a) 0 V and (b) -0.58 V vs. the SCE for pyridine species in solution at different pH. (c) Pourbaix diagram depicting the most thermodynamically stable species at a given pH and electrode potential. Calculation data here used high level (U)CCSD(T)-F12/aug-cc-pVTZ-F12 calculations. Reproduced from ref. [54] with permission from The Royal Society of Chemistry

photochemical production (which we address below). The proton and electron addition to PyH^\bullet to form dihydropyridine species are much more favorable and occur at easily achievable pH (4.1) and electrode potentials (0.11 V vs. SCE) respectively. Once formed, they report barrier heights for elementary steps to reduce CO_2 into methanol through a series of coupled proton-hydride transfers with reaction barriers between 6 and 20 $\text{kcal} \cdot \text{mol}^{-1}$ and quite exoergic reaction free energies between -15.5 and -36.7 $\text{kcal} \cdot \text{mol}^{-1}$.

Other experimental studies have presumed that pyridine assisted CO_2 reduction occurs through the PyH^\bullet species. MacDonnell and coworkers reported photochemical catalytic CO_2 reduction to formate and methanol using a ruthenium(II) trisphenanthroline chromophore

and pyridine.[45] They achieved 76 and 0.15 turnovers per Ru for formate and methanol, respectively. It was presumed that once the PyH^\bullet would be formed, it could proceed to reduce CO_2 by mechanisms similar to those originally postulated by Bocarsly and coworkers. PyH^\bullet can also be generated through photolysis and then react with CO_2 to form a $\text{PyH-COO}^{\bullet-}$ complex as demonstrated by Colussi and coworkers.[53] Although the mechanism of generating PyH^\bullet is different in photolysis experiments, there is indication that high energy PyH^\bullet may result in $\text{PyH-COO}^{\bullet-}$ complexes.

1.1.4 Studies of Surface Catalyzed ANH Reaction Mechanisms

We now turn to discuss studies of pyridine/ANH assisted CO_2 reduction processes that explicitly studied the role of electrode surfaces. Batista and coworkers were the first to report reaction pathways consisting of a proton coupled hydride transfer (PCHT) for ANH chemistry.[60] Their mechanisms involved the formation of a metal hydride on the platinum surface that then transferred to CO_2 while a nearby pyridinium ion donates a proton to result in CO_2 reduction into formic acid (HCOOH). The surface hydrogen could then regenerate by the one electron reduction of pyridinium ion near the electrode surface to regenerate a pyridine and a surface bound hydrogen atom. This process has a free energy barrier of 13 $\text{kcal} \cdot \text{mol}^{-1}$, and is predicted to occur at $E^0 = -0.72 \text{ V vs SCE}$, in good agreement with the original experimental redox potential reported for this process. In addition to providing protons during CO_2 reduction, pyridinium ions help establish a high proton concentration near the electrode surface necessary for the PCHT reaction. They later predicted that imidazole would exhibit similar electrochemical properties and facilitate CO_2 reduction with the same mechanism.[61] While their predicted redox potentials are in good agreement with the experimental measurements[62] for both pyridine and imidazole, CO_2 reduction products were not observed in the presence of acetic acid[42] (a weak acid with a $\text{p}K_a$ similar to pyridine) as one might predict if pyridine only served as a proton shuttle as suggested by this mechanism.

Belanger and coworkers reported surface dependence of pyridinium reduction in the context of CO_2 reduction by using cyclic voltammetry on different metal surfaces.[63] However,

Lucio and Shaw reported that gold electrodes behave differently than the earlier work with platinum electrodes.[41] They observed an irreversible reduction wave that they attribute to the one electron reduction of pyridinium to the PyH^\bullet at -1.0 V vs Ag/AgCl. They also noted an increase in reduction current when CO_2 and pyridine were present in solution, but no CO_2 reduction products. This is consistent with work by Savéant which showed that this current enhancement was likely due to carbonic acid catalyzing the hydrogen evolution reaction.[44]

Keith and Carter have also reported calculations for ANH assisted CO_2 reduction on models for GaP photoelectrodes.[64, 65] Their calculations predicted that proton and pyridinium ion reduction will be energetically unfavorable except at very negative electrode potentials, but the two electron/two proton reduction of pyridine to dihydropyridine on the GaP surface should be thermodynamically feasible ($E^0 = -0.63$ to -0.71 V vs SCE). Studies by Bocarsly using GaP photoelectrodes reported very high faradaic efficiencies for CO_2 reduction. Keith and Carter suggested that the standard reduction potential of 1,4-dihydropyridine is not that different as that obtained in aqueous solution and thus remains similar to that needed to electrochemically convert CO_2 into a variety of products. This contrasts with previous arguments that the illuminated p-GaP electrode can produce pyridnyl radicals.[56]

To address this point, Lessio and Carter reported that the transfer of photoexcited electrons to pyridinium from the GaP electrode as well as pyridinium adsorption to the GaP surface were not energetically favorable.[66] The conduction band minimum of the GaP electrode lies too low in energy to transfer electrons to PyH^+ . Investigating alternative mechanisms showed that reducing pyridinium to pyridine and an adsorbed hydrogen atom was more likely to occur than direct pyridinium reduction. This further supports a mechanism involving more than one electron reductions. Koel and coworkers used STM to experimentally probe the spatial positions of the LUMO of pyridine adsorbed to a GaP surface. This technique can determine atomic sites most susceptible to nucleophilic attack. Figure 1.5 compares the experimental STM to simulated data from DFT, and a simpler DFT side view. The STM data clearly identifies the sites that would be susceptible to nucleophilic attack from a surface hydrogen to form an adsorbed dihydropyridine. While not conclusive proof of this mechanism, it lends further support to a mechanism involving dihydropyridine like species

that has been recently investigated with computational theory[67] and experiment.[68] As with the homogeneous studies, insight from high quality studies of barrier heights will likely be needed.

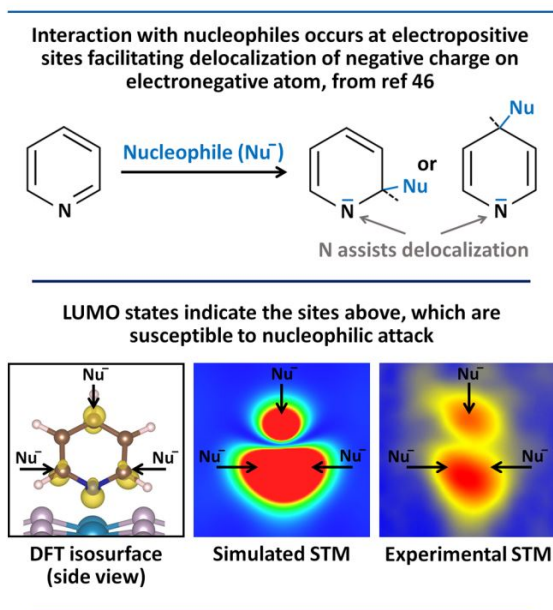


Figure 1.5: Combined experimental and DFT results showing that by spatially resolving the LUMO, the STM images predict the sites susceptible to nucleophilic attack[69] on adsorbed pyridine by adsorbed hydrides and protons from solution to produce 1,2- and 1,4-dihydropyridine, as described in ref [65]. Reprinted with permission from [70]. Copyright (2015) American Chemical Society.

1.2 MODELING THE ATOMISTIC REACTIONS THAT DRIVE CORROSION

All metals corrode and degrade if left unprotected. The resulting damage can lower a material's strength, hurt its appearance, and increase its susceptibility to future harm. Developing new technologies to inhibit corrosion rates can help increase the lifespan of materials and decrease the amount of required maintenance. Anti-corrosion coating improvements are often

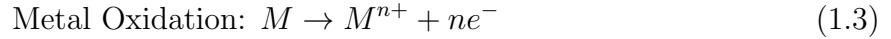
produced by trial-and-error rather than by utilizing a thorough understanding of the atomic scale corrosion reaction mechanisms involved. While this has produced very effective anti-corrosion technologies, first principles based quantum mechanics (QM) can help intelligently guide anti-corrosion technology design by providing additional insight into the atomic-scale reaction mechanisms that drive corrosion. Fortunately, these aspects can be explored faster and more accurately than ever before due to improvements in computational power.

1.2.1 Corrosion Chemistry

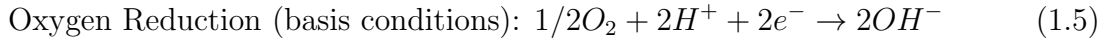
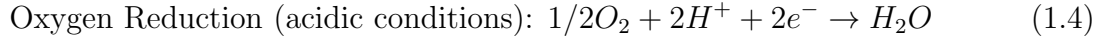
Corrosion damage can occur through many different mechanisms. The most common form of corrosion, general attack corrosion, degrades an entire exposed metal surface.[71] Despite being the most common type of corrosion, general attack corrosion is considered a predictable form of corrosion because it degrades the material uniformly. Other categories of corrosion such as localized corrosion, flow-assisted corrosion, and intergranular corrosion produce less-predictable damage and are more challenging to manage.[72] Galvanic corrosion is powerful enough that it can cause materials that are normally corrosion resistant to degrade.[73] Galvanic corrosion occurs when contact between two different metals produces a galvanic couple that greatly accelerates the corrosion rate of the less noble metal. This effect produces a driving force large enough to corrode aircraft grade aluminum alloys that are normally corrosion resistant in isolation.[74, 75, 76, 77] These types of metal contacts frequently occur near metal fasteners where strength and/or weight requirements can necessitate the use of different metal alloys.

From an atomistic perspective, corrosion damage is caused by metal oxidation at an anodic reaction site (eq. 1.3) producing electrons that drive reduction reactions at a nearby cathodic reaction site (eq. 1.4 or 1.5).[78] Water molecules can then solvate and remove the metal ions to produce the pitting damage often associated with corrosion.

Anodic reaction



Cathodic Reactions



During most corrosion processes these reactions occur on cathodic or anodic regions within one metal surface. Galvanic corrosion is unique because the anodic and cathodic reactions occur on entirely different surfaces as shown in Figure 1.6. The this contact causes a potential difference between the two metals and leads to the preferential oxidation of the less noble metal while the more noble metal facilitates the cathodic reduction reactions. If the cathodic reaction rates decrease, electrons produced from metal oxidation build up and decrease the driving force for metal oxidation. The ORR is the main cathodic reaction occurring at galvanic corrosion conditions in atmospheric environments,[79, 80, 81] and inhibiting the ORR provides an opportunity to decrease galvanic corrosion rates.

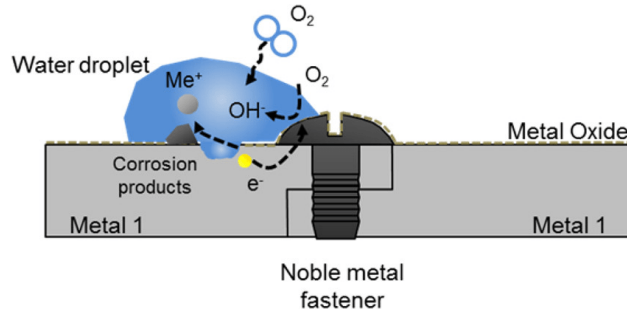


Figure 1.6: Illustration of galvanic corrosion in an atmospheric environment. The junction of the two plates of metal 1 with a noble metal fastener establishes the galvanic junction of dissimilar metals that can cause corrosion once a droplet of water forms on the surface. The high surface area-to-volume ratio of the droplet allows a high dissolved oxygen concentration even once the reduction reaction begins consuming oxygen.

1.2.2 Anti-Corrosion Technology

Many different anti-corrosion technologies are currently used. Barrier coatings that limit surface exposure, such as paint, can be easy to apply, but their effectiveness often depends on their durability, exposure, and method of application.[82, 83, 84] Alternatively, zinc galvanization can coat the material in a layer of zinc that sacrificially corrodes to preserve the underlying metal.[85] While zinc galvanization effectively suppresses corrosion, it requires high temperatures and exposure to molten zinc (Approximately 460°C). These conditions can be detrimental to the underlying material.

Corrosion can also be prevented by forcing the metal surface to be the cathode of an electrical cell via cathodic protection systems.[86, 87] Cathodic protection systems will use a sacrificial anode (similar to zinc galvanization) to protect the substrate and may supply electrical current to further suppress corrosion.[88, 87] While effective, cathodic protection systems are often difficult to implement because of the inability to provide an external power supply or sacrificial anode due to weight requirements.

Most metals have native oxide coatings that will spontaneously form on the metal surface. Native oxides are lighter than other types of coatings, do not require extreme application conditions, and naturally regenerate if damaged. Most native oxides are fairly stable, but further improving their protective ability can decrease the need for traditional barrier coatings. While oxides have previously been used to provide cathodic protection via photo-generated electrons,[89, 90] incorporating dopants into metal oxides to limit ORR activity to decrease the chemical driving force for metal oxidation has not yet been extensively tested.

1.2.3 Electrochemical Reaction Overpotentials

Reaction overpotentials are a simple criterion that can be used to evaluate an electrocatalyst’s activity. The reaction overpotential is the difference between a reaction’s thermodynamic redox potential and the potential where the reaction is first experimentally observed. Optimal electrocatalysts have small reaction overpotentials, while poor electrocatalysts have large reaction overpotentials. The reaction overpotential and reduction current are related with the Butler-Volmer equation (eq. 1.6).

$$i = i_0 \left(\exp\left(\frac{\alpha_a z F}{RT} \eta\right) - \exp\left(-\frac{\alpha_c z F}{RT} \eta\right) \right) \quad (1.6)$$

i is the total current density, i_0 is the current density if the presence of no overpotential (η), α_a and α_c are anodic and cathodic charge transfer coefficients, z is the number of electrons involved, F is Faraday’s constant, T is the absolute temperature, and R is the universal gas constant. Small overpotential changes can produce large changes in the reduction current density because of the exponential dependence on the reaction overpotential.

The computational hydrogen electrode model, first presented by Nørskov et. al.,[30] is one of the most common computational techniques used to predict the overpotentials of electrocatalysts. This model has been used to successfully study the oxygen evolution reaction, oxygen reduction reaction, and hydrogen evolution reaction on a variety of metal, metal alloy, and metal oxide surfaces.[91, 92, 93, 94] These studies are frequently found in the fuel cell literature, where optimal ORR catalysts are required to increase the overall energy efficiency of fuel cells. The model is based on the reversible hydrogen electrode (RHE) in which reaction 1.7 is in equilibrium at an applied potential of 0 V_{RHE} (for all pH values, all temperatures, and P_{H₂} = 1 atm).



The chemical potential of $\frac{1}{2} H_2$ ($\frac{1}{2} \mu_{H_2}$) is related to the chemical potential of H^+ (μ_{H^+}) and an electron (μ_{e^-}) with equation 1.8. A linear term accounts for the free energy change of an electron at applied potentials other than 0 V_{RHE} ($\Delta G = -eU$). Where e is the elementary positive charge, and U is the applied potential. This produces reaction energies that scale

with the applied potential. Applying this model to the associative ORR mechanism shown in Figure 1.7a produces the relative energies shown in Figure 1.7b for the reaction on an amorphous TiO₂ surface.

$$\mu(H^+) + \mu(e^-) = \frac{1}{2}\mu(H_2) - eU \quad (1.8)$$

The reaction overpotential (η) is defined as the difference between the thermodynamic equilibrium potential (1.23 V_{RHE}) and the potential where all the reaction steps are first downhill in energy (~ 0.73 V_{RHE}). While others have studied electrochemical reaction mechanisms by characterizing potential dependent barrier heights[95] or performing constrained molecular dynamics simulations,[96, 97] calculating reaction overpotentials with the computational hydrogen electrode model often provides similar accuracy while requiring less computational resources.

1.2.4 Modeling Reactions on Amorphous Oxide Surfaces

Modeling electrochemical reactions on crystalline metals or metal oxides is relatively straightforward. The most stable surface is either well known from previous studies or easily determined, and crystalline surfaces contain only a few unique reaction intermediate adsorption sites. If metal oxides are exposed to the environment, they are more likely to have an amorphous surface structure than a crystalline surface structure.[98] Modeling reactions on an amorphous surface is more complicated because one must create a valid amorphous surface structure with expensive annealing simulations and then test a larger number of unique reaction intermediate adsorption sites. Even after obtaining a low energy amorphous surface structure, the catalytic effects of high energy defects such as oxygen vacancies must be considered.[99]

Studying the reactions that occur on natively formed oxides of metal alloys is even more challenging because the oxide structure and composition are not so easily determined with computational tools.[100] This is further complicated by the fact that metal alloys (such as Ti-6Al-4V) can be composed of different phases that each contain different concentrations of the metals in the alloy. Each phase can have relative enrichment or depletion of any

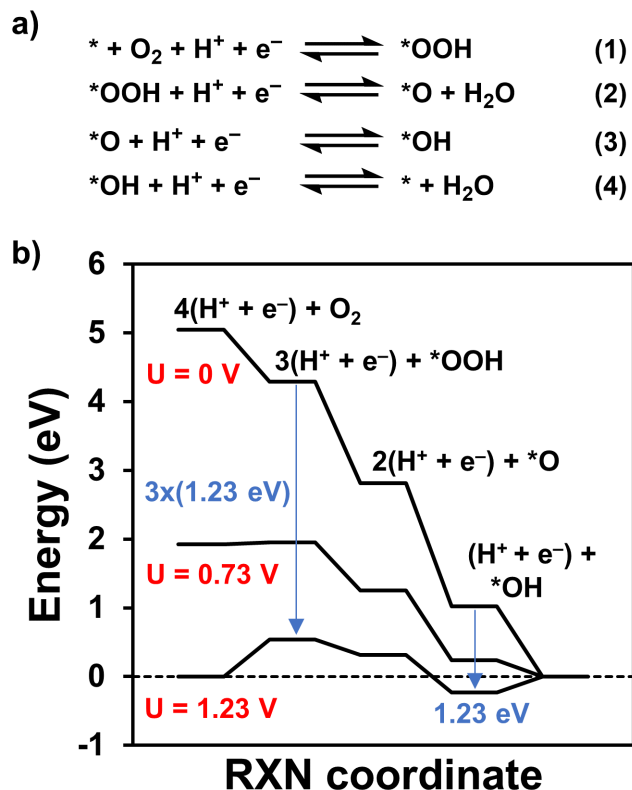


Figure 1.7: a) The associative ORR mechanism. * denotes a surface site. b) ORR reaction energies calculated on an amorphous TiO_2 surface plotted at an applied potential of 0, 0.73, and 1.23 V_{RHE} . The blue arrows show the scaling relationship between reaction energies and the number of electrons involved.

alloy component in their respective native oxides as shown in Figure 1.8.[101] It is extremely challenging to predict the growth mechanism and representative surface structures of the oxides that natively form on complex metal alloys. Sankaranarayanan and Ramanathan previously used molecular dynamics simulations to model the growth of an oxide film on a Ni-Al metal surface using the embedded atom model (EAM).[102] Unfortunately, no EAM potentials exist for Ti-Al-V-O systems, and the simulations required to study these oxide growth mechanisms with ab initio methods are not an efficient use of computational resources. Computational studies often utilize insight from experimental surface characterization to build

smaller surface models that contain the different types of reaction sites that would be present on a natively grown oxide surface. These surface models avoid modeling the growth of the oxide and can provide valuable insight into reaction trends.

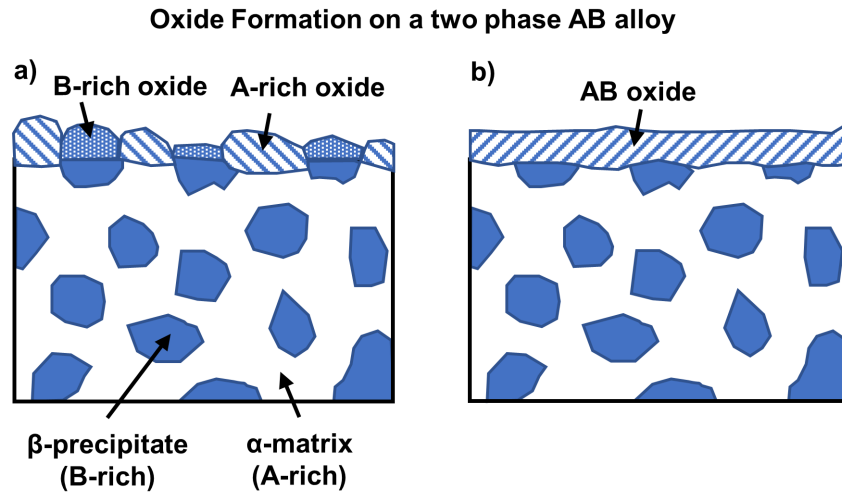


Figure 1.8: Two possible types of oxide growth that can occur on a binary component, two-phase alloy. A) The α and β phases oxidize independently to form oxides enriched in the components of each phase. B) The α and β phases oxidize cooperatively to form an oxide with uniform composition.

1.3 DISSERTATION OVERVIEW

The ANH studies discussed in Section 1.1 present a tantalizing process where energetically efficient CO₂ reduction to form methanol occurs, but there still is a lack of clarity how reaction mechanisms proceed. DFT calculations have indicated that one-electron standard redox potentials to form pyridinyl radicals are very negative, and other pathways are being pursued. In all cases, there is an important need to account for reaction barriers accurately as well as obtain spectroscopic characterization of intermediates. Chapters 2 through 4 describe our work calculating and comparing the redox properties of small ANH molecules, as well as our work benchmarking the study of CO₂ reduction via hydride transfer reactions. These studies shed light on the thermodynamic properties of effective CO₂ reduction catalysts.

Section 1.2 showed that modeling atomistic corrosion processes is difficult and computationally expensive. Fortunately, we can use ORR overpotentials as a descriptor for galvanic corrosion rates because the ORR is a major limiting factor for atmospheric galvanic corrosion processes. Chapters 5 through 6 describe our work predicting how the oxides that form on Ti and a Ti-6Al-4V (a Ti alloy) catalyze the ORR. By creating representative surface models for the oxides of each metals and calculating ORR overpotentials, these studies help determine the factors that most contribute to ORR activity. These insights can be used to guide the design of metal alloys that better resist corrosion damage in galvanically coupled systems. Despite the differences between these two topics, thermodynamic descriptors are valuable tools that can be used to help improve catalyst design.

2.0 STRUCTURAL AND SUBSTITUENT GROUP EFFECTS ON MULTIELECTRON STANDARD REDUCTION POTENTIALS OF AROMATIC N-HETEROCYCLES

The content of this chapter is taken from M. C. Groenenboom, K. Saravanan, Y. Zhu, J. M. Carr, A. Marjolin, G. G. Faura, E. C. Yu, R. N. Dominey, and J. A. Keith, "Structural and substituent group effects on multielectron standard reduction potentials of aromatic N-heterocycles" *J. Phys. Chem. A.* 120 (2016) 6888-6894.

2.1 INTRODUCTION

Increasing worldwide demand for energy continues to drain our finite supply of fossil fuels.[10] Generating renewable fuels from CO₂ through photo and electrocatalytic processes is desired for sustainability, but achieving high efficiency and product selectivity with these methods remains challenging.[103, 19, 104, 105, 106, 107, 39] An intriguing route for CO₂ reduction involves aromatic N-heterocycle (ANH) molecules to promote CO₂ reduction in aqueous electrochemical cells. While these molecules are the subject of many experimental and/or computational studies,[108, 109, 110, 41, 111, 59, 61, 60, 46] there is little consensus about how this chemistry operates.

For instance, contrary to previous reports, Savant and co-workers have reported seeing no evidence of CO₂ reduction either with PyH⁺ on Pt[44] or with a mercaptopyridin on glassy carbon electrodes.[40] On the other hand, Portenkirchner and co-workers[42] have reported observing methanol with PyH⁺ on Pt electrodes (albeit observed with lower faradaic efficiencies than prior studies). Interestingly, in that study methanol formation was not observed

when the same experiment was run with acetic acid, a molecule with a similar pK_a as PyH^+ , indicating that ANH molecules are a key component to this chemistry. Several computational mechanistic studies have carried out to elucidate this chemistry. Notably, Musgrave and coworkers have used similar computational models as we do to calculate proton and electron transfer pathways that result in the conversion of PyH^+ into dihydropyridines as well as quantifying reaction barriers for subsequent hydride transfers to CO_2 .^[59] Though useful for quantifying reaction energetics, their mechanism assumes the formation of pyridinyl radicals. Such species have been observed to form in the presence of high energy photons and reduce CO_2 ,^[53] but there is mounting evidence against pyridinyl radicals forming under electrochemical conditions.^[108, 52, 66, 70] Other processes might be possible such as the proposal by Batista and co-workers, where a proton-coupled hydride transfer between surface hydrides and PyH^+ on Pt surfaces was proposed.^[61, 60, 62] An open question for this mechanism is why results from Portenkirchner and co-workers^[42] suggest that ANH molecules play a role beyond that of just being a Brønsted acid.

Since ANH molecules are widely used in electrochemical environments (particularly as components of ionic liquids), we set out to compute physical properties of these molecules to obtain a better understanding of how different ANH molecules would participate in CO_2 reduction processes besides just PyH^+ . As in our previous work, we use Pourbaix diagrams to illustrate multi-proton and multi-electron standard redox potentials (SRPs) as well as the conditions at which electrochemical conditions redox couples would be aligned for energetically efficient proton and hydride transfers according to the Sabatier principle. We note that our study does not provide details about the kinetic barriers of these processes, but it is informative to understand the thermodynamics for various electrochemical transformations to assess which warrant consideration for further mechanistic studies. The present work is a significantly larger study of ANH molecules than what has been reported previously.^[54, 55] Here, we report how different SRPs vary across a wide range of ANH molecules and discuss how conjugated system size, number of heteroatoms within each molecule, and substituent groups affect their physical properties.

2.2 EXPERIMENTAL METHODS

2.2.1 pK_a Measurements

Acid dissociation constants, pK_{as} , were measured by a modification of standard NMR monitored titration methods.[112, 113, 114] Typical titrations were performed on 0.025M ANH (*aq*) solutions prepared with 0.6M HCl (*aq*) as solvent as well as with 0.6M NaOH (*aq*) as solvent; all solutions were prepared with RO water rather than a D₂O/H₂O mixture. The analytical concentrations of the ANH molecule were kept constant during each titration by making incremental additions of one solution to the other, and visa versa, yielding a minimum of at least two titrations per sample. Measurements of pH were made in the NMR tube using a Sigma-Aldrich glass micro pH combination electrode immediately before and immediately after collecting an ¹H NMR spectrum. Water suppression 1D ¹H NMR spectra were collected on a Bruker AVANCE 500 MHz spectrometer using the standard Bruker zgcprr pulse sequence under variable temperature control, thermostatted at 300K and with a 5 minute thermal equilibration delay at the front-end of the pulse sequence. A Wilmad coaxial insert filled with D₂O provided the lock signal. Multiple ¹H NMR signals were monitored for each ANH molecule during the titrations, with each signal that was monitored giving nearly indistinguishable computed pK_a values ($\pm 0.05 pK_a$ units) in both the acid addition and base addition titrations. The NMR and pH data were analyzed to compute pK_{as} using the method reported by Gift.[113]

2.2.2 COMPUTATIONAL METHODS

Electrochemical calculations reported here use a mixed implicit/explicit solvation calculation scheme described previously.[54] Briefly, gas phase molecular structures were optimized using Kohn-Sham density functional theory (DFT) using GAMESS-US.[115, 116] We performed a vibrational frequency analysis to determine that all geometries were minimum energy stationary points. Geometries and vibrational frequencies were computed for single-ring molecules (pyridine, imidazole, diazine, etc.) at the B3LYP/aug-cc-pVDZ level. Geometries and vibrational frequencies for multi-ring molecules (quinoline, naphthyridine, etc.) were obtained at

the B3LYP/6-31+G* level. Single-point electronic energies for all optimized geometries were calculated using B3LYP/aug-cc-pVDZ. In test cases, errors of less than 0.1 kcal/mol were calculated using B3LYP/6-31+G* optimized geometries opposed to B3LYP/aug-cc-pVDZ optimized geometries (see Appendix A).

Free energy contributions were calculated using the ideal gas, rigid rotor, and harmonic oscillator approximations.[117] Vibrational frequencies were scaled with the appropriate scaling factors from the NIST database to account for anharmonicity.[118] Standard state solvation energies were calculated with GAMESS-US using the Continuum Polarizable Conductor Model (CPCM) protocol with simplified united atomic radii for Hartree-Fock (SUAHF) in a mixed implicit-explicit solvation scheme using default water parameters and one explicit water molecule.[57, 119, 120] We note that B3LYP and CCSD(T)-F12/aug-cc-pVDZ yielded comparable pK_a s and redox potentials as found in a previous study,[57] and so only results from the B3LYP are reported here.

For Pourbaix diagrams, we considered all molecules resulting from up to three proton and two electron transfers. This is straightforward for small molecules, but larger molecules (adenine, purine, pteridine, mecapteridine, etc.) have multiple protonation sites that made choosing the most stable configuration difficult. To expedite this search, we employed a screening procedure using semiempirical methods. First, we optimized geometries for all possible combinations of proton and electron transfers to the molecule using the semiempirical PM7 method in MOPAC.[121] We then calculated B3LYP/6-31+G* single point energies for these geometries in water (using the CPCM protocol) using GAMESS-US. The most stable chemical species for each combination of proton and electron transfers at this level were then fully optimized at the B3LYP/6-31+G* level for final analysis as described above. An implementation of this screening procedure is available in the ADF modeling suite and is discussed in Appendix B.

2.3 RESULTS

We previously showed that calculated Pourbaix diagrams can illustrate electrochemical conditions that appear to correlate to experimental conditions utilized for molecular promoted CO₂ reduction with substituted pyridines, imidazoliums, and phenanthroline.[55] We now report an expanded set of Pourbaix diagrams considering for more than 27 ANH molecules (Figure 2.1) that have multiple conjugated rings, and/or multiple nitrogen atoms. These molecules better span the chemical space of ionic liquids, inorganic complex ligands, and biomolecules that might be utilized for molecular or even extended structure electrocatalysts.

We first report a benchmarking of our calculated pK_a s for available molecules shown in Figure 2.1. While error bars for pK_a are not large, consistent pK_a data across a range of molecules is often hard to obtain. For a more precise benchmarking, we determined pK_a s for a subset of ANH molecules that were readily soluble in water using NMR and compared them to experiment (Table 2.1). We also report pK_a s obtained using the ChemAxon online empirical pK_a calculator,[122] pK_a s calculated using direct calculations,[123] and pK_a s obtained using a linear regression of the direct calculations (using a similar approaches to Muckerman[124] and Keith[125]). The mean unsigned error (MUE), max error (MAX), and standard deviation (SD) are calculated with respect to our measured pK_a s when available and otherwise references against previous experimental measurements. As expected, the empirical pK_a calculator provides quite accurate pK_a s, MUE = 0.46. However, to our knowledge there are no empirical SRP calculators and so QM methods are used for consistency of pK_a s and SRPs. pK_a s calculated from first principles QM can bring larger mean unsigned errors, 0.86, but errors are reduced using error cancellation schemes such as an empirical linear regression reduces MUEs to 0.37.

Figure 2.2 shows a list of CO₂ redox reactions (1.1-1.3 and 1.5), the hydrogen evolution reaction (1.4), and molecular redox reactions that are specific to ANH molecules (1.6-1.10). Calculated data for these reactions is reported in Figure 2.3. We also include the electrochemical reduction of CO₂ to CO₂⁻ (1.1), formic acid (1.2), carbon monoxide (1.3), and methane (1.5) as reference points for comparison to the other ANH molecule redox reactions.

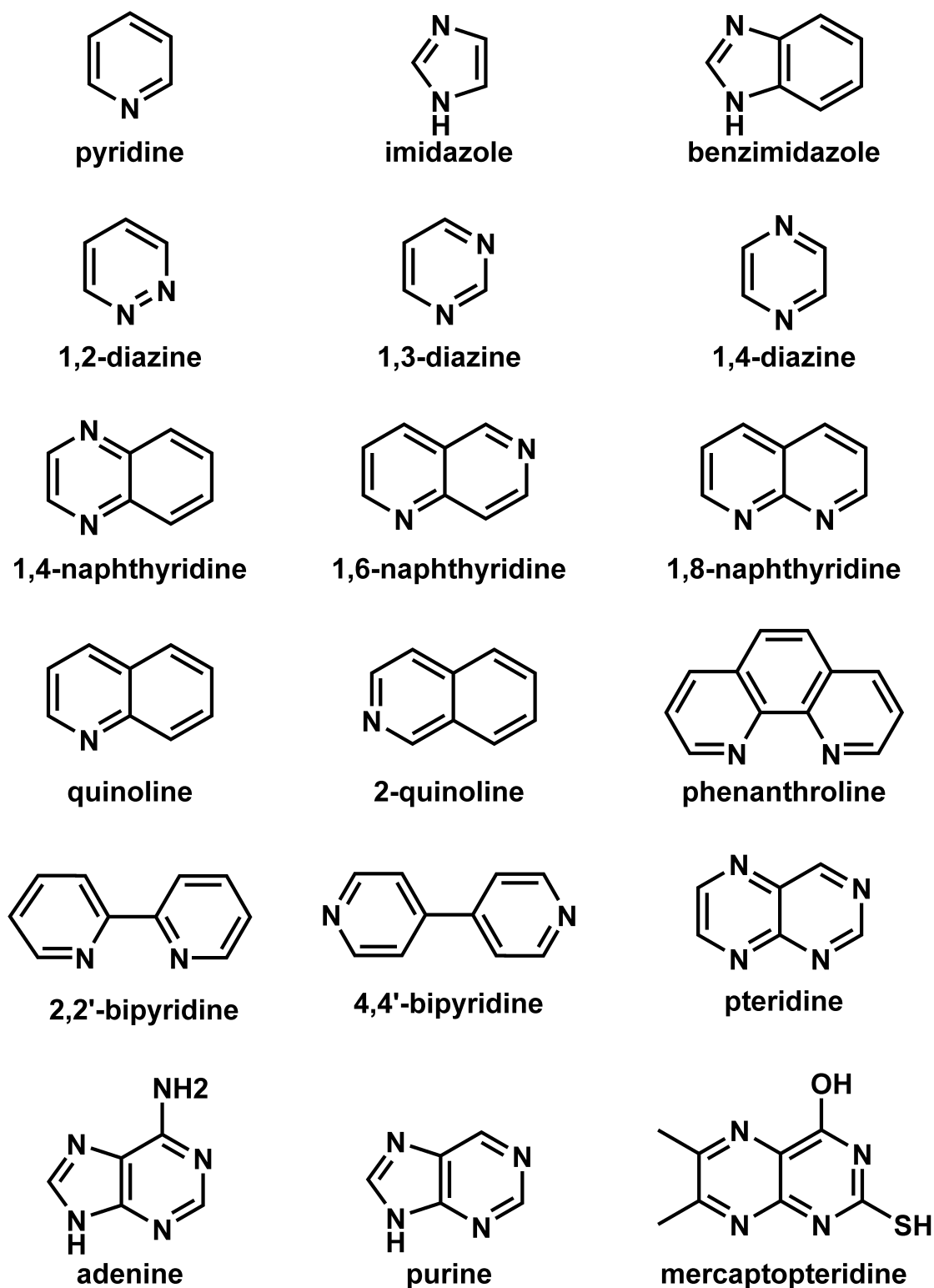


Figure 2.1: Aromatic N-heterocycles (ANH) molecules considered in this work.

Table 2.1: Experimental and calculated pK_a s for ANH molecules in this work.

Molecule	Exp. (previous) (this work)	Predicted (Empirical calculator)	Predicted (QM. Calc.)	Predicted Regression
imidazole	7.05/ 7.10	7.00	6.40	6.23
pyridine	5.21/ 5.42	5.10	5.70	5.76
1,2-diazine	2.24	2.20	0.55	2.23
1,3-diazine	1.10	1.30	-0.46	1.54
1,4-diazine	0.37	0.60	-1.26	0.99
2,2-bipyridines	4.33	3.00	2.53	3.59
4,4-bipyridines	4.80	5.00	4.05	4.63
1,4-naphthyridine	0.56	1.60	-1.30	0.97
1,6-naphthyridine	3.78	1.70	3.25	4.08
1,8-naphthyridine	3.39	0.60	3.13	4.00
quinoline	4.85/ 5.05	4.50	4.63	5.02
2-quinoline	5.42	5.30	5.20	5.41
benzimidazole	5.60	5.80	4.87	5.19
4-acetylquinoline	2.50	2.50	3.28	4.10
phenanthroline	4.86	4.50	5.47	5.60
purine	2.30	2.40	0.85	2.44
adenine	4.15	4.30	5.50	5.62
2-picoline	5.96/ 6.25	5.80	5.85	5.86
3-picoline	5.63/ 5.97	5.60	5.44	5.58
4-picoline	5.98	5.80	6.30	6.17
2,6-lutidine	6.60/ 6.96	6.50	7.29	6.84
3,5-lutidine	6.15/ 6.28	6.10	6.00	5.96
4-aminopyridine	9.11/ 9.22	8.90	10.20	8.83
DMAP	9.60/ 9.81	8.80	10.81	9.25
nicotinamide	3.35/ 3.41	3.60	2.36	3.47
MUE	-	0.46	0.86	0.37
MAX	-	2.79	1.86	1.60
SD	-	0.78	0.96	0.36

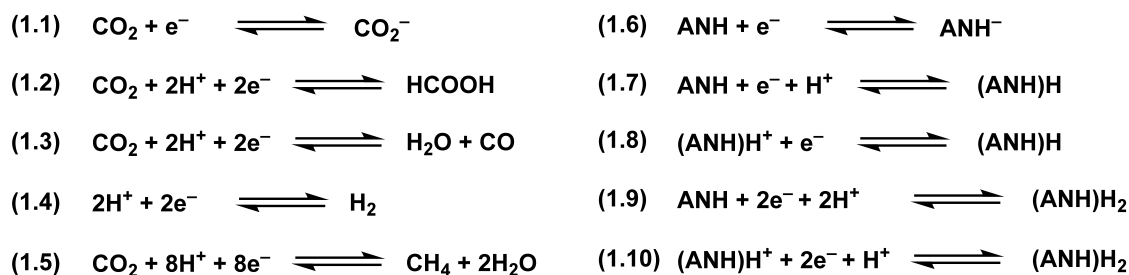


Figure 2.2: Redox reactions reported in Figure 2.3.

The ANH SRPs in Figure 2.3 reveal several clear trends. First, one electron reductions require the most negative potentials, and nearly all of our studied molecules require more negative potentials than the one electron reduction of CO_2 . Thus, if they could be formed, most ANH radical anions would all would have the thermodynamic capability to reduce CO_2 via 1-e^- transfers. Second, molecular SRPs are significantly less negative when encountered as proton coupled electron transfers (PCET). Protonating the nitrogen atom in the ANH molecules lowers the LUMO energy and increases the molecule’s susceptibility to nucleophilic attack. Despite this, the potentials required to form pyridinyl radical analogues are still quite negative. However, the lowering of the LUMO energy results in energetically accessible two electron/two proton processes as well (Reaction 1.10 in Figure 2.2 and Figure 2.3) that have SRPs similar to the reduction of CO_2 to methane, CO, or formic acid.

In addition to involvement of protons in the redox process, the three factors that most influence 1-e^- and $1\text{-e}^-/1\text{-H}^+$ redox potentials: 1) π -system size, 2) number of nitrogen atoms in the ring, and 3) presence of substituent groups (e.g. chlorine, or methyl group).[55] However, these factors are dramatically muted when considering the standard redox potentials involving multiple protons and electrons. These factors are discussed in more detail below for PCET processes.

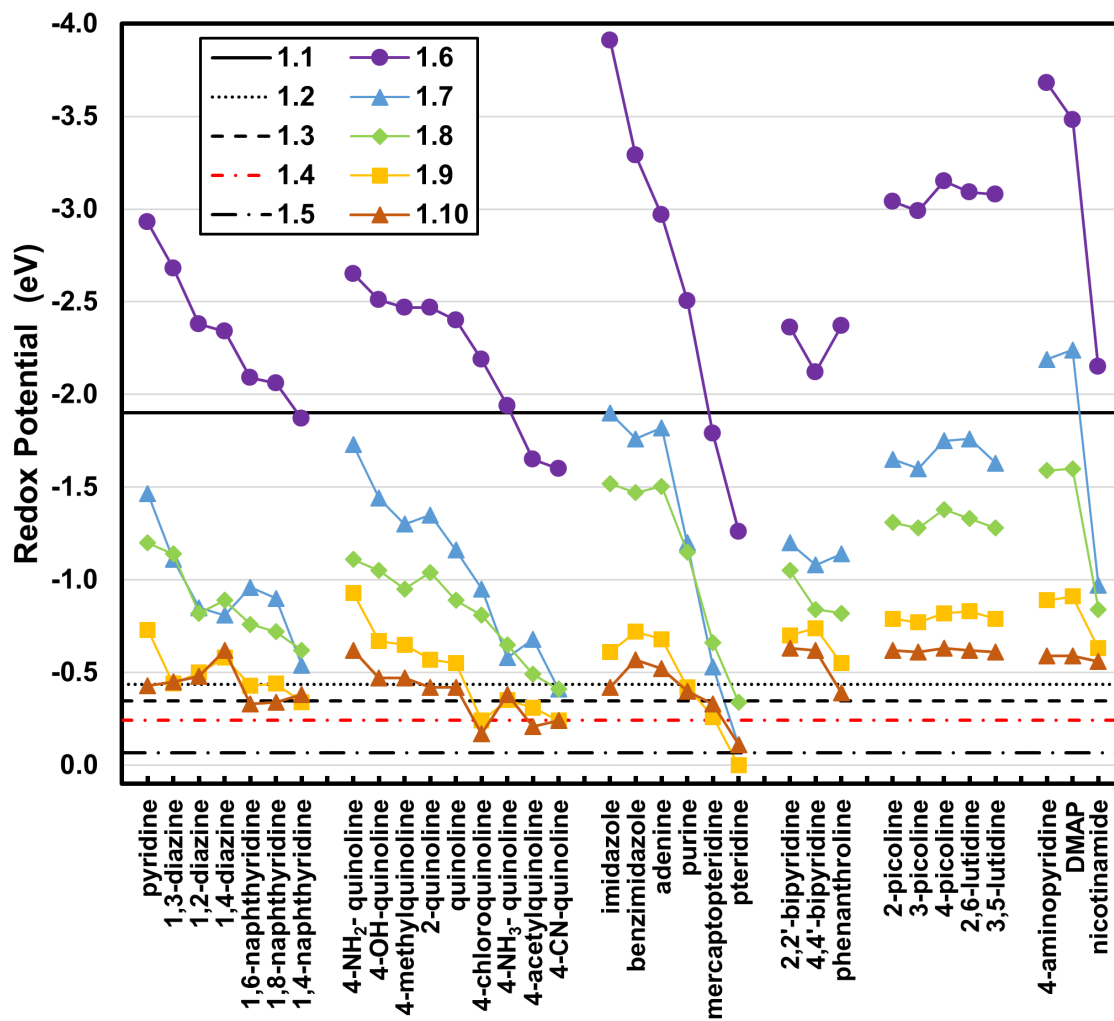


Figure 2.3: Redox potentials for 20 ANH molecules calculated at 0 pH. Lines correspond to redox processes shown in Figure 2.2. DMAP corresponds to N,N dimethyl-aminopyridine.

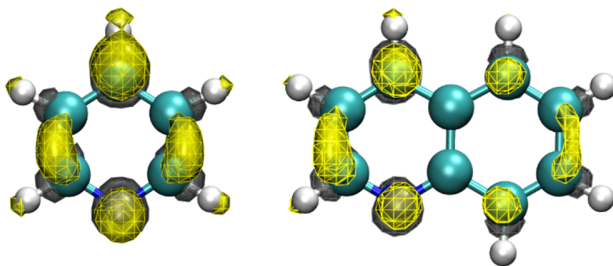


Figure 2.4: Electron density difference plots for transferring 1-e^- to pyridine (left) and quinoline (right). Yellow areas correspond to higher electron density in the radicals after 1-e^- addition while gray areas correspond to lower electron density. Isovalue = 0.004 for both cases.

Molecules with larger conjugated π -systems expectedly have less negative (and more energetically favorable) SRPs. The electron transfers become more favorable because the energy gap between the π and π^* orbitals decreases as the conjugated π -system size increases. Another way of rationalizing this is that electrons can transfer more easily into molecules with larger π/π^* -systems because they delocalize across more atoms (i.e. similar to the quantum mechanical particle in a box problem). Electron density difference plots qualitatively illustrate this effect by showing how electrons delocalize over molecules with different degrees of π -system conjugation. Figure 2.4 depicts a 1-e^- transfer to pyridine, and quinoline. The transferred electron distributes across each molecule's π^* -system. Quinoline has a larger π^* -system and a smaller HOMO-LUMO gap, so electrons transfer to quinoline (-2.4 eV) more favorably than to pyridine (-2.93 eV).

Replacing carbon atoms with nitrogen atoms in an otherwise identical molecule can alter the reactivity of the molecule. For example, the redox potentials of 1,4/1,6/1,8-naphthyridine shown in Figure 2.3 are all less negative than those of quinoline, despite the only difference being the incorporation of an additional nitrogen atom. We hypothesize that nitrogen's higher electronegativity relative to carbon inductively withdraws electron density from the remaining carbon atoms and this further stabilizes the reduced species. Density difference

plots do not illustrate this effect, but this is qualitatively supported by Löwdin population differences between quinoline and 1,8-naphthyridine. The additional nitrogen atom in 1,8-naphthyridine has increased negative charge compared to the corresponding carbon atom in quinoline (-0.07 charge units). Additionally, all of the carbon atoms in 1,8-naphthyridine are more positively charged than those in quinoline by up to 0-0.12 charge units.

Substituent groups help further tune ANH redox energetics. Adding π -electron donating groups to quinoline yielded more negative redox potentials (R-NH₂, R-OH), while adding π -electron withdrawing groups (R-acetyl) yielded less negative redox potentials. Substituent groups that act inductively behaved similarly with electron withdrawing groups (R-Cl, R-NH₃⁺, R-CN) yielding less negative redox potentials and electron donating groups (R-Me) making redox events less energetically favorable. For example, the 1 e⁻ reduction potential for quinoline is more negative than that of 4-CN-quinoline (-2.4 vs. -1.6 V) but less negative than that of 4-OH-quinoline (-2.4 vs. -2.51 V). The electron withdrawing groups remove electron density from the molecule, which facilitates electron transfers. Electron donating groups do the opposite. This effect increases with the donating or withdrawing strength of the substituent group.

There are several apparent inconsistencies in these trends we will now attempt to explain. In Figure 2.3, reactions 1.7 and 1.8 switch order for several ANHs. This switch is due to our calculated SRP being referenced at pH = 0. If a molecule's p*K*_a is less than the reference pH, the unprotonated molecule will be more stable than the protonated molecule at that reference pH and vice-versa. Therefore, if the molecule's calculated p*K*_a is less than 0 (the reference pH of Figure 2.3) then the free energy change for reaction 1.8 (ANH + H⁺ + e⁻) will be more uphill (i.e. giving a more negative redox potential) than reaction 1.7 ((ANH)H⁺ + e⁻). This same reasoning applies to reactions 1.9 and 1.10.

Molecular Pourbaix diagrams are essentially electrochemical phase diagrams; they display the molecule with the most favorable chemical potential at any pH and applied potential. Although molecular Pourbaix diagrams contain no information about kinetics of proton and electron transfer processes, they provide a visual summary of the reaction thermodynamics for processes involving proton, electron, and/or hydride transfers. Boundaries and triple points indicate conditions where two, or three molecules have equal chemical potentials.

Thus, at these conditions the molecules would be expected to rapidly exchange some combination of protons and electrons in accordance to the Sabatier principle. Based on the relative ease of protonating most heterocycles, we (as well as Musgrave and Batista) posit that CO₂ reduction occurs via some form of coupled hydride-proton transfer. However, we propose that a molecular structure capable of efficiently catalyzing CO₂ reduction must have: 1) a boundary/triple point corresponding to a two electron and two proton process, and 2) that boundary/triple point must be near to (i.e. ideally slightly more negative than) the CO₂ thermodynamic reduction potentials.

Above we showed that variations in molecular structures can modulate molecular redox properties, and in turn these changes will alter the boundary and triple point locations on Pourbaix diagrams (Figure 2.5). For instance, quinoline has a single triple point and three separate boundaries separating quinoline, protonated quinoline, and dihydroquinoline. The Pourbaix diagram for 1,8-naphthyridine has the analogous species (1,8-naphthyridine, protonated 1,8-naphthyridine, and dihydro-1,8-naphthyridine) as well as a new domain (protonated dihydro-1,8-naphthyridine) and a second triple point. The exact position of these boundaries are controlled by molecular pK_a s (vertical lines) and other redox properties (horizontal/diagonal lines). The 2-electron and 2/3 proton transfer processes for quinoline and naphthyridine fall near to ideal CO₂ reduction potentials (Figure 2.5). Thus, our approach predicts that quinoline and 1,8-naphthyridine would be comparably effective as PyH⁺ moieties in CO₂ reduction. Pourbaix diagrams for the remaining ANH molecules are available in Appendix A. Comparing molecular Pourbaix diagrams computed with DFT against CO₂ Pourbaix diagram obtained from experimental data can introduce systematic errors into the comparison. These errors could be easily quantified by comparing molecular redox potentials computed with DFT against their experimentally measured values.[126]

Figure 2.6 shows a compilation of molecular triple points computed for each studied molecule. Triple point conditions vary across the classes of ANH molecules, but nearly all the triple points fall near experimental CO₂ reduction conditions. Although the exact reaction mechanisms for all molecules are not clear, we propose that molecular triple points will be useful descriptors for a molecule’s ability to participate in energetically efficient electrochemical processes.

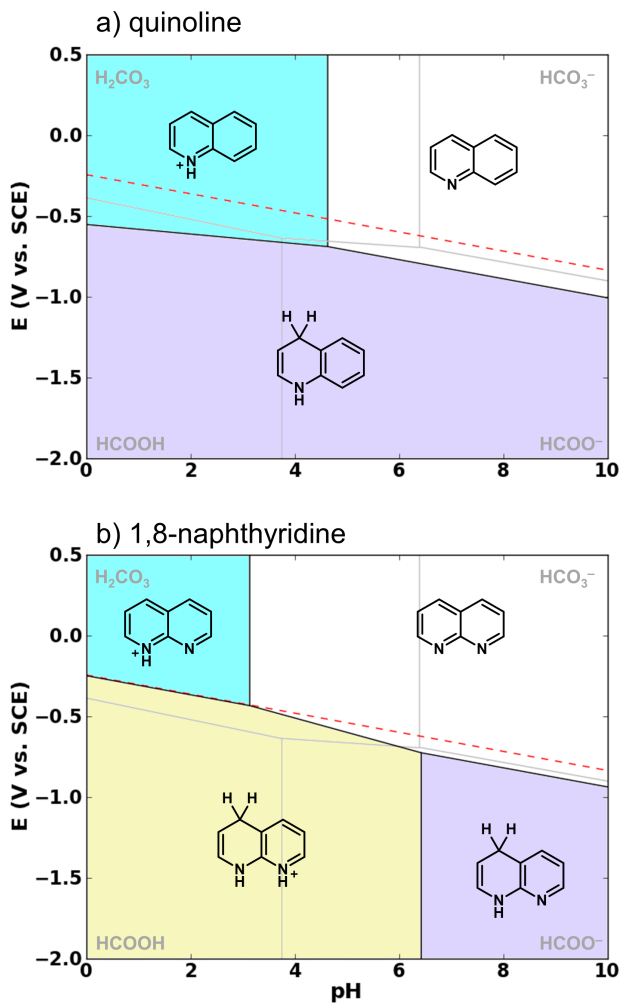


Figure 2.5: a) quinoline and b) 1,8-naphthyridine Pourbaix diagrams. The gray lines represent equilibrium between H_2CO_3 , HCO_3^- , and their potential reduction products (formic acid/formate). The red dashed line represents the hydrogen evolution reaction.

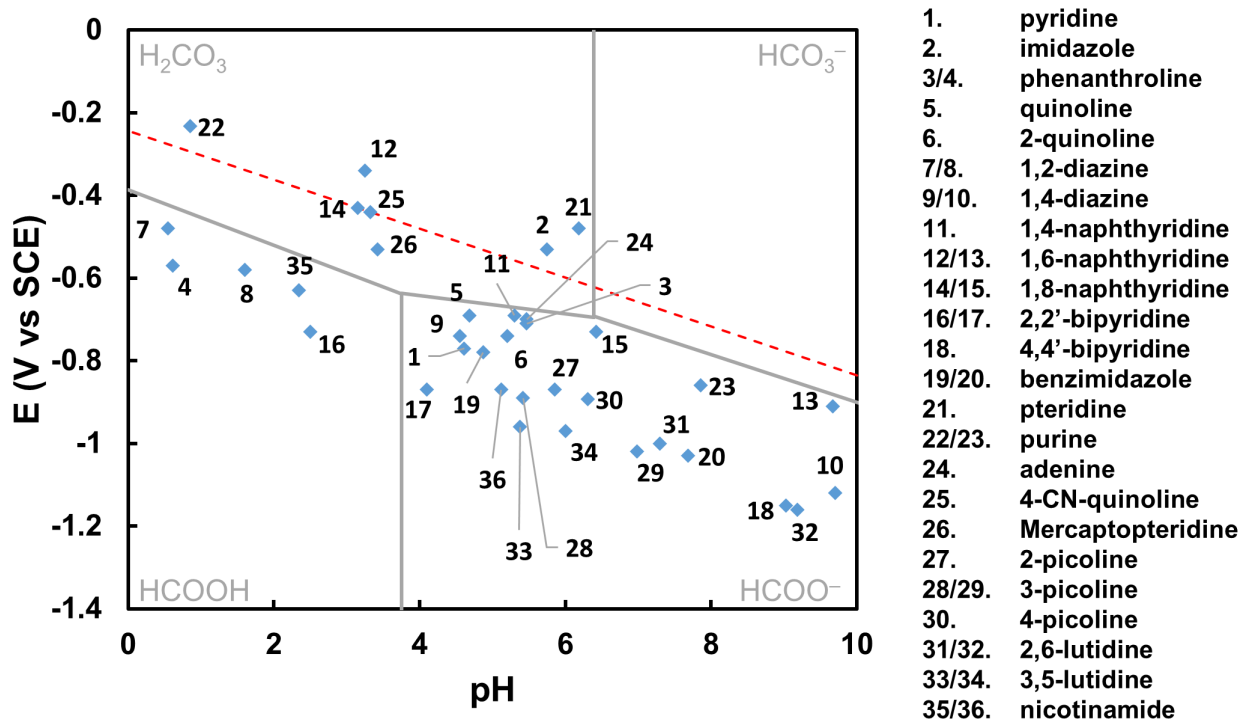


Figure 2.6: Compiled Pourbaix diagram triple point conditions for all considered molecules. The red dashed line corresponds to the hydrogen evolution reaction. Gray lines correspond to the CO_2 equilibrium products and standard redox potentials in an aqueous environment.

2.4 CONCLUSIONS

We have investigated the degree that redox reaction energetics and Pourbaix diagram isobars vary across a wide variety of ANH molecules. We used first principles quantum chemistry to quantify the degree that nitrogen atoms, aromatic rings, and/or electron withdrawing groups within molecular structures cause substantially less negative redox potentials. Although molecular redox potentials and pK_a s are sensitive to molecular structure, Pourbaix diagrams for nearly all of the reported ANH molecules have at least one triple point near the equilibrium potentials for CO_2 reduction at the same pH. This signifies that ANH molecular moieties in general may be used to shuttle protons, electrons, and possibly hydrides at appropriate electrochemical conditions. Although experimental validation of ANH-promoted CO_2 reduction mechanisms is still needed, calculated triple points are a theoretically sound descriptor for screening a molecule's (or material's) capability for catalyzing electrochemical reductions. Similar analyses can be performed straightforwardly with quantum chemical accuracy to assist in the identification of molecular co-catalysts for electrochemical reactions.

3.0 EXPLICITLY UNRAVELING THE ROLES OF COUNTER IONS, SOLVENT MOLECULES, AND ELECTRON CORRELATION IN SOLUTION PHASE REACTION PATHWAYS

The content of this chapter is taken from M. C. Groenenboom, and J. A. Keith, "Explicitly Unraveling the Roles of Counter Ions, Solvent Molecules, and Electron Correlation in Solution Phase Reaction Pathways" *J. Phys. Chem. B* 120 (2017), 10797-10807.

3.1 INTRODUCTION

Increasing world populations intensify the worldwide demand for energy,[\[10\]](#) but humanity's use of fossil fuels correlates with extreme weather patterns and climate change.[\[127, 128\]](#) To address this, scientists and engineers pursue the development of alternatives to fossil fuels such as renewable and sustainable energy technologies that would utilize solar energy to produce H₂ from H₂O[\[129, 130\]](#) or hydrocarbons from CO₂.[\[15, 131\]](#) Many of these technologies require economical catalysts that facilitate energetically efficient proton and electron transfers. Detailed experimental studies of these processes can be challenging and expensive, but first principles quantum chemistry (QC) plays an ever-growing role helping interpret experimental observations and guiding improvements in catalyst designs.

Computational QC is particularly useful for studying reaction mechanisms. Complex reaction mechanisms comprised of many reaction pathways can be modeled using computational procedures such as metadynamics[\[132, 133, 134, 135, 136, 137, 138, 139\]](#) and transition path sampling.[\[140\]](#) These approaches use computationally expensive Born-Oppenheimer molecular dynamics (BOMD) simulations to directly sample the free energy surface and ex-

explicitly capture interactions between solute and solvent molecules while modeling condensed phase chemical processes. While these methods can provide accurate free energies of reaction, they necessitate the use of relatively less computationally inexpensive QC methods. As a result, levels of QC theory more computationally expensive than Kohn-Sham density functional theory (KS-DFT) with generalized gradient approximation (GGA) exchange correlation functionals are not usually feasible. Instead, KS-DFT with exchange correlation functionals such as PBE[141, 142] and PW91[143] or other semiempirical methods are used, even though these levels of theory may have well-established deficiencies when modeling molecular energetics.[118, 117]

QM/MM schemes have also been widely used to study reaction free energy surfaces.[144, 145, 146, 147, 148, 149] These calculations treat a small region of the system with accurate QC calculations and the remainder of the atoms and molecules with different classes of forcefields. QM/MM allows greatly reduced computational cost for reaction pathway sampling (e.g. via metadynamics or umbrella sampling), and it allows the study of significantly larger systems than what is possible with full QC models. QM/MM schemes are often employed to study enzymatic reactions,[150, 151, 152] or small molecules reacting in a condensed phase[153] by treating the substrate, enzyme active site and/or neighboring solvent molecules with QM embedded within enzymes/solvent molecules modeled with forcefields. However, in practice the results are dramatically impacted by technical aspects of how the QM and MM regions are coupled as well as the type and parameterization of the forcefield employed.[154] Newer adaptive QM/MM (adQM/MM) schemes can account for diffusion of molecules between the QM and MM regions,[155] but in general, BOMD simulations using full QC methods are more accurate and straightforward as long as the systems modeled are computationally viable.

If higher levels of QC theory are needed, reductionist models can be used. Reaction pathways ranging from aldol additions[156, 157, 158] to Ziegler-Natta catalysis[159] have been studied by modeling fewer numbers of reacting atoms in tandem with continuum solvation models. While such methods are much less computationally expensive than BOMD approaches, they can also be highly sensitive to factors such as the level of QC theory and/or the quality of approximations used to calculate the free energies in solution.[160] Addition-

ally, these reductionist models necessitate that the user has significant chemical intuition about the modeled system. For instance, Siegbahn demonstrated the importance of explicit water chains in modeling solution phase chemistry in the mid-1990s,[58] but there are few if any procedures that can a priori determine the number and location of explicit solvent molecules needed to obtain accurate and physically significant barriers without using fully explicit solvation modeling. Similarly, it is known that counter ions, which are often assumed to be innocent bystanders in solution phase reactions, can significantly change reaction pathway energetics.[125]

Our motivation for this study is to develop a novel computational procedure that can more accurately and reliably model solution phase reaction pathways. To this end, we hypothesize that a tractable way to include higher levels of QC theory into reaction dynamics simulations along a reaction pathway is via the expression: $\Delta G_{highlevel} \approx \Delta G_{lowlevel} - \Delta E_{lowlevel} + \Delta E_{highlevel}$, where a more accurate high level free energy for a reaction can be obtained by substituting E values along a minimum energy pathway obtained from a low level of theory with data from a higher level of theory. This is essentially the same in spirit as the IRCMax method of Petersson and Montgomery,[161] but now used in a procedure that is applicable for condensed phase reaction mechanisms.

To obtain nuclear coordinates suitable for high level QC theory calculations, we employ a combination of high temperature BOMD simulations and nudged elastic band (NEB) calculations to locate reaction pathways in solvent in the presence of counter ions as done previously.[162] The 0 K energetics (ΔE values) from the NEB calculations are not relatable to free energy pathways at ambient conditions, but we assume here that the hydride transfer processes involve a relatively small number of atoms directly participating in the reaction (compared to a protein or an enzyme with many degrees of freedom that can effect reaction free energies[163]). Thus, at first glance it would seem reasonable that 0 K pathways may not be significantly different from the pathways operational at room temperature.

Another benefit to obtaining these pathways in this manner is that potentials of mean force can be straightforwardly obtained using umbrella sampling procedures once a single reaction pathway is defined.[164, 165, 166] Here, we benchmark the effect of different levels of QC theory on aqueous hydride transfer reactions with different treatments of local solvation effects along reaction pathways. Free energy contributions obtained via different computational methods will be benchmarked in future work.

In our procedure, we first used high temperature BOMD simulations to discover reaction process with minimal a priori knowledge of the reaction. Next, we quenched reactant and product states from the BOMD trajectories to obtain minimum energy configurations that were then used as end points for generalized solid state (gSS-)NEB calculations that determined reaction pathways. Finally, we generated molecular clusters using subsets of atoms from the optimized NEB images and calculated solution phase energetics using continuum solvation and several different levels of theory, some of which are not currently permissible within periodic boundary conditions.

While sampling obtained from this approach provides less mechanistic information than metadynamics or transition path sampling, because the costly dynamical sampling is eventually carried out along only a single pathway, this approach would be much less computationally expensive than dynamics simulations that explore entire reaction mechanisms. Furthermore, having well-defined 0 K structures opens the possibility of approximating reaction free energies using cluster-continuum modeling[167, 168, 169] on structures obtained from the NEB pathway. The validity of these possibilities requires understanding which chemical models (i.e. continuum vs. explicit solvation methods) and levels of theory adequately describe ΔE values for solution phase reaction pathways. We previously reported that NaBH_4 and NaBH_3OH are strong enough hydride donors than they can reduce CO_2 in aqueous solutions.[170] We pursued fundamental reaction pathways for these processes as a test case both for relevance in computational modeling and for research in CO_2 reduction in solution.

3.2 COMPUTATIONAL METHODS

Unless explicitly stated, all non-periodic calculations were performed using ORCA[171] and the RI-J, RI-JK, and RIJCOSX approximations for non-hybrid KS-DFT (PBE[141, 142]), hybrid KS-DFT (PBE0[172]/B3LYP[173]) and MP2[174, 175] calculations, respectively.[176, 177, 178, 179, 180] We also used Riplinger and Neese’s linear-scaling domain based local pair natural orbital CCSD method (DLPNO-CCSD[181]) with RIJCOSX approximations as implemented in ORCA. Transition state geometries for non-periodic systems were optimized at the B3LYP/def2-SVP level using COSMO continuum solvation (using default parameters for water)[182] and the D3 dispersion-correction model with Becke-Johnson damping.[183] Optimized transition states for molecular clusters had only one imaginary frequency corresponding to the normal mode for the reaction pathway. We located reactant and product states for non-periodic systems by nudging coordinates in the forward and backward directions of the corresponding imaginary frequency and allowing geometries to fully relax to minimum energy structures having no imaginary frequencies. Reactant, transition state, and product single-point energies were then recalculated using the B3LYP/def2-TZVP model chemistry with COSMO continuum solvation and D3 dispersion with Becke-Johnson damping as well as with other levels of theory reported in the Appendix C.

Periodic BOMD simulations and NEB calculations were carried out using the Vienna ab initio simulation package (VASP).[184, 185, 186, 187] These calculations used the Perdew-Burke-Ernzerhof (PBE) GGA exchange correlation functional and described core electrons with the projector augmented wave (PAW) method.[188, 189] Planewave cutoff energies were set at 520 eV after finding this gave well-converged structures and total energies. Periodic calculations used a 14 Å cubic simulation cell that contained 70 H₂O molecules, one CO₂, and one NaBH₄ (or NaBH₃OH) molecule. The density of water in the simulation cell was consistent with real aqueous systems. Multiple BOMD simulations were run for 10 ps at 2000 K to witness reaction events. While the high temperature accelerated reaction kinetics and increased the chance of viewing a reaction over a relatively short simulated timespan, the observed reactions from this approach will be biased towards entropically favored pathways. This approach is not intended as a substitute for extensive sampling over regions of a

potential energy surface, but it is used rather to extract refined reaction pathways for processes observed in BOMD simulations. The reactant and product species from the BOMD simulations were then fully relaxed and used to generate reaction pathways with gSS-NEB calculations.[190]

All gSS-NEB calculations were performed at 0 K using Henkelman’s climbing image approach to locate transition states.[191, 192] We optimized each gSS-NEB with the QuickMin optimizer[193] until the forces on all atoms were less than 0.015 eV/Å. Relative energies changed by less than 0.01 eV between gSS-NEB calculations completed with forces/atom equal to 0.02 and 0.015 eV/Å leading us to believe that this tolerance is sufficient. Occasionally, gSS-NEB calculations found images that resembled the reactant or product state but were lower in energy due to solvent molecule rearrangements. In these cases, we fully relaxed the lowest energy image and then used that structure as the new reactant (or product) for new gSS-NEB calculations. All gSS-NEBs were also optimized with the PW91 exchange correlation functional (the method used in ref. [162]) and the difference between the PBE and PW91 barrier heights was found to be negligible (< 0.05 eV).

After defining gSS-NEB reaction pathways that accounted for explicit intermolecular interactions, we selected subsets of atoms from those images for single point energy calculations from ORCA using different levels of theory including PBE/PBE0/B3LYP/def2-TZVP, RI-MP2/def2-TZVP, and DLPNO-CCSD/def2-TZVP, each with COSMO continuum solvation free energy contributions. We used four different types of molecular clusters: 1) nuclear coordinates involving reacting atoms without any additional explicit solvent molecules or the counter ion, 2) the same system but with the counter ion, and 3) and 4) those systems but now including the entire first solvation shell. The first shell of explicit water molecules for the full systems contained all water molecules within 4.5 Å of the reacting atoms in any gSS-NEB image (see Figure 3.1). All data points along each reaction pathway involved a single point energy calculation using clusters containing a consistent number of atoms and basis functions to maximize error cancellation. When modeling the explicitly solvated cluster without the counter ion, we omitted water molecules that were only coordinated to the counter ion (represented by the gray region in Figure 3.1).

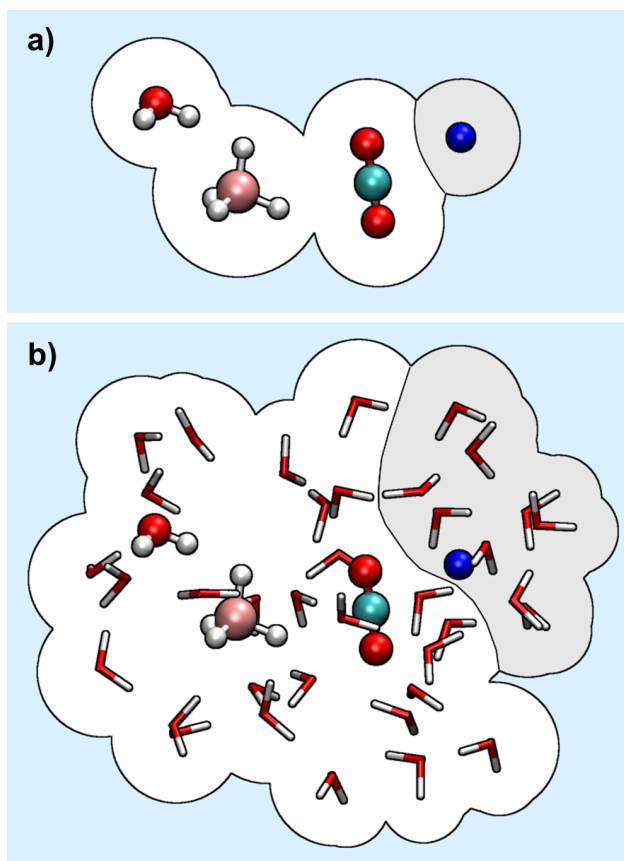


Figure 3.1: Continuum solvated clusters created from gSS-NEB optimized coordinates containing a) only the reacting atoms, and b) the reacting atoms and the first solvation shell. Calculations without the counter ion use clusters that omit atoms in the shaded regions.

Electron density difference plots were calculated on molecular clusters using GAMESS[116, 115] (PBE/6-31+G* with CPCM[119, 120] continuum solvation). Calculations involved subtracting the electron density of the reacting molecules (subsystem 3.2) and the explicit water solvation shell (subsystem 2, if present) from the electron density of the full system. Figures were produced using VMD.[194]

3.3 RESULTS AND DISCUSSION

Catalytic hydride transfers have been studied for over 50 years.[195, 196] Although more commonly considered in enzyme catalyzed processes,[163, 197] there are many other catalysts that function as hydride donors in different chemical environments.[198, 199] Hydride transfers in aqueous solution in particular are considered challenging because they typically lead to H₂ evolution, an unwanted side reaction in CO₂ reduction. Since computational chemistry can be used for refined studies of reaction mechanisms, our goal was to provide fundamental insight into how hydride transfers occur in different chemical environments.

Specifically, our aim was to establish a computational procedure that could determine hydride (and if relevant, proton-coupled hydride) transfer pathways that explicitly considered different intermolecular interactions arising from the local solvation environment. Hydride transfers under enzymatic conditions[200] as well as proton transfers in aqueous phase are also considered electronically adiabatic due to strong hydrogen bonding from water molecules.[36] In this work, we assumed that proton and hydride transfers in aqueous solution will likewise be electronically and vibronically adiabatic, and therefore the use of single determinant QC methods with BOMD is appropriate. As explained above, our focus is to understand the relative importance different electronic energy barriers of aqueous phase processes under the influence of continuum solvation. As was discussed for free energies, other factors such as zero point energies, thermal energy contributions, and other quantum nuclear effects (e.g. proton tunneling) can be incorporated along these pathways using harmonic oscillator approximations or path integral MD models.[201] The significance of these other effects in these aqueous phase barriers will be addressed in future work.

3.3.1 Model 1: Cluster models of reacting atoms with explicit water molecules and continuum solvation

We now discuss transition states for the reaction shown in Figure 3.2 using different models. The first model we considered is simple and involves the cluster of atoms in Figure 3.2 with different numbers of explicit water molecules all embedded in a continuum solvation model. We used this model as a starting point for understanding the significance of explicit solvation in this reaction. By inspection, this reaction might be assumed to take place as a single barrier S_N2 reaction featuring a concerted hydride transfer and water addition. One might also assume for added simplicity that the Na^+ counter ion becomes fully solvated in aqueous environments and is merely an innocent bystander in this reaction.



Figure 3.2: Reduction of CO_2 to formate by BH_4^- .

BH_3OH_2 was previously found to spontaneously deprotonate in a simulation box of water,[162] so we added explicit H_2O molecules nearest to the adding H_2O molecule to stabilize this deprotonation should it occur. Figure 3.3 shows the optimized transition states for this reaction modeled with zero, one, or three additional water molecules. None of the key transition state bond lengths (C-H, B-H, and B-O) change significantly when adding explicit water molecules (see Figure 3.3) despite the different number of participating water molecules.

In all cases the forward barrier height was found to be almost the same (~ 0.69 eV) regardless of the number of water molecules that were added in these calculations. This is consistent with the similar transition state structures in each case (Figure 3.4). However, adding water molecules caused the reaction energies to become significantly downhill in energy (shifting energetics by more than 0.8 eV). This decrease was due to the product being stabilized by hydrogen bonding between the explicit H_2O molecules and BH_3OH_2 .

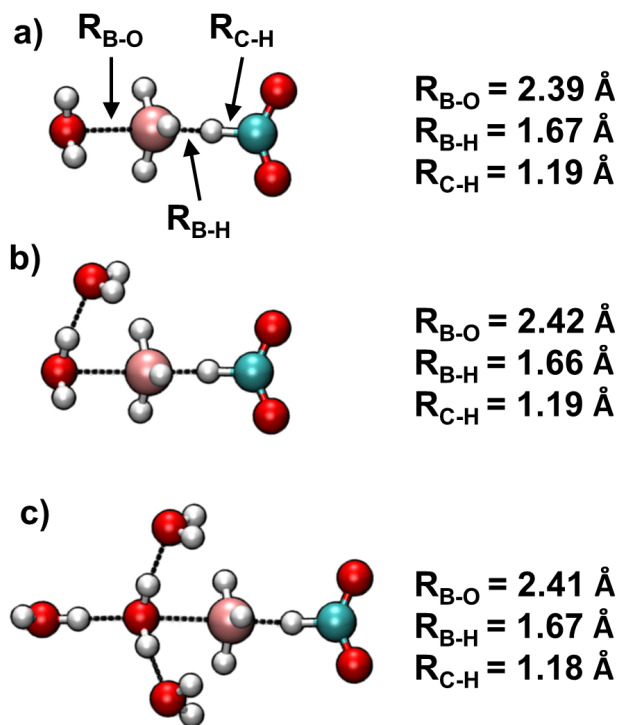


Figure 3.3: Model 1 transition state structures for $BH_4^- + CO_2$ being converted to formate and BH_3OH_2 with a) zero, b) one, and c) three explicit H_2O molecules to stabilize the product (BH_3OH_2).

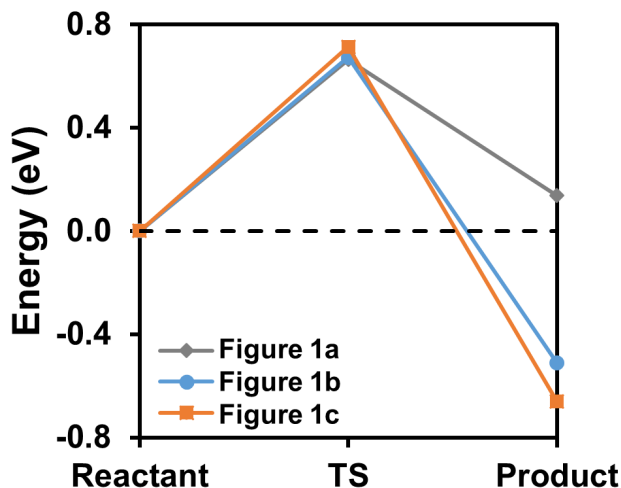


Figure 3.4: Relative reactant, intermediate, and product energies from ORCA optimized structures using Model 1.

Although the explicit H_2O molecules had minimal impact on transition state energetics in this case, the addition of one water molecule made a significant difference in the overall reaction energetics. The influence of adding a third H_2O molecule was found to be much less than that found when adding the second H_2O molecule. In all cases, this model yielded a process with a single barrier corresponding to an $\text{S}_{\text{N}}2$ reaction with a concerted hydride transfer and water addition as might have been assumed by inspection of Figure 3.2. Additional data showing the energetics of the structures in Figure 3.1 at different levels of QC theory are available in Appendix C.

3.3.2 Model 2: Explicit solvent models with pathways determined from gSS-NEB calculations within periodic boundary conditions

Experienced users of continuum solvation models are well aware that they can be highly unreliable when describing solvation of strongly interacting solutes. For this reason, explicit solvent molecules are sometimes added to the calculation, but knowing when and where

explicit solvent molecules participate becomes increasingly challenging with more complex reaction environments. For instance, Model 1 could have also incorporated the counter ion and/or additional explicit solvent molecules to stabilize the formate product. Explicit solvation models in principle will capture all intermolecular interactions between solutes and the solvent, but the accuracy of such models will naturally depend on the quality of the level of theory employed. Pure GGA exchange correlation functionals such as PBE and PW91 are widely used for modeling condensed phase systems under periodic boundary conditions, but it is not often clear if the GGAs used can capture the same level of electronic correlation as higher levels of QC theory that are more easily obtained using non-periodic calculations. For deeper understanding we now compare reaction pathways from Model 1 with those determined by an explicit solvent model employing the PBE exchange correlation functional under periodic boundary conditions.

High temperature BOMD simulations were carried out to model the reduction of CO_2 with BH_4^- (Scheme 3.2) but now involving the counter ion to ensure charge neutrality in the simulation box. Reactant and product states were then used for pathway determinations using gSS-NEB (see computational methods for details). Snapshots along the BOMD trajectory indicated an overall reaction pathway similar to the direct $\text{S}_\text{N}2$ hydride transfer-water addition from our cluster model calculations. However, the gSS-NEB calculations revealed this pathway has two barriers with a metastable intermediate state that was not found using Model 1. Figure 3.5 shows the gSS-NEB determined reaction pathway energy profile. The reaction begins with BH_4^- and CO_2 associating to form a metastable intermediate (barrier = 0.43 eV, relative intermediate energy = 0.21 eV) with a bridging hydride. The second step involves the hydride transferring completely to the CO_2 , resulting in a BH_3 species that spontaneously forms a donor-acceptor bond to an adjacent H_2O molecule (barrier = 0.14 eV, relative reaction energy = -1.00 eV). The metastable intermediate’s structure is compared to the reactant and product structures in Figure 3.6.

The formation of this complex was unexpected, but not entirely unprecedented since borohydride forms interesting coordination complexes involving three-center two-electron bonds.[202] Explicit solvation models can account for adjacent solvent molecules (and counter ions) relaxing and rearranging over the course of the reaction pathway to stabilize intermedi-

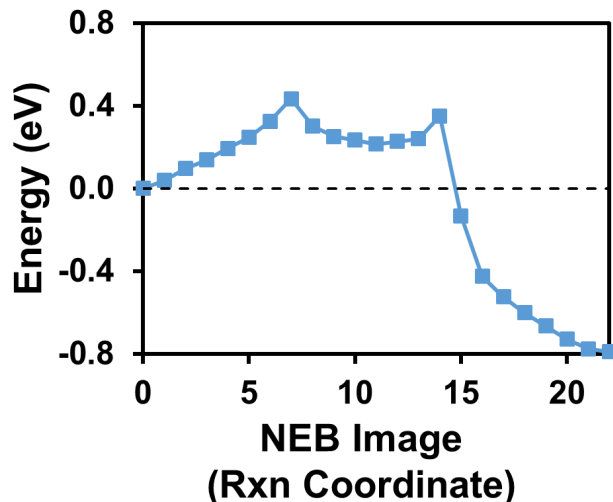


Figure 3.5: The relative energies of the gSS-NEB for BH_4^- reacting with CO_2 to produce formate. This reaction is qualitatively different from that identified using Model 1.

ate and product species. Recreating all of these interactions that stabilize this intermediate without a priori knowledge of the first solvation shell would be very difficult using Model 1. The BOMD simulations naturally capture these interactions, but this intermediate was not identified until we used the gSS-NEB analysis for the reaction pathway.

Closer inspection of bond lengths relevant to the reaction showed that the Na^+ counter ion in the simulation cell moves significantly closer to the reacting atoms over the course of the reaction (from 3.99 Å to 2.31 Å, see Table 3.1 and Figure 3.6). This suggests the simulation itself detected that the counter ion plays a non-innocent role in this reaction by stabilizing the negative charge on CO_2 as it is converted to formate. Bond length comparisons also show that the transition states and metastable intermediate differ by only relatively small changes in the B-H and C-H bond lengths (Table 3.1).

Full hessian calculations performed with VASP on the two transition states both resulted in one sizable imaginary frequency (on the order of $250i \text{ cm}^{-1}$) corresponding to the reaction coordinate as well as four much smaller frequencies (on the order of $25i \text{ cm}^{-1}$) corresponding to solvent molecule librations. Full hessian calculations on the metastable intermediate

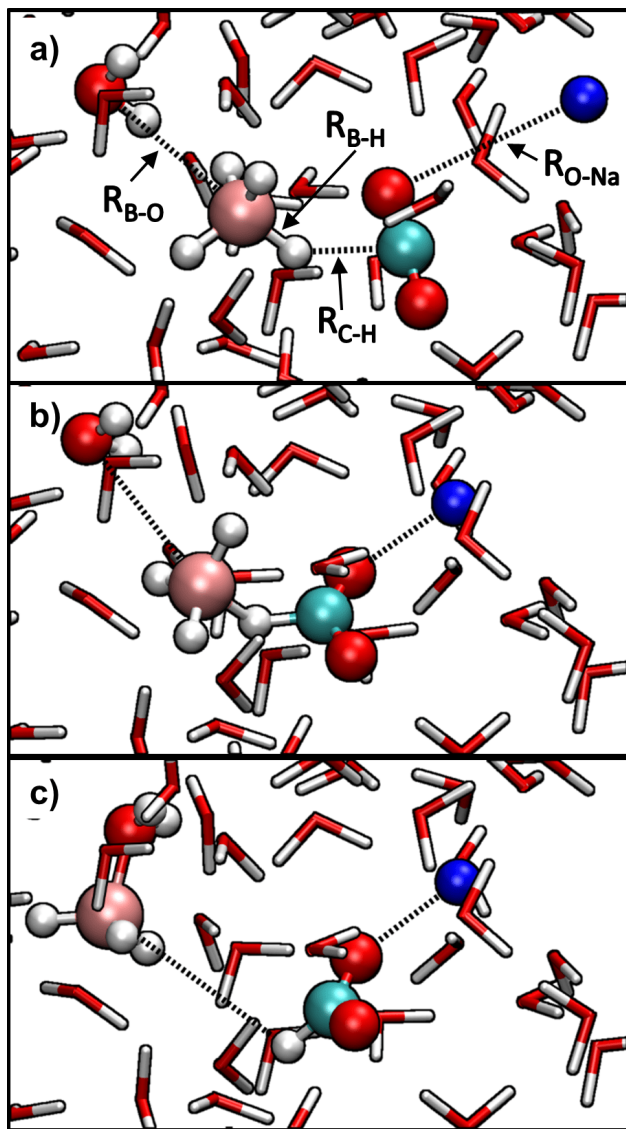


Figure 3.6: The gSS-NEB determines a) reactant, b) metastable intermediate, and c) product geometries for Figure 3.2. The dashed lines denote key interatomic distances (see Table 3.1).

Table 3.1: Bond lengths for the relevant bonds in the gSS-NEB determined reaction pathway.

	Bond Distance (Å)			
	R_{C-H}	R_{B-H}	R_{B-O}	R_{O-Na}
R	2.80	1.24	3.38	3.99
TS1	1.74	1.26	3.26	2.47
I	1.24	1.43	3.34	2.31
TS2	1.15	1.90	2.63	2.32
P	1.11	4.19	1.11	2.31

found just four similarly small imaginary frequencies corresponding to solvent librations. The frequencies corresponding to librations might be attributed to numerical errors in the hessian calculation, but this analysis gives us confidence that the gSS-NEB method located two realistic transition states and one metastable intermediate that is not an artifact of a bifurcated reaction pathway.

We then optimized the geometry of the metastable intermediate as a cluster considering the role of the entire first solvation shell, the Na^+ counter ion, and continuum solvation (see Figure 3.1) using PBE/def2-TZVP calculations with ORCA. When the continuum solvation model was enabled during the geometry relaxation, the complex relaxed into a stable structure in every case except when neither the counter ion nor the explicit solvation shell were included. Without continuum solvation, the intermediate complex always dissociated into reactants ($BH_4^- + CO_2$) or products ($BH_3OH_2 + HCOO^-$). This indicates that energetic contributions from the explicit solvation shell, the counter ion, and effects from the continuum solvation model all contribute significantly to stabilizing the metastable intermediate complex.

Bader charge integration using the Yu and Trinkle procedure[203] showed that all of the system’s charge was almost entirely contained on the reacting atoms (BH_4^- , CO_2 and Na^+), and water molecules in the explicit solvation shell carry essentially no excess charge. The Bader charges were used to qualitatively track the progress of charge transfer as shown

in Figure 3.7. The decreasing negative charge on the hydride and BH_3 fragments (and related increasing negative charge on CO_2) indicated the charge transfer is localized despite stabilization from the surrounding solvent and counter ion.

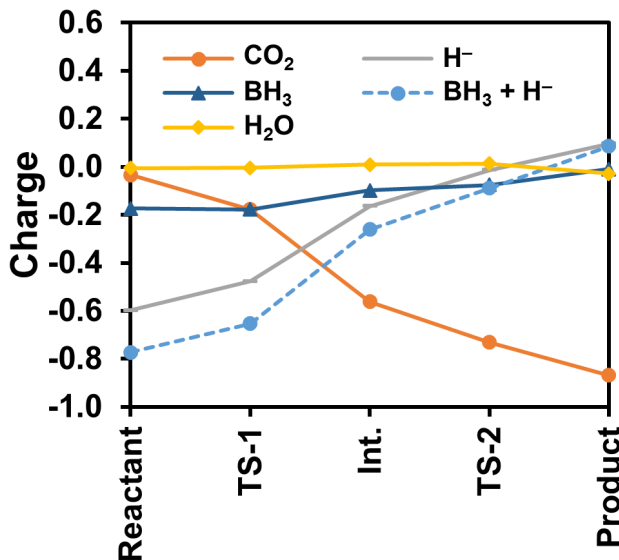


Figure 3.7: Bader charge analysis on reacting fragments. The charge transfers from BH_3 and the transferred hydride to CO_2 over the course of the reaction. Na^+ (not shown here) has a consistent +0.85 charge over the course of the reaction.

3.3.3 Model 3: Fully microsolvated clusters obtained from gSS-NEB reaction pathways embedded within continuum solvation models

It is widely known that the PBE exchange correlation functional over delocalizes electron density and lacks static correlation. Thus PBE transition state energetics may always be considered suspect. To test the validity of energetics from these structures as well as probe the roles of the counter ion and explicit solvent molecules on reaction pathway energetics, we performed single point energy calculations on molecular clusters selected from subsets of atoms from the gSS-NEB images using various levels of QC theory (PBE/PBE0/B3LYP/MP2/DLPNOCCSD) as described in the computational methods section. A representative set of clusters are shown in Figure 3.1.

We first modeled the nuclear coordinates of only the reacting atoms (BH_4^- and CO_2) along the gSS-NEB reaction pathway with continuum solvation. Without either the counter ion or the explicit solvation shell, the reaction energy profile hardly resembles that of the original NEB pathway (Figure 3.8a). The recalculated KS-DFT reaction barriers are ~ 0.6 eV higher than the NEB predicted barrier, the intermediate species appears to be unstable, and the overall reaction energy suggests a process that is ~ 1.25 eV higher in energy than that found in the NEB pathway. Including the counter ion in these calculations stabilizes the intermediate, transition state, and product by as much as 0.4-0.5 eV (Figure 3.8b), but the process still appears to have a single barrier and no metastable intermediate.

Including the first solvation shell with BH_4^- and CO_2 (the cluster seen in Figure 3.1b) yields an energy profile qualitatively similar to the original NEB profile using Model 2. As seen in Figure 3.8c, the reaction profile has two barriers and is overall downhill in energy. Quantitatively, the barriers and intermediate species are ~ 0.2 eV less stable and the products are ~ 0.5 eV less stable compared to the reactants. Just as with the minimal atom clusters in Figure 3.8a and Figure 3.8b, including the counter ion (and explicit water molecules in its coordination sphere) further stabilizes the intermediate, transition states, and products by 0.5-0.6 eV. In this case, including the counter ion and first solvation shell (Figure 3.8d) yields an energy profile very similar to that of the original NEB profile. This stabilization due to the counter ion is consistent across the different QC methods and is more than twice the maximum observed differences between pathways calculated using different QC methods (0.2 - 0.3 eV). Interestingly, within 0.30 eV, the energetics of the PBE profiles using Model 2 and Model 3 are the same. We note that an energy difference of 0.30 eV is approximately 4% of the magnitude of the absolute solvation energy for the metastable intermediate obtained from the COSMO model, -7.02 eV. This shows a reasonable degree of calibration possible using continuum solvation model as a substitute for solvation beyond the first solvation shell.

Overall, we found that the level of QC theory in this particular hydride transfer reaction is less important than the role of counter ions and a full solvation shell. Although the difference between reaction pathway energetics calculated using different QC methods is significant (0.2 - 0.3 eV), we find that GGA, hybrid DFT, and post-HF wavefunction methods all have qualitatively similar reaction pathway energetics. Contrarily, the inclusion of explicit solvent

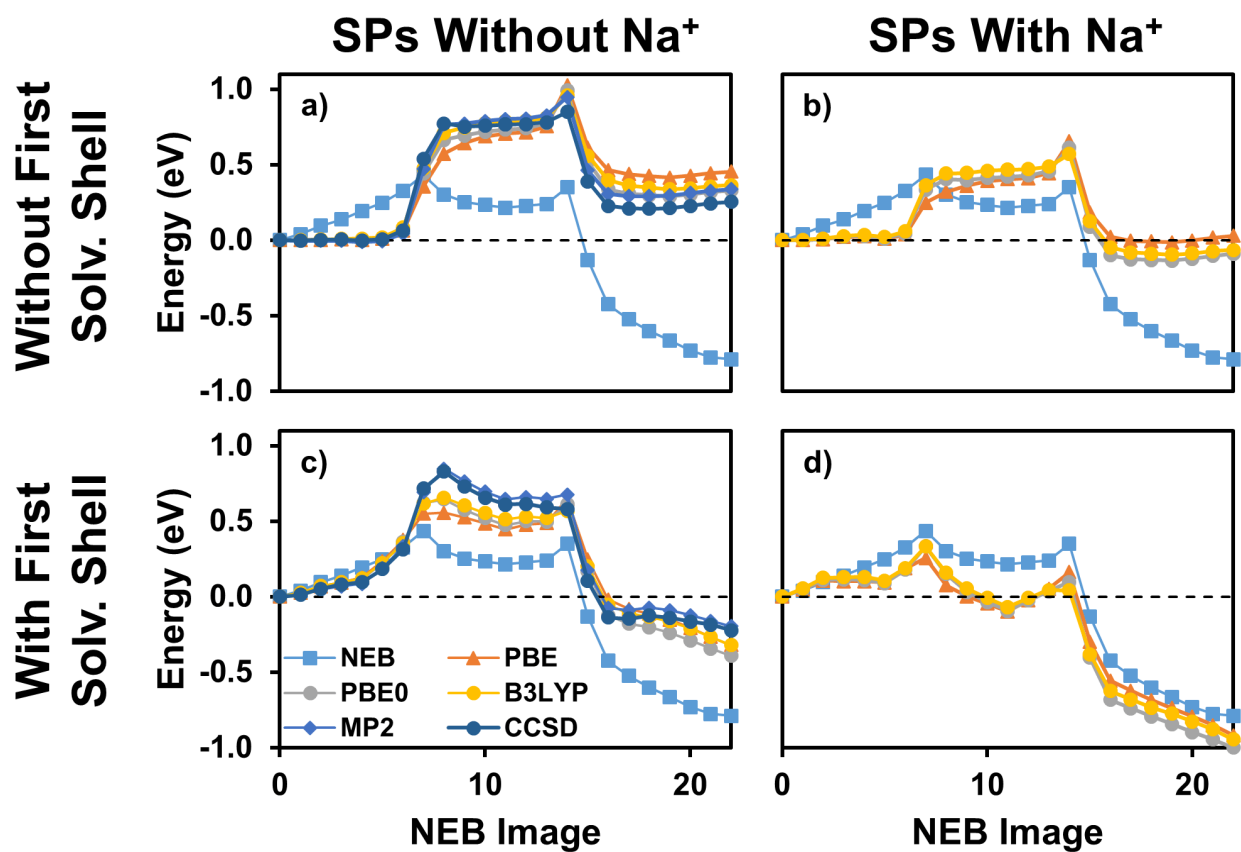


Figure 3.8: Single point energy (SP) calculations on clusters from gSS-NEB optimized pathways for the reaction given in Figure 3.2. Energies were calculated with several different exchange correlation functionals as well as RI-MP2 (labeled as MP2) and DLPNO-CCSD (labeled as CCSD) in figures a) and c). See the main text for more details.

molecules and the counter ion has a larger impact on the reaction pathway energetics (0.4 - 1.2 eV) and these factors can qualitatively alter the reaction pathway as shown in Figure 3.8. For instance, substituting out the first solvation shell and counter ion but keeping the continuum solvation model yields a single barrier endothermic process by ~ 0.4 eV (Figure 3.8a) while calculations on the full cluster predict a strongly exothermic process (by ~ 0.9 eV) with two barriers bracketing a metastable intermediate (Figure 3.8d).

We note that our RI-MP2 and DLPNO-CCSD calculations yielded some spurious energetics at some points along the pathways that included the counter ion (Fig 3.8b and 3.8d). We attribute the problematic cases to difficulties completing post-HF treatments on zwitterionic states involving the Na^+ ion. However, since the counter ions are expected to contribute only via coulombic interactions, we assume that post-HF methods would not result in qualitative differences in energetics. We also note that the T1 diagnostic for all DLPNO-CCSD calculations that converged was always less than 0.016, indicating a lack of multiconfigurational wavefunction character and thus a lack of significant static correlation. CASSCF[204] and NEVPT2[205, 206, 207] ORCA calculations on the reactant, transition state, and intermediate geometries (with up to 12 electrons in 12 orbitals) also showed good agreement with the energy profiles displayed in Figure 3.8. As such, single determinant methods appear suitable for modeling these hydride transfer reactions in aqueous solution.

To further investigate the effect of explicit solvation, we compare the polarization on the reacting atoms arising due to continuum solvation (Figure 3.9a) and the explicit solvent shell (Figure 3.9b) using electron density difference plots. The polarization due to interactions between the reacting atoms and the explicit solvent molecules is substantially different than what is observed using just the continuum solvation model on the reacting atoms. From this analysis, we found that as many as nine water molecules interact strongly with the metastable intermediate species. We then created molecular clusters using the reacting atoms, the counter ion, and these nine water molecules identified by inspecting the density difference plot. The resulting single point energy calculations in Figure 3.9c retain some of the character of the NEB energy profile but the intermediate and product species are higher in energy, and there is only one observed barrier. The product species with significant charge separation will likely be stabilized with additional H_2O molecules other than just

those shown in Figure 3.9c. Although this suggests that the overall reaction profile might be reproducible with fewer water molecules than the entire first solvation shell, one would normally not know how to correctly identify these molecules without already having the full solvation shell determined. Finally, Figure 3.9d shows the influence of different continuum solvation models (COSMO and SMD[208]) on the reaction energies. The average difference between the two energy profiles is less than 0.1 eV, and solvation energies from the SMD model are found to be in slightly better agreement with energetics of Model 2.

3.3.4 Other reactions: BH_3OH^- as a reducing agent

We now consider a different hydride transfer for comparison. In previous work we found that BH_3OH^- can also reduce CO_2 in aqueous solution,[170] and it is also a proposed byproduct of Figure 3.2. Thus, we modeled the reaction shown in Figure 3.10 as a second test reaction for our method.

We find this reaction is more straightforward than the reaction in Figure 3.2. Calculations using Model 1 predict a single barrier involving a direct hydride transfer as shown in Figure 3.11. No explicit waters are included because we previously found that BH_2OH is stable in solution with an empty p orbital, and there is no spontaneous addition of water to form $\text{BH}_2\text{OH}(\text{OH}_2)$. The Figure 3.10 transition state (Figure 3.11a) has ~ 0.2 Å shorter B-H bond and an ~ 0.8 Å shorter C-H bond length than the Figure 3.2 transition states (Figure 3.3). This reaction has a significantly smaller activation barrier than Figure 3.2 (0.22 eV vs. ~ 0.7 eV), and is 0.35 eV more exothermic than the most favorable case model one results for Figure 3.2. Energetics for Figure 3.10 using different levels of theory are available in Appendix C.

BOMD simulations on Figure 3.10 showed a direct hydride transfer from BH_3OH^- to CO_2 yielding formate and BH_2OH . Unlike our previous BOMD simulations for the reduction of CO_2 with BH_4^- , the hydride transfer in this reaction was not coupled to H_2O adding to BH_2OH . BH_2OH did not react with any H_2O molecules over the remainder of the BOMD simulation and appeared to be stable in solution. This is consistent with our Model 1 results on the previous page and previous work which showed that $\text{BH}_2\text{OH}(\text{OH}_2)$ was less stable

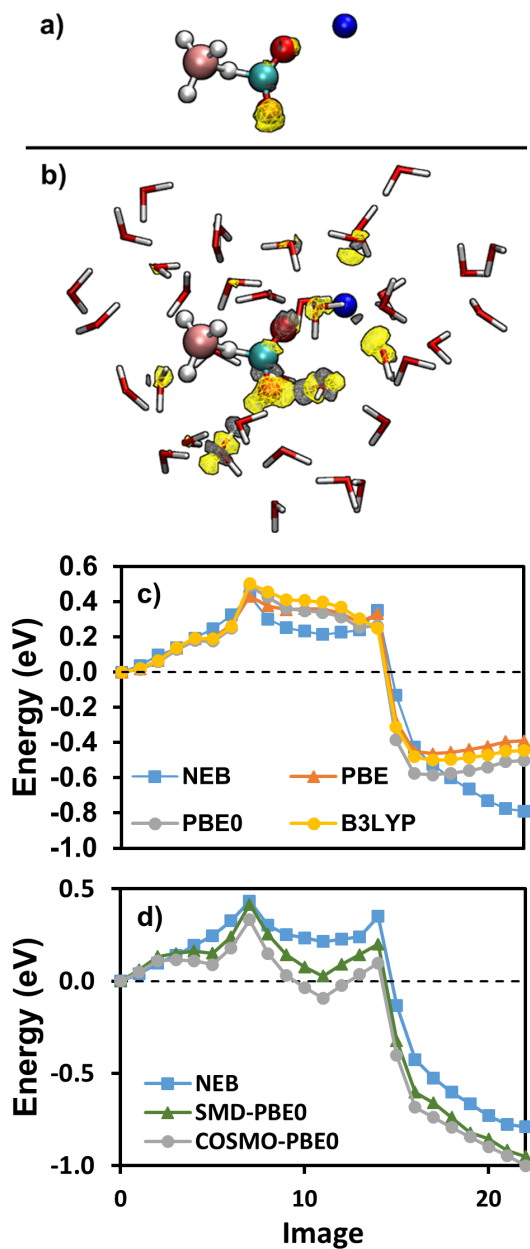


Figure 3.9: Electron density different plots showing the effect of a) continuum solvation on the isolated intermediate, b) the explicit waters in the first solvation shell interaction with the intermediate, c) a comparison of the NEB energy profile in Fig. 3.5 compared to different calculations using the reacting atoms, the counter ion, and the nine explicit waters that appeared active from Fig. 3.9b, d) a comparison of the NEB energy profiles using COSMO or SMD-embedded molecular clusters containing the counter ion and the explicit solvation shell. Single point energies were performed at the PBE0/def2-TZVP level.



Figure 3.10: CO₂ reduction with BH₃OH⁻ to produce formate.

than BH₂OH + H₂O.[170] Further gSS-NEB studies on this pathway confirmed that the process takes place as single barrier hydride transfer. The transition state and energy profile for this pathway are shown in Figure 3.12a and Figure 3.12b, respectively. The reaction has a single barrier ($E_a = 0.15$ eV) and is 0.12 eV downhill in energy. The barrier height found here is similar to that from Model 1, but the overall reaction energy from Model 2 is significantly less exothermic. We attribute this to stabilization of the reactants and transition state by the presence of explicit water molecules when using Model 2.

As before, we created four sets of clusters from the gSS-NEB optimized coordinates for each NEB image as described in the computational methods. Similar trends as seen before also hold for these sets of calculations. Comparing the reaction profiles of the molecular clusters with and without the counter ion (Figure 3.13) shows that the counter ion has a noticeably smaller effect on reaction energies compared to the reaction in Figure 3.2. This is likely due to the fact that in this reaction pathway, the counter ion remains within ~ 2.5 of the CO₂ molecule over the course of the reaction (see Appendix C), and thus solvent relaxation effects are less than those arising in the reaction for Figure 3.2. Indeed, visual inspection of the structures (reported in Appendix C) shows that hydrogen bonding between explicit solvent molecules and the CO₂/formate stabilizes the increasing negative charge on CO₂. This may explain why the counter ion in the reaction in Figure 3.10 has a smaller energetic impact than in the reaction in Figure 3.2. Figure 3.13 also shows that the effect of the counter ion lowers reaction energetics by 0.25 eV, but this effect is reduced when explicit solvation destabilizes the product species compared to the reactant state when the counter ion is present.

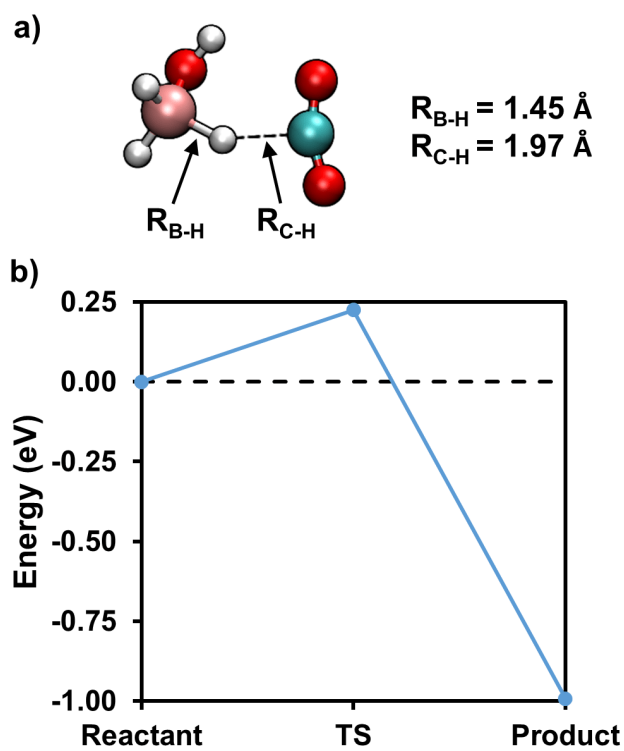


Figure 3.11: A) The transition state structure for the hydride transfer from BH_3OH^- to CO_2 to produce formate. B) The reaction pathway energies for the reaction in Figure 3.10 calculated using ORCA (B3LYP/def2-TZVP embedded in COSMO solvation).

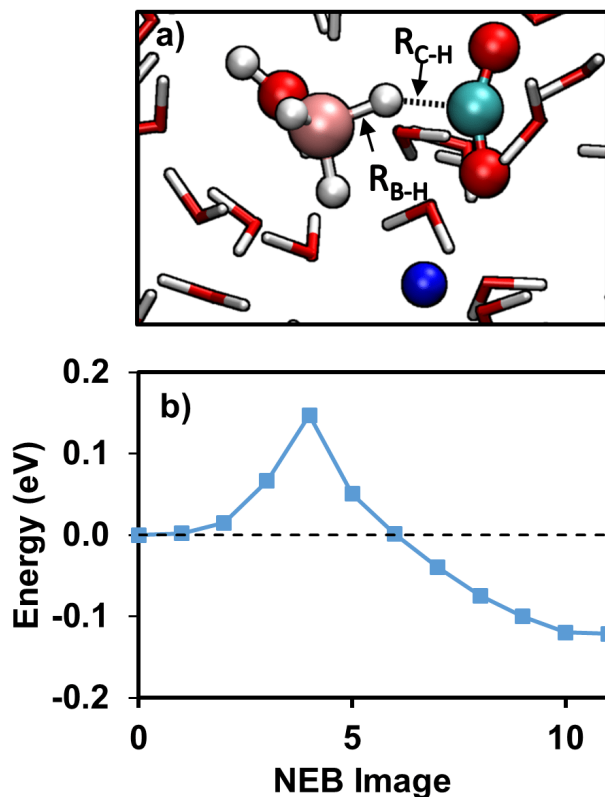


Figure 3.12: A) The transition state structure for the hydride transfer from BH_3OH^- to CO_2 to produce formate. B) The reaction pathway energies for the reaction in Figure 3.10 calculated using ORCA (B3LYP/def2-TZVP embedded in COSMO solvation).

The 0.33 eV difference between the PBE and DLPNO-CCSD barriers seen in Figures 3.13a and 3.13c also illustrates greater variance between model chemistries than what was observed with the reaction shown in Figure 3.2. It may also signify that the formation of the under-coordinated BH_2OH^- species requires higher levels of theory for accuracy. Overall, based on comparisons of the data in Figure 3.13, it appears that the energy deviations between different levels of theory (0.33 eV) for this reaction are on a similar scale as the energy differences observed when modeling the full solvation shell with the counter ion (0.25 eV).

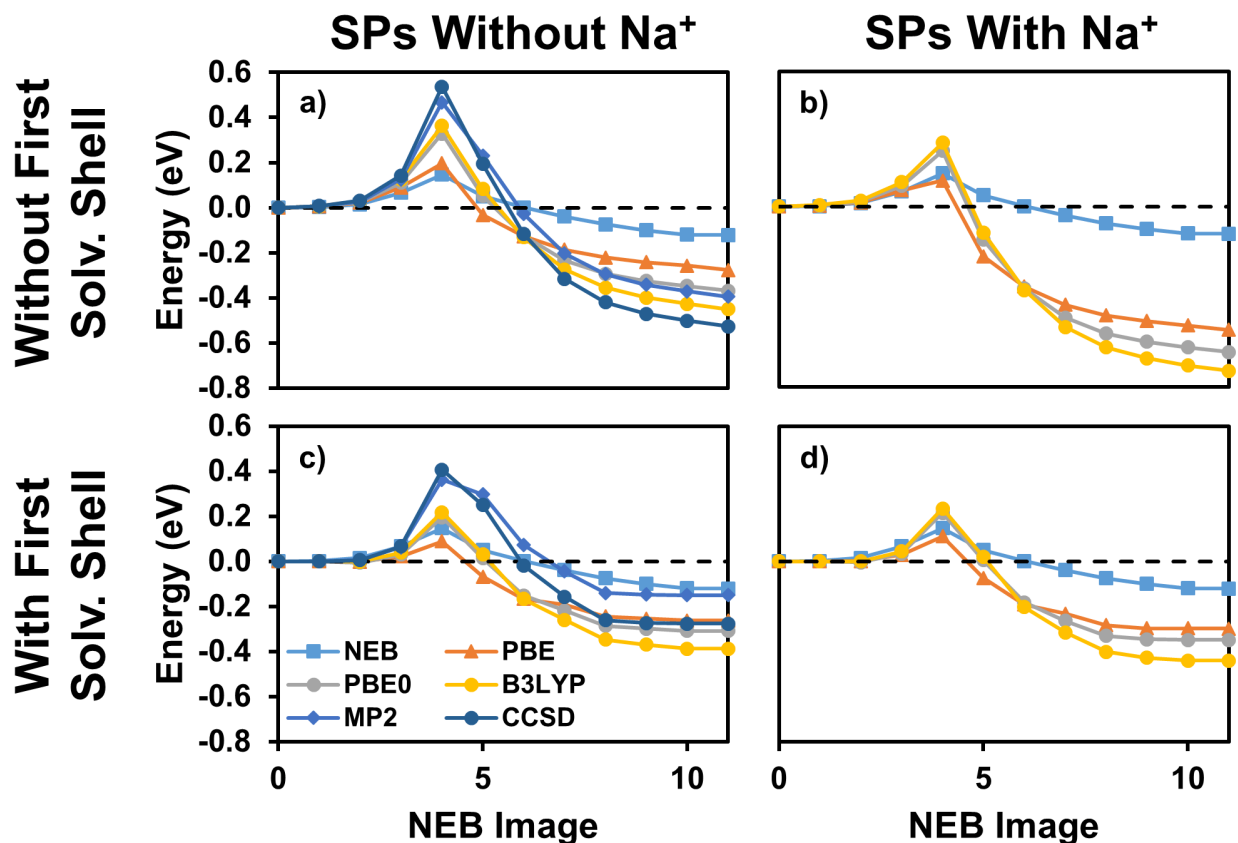


Figure 3.13: Single point energy (SP) calculations on clusters from gSS-NEB optimized pathways for the reaction given in Figure 3.10. Energies were calculated with several different types of KS-DFT as well as RI-MP2 (labeled as MP2) and DLPNO-CCSD (labeled as CCSD) for all of the clusters described in the computational methods on a) only the reacting atoms without Na^+ , b) the reacting atoms with Na^+ , and c/d) the geometries from a) and b) with the first solvation shell.

3.4 CONCLUSIONS

We have investigated the degree that different solvation models and levels of quantum chemistry theory influence reaction pathways in condensed phases using CO_2 reduction by NaBH_4 and NaBH_3OH as test cases. We benchmarked reaction pathways to those obtained from

NEB calculations that identify reaction pathways for processes discovered from high temperature BOMD simulations. We then presented a mixed explicit-continuum solvation model approach that qualitatively agrees with explicit solvation models using periodic boundary conditions. A benefit to the mixed explicit-continuum approach is that it allows the use of high level quantum chemistry theory when studying reaction pathways in solution in an IRCMax-like approach. Procedures such as this may also lead to more computationally efficient workflows for free energies of solvent phase reactions.

We have found that reaction energy profiles and even observed intermediates over the course of a reaction can be qualitatively different depending on the computational models and approximations used. In particular, reliably modeling aqueous phase reaction pathways likely necessitates explicit treatments of solvent molecules and counter ions. In the hydride transfer reactions we considered, using different models for solvation as well as including counter ions results in very large energy differences ranging from 0.25 - 1.25 eV, and the magnitude of these differences can cause qualitative changes in reaction energetics. Alternatively, using different levels of theory on these reactions can result in more moderate energy differences ranging from 0.2 - 0.3 eV, and these did not result in qualitative changes in reaction energetics.

Based on these results we conclude that the treatments of explicit solvation and counter ions will play an equal if not much greater role than the level of theory used (whether obtained from pure GGA, hybrid KS-DFT, or other post HF methods, including multi-configurational correlated wavefunction methods) when modeling adiabatic hydride transfer reactions. Future work will focus on using this approach to model reactions with more complex electronic structures as well as developing determining workflows for calculating free energy contributions necessary for rate constant determinations at ambient temperatures.

4.0 QUANTUM CHEMICAL ANALYSES OF BH_4^- AND BH_3OH^- HYDRIDE TRANSFERS TO CO_2 IN AQUEOUS SOLUTION WITH POTENTIALS OF MEAN FORCE

The content of this chapter is taken from M. C. Groenenboom, and J. A. Keith, "Quantum Chemical Analyses of BH_4^- and BH_3OH^- Hydride Transfers to CO_2 in Aqueous Solution with Potentials of Mean Force" *chemphyschem* 2017, DOI: 10.1002/cphc.201700608R1.

4.1 INTRODUCTION

Finding ways to utilize anthropogenic CO_2 before it enters the environment is critically important as we seek to limit rising atmospheric CO_2 concentrations. There are ongoing efforts to develop efficient and sustainable processes that would convert CO_2 into chemical feedstocks such as formate, methane, methanol, or larger alcohols and/or hydrocarbons.[131, 15, 209] Producing these products requires CO_2 hydrogenation processes that may be classified as chemical hydrogenations,[210] electrochemical reductions,[20] or hydride transfers.[211] Studies on biological systems have identified efficient hydride transfer agents such as nicotinamide adenine dinucleotide (NAD) that are integral components in enzyme-catalyzed CO_2 reduction reactions.[212]

Our group is one of several that have been investigating whether aromatic N-heterocycle containing molecules (a molecular motif found in NAD and sometimes implicated as a catalyst in CO_2 reduction[39]) are catalyzing biomimetic hydride transfer reaction pathways in specific electrochemical environments.[213, 214, 215, 68] Key questions remain about the specific barrier heights for different reaction steps and how best to model these reaction path-

ways using computational methods. Instead of considering electrochemical CO₂ reduction with aromatic N-heterocycles, the present study focuses on the detailed study of a simpler and less controversial chemical reduction.

We previously investigated reaction barriers for CO₂ reduction involving NaBH₄, a powerful chemical reducing agent that was shown to reduce CO₂ in aqueous environments.[170] This is a notable result since hydride transfer reactions usually necessitate aprotic conditions to prevent competitive hydrogen evolution reactions, but the high hydricity of NaBH₄ in part overcomes this hurdle. We later showed that reaction pathways for hydride transfers are significantly more sensitive to how the surrounding solvation and co-solute interactions are modeled than the level of computational theory that is used.[216] The next aspect to address is the quantitative degree that free energy contributions such as solvent configurations and entropy affect reaction energy profiles for hydride transfers to CO₂ in aqueous solution.

Different computational quantum chemistry approaches can be used to characterize reaction mechanisms. The simplest approach might use small molecular clusters embedded within continuum solvation models,[159, 156, 160] but results from these approaches can be very sensitive to solute-solvent interactions or configurations of solvating molecules.[216, 58] More robust computational treatments such as metadynamics[139, 133, 137] or transition path sampling[140] explicitly model solvent environments and can more physically identify complete reaction mechanisms through extended molecular dynamics simulations, but these approaches bring far higher computational costs. The use of semi-empirical or QM/MM methods can decrease computational expense,[145, 148, 217] but these approaches may also have lower accuracy and be less transferrable than ab initio (or Born-Oppenheimer) molecular dynamics simulations.[154]

In the present study, we modeled solvent phase free energies along specific hydride transfer pathways with umbrella sampling simulations using Kohn-Sham density functional theory. Potentials of mean force (PMF) from these simulations were then calculated to yield free energy changes over the course of a chemical reaction at room temperature while explicitly modeling all intermolecular interactions (involving solvent molecules and co-solutes species) along these pathways. This work complements other computational studies of free energies along reaction pathways.[218, 219, 220, 221]

The umbrella sampling simulations were run along CO₂ reduction pathways involving hydride transfers from NaBH₄ and NaBH₃OH obtained using generalized solid-state nudged elastic band (G-SSNEB) methods.[216] This allows the direct comparison of reaction energy profiles obtained at 0 K against free energy profiles modeled at 300 K. Our PMF data provides what should be a definitive prediction of hydride transfer free energy barriers to CO₂ from two different and strong hydride donors in aqueous solution. This work also shows that not accounting for configurational sampling and solvent entropy at room temperature can result in somewhat similar barrier heights (observed within 0.2 eV of the 0 K pathways), but energy profiles can be significantly different.

4.2 COMPUTATIONAL METHODS

We previously reported generalized solid state nudged elastic band (G-SSNEB) optimized reaction pathways for the chemical reduction of CO₂ with BH₄⁻ and BH₃OH⁻. [216] These systems consisted of a BH₄⁻ (or BH₃OH⁻), CO₂, Na⁺, and 71 H₂O molecules (70 H₂O molecules for BH₃OH⁻) in a nearly 13 Å cubic box. The box dimensions changed by < 5% during the G-SSNEB optimization.

Our umbrella sampling procedure is similar to that used by Ivchenko et. al.[222] We performed umbrella sampling simulations along our previously optimized 0 K reaction pathways using CP2K.[223] All CP2K calculations used the PBE density functional,[141] and GTH pseudopotentials[224, 225, 226] in conjunction with double-zeta basis sets (DZVP).[227] All umbrella sampling simulations were periodic in the X, Y, and Z directions, and simulations were performed for 10 ps with a 0.5 fs timestep. All hydrogen atoms were substituted with deuterium to enable the use of a relatively large timestep. Barriers obtained from umbrella sampling simulations using an 0.25 fs timestep were in good agreement with those obtained using an 0.5 fs timestep (reported in Appendix D). The coordinates from our previous reaction pathway studies had been fully relaxed prior to the G-SSNEB reaction pathway optimizations, so we do not perform a separate equilibration run here. We used a 400 Ry cutoff energy as this gave well converged system energies. All simulations used the NVT ensemble

and were performed at 300 K using the velocity-rescaling thermostat.[228] We enforced harmonic bond constraints on the B-H and C-H bonds for reaction 1 (Figure 4.1), the B-H and B-O bonds for reaction 2 (Figure 4.1), and the B-H and C-H bonds for reaction 3 (Figure 4.1). The exact bond lengths and bond constraints for each umbrella sampling window as well as the overlap between the umbrella sampling windows are reported in Appendix D.

The activation barrier and reaction energies for each reaction were determined by calculating a potential of mean force (PMF) using the 2D weighted histogram analysis method (WHAM).[229] We excluded the first 3 ps of each simulation from the WHAM analysis as we consider this to be the equilibration time for each set of reaction coordinates. We set the WHAM convergence criteria to 1E-05 eV.

4.3 RESULTS AND DISCUSSION

In previous work[170] we found that some of the oxidized borohydrides that are expected to be formed from NaBH_4 hydrolysis[162] have a thermodynamic preference toward reducing protons rather than CO_2 in aqueous solutions. We then reported three different G-SSNEB optimized reaction pathways at 0 K for the aqueous phase reduction of CO_2 with NaBH_4 and NaBH_3OH (Figure 4.1).[216] Those optimized pathways showed that BH_4^- reacted with CO_2 to form a metastable intermediate complex (Reaction 1 in Figure 4.1). The complex then decomposed after an H_2O molecule added to BH_3 to form a partially oxidized borohydride (BH_3OH^-) and a formate anion (Reaction 2 in Figure 4.1). BH_3OH^- can also competitively reduce CO_2 to formate through a direct, single step hydride transfer (Reaction 3 in Figure 4.1). Below we compare the reaction pathways and energetics obtained from PMFs determined from the weighted histogram analysis method (WHAM) of umbrella sampling simulations at $T = 300$ K against those obtained from G-SSNEB optimized reaction pathways at $T = 0$ K to quantify the significance of free energy contributions in these reaction pathways. The difference in the energetics of these two models represents a combination of solvent configurations and solvent entropy effects. Although free energies of our PMF simulations were smoothly converged, smoothly converged average potential energies for each

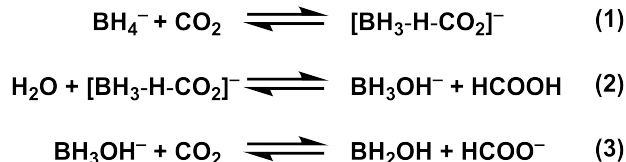


Figure 4.1: Three pathways characterized with umbrella sampling. Reactions 1 and 2 are parts of a sequential, two-step hydride transfer reaction. Reaction 3 is a different one-step hydride transfer from a partially oxidized borohydride species (BH_3OH^-). These reaction pathways all involve explicit solvation and a Na^+ counter ion and were obtained with G-SSNEB calculations in previous work.[\[216\]](#)

umbrella sampling window would require much longer simulations. Thus, we cannot quantitatively allocate free energies due to configurational sampling versus other entropy at room temperature.

Umbrella sampling simulations require defining a set of collective variables for each reaction pathway. Reaction 1 is characterized by the boron-hydride and carbon-hydride distances. Figure [4.2](#) shows the minimum energy reaction pathway along the B-H and C-H distances, and Figure [4.2B](#) shows the reaction energies as the C-H distance decreases (i.e. as the intermediate complex is formed). Figure [4.2A](#) and Figure [4.2B](#) respectively compare the PMF reaction coordinates and the PMF energy profile against those determined from G-SSNEB reaction pathway optimizations.

The transition state structures and minimum energy reaction pathways for Reaction 1 from PMF and G-SSNEB modeling are very similar (see Figure [4.2A](#)). The similarities between the PMF and G-SSNEB minimum energy reaction pathways show that sampling different solvent configurations does not cause the 300 K reaction pathway to significantly deviate from the 0 K G-SSNEB reaction pathway. It also shows that our free energy simulations are sampling configurations similar to the NEB reaction coordinate of the hydride transfer transition state. (The pairs of B-H and C-H distances used for each umbrella sampling window are discussed more in Appendix [D](#) supporting information.)

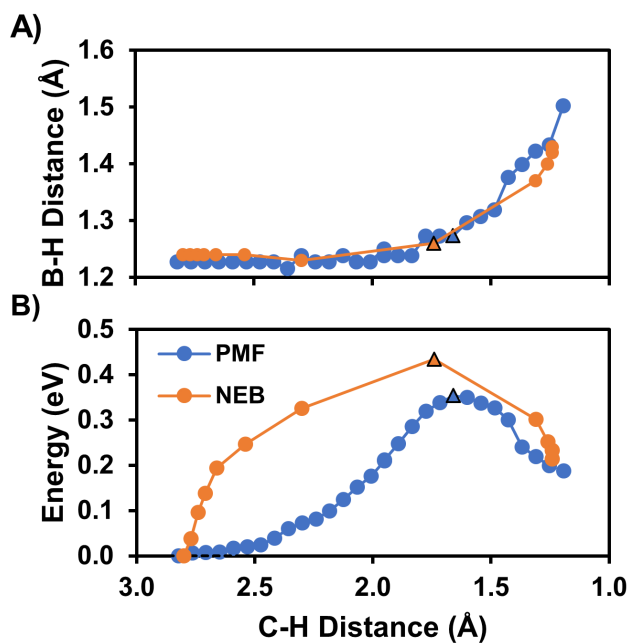


Figure 4.2: Reaction pathway analyses of Reaction 1 (Figure 4.1) using C-H bond distance as the reaction coordinate. A) Plot of B-H distance vs. C-H distance over the course of Reaction 1. Transition states are marked with a triangle. B) Minimum free energy reaction pathways determined from WHAM analysis (labelled PMF), G-SSNEB reaction pathway optimizations at 0 K (labelled NEB[216]).

However, Figure 4.2B shows that the energy profiles of these two methods differ more significantly. The free energy profile from PMF modeling is lower relative to the G-SSNEB pathway. The G-SSNEB pathway is as much as 0.25 eV higher in energy at some points along the reaction pathway while the transition state is 0.08 eV higher than that found from the PMF modeling. Although these are relatively small quantities, note that similarly small differences in barrier heights would result in dramatic changes in reaction rates, and just a 0.08 eV barrier height decrease corresponds to a 22x increase in Arrhenius rate constants. The overall G-SSNEB and PMF reactant and product state energies for Reaction 1 are nevertheless in good agreement.

Reaction 2 is characterized by 1) an increasing B-H bond distance as the intermediate complex breaks apart and 2) a decreasing B-O bond distance as the water molecule participates in an S_N2 attack on BH_3 (see Figure 4.3A). The PMF and G-SSNEB reaction coordinates deviate more in Figure 4.3A compared to Figure 4.2A. This shows Reaction 2 is more sensitive to solvent configurations, which is not surprising since Reaction 2 explicitly involves addition of H_2O . While the minimum energy reaction profiles deviate slightly at small B-H distances, the transition states and reactant and product states occur at similar sets of B-O and B-H bond lengths. Two transition states are marked in the PMF pathway in Figure 4.3 because two different states were observed having nearly identical energies and B-H distances, but both had significantly different B-O distances.

Figure 4.3B projects out the reaction energy using the B-H distance as the reaction coordinate. As was found with Reaction 1, the PMF pathway at 300 K has lower energies than was predicted from the G-SSNEB at 0 K at most intermediate reaction coordinates. The G-SSNEB barrier for Reaction 2 (relative to the product state in Reaction 1) is 0.14 eV. In contrast, the PMF barrier is 0.07 eV.

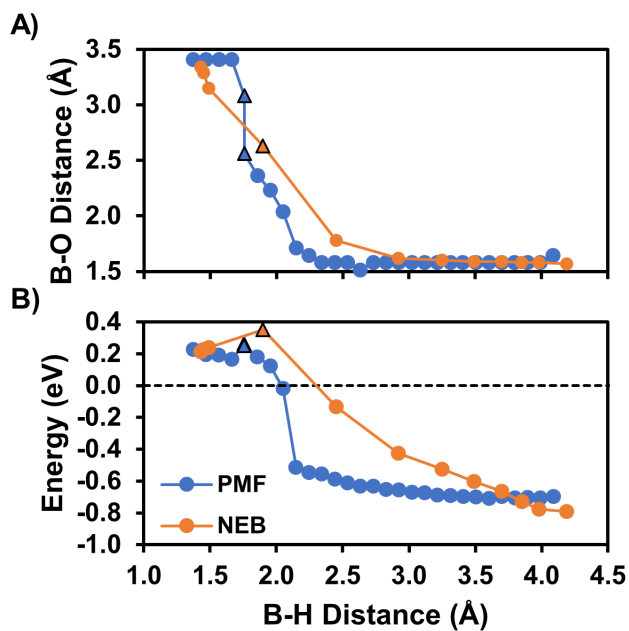


Figure 4.3: Analysis of Reaction 2 in Figure 4.1. A) Minimum energy reaction pathways determined from WHAM analysis (labelled PMF) or obtained from G-SSNEB reaction pathway optimizations (labelled NEB). Transition states are marked with a triangle. B) Reaction energies determined from WHAM analysis or obtained from G-SSNEB reaction pathway optimizations.[216]

The barrier for Reaction 2 is due to BH_3 undergoing a nucleophilic attack from H_2O . The lower PMF barrier height can be attributed to weaker average interactions between all neighboring water molecules at 300 K. A smaller Reaction 2 barrier relative to the reverse Reaction 1 barrier (0.17 eV) increases the likelihood that the reaction will move towards products (formate and BH_3OH^-) as opposed to regenerating BH_4^- and CO_2 . Reactions 1 and 2 would presumably proceed faster as a pseudo-single step reduction reaction (limited by the barrier to Reaction 1) if the Reaction 2 barrier could be further decreased.

CO_2 reduction by BH_3OH^- (Reaction 3 in Figure 4.1) is characterized by increasing B-H bond distances and decreasing C-H bond distances. The B-H and C-H bond distances involved in the reaction coordinate (Figure 4.4A) are similar in both the G-SSNEB and PMF models, showing that sampling different solvation configurations does not significantly affect this reaction coordinate. The PMF pathway involves longer C-H bond distances during the second half of the reaction (C-H distances ranging from 1.5 - 1.1 Å), but the product has similar sets of C-H/B-H distances.

Figure 4.4B shows that the forward PMF reaction barrier (0.27 eV) is nearly twice as large as the forward G-SSNEB reaction barrier (0.15 eV). More noticeable is that the PMF reaction energy at 300 K (-0.74 eV) is significantly more downhill in energy than the G-SSNEB pathway at 0 K (-0.12 eV). The reaction energy from the PMF pathway is comparable to the combined reaction energies of reactions 1 and 2 (-0.70 eV). In terms of kinetic modeling, using data from PMF simulations rather than NEB calculations for this reaction would significantly decrease reaction rate constants ($k = 0.006 * k_{NEB}$) and increase the equilibrium constant ($K_{PMF} \approx 10^{13} * K_{NEB}$). Although transition states from NEB and PMF modeling resemble each other, the configurational sampling of solvent molecules clearly plays a very important role in determining reaction thermodynamics.

To elaborate further, we assume that differences between the PMF and G-SSNEB reaction pathways in Figure 4.4A are not large enough to produce the energy differences in Figure 4.4B. The difference between the PMF and NEB reaction energies are most likely due to configurational sampling because the difference between the average potential energies of the reactant and product umbrella sampling windows is similar to the PMF reaction free energy (-0.78 vs. -0.74 eV), see Appendix D. However, the barrier height predicted from the

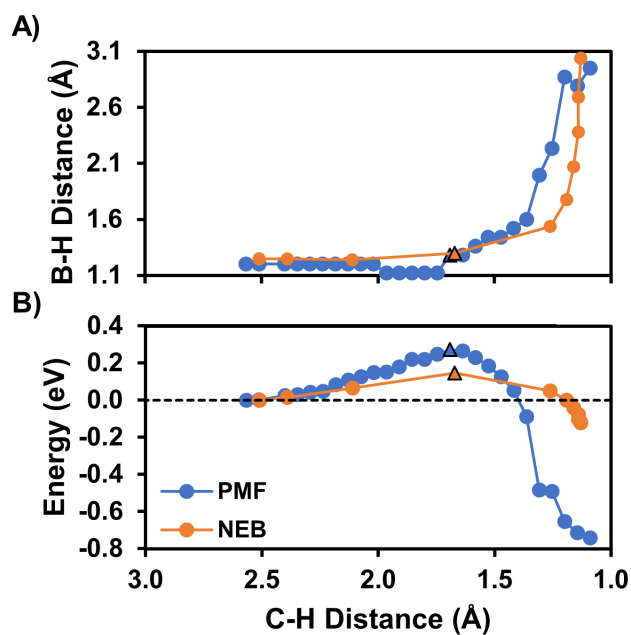


Figure 4.4: Analysis of Reaction 3 in Figure 4.1. A) Minimum energy reaction pathways determined from WHAM analysis (labelled PMF) or obtained from G-SSNEB reaction pathway optimizations (labelled NEB). Transition states are marked with a triangle. B) Reaction energies determined from WHAM analysis or obtained from G-SSNEB reaction pathway optimizations.[216]

umbrella sampling window average potential energy (0.78 eV) is significantly higher than either the PMF (0.27 eV) or the NEB (0.15 eV) profiles. Therefore, the difference in reaction energetics can mostly be assumed to be due to more favorable solvent configurations sampled in PMF simulations, but the remaining differences in barrier heights reflect a combination of free energy contributions. Although G-SSNEB calculations at 0 K were carried out using geometrically relaxed structures from molecular dynamics equilibrations at 300 K,^[216] the product structure used in the NEB calculation here was probably a relatively high energy local minimum. This in turn resulted in G-SSNEB energy profiles dramatically different from the PMF simulations on the same pathway that appear to correct this problem by providing enough kinetic energy to escape local energy minima and more fully sample the potential energy surface. Thus, PMF studies on pathways discovered from G-SSNEB calculations appear to be a robust modeling approach to analyze individual reaction pathways at realistic operating temperatures.

Interestingly, umbrella sampling barriers and reaction energies for Reaction 3 are qualitatively similar to results from modeling small molecular clusters embedded in continuum solvation as discussed in our previous study ($\Delta G_{\ddagger}^{\text{cluster}} = 0.23$ eV, $\Delta G_{\text{cluster}} = -0.99$ eV).^[216] In contrast to Reaction 3, modeling Reactions 1 and 2 with small clusters embedded in continuum solvent resulted in a single step reaction process with a significantly larger barrier height ($\Delta G_{\ddagger}^{\text{cluster}} = 0.71$ eV) instead of the 2-step reaction pathway found from G-SSNEB calculations. This reaffirms that continuum solvation models may sometimes appear to be more reliable for calculating overall reaction energies, but reaction pathways obtained from small cluster models run the risk of being qualitatively different from those obtained using explicitly solvated modeling. Computationally studying hydride transfers in solvent phase (and perhaps at a solid/liquid interface) appears to require explicit solvation treatments that account for configurational entropy at finite temperatures.

4.4 CONCLUSIONS

We have investigated the role of reaction free energies in prototypical hydride transfer reactions to CO₂ in aqueous solvent. We find that reaction pathways from G-SSNEB calculations and subsequent PMF simulations are generally similar, and this shows that PMF simulations can provide additional insight into how free energies at ambient temperatures affect reaction energies along predefined reaction coordinates. A notable result is that the much more computationally intensive PMF reaction energies sometimes are consistent with reaction energies from G-SSNEB or cluster-continuum models, but sometimes they are very different. This suggests more insight is needed to address when PMF simulations would be needed and when less computationally intensive models would suffice. Overall, the PMF studies here show what should be highly accurate energy profiles for CO₂ reductions from hydride donating agents at room temperature. By using a combination of G-SSNEB and PMF methods one can develop computational workflows that analyze reaction pathways to identify more effective and more efficient CO₂ reduction catalysts.

5.0 DOPED AMORPHOUS TI OXIDES TO DEOPTIMIZE OXYGEN REDUCTION REACTION CATALYSIS

The content of this chapter is taken from M. C. Groenenboom, R. M. Anderson, D. J. Horton, Y. Basdogan, D. F. Roeper, S. A. Policastro, and J. A. Keith, "Doped Amorphous Ti Oxides to Deoptimize Oxygen Reduction Reaction Catalysis" *J. Phys. Chem. C* 121 (2017) 16825-16830.

5.1 INTRODUCTION

Worldwide efforts to prevent and remediate corrosion damage cost approximately 3.4% of the global GDP per year.[230] Even materials that are normally resistant to corrosion in isolation can degrade due to galvanic couples that form between dissimilar metals. This effect is powerful enough to corrode aircraft grade aluminum alloys despite being covered by their stable, corrosion resistant metal oxides.[74, 75] Problems such as these have inspired many efforts to create better functional coatings that physically block corrosive conditions,[82, 83] sacrificially corrode to protect the substrate,[88] or kinetically slow corrosion rates.[231, 232]

Galvanic corrosion occurs near boundaries between dissimilar metals (see Figure 1.6). Metal oxidation on the less noble metal surface (anodic site) provides electrons that drive the oxygen reduction reaction (ORR) on the more noble metal surface (cathodic site). Because the driving force for metal oxidation decreases if these electrons are not consumed, the ORR is a major factor that controls the overall galvanic corrosion rate in atmospheric environments.[80, 79] Thus, inhibiting catalytic ORR activity at the cathodic site is an opportunity to decrease the rate of galvanic corrosion.

Amorphous Ti oxides are an ideal candidate material to reduce cathodic kinetics because fasteners made from Ti alloys commonly form galvanic couples with other metals, such as Al and its alloys. These amorphous Ti oxides can be doped with other metals to further alter cathodic kinetics. Doped Ti oxides are reasonably stable and can be natively formed on doped Ti metal surfaces without the need for traditional barrier coatings. Moreover, the dopants can be alloyed in the Ti bulk material so the doped Ti oxide will spontaneously regenerate if damaged. Previous efforts to use TiO_2 to inhibit galvanic corrosion have attempted to provide cathodic protection via photo-generated electrons from TiO_2 photoanodes.[90] In contrast to those works, our study focuses on identifying dopants that decrease ORR electrokinetics on amorphous Ti oxide surfaces.

Computational quantum chemistry studies frequently use thermodynamic descriptors and Sabatier volcano curves to identify optimal catalysts that lie near the top of the activity volcano (see for example the large body of fuel cell literature[30, 91, 92, 93, 94]). While this level of modeling works well in predicting dopants that maximize the catalytic activity of a material, these *in silico* models are not normally used to predict dopants that minimize catalytic activity, i.e. dopants that lie near the bottom of the Sabatier volcano plots. We report an integrated computational and experimental study that demonstrates that simple Sabatier volcano descriptors can be used to qualitatively predict metal dopants that experimentally decrease ORR currents by as much as 77% when impregnated in amorphous TiO_2 at doping concentrations of 1%. This report focuses on using modeling and experiment to understand ORR catalysis on doped Ti oxide surfaces. The overall effectiveness of these coatings at reducing galvanic corrosion will be addressed in future work.

5.2 COMPUTATIONAL METHODS

Unless otherwise specified, all presented energies and structures were determined using Kohn-Sham density functional theory (DFT) in the Vienna Ab initio Simulation Package (VASP)[184, 185, 186] utilizing the Perdew-Burke-Ernzerhof (PBE)[141] GGA exchange correlation functional and the projector augmented wave (PAW) method[189] with spin polar-

ization. Planewave energy cutoffs of 450 eV and a 2x2x1 k-point grid gave well-converged energies. We approximate the zero point energy, entropic, and solvation free energy of water by using the values predicted by Valds et. al. for the ORR intermediates adsorbed to TiO₂.^[233] When noted, VASPsol was used to account for solvated reaction energetics,^[234, 235] using the relative permittivity of water (78.4) along with the previously mentioned parameters (PBE, PAW potentials, spin polarization enabled, 450 eV energy cutoff, and 2x2x1 k-point grid). Additional energy calculations using the HSE06 hybrid DFT functional^[236] (PAW method, spin polarization enabled, 450 eV energy cutoff, and a gamma-point calculation) were performed on PBE optimized structures to determine the impact that higher levels of theory have on intermediates adsorbed to doped amorphous Ti oxides. HSE06 calculations were performed for dopant systems where we also obtained experimental data.

We created amorphous TiO₂ surfaces by annealing crystalline TiO₂ slabs using the reax/c^[237] implementation of ReaxFF^[238] in LAMMPS.^[239] All annealing simulations used the forcefield parameterized by Kim and Kubicki.^[240] Rutile TiO₂ slabs were heated from 0 K to 1100 K at a rate of 0.06 K/fs using a 1 fs timestep. After 300 ps at 1100 K, we quenched the structures to 0 K at a rate of 0.05 K/fs. The resulting structures were then fully relaxed using DFT in VASP as described previously (PBE, PAW potentials, spin polarization enabled, 450 eV energy cutoff, and 2x2x1 k-point grid).

5.3 EXPERIMENTAL METHODS

Titanium-doped alloys were arc-melted using high purity metals (greater than 99.995 at%). Ingots were subsequently suction cast into a cylindrical copper mold. The cylinder rods were then machined to 1.1 cm and then ground to a final dimension of 1 cm. After casting, a four-hour solution anneal in argon was performed at 827°C (Ag, Al, Cr, Sn, and Ti), 685°C (Co), or 550°C (Mn), within the single-phase HCP region, followed by a water quench. The crystal structure was determined using Bragg-Brentano X-ray diffraction (XRD), with a Cu k- α source of wavelength 1.5405 Å. XRD and XPS results are summarized in Figures E.1, E.2, and table E.1 in the Appendix E. Samples of 1 cm diameter were then mounted

in insulating epoxy and the surface areas were measured. Prior to electrochemical testing, samples were abraded using successively finer grits to 1200 grit SiC paper and then polished using 1 μm alumina and sonicated in water. Because titanium in its pure state is highly reactive with oxygen, the native oxide was assumed to begin formation almost immediately upon completion of the polishing step. No additional anodic polarization was used to drive the oxide formation.

ORR activities on the oxides were then evaluated using traditional cathodic polarization scans in 0.6 M NaCl adjusted to pH 12 with NaOH. These conditions should represent those near the cathodic material in a galvanic couple under a water droplet in atmospheric conditions.[81] After an 18-hour open circuit (OC) hold, the potential was scanned in the negative direction from +0.02 V above EOC to -2.0 VSCE at 0.167 mV/s using a graphite counter electrode. Each experiment was performed in triplicate. An 18-hour OC hold showed less scatter than the 1-hour hold used in previous work,[241] and therefore we have higher confidence in the values presented here.

5.4 RESULTS AND DISCUSSION

5.4.1 Amorphous TiO_2 Model

We used an atomistic reactive forcefield (ReaxFF[240]) to create an amorphous oxide surface model as has been done by others.[242] A crystalline TiO_2 surface composed of 3x3 rutile unit cells (3 tri-layers thick) was annealed using ReaxFF as described in the computational methods section. As shown in Figure 5.1, radial distribution functions for the slab structures agree well with experimental data for amorphous TiO_2 nanoparticles after full optimization using DFT. The ReaxFF annealed structure for our system itself did not agree with experimental data.[243] Although our system has a distinct unit cell and therefore is not truly amorphous, the agreement with experimental data displayed in Figure 5.1 shows that our system is a reasonable model for a structurally relaxed facet on an amorphous TiO_2 surface where ORR could be expected to occur.

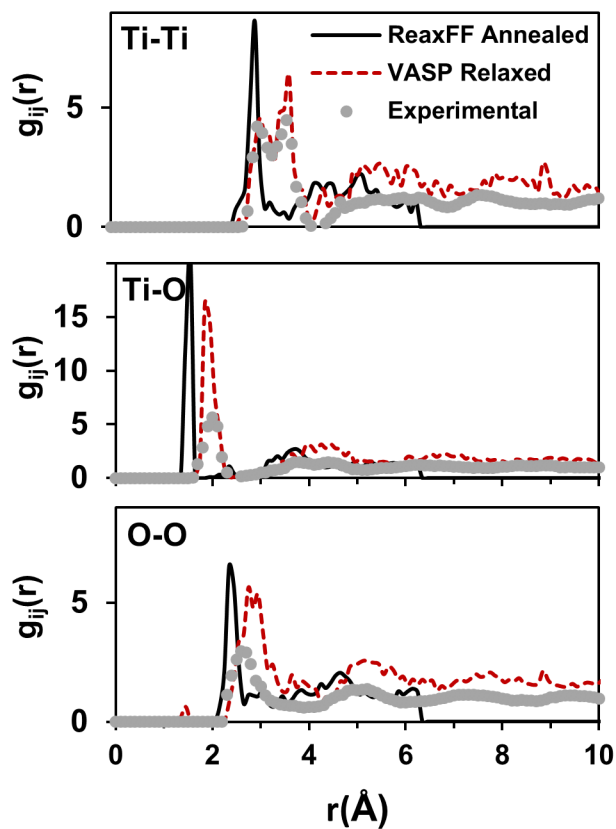


Figure 5.1: The radial distribution functions for the Ti-Ti, Ti-O, and O-O pairs from the ReaxFF annealed structure, the annealed structure after being optimized with density functional theory in VASP, and experimental data.^[243] The QM optimized structure agrees with experimental data.

5.4.2 Calculating ORR Overpotentials

Calculating reaction overpotentials with the computational hydrogen electrode model[30] is normally the first step toward modeling electrocatalytic activity. This model can yield robust insight into electrocatalytic reaction rate trends despite not explicitly calculating reaction barriers or accounting for other factors such as defects. We used this approach to calculate reaction overpotentials for the associative ORR mechanism commonly used to describe the ORR on metal oxides as shown in Figure 5.2.[244, 245] Overpotentials for the two electron ORR mechanism are considered in Appendix F. Because the hydrogen evolution reaction ($1/2 \text{H}_2 \rightleftharpoons \text{H}^+ + \text{e}^-$) is in equilibrium at 0 V vs. the standard hydrogen electrode (V_{SHE}), the energies of protons and electrons in electrochemical reduction steps were modeled as half the energy of an H_2 molecule plus a linear energy correction to account for an applied potential. Using these energy corrections, we calculated the theoretical reaction overpotential by finding the applied potential at which all four reaction steps are downhill in energy. Mathematically, this was determined by the most uphill reaction step at the equilibrium potential for the ORR ($1.23 V_{SHE}$). This approach assumes that the activation barrier for the rate limiting step will be at least equal to the most uphill reaction step, and this assumption has been used to successfully study electrochemical reactions (including the ORR) on metals and metal oxides.[79, 80, 90, 30, 91]

Our amorphous TiO_2 surface model contained four unique surface sites (each at a four-coordinate surface Ti atom) on which ORR steps were considered to take place. Modeling the ORR energies on the sites shown in Figure 5.2b yielded overpotentials that vary by nearly 0.8 V, but the most active site (Site 1) had predicted overpotentials calculated with our PBE (without solvation) and HSE06 (with solvation) models that were in good agreement with the experimental overpotential for TiO_2 ($\eta_{PBE}^{ORR-noSolv} = 0.5 \text{ V}$, $\eta_{HSE06-Solv}^{ORR} = 0.43 \text{ V}$, and $\eta_{exp}^{ORR} = 0.45 \text{ V}$).[246] The local coordination environments at active sites has been used to describe catalytic activities.[247, 248] However, changes in local coordination environment were quite subtle in these amorphous structures and not pursued as a descriptor for catalysis. The agreement between previously measured ORR overpotentials and those calculated here validated that our amorphous TiO_2 model can be used to study ORR mechanisms.

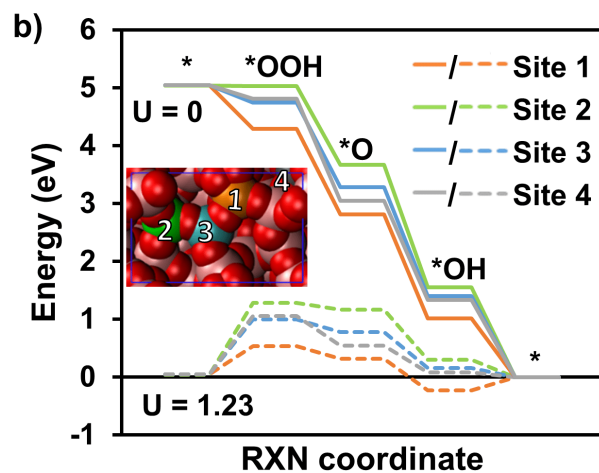
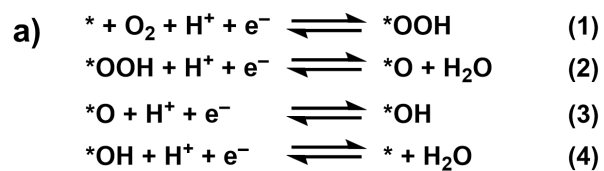


Figure 5.2: a) The associative ORR mechanism modeled in this work. * denotes an empty surface site on the material. b) ORR reaction energies calculated with PBE for four different surface sites in the undoped TiO_2 surface (labeled 1-4) plotted at an applied potential of 0 and 1.23 V_{SHE} . The intermediates correspond to the reactions in Figure 5.2a.

5.4.3 Dopant Screening

We considered different metal dopants that could be introduced into the amorphous oxide surface to increase ORR overpotentials. Each dopant atom was embedded into the surface at its preferred oxidation state given by experimental Pourbaix diagrams[249] at our experimental operating conditions, -0.8 V vs the saturated calomel electrode (V_{SCE}) at pH 12 (See Figure E.4 and Table E.2 for further discussion). We compared the stability of each dopant at all four different active sites as shown in Figure 5.2b to identify the most stable substitution site (Figures E.7, E.8, E.9, E.10, and E.11 show the surface models). We assumed that the most thermodynamically stable site would reflect the atomic configuration that would be least likely to reconstruct and would therefore have the largest effect on electrochemical ORR rates. Following work by Carter and co-workers,[92] we then predicted the maximum impact of each dopant on the ORR activity by modeling the ORR intermediates adsorbed directly to the dopant atom embedded in the amorphous surface at its most stable site.

The predicted maximum overpotential for each metal dopant is displayed in the Sabatier volcano diagrams shown in Figure 5.3. Unlike studies on fuel cell catalysis where the ideal catalyst is found at the top of the activity volcano, we sought to identify dopants at the bottom of the volcano that optimally reduce ORR rates. Our rationale for this now follows. When a reaction site near a dopant has a higher ORR overpotential than the undoped surface, that reaction site is less likely to contribute to the overall activity. Furthermore, it is highly unlikely that all reaction sites will be at a dopant because of their relatively low concentrations in the oxide (0.5-6.2%). However, dopants with high reaction overpotentials will still affect adsorbate binding energies multiple sites away,[250] and the dopant's influence on the overpotential will decrease the further the dopant is away from the reaction site.

For example, the ORR overpotential at the most active site on undoped TiO_2 (site 1 in Figure 5.2) is 0.50 V. The same site with the Al^{3+} dopant one nearest neighbor site away increases the overpotential at this site to 0.65 V. We note that the maximum calculated overpotential due to Al^{3+} is 1.43 V. Thus, the effect of the dopant on ORR overpotentials reflects the upper limit to what would be experimentally observed, but the overall trend for how dopants affect ORR activity will still be reflected by the activity volcano based on maximum dopant impact. This effect is discussed further in Appendix F (see Table F.1).

We use a relatively simple surface model to screen dopants by their maximum potential to inhibit ORR activity. The model assumes that dopants at low concentrations will be distributed throughout a Ti oxide. For the cases considered here, experimental XPS measurements show that most dopants are present in the oxide at concentrations comparable to the original alloys (only Cr is present at higher than 2.2%, see Table E.1) and so chances of segregation would be considered low. This may not always be the case when modeling complex oxides, especially those with higher dopant concentrations, and segregation may occur.[251] In the best case, our model would overestimate the impact of the dopants in a segregated oxide because segregation would result in more uninhibited Ti active sites, but the trends predicted by our model would still hold. In the worst case, segregation would change the overall structure of the material which may unpredictably affect overall trends.

We now discuss dopants that we verified experimentally using potentiodynamic polarization in this work (Ag, Sn, Cr, Co, Al, Mn, and V) or have been previously studied (Nb) shown in Figure 5.3a.[246] Our computational modeling predicted that Mn and Al would bring the highest ORR overpotentials in the cases considered and thus would be the best dopants for suppressing ORR activity. Co, Sn, and Cr in turn should be moderate ORR inhibitors, and Nb and Ag should increase ORR activity relative to pure amorphous TiO_2 . This is consistent with previous work by Arashi and coworkers who showed that doping amorphous TiO_2 with Nb slightly lowers the ORR overpotential.[246] Vanadium is more challenging to characterize because it has two stable oxidation states near our experimental conditions (V^{3+} and V^{5+}). Thus, V dopants are likely present as a mixture of V^{3+} and V^{5+} . At more negative applied potentials, the ratio of $\text{V}^{3+}/\text{V}^{5+}$ should favor V^{3+} and the ORR activity of the oxide should decrease. This suggests that dopants could have differ-

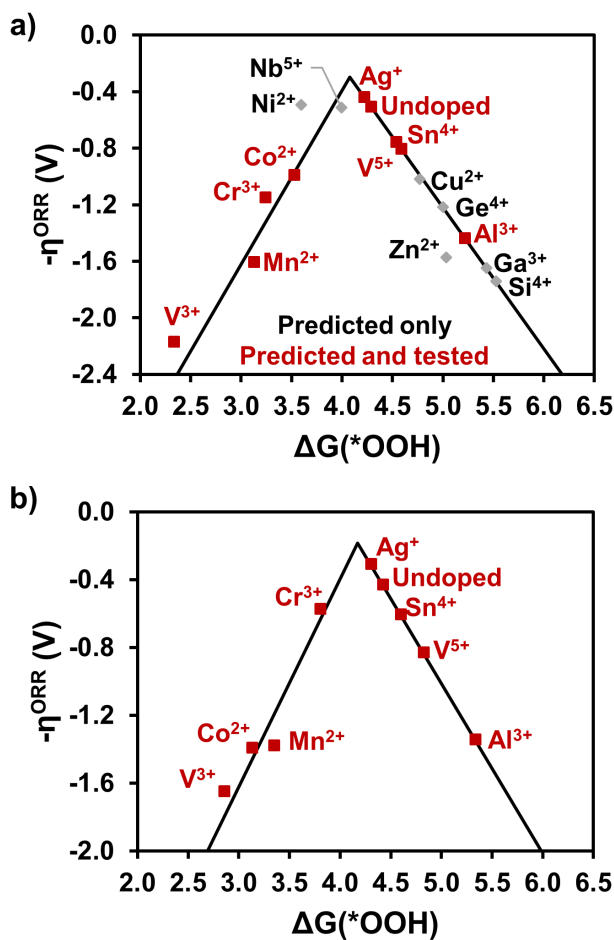


Figure 5.3: Sabatier volcano plots of computationally predicted dopant overpotentials. Dopants that were predicted and tested in this work are labeled in red, and dopants not yet experimentally verified are labeled in black. a) overpotentials calculated with PBE without solvation effects, b) overpotentials calculated with HSE06 and including solvation energies. HSE06 calculations were only performed for dopants with available experimental data. The effect of solvation is discussed further in Figure E.6.

ent capacities to suppress ORR rates at different applied potentials in our experiments. The Pourbaix diagrams for all other considered dopants have only one stable oxidation state near our experimental conditions. We experimentally verified trends for these eight systems, but we also computationally predicted that Ga, Zn, and Si could be even better ORR inhibitors than Al and Mn.

Appendix E (Figure E.6) reports how Sabatier volcano diagrams are influenced using PBE/HSE06 and/or VASPsol. Figure 5.3b shows that using a higher level of theory (HSE06) while also accounting for solvation (VASPsol continuum solvation) does not appear to significantly alter the model predictions from PBE without solvation in most cases studied here. While the overpotentials of most of the dopants shift from those shown in Figure 5.3a, only Mn^{2+} ($\Delta\eta_{ORR} = 0.22$ V), Cr^{3+} ($\Delta\eta_{ORR} = 0.57$ V), Co^{2+} ($\Delta\eta_{ORR} = 0.4$ V), and V^{3+} ($\Delta\eta_{ORR} = 0.52$ V) change by more than 0.15 V. Even considering these overpotential changes the relative dopant ordering is generally preserved. The only exception to this are the predicted overpotentials of Cr^{3+} and Co^{2+} . In these cases, HSE06 with VASPsol predicts that Cr^{3+} will be relatively less effective at inhibiting corrosion, while Co^{2+} should be more effective than originally predicted in Figure 5.3a.

5.4.4 Cathodic Polarization Scans

Figure 5.4 shows representative cathodic polarization scans for all alloys that were investigated experimentally. Note that the polarization scans were started at 20 mV above the OC potential of the alloy and scanned in the electronegative direction at a rate of 0.167 mV/s. The current density values at -0.8 V_{SCE} , (the galvanic corrosion potential between Ti and Al alloys),^[81] were measured in triplicate and then averaged. The percent change for each alloy with respect to the undoped Ti are shown in Table 5.1.

At potentials more positive than -0.8 V vs SCE, the trend for ORR suppression is consistent with what was observed at -0.8 V vs SCE - with the exception of the catalysis of the ORR on the Ti-Al and Ti-Mn alloys. The tafel slope for the ORR on both of these oxides changes around -0.65 V vs SCE which suggests that there was a change in oxidation state of the dopant atoms as the potential decreased. For example, as seen in Figure 5.3a,

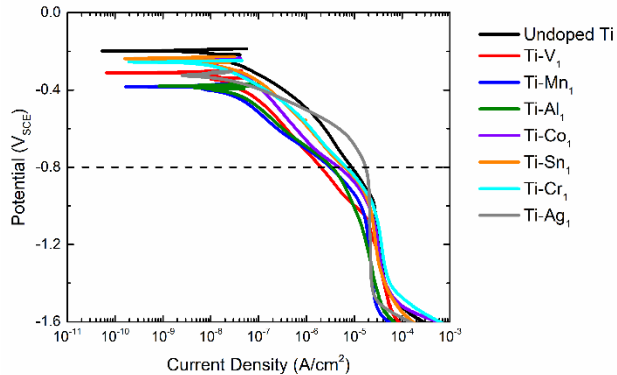


Figure 5.4: Cathodic polarizations scans of the undoped titanium and the 1 at% doped titanium samples in air-saturated 0.6 M NaCl at pH 12 with a scan rate of 0.167 mV/s. Each scan began after an 18-hour OC hold.

V^{3+} and V^{5+} differ significantly in predicted overpotential values. As the applied potential decreases, the ratio of V^{3+}/V^{5+} in the material should increase resulting in an oxide with a higher average overpotential.

5.4.5 Comparison to Experiment

Our quantum chemistry predictions almost exactly mirror our experimental results. The trend in dopant performance predicted by computational modeling were:

$Ag > \text{undoped} > Sn > Co > Cr > Al \geq Mn > V^{3+}$ (Figure 5.3a)

and

$Ag > \text{undoped} > Sn \approx Cr > Al \approx Mn \approx Co > V^{3+}$ (Figure 5.3b)

while experimental potentiodynamic polarization measurements found almost the same ranking:

$Ag > \text{undoped} > Sn \geq Cr > Co > Al \geq Mn > V$

Overpotentials calculated with PBE appear to overestimate the overpotential of Cr relative to Co, but these fall quite close on our volcano plot within 0.2 V (Figure 5.3a). While calculating the overpotentials with HSE06 and VASPsol appears to correct the relative order-

Table 5.1: Percent Change and standard deviation in current at $-0.8 V_{SCE}$ of alloy samples versus the undoped Ti.

Alloy	Current Density ($\mu A/cm^2$)	Percent Change
Ti-Ag ₁	17.3	+95 \pm 13
Ti	8.8	N/A
Ti-Sn ₁	6.9	-21 \pm 11
Ti-Cr ₁	6.2	-30 \pm 8
Ti-Co ₁	4.7	-47 \pm 5
Ti-Al ₁	3.4	-61 \pm 11
Ti-Mn ₁	3.1	-65 \pm 4
Ti-V ₁	2.0	-77 \pm 3

ing of Co and Cr, these predictions now appear to overstate the effectiveness of Co relative to Al, Mn, and V^{3+} . The trends observed for the remaining dopants (Ag, the undoped system, Sn, Al, Mn, and V^{3+}) are consistent between both computational models and the experimental results. Ag was anticipated to enhance electrocatalysis overall, and while the measured current increase for the Ti-Ag oxide at $-0.8 V_{SCE}$ agrees with our predictions, Ag exhibits anomalous polarization behavior. This may be due to Ag catalyzing additional reactions or Ag^+ being reduced under operating conditions, but further analysis is outside the scope of the current study. While we exclude it from our experimental trend, our model was also in good agreement with prior studies of the ORR on Nb doped amorphous TiO_2 as previously stated.

The other measured current trends are consistent with the OC potential ordering until the slope of the Ti-Al and Ti-Mn alloys change relative to the other materials at approximately $-0.65 V_{SCE}$ causing the Ti-V and Ti-Al/Ti-Mn alloys to switch order. This may be due to the onset of different ORR mechanisms on the Ti-Al and Ti-Mn alloys, or the Ti-V alloy may become less active as the $V^{3+}:V^{5+}$ ratio increases. At potentials more negative than

-0.9 V_{SCE} , the dopants could be reduced to other oxidation states not accounted for in our computational model. Still, this shows that simple Sabatier analyses are robust enough to identify dopants for materials having low catalytic activities and can be used to aid the design of protective surface treatments.

The ability of the dopant atoms to bind the ORR intermediates was hypothesized to correlate with the total charge of each intermediate after it is bound to the surface. Bader charge analysis shows that *OOH bound to Al^{3+} , Ti^{2+} , or V^{3+} has a charge of -0.70, -0.97, or -1.05, respectively. Dopants with larger degrees of charge transfer bind the intermediates more tightly, effectively poisoning the surface, and they are limited by reaction 4 in Figure 5.2a. On the other hand, dopants that transfer less charge form weaker bonds that are less likely to form reaction intermediates and are limited by reaction 1 in Figure 5.2a.

For dopants at intermediate oxidation states (i.e. V^{3+} , Mn^{2+} , Cr^{3+} , Co^{2+} , and Ag^+), the ability to donate electron density appears to correlate with their approximate redox potentials from Pourbaix diagrams in the literature ($V_2O_3 \rightleftharpoons V_3O_5$ at $E^0 = -0.5 V_{SHE}$, $Mn^{2+} \rightleftharpoons Mn_2O_3$ at $E^0 = 0.3 V_{SHE}$, $Cr_2O_3 \rightleftharpoons CrO_4^{2-}$ at $E^0 = 0.2 V_{SHE}$, $CoO \rightleftharpoons Co_3O_4$ at $E^0 = 1.0 V_{SHE}$).^[249] For dopants at their highest oxidation state, (i.e. Nb^{5+} , Ti^{4+} , Sn^{4+} , and Al^{3+}) the ability to bind to ORR intermediates correlates with their calculated atomic radii ($Nb = 1.98 \text{ \AA}$, $Ti = 1.76 \text{ \AA}$, $Sn = 1.45 \text{ \AA}$, and $Al = 1.18 \text{ \AA}$). Although this trend might be coincidental, bonding orbitals in smaller dopants (such as Sn and Al) have less orbital overlap which makes it more difficult to transfer electron density to the adsorbed intermediates than larger dopants (such as Nb). This results in weaker bonds and higher overpotentials.

5.5 CONCLUSIONS

We have created a model amorphous TiO_2 surface that matches experimental data and shown that it contains reaction sites that predict ORR overpotentials in good agreement with experimentally measured values. Our computational models correctly predicted dopant trends and successfully identified dopants that were experimentally validated to lower ORR

rates as much as $-77 \pm 3\%$. Optimizing the dopant concentration in the oxide can likely result in further ORR activity decreases. While we have demonstrated a straightforward method to predict dopants that modify metal oxides so that they more effectively suppress cathodic reduction kinetics, future work will address the ability of these doped Ti oxides to inhibit galvanic corrosion in realistic environments. Additionally, this doping approach should be able to increase the effectiveness of oxide protective coatings used on other materials/devices that suffer from corrosion damage (such as solar cell photoanodes[[252](#), [253](#)]).

6.0 INHIBITING THE OXYGEN REDUCTION REACTION ACTIVITY ON THE OXIDES OF TI-6AL-4V

6.1 INTRODUCTION

Corrosion causes significant, non-uniform damage that can limit the operational lifetime of a material or cause mechanical failure. The costs associated with preventing and repairing corrosion damage affect a wide variety of industries and are estimated to consume nearly 3.4% of the global GDP per year.[230] Efforts to decrease this cost have motivated the development of corrosion resistant alloys,[254] cathodic protection systems,[255, 256] and coatings that physically block corrosive conditions or chemically slow corrosion reactions.[257, 258, 259, 260] Unfortunately, contact between two dissimilar metals or metal alloys can produce a galvanic couple that is powerful enough to corrode materials that normally resist corrosion, such as aircraft grade aluminum alloys[74, 261] or stainless steels.[262, 263]

The high strength, low weight, and improved corrosion resistance of Ti-6Al-4V make it an ideal material for applications ranging from aerospace components to biological implants. When Ti-6Al-4V is used to fasten materials made from less noble metals, the contact between the two metals forms a galvanic couple that causes the preferential corrosion of the less noble metal (see Figure 6.1). The electrons produced by the oxidation of the less noble metal (metal 1) are consumed by cathodic reduction reactions on the more noble metal surface. Galvanic corrosion rates are highly dependent on both the corroding system and the surrounding environment, [264, 265] but the oxygen reduction reaction (ORR) is a major limiting factor for galvanic corrosion rates in atmospheric conditions.[79, 80] Thus, designing metal alloys and their native surface oxides to be less effective ORR catalysts is an opportunity to decrease the galvanic corrosion driving force in atmospheric conditions.

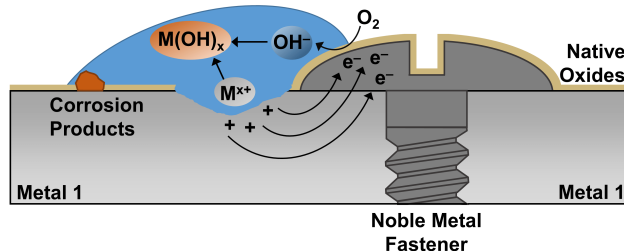


Figure 6.1: An illustration of galvanic corrosion in an atmospheric environment. The contact between metal 1 and the noble metal fastener forms a galvanic junction that can corrode metal 1 when a water droplet is present on the surface.

Computational quantum chemistry studies frequently utilize ORR overpotentials computed using the computational hydrogen electrode approximation[30] to design optimal electrocatalysts.[266, 267, 268, 269, 270] We previously showed that these descriptors can also identify dopants that inhibit the ORR activity of amorphous TiO_2 (even at low doping concentrations).[271] Developing accurate oxide surface models using current computational tools is challenging and computationally expensive.[102, 272] Fortunately, experimental studies have shown that the oxides of Ti-6Al-4V are primarily composed of Ti oxides and a Ti-Al oxide (believed to be $TiAl_2O_5$).[273, 274, 275] Using this information we can construct simple oxide surface models that represent the active sites present in the oxides of Ti-6Al-4V.

We previously studied ORR catalysis on amorphous TiO_2 , and we now report a computational study that uses density functional theory (DFT) to demonstrate how surface morphology and metal dopants affect the ability of $TiAl_2O_5$ to catalyze the ORR. First, we describe how neural networks trained to the density functional theory (DFT) energies and forces of oxide structures can be used to create defective and amorphous surface models. We then calculate the ORR overpotentials of six different $TiAl_2O_5$ surfaces with DFT. Finally, we use DFT to show how the ORR overpotentials of crystalline and amorphous $TiAl_2O_5$ surfaces are influenced by the presence of dopants. These calculations can provide key insights into the atomic scale factors that govern ORR electrocatalysis.

6.2 COMPUTATIONAL METHODS

All Kohn-Sham density functional theory (KS-DFT) calculations were performed with the Vienna *Ab initio* Simulation Package (VASP).[184, 185, 186] All geometry optimizations and energy calculations were carried out using the Perdew-Burke-Ernzerhof (PBE)[141] GGA exchange correlation functional, the projector augmented wave (PAW) method,[189] a 700 eV energy cutoff, and spin-polarization. Surface structures were periodic in the x and y directions and used a 2x2x1 k-point grid. Bulk structures used a 2x2x2 k-point grid. Solvation energies were calculated using VASPsol (relative permittivity of water = 78.4) and the previously mentioned parameters.[234, 235] Additional hybrid DFT energy calculations were carried out on PBE optimized structures using the HSE06 hybrid DFT functional,[236] the PAW method, a 700 eV energy cutoff, a gamma-point, and spin-polarization.

We generated a database that contained the atomic coordinates, energies, and forces of 1077 TiAl_2O_5 structures. The structures were a combination of crystalline equation of state data, crystalline unit cell deformations along the A, B, and C unit cell vectors, crystalline structures with individual Ti, Al, and O atoms moved in the x, y, and z directions, surface and bulk vacancy diffusion pathways, and snapshots from high-temperature AIMD simulations of crystalline surfaces and bulk structures. We later supplemented the database with 100 additional amorphous surface structures that were produced by annealing crystalline TiAl_2O_5 surfaces. The computational annealing procedure is described below. All of these calculations were carried out with VASP using PBE and the previously described parameters. The database is supplied as a json database file, and further information about the training set is available in Section G.1 of Appendix G.

We selected a training set of 850 structures from the database and used the remaining structures as a validation set. We trained neural networks to the structures in the training set with the Atomistic Machine-learning Package (AMP)[276] created by Khorshidi and Peterson and the atomic simulation environment (ASE).[277] We used Behler-Parrinello descriptors with a cutoff radius of 4.5 Å to describe atomic structures. This provided adequate accuracy while maintaining a low computational cost. Using a larger cutoff radius improved the accuracy of the resulting neural network but dramatically increased its computational cost.

We carried out annealing simulations with a neural network trained to the original training set (NN1). Amorphous surface structures created by these annealing simulations were added to the database and used to train a second neural network (NN2). NN2 was used to carry out the annealing simulations reported here. Both neural networks had similar average errors, mean unsigned errors, and standard deviations for the validation set and the training set. This indicated that our neural networks were not overfit.

We annealed crystalline TiAl_2O_5 structures by performing molecular dynamics simulations with NN1 and NN2 using AMP and ASE. We rapidly heated structures from ~ 0 K to 2400-2600 K using the Langevin thermostat and a large friction coefficient (0.50 atomic units). The simulation maintained the desired temperature for 20-30 ps (Berendsen thermostat with $\tau = 200$ fs). We observed that this amount of time was sufficient to allow the crystalline material to transition to an amorphous state. We then selected structures from various times during the annealing simulation and quenched each structure to 10 K. Each structure was quenched by a molecular dynamics simulation that used a Berendsen thermostat ($\tau = 100$ fs) to sequentially cool the structures to target temperatures of 2100, 1800, 1500, 1200, 800, 400, 200, and 10 K for 1.0 ps each. The quenched structures were then fully relaxed with VASP using the PBE functional and previously described parameters. All molecular dynamics simulations used a 1.0 fs timestep.

We previously developed a model that successfully predicted the ORR reactivity trends of doped TiO_2 .^[271] We now utilize our approach to test how dopants affect ORR energetics on TiAl_2O_5 surfaces. Briefly, we embedded metal dopants in the oxide surfaces and fully optimized their structures using PBE and the previously described parameters. The oxidation state of each dopant was determined by analyzing their Bader charge and local coordination environment as discussed in Section G.4 of Appendix G. After determining the most stable dopant substitution site in the surface for each dopant, we used KS-DFT to calculate $^*\text{OOH}$, $^*\text{O}$, and $^*\text{OH}$ binding energies to the dopant atom. We then calculated the reaction overpotentials for the associative 4-e^- ORR mechanism using the computational hydrogen electrode model. The zero point energy and entropic energy contributions of ORR intermediates adsorbed to the oxide were approximated using the values predicted by Valdéz et. al for ORR intermediated adsorbed to TiO_2 .^[233]

6.3 RESULTS AND DISCUSSION

6.3.1 Training Neural Networks

We previously calculated the ORR energetics of an amorphous TiO_2 surface model because TiO_2 surfaces become amorphous after prolonged exposure to an electrolyte.[98] Performing an analogous study of TiAl_2O_5 required an amorphous TiAl_2O_5 surface model. Amorphous structures are typically generated by annealing crystalline structures at high temperatures using molecular dynamics simulations.[242] Performing these simulations with DFT is extremely computationally expensive and limits the number of potential surface models that can be created. Molecular dynamics simulations could be performed with a forcefield, but no forcefield parameters exist for TiAl_2O_5 . To facilitate less computationally expensive molecular dynamics simulations, we trained neural networks to TiAl_2O_5 data. While neural networks are more computationally expensive than forcefields (such as ReaxFF), they are significantly less computationally expensive than DFT. Neural networks can also be more accurate than forcefield based approaches, and their accuracy can be continuously refined with the addition of more training data.[278]

We trained a neural network (NN1) to the energies and forces of 850 crystalline structures from our dataset. We used NN1 to perform annealing simulations as described in the computational methods section. NN1 had significant errors when compared against the DFT energetics for both amorphous surface structures obtained from during the annealing simulation trajectory (Figure 6.2a) and fully quenched amorphous surface structures (Figure 6.2b). These deviations result from the lack of amorphous structures in our original training set.

Adding the amorphous surface structures generated with NN1 to the training set of our second neural network (NN2) dramatically improved its ability to model amorphous surface structures. The energies of the training set structures and the additional surface structures obtained from a new annealing simulation carried out with NN2 agreed much better with the DFT energies of the corresponding structures (see Figure 6.2a). Fortunately, the addition of high energy amorphous surfaces to the training set also improved the ability

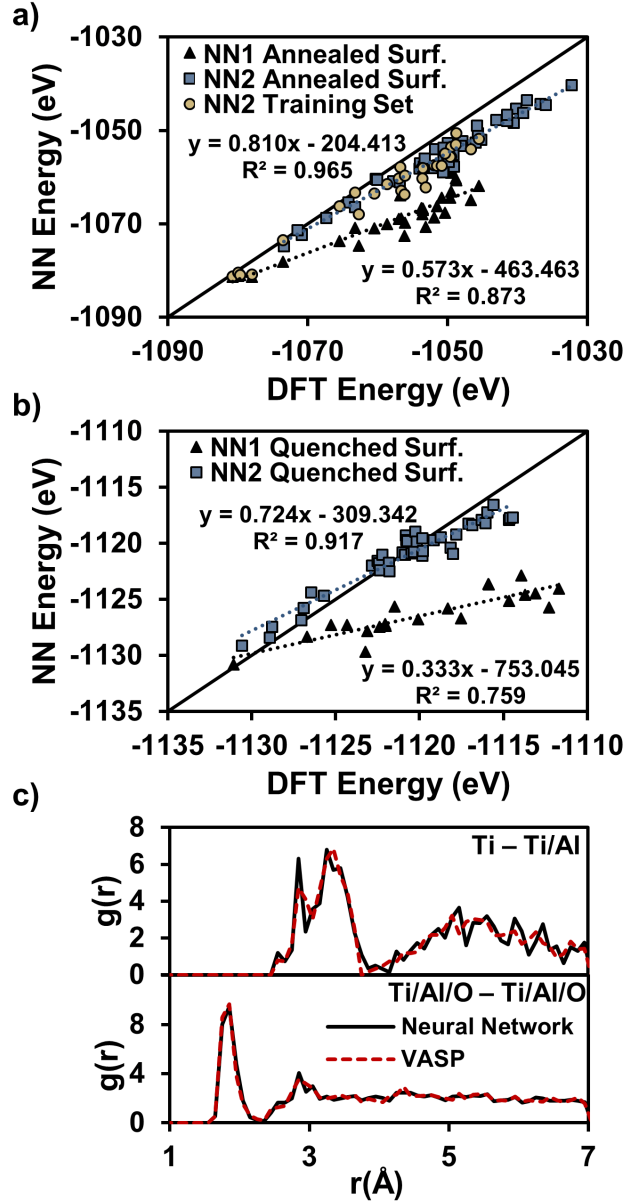


Figure 6.2: Parity plots of neural network (NN) and DFT absolute energies for surface structures that were a) annealed and b) annealed and quenched with neural network one (NN1) and two (NN2). All DFT energies were calculated with PBE. c) The Ti/Al/O-Ti/Al/O and Ti-Ti/Al radial distribution functions for an amorphous TiAl_2O_5 slab after being quenched with NN2 and fully relaxed with DFT.

of NN2 to describe the fully quenched amorphous surface structures despite the absence of training data in this region of phase space (see Figure 6.2b). This type of training-validation feedback loop could be used to continuously improve the accuracy of neural networks for specific types of surface structures. These improvements do not degrade the ability of NN2 to model crystalline bulk and surface structures. Both NN1 and NN2 have similar error distributions for the crystalline bulk and surface structures in the training and validation sets (as seen Table G.2 in Appendix G).

By comparing two representative radial distribution functions (RDFs), Figure 6.2c shows that an amorphous surface structure annealed with NN2 (labeled Neural Network) remained relatively unchanged after being fully relaxed with DFT (labeled VASP). While there is some broadening of the peaks at distances greater than 4 Å, the short range peaks in both RDFs show that the neural network is adequately capturing short range structural interactions. This agreement is a significant improvement from our previous comparison of amorphous TiO₂ structures obtained with ReaxFF and those fully relaxed with DFT.[271] Additional RDF comparisons can be seen in Figure G.5 in Appendix G.

6.3.2 Creating Surface Models

We performed five simultaneous annealing simulations with NN2 to ensure that we sampled a diverse set of amorphous surface structures. Each simulation started from a TiAl₂O₅ (010) surface (9.78 x 10.86 Å, 13.35 Å thick) and was annealed as described in the computational methods section. Similar amorphous structures were observed when we annealed a (100) crystalline surface. We selected to start the majority of our annealing simulations from a (010) surface because it had the lowest surface formation energy when compared against a number of low index TiAl₂O₅ surfaces (see Table 6.1). Randomly selected structures from the annealing trajectories were quenched from 2400 K to 10 K. These structures were then fully relaxed with DFT in VASP.

Components made from Ti-6Al-4V may experience extreme temperatures, but they are more commonly used in environments with moderate temperatures (300 ± 100 K). It is important to understand what types of surfaces facets could be present at realistic oper-

Table 6.1: TiAl_2O_5 surface formation energies

Surface Facet	Surface Energy (J/m^2)
(010)	1.078
(001)	1.202
(100)	1.899
(101)	1.134
(110)	1.301

ating temperatures. Figure 6.3a compares the energies of defective and amorphous surface structures produced from the annealing simulations performed with NN2. We approximated the temperature required to access different amorphous structures from the original (010) crystalline surface by comparing the energy of each structure against the amount of kinetic energy present in the system at various temperatures. The DFT energies suggest that all of the amorphous surfaces are significantly too unstable to form near room temperature. Even the lowest energy amorphous structure located by our procedure was unlikely to form below 450 K. Comparatively, the defective surfaces produced by the annealing simulations were lower in energy, and fall near or below the 400 K reference line.

We selected six surface models to test how ORR activity was affected by surface stability: a (010) crystalline surface, two (010) crystalline surfaces with swapped Al/Ti atoms, two defective surfaces, and the lowest energy fully amorphous surface. These surfaces are listed in order of increasing instability. The crystalline surface models were created by relaxing (010) crystalline surfaces, and the defective and amorphous surfaces were located with annealing simulations. Every surface model originated from a 3×2 supercell of a (010) surface that was two layers thick, consisted of 144 atoms, 20 Å of vacuum space, and had 9.78×10.86 Å surface. The surface structures are shown in Appendix G (see Figure G.7).

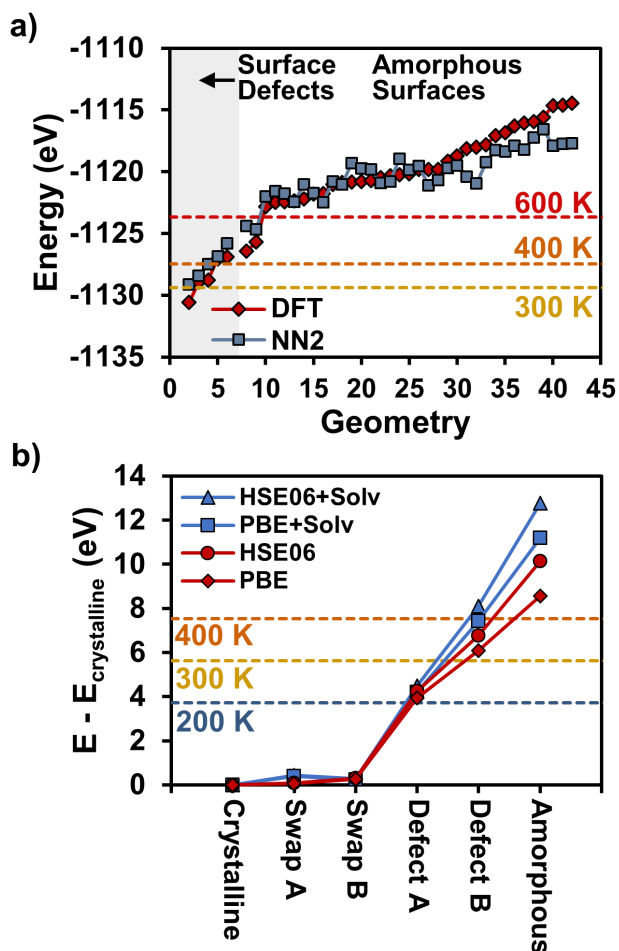


Figure 6.3: a) A comparison of neural network (NN) and DFT absolute energies for defective and amorphous surface structures annealed and quenched with neural network two. b) The energy of defective surfaces compared against the energy of the crystalline surface in the gas phase and solvated with VASPsol. The 200, 300, 400, and 600 K lines correspond to the kinetic energy present at each temperature added to the energy of the relaxed (010) crystalline surface ($E = -1134.97$ eV).

Figure 6.3b shows the energies of the selected surfaces compared against the energy of the (010) crystalline surface. PBE energy calculations showed that the defective and amorphous surfaces are significantly less stable than the crystalline surface. Hybrid DFT (HSE06)

energies and VASPsol solvation effects both further destabilized the defective and amorphous surfaces relative to the crystalline structures. The crystalline surfaces with swapped Ti and Al atoms are nearly as stable as a perfect crystalline TiAl_2O_5 surface, suggesting that these defects could easily form at room temperature. Surfaces resembling defect A are stable enough to form at lower temperatures, but defect B and amorphous surface structures are too high in energy to be accessible. Interactions with explicit water molecules or ions could stabilize defect B and the amorphous surface, but it is more likely that crystalline surfaces would segregate out of an amorphous phase at lower temperatures.

6.3.3 Calculating ORR Overpotentials

ORR overpotentials computed with the computational hydrogen electrode model often yield robust insight into electrocatalytic reaction rates despite not explicitly determining any reaction barriers.^[30] We utilize this approach to calculate reaction overpotentials for the four-step associative ORR mechanism shown in Figure 6.4a.^[244, 245] The computational hydrogen electrode model allows us to compute reaction energies for the reactions shown in Figure 6.4a by assuming that $E(\text{H}^+ + \text{e}^-) = 1/2E(\text{H}_2) - eU$. U is an applied potential referenced against the reversible hydrogen electrode, and e is the elementary charge. Using this approximation, we calculated reaction overpotentials by determining the applied reaction potential at which all reaction steps are first downhill in energy.

Each surface had a number of unique reaction sites. We modeled the ORR intermediates adsorbed to each reaction site and computed their ORR overpotentials. The minimum overpotential (most reactive site) for each surface model is shown in Figure 6.4. The full distribution of reaction overpotentials for every surface are shown in Appendix G (Figures G.9 and G.10). Overpotentials computed with PBE in the gas phase suggest that most of the materials have similar ORR overpotentials (see Figure 6.4b). Incorporating solvation effects shows that the less stable surfaces have lower ORR overpotentials and are more reactive. This trend is echoed by the overpotentials computed with HSE06 with and without solvation effects (as seen in Figure 6.4c). This agrees with conventional catalysis knowledge that more stable reaction sites are typically less reactive.

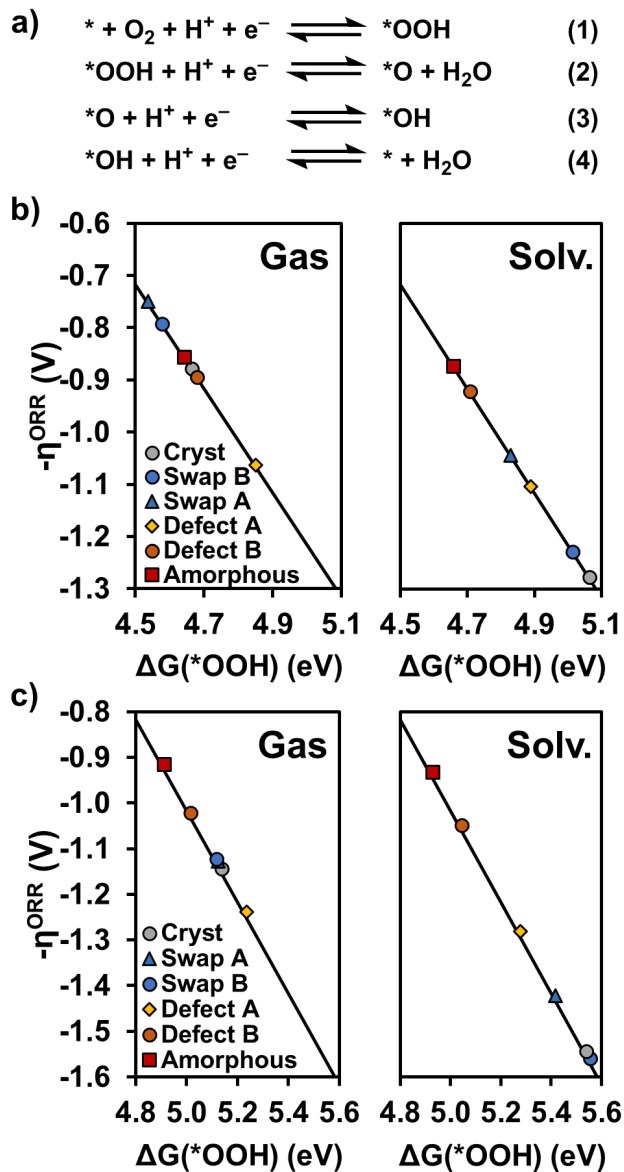


Figure 6.4: a) The associative ORR mechanism modeled in this work. The minimum gas and solvent phase ORR overpotentials for each surface calculated using b) PBE and c) HSE06.

While PBE can yield accurate reactivity trends, DFT+U or hybrid DFT functionals (such as HSE06) should provide more reliable reactivity trends for metal oxides.[279, 280] In the case of TiAl_2O_5 , the HSE06 energy calculations predict that all of the surfaces are less

capable of adsorbing ORR intermediates than was predicted by PBE energy calculations. The weaker binding of ORR intermediates results in larger predicted overpotentials and causes the surfaces to shift right along the volcano plot. The overpotentials of all tested TiAl_2O_5 surfaces are significantly larger than that of amorphous TiO_2 ($\eta_{\text{ORR}} = 0.45$ V). Ti oxides are present on the surface of Ti-6Al-4V at higher concentrations than TiAl_2O_5 , but the increased ORR overpotentials of the TiAl_2O_5 surfaces could correspond to slower cathodic reduction reaction rates across the oxide surface. This effect could be partially responsible for the increased resistance of this Ti alloy against corrosion.

6.3.4 Dopant Screening

We considered metal dopants that could be incorporated into the TiAl_2O_5 oxide to further inhibit ORR activity. We constructed a list of dopants from those that we had previously predicted and tested with TiO_2 (Mn^{2+} , Cr^{3+} , Co^{2+} , Nb^{5+} , Ga^{3+} , Sn^{4+} , and Si^{4+}). Despite being tested in TiO_2 , V^{3+} and V^{5+} were excluded because vanadium was experimentally shown to not segregate into the oxides of Ti-6Al-4V. We used our previously described approach to determine the maximum impact of each metal dopant. Briefly, we modeled each dopant embedded into the amorphous surface at their preferred oxidation states given by experimental Pourbaix diagrams at experimentally relevant conditions (-0.8 V_{SCE} and pH 12).^[249] A more in-depth discussion of how the oxidation state of each dopant was controlled within our computational model is included in section G.4 of Appendix G. We compared the stability of each dopant at multiple sites in the amorphous surface. We then modeled ORR intermediates adsorbed to each metal dopant in their most favorable substitution site and calculated their ORR overpotentials. Because our amorphous surface was highly unstable compared to the (010) crystalline surface, we performed an identical analysis on the doped (010) crystalline surface.

The maximum overpotential for each dopant is shown in Figure 6.5. The overpotentials of the amorphous and crystalline surfaces computed with PBE (Figure 6.5a and 6.5b) suggest that the inclusion of Si^{4+} , Sn^{4+} , and Ga^{3+} should always decrease ORR activity. Dopants like Nb^{5+} and Co^{2+} are consistently predicted to increase ORR activity. The impact of

the remaining dopants (Mn^{2+} and Cr^{3+}) is difficult to conclusively predict. These dopants are predicted to inhibit ORR activity of amorphous slabs, but they are weaker inhibitors on crystalline surfaces and may even increase ORR activity. Because there are models that suggest these dopants could increase ORR activity of various TiAl_2O_5 surfaces, we cannot recommend any dopants besides Si^{4+} , Sn^{4+} , and Ga^{3+} as ORR inhibitors based on overpotentials calculated with PBE.

As was the case with the undoped surfaces, the HSE06 calculations (Figure 6.5b and 6.5d) show that the ORR intermediates are almost always bound more weakly than predicted by PBE. This causes the dopants to shift to the right along the volcano plot. A consequence of this shift is that the dopants on the left leg of the volcano plot, such as Mn^{2+} , Cr^{3+} , and Co^{2+} , are predicted to bind ORR intermediates more optimally and produce a significant activity increase. With a few exceptions, the overpotential trends are fairly consistent between the gas and solvent phases.

Overpotentials predicted from HSE06 energy calculations for the amorphous and crystalline surfaces (Figure 6.5b and 6.5d) helped clear up the discrepancies in the PBE overpotential trends. Overpotentials computed with HSE06 show that Cr^{3+} , Mn^{2+} , Nb^{5+} , and Co^{2+} are predicted to activate ORR activity for the crystalline and amorphous surface models considered here. Only Ga^{3+} , Sn^{4+} , and Si^{4+} are predicted to decrease the ORR activity of the amorphous TiAl_2O_5 surface model (Figure 6.5b). The crystalline surface is harder to analyze because the most stable crystalline surface has a high ORR overpotential, but switching a Ti and Al atom in the surface produces a higher activity surface site (see Figure 6.5d). These swapped Al/Ti atoms are nearly as stable as the perfect crystalline surface (see Figure 6.3) and may appear in the surface at relatively high concentrations. Figure 6.5d shows that Si^{4+} and Sn^{4+} have similar or larger ORR overpotentials compared to the crystalline surface and the crystalline surface with swapped Ti/Al atoms, but Ga^{3+} has a lower ORR overpotential than both crystalline surface sites. Because Ga^{3+} would increase the ORR activity of crystalline TiAl_2O_5 surfaces, we cannot recommend any dopants besides Si^{4+} and Sn^{4+} as potential ORR inhibitors for the amorphous and crystalline TiAl_2O_5 surfaces as well as amorphous TiO_2 .^[271]

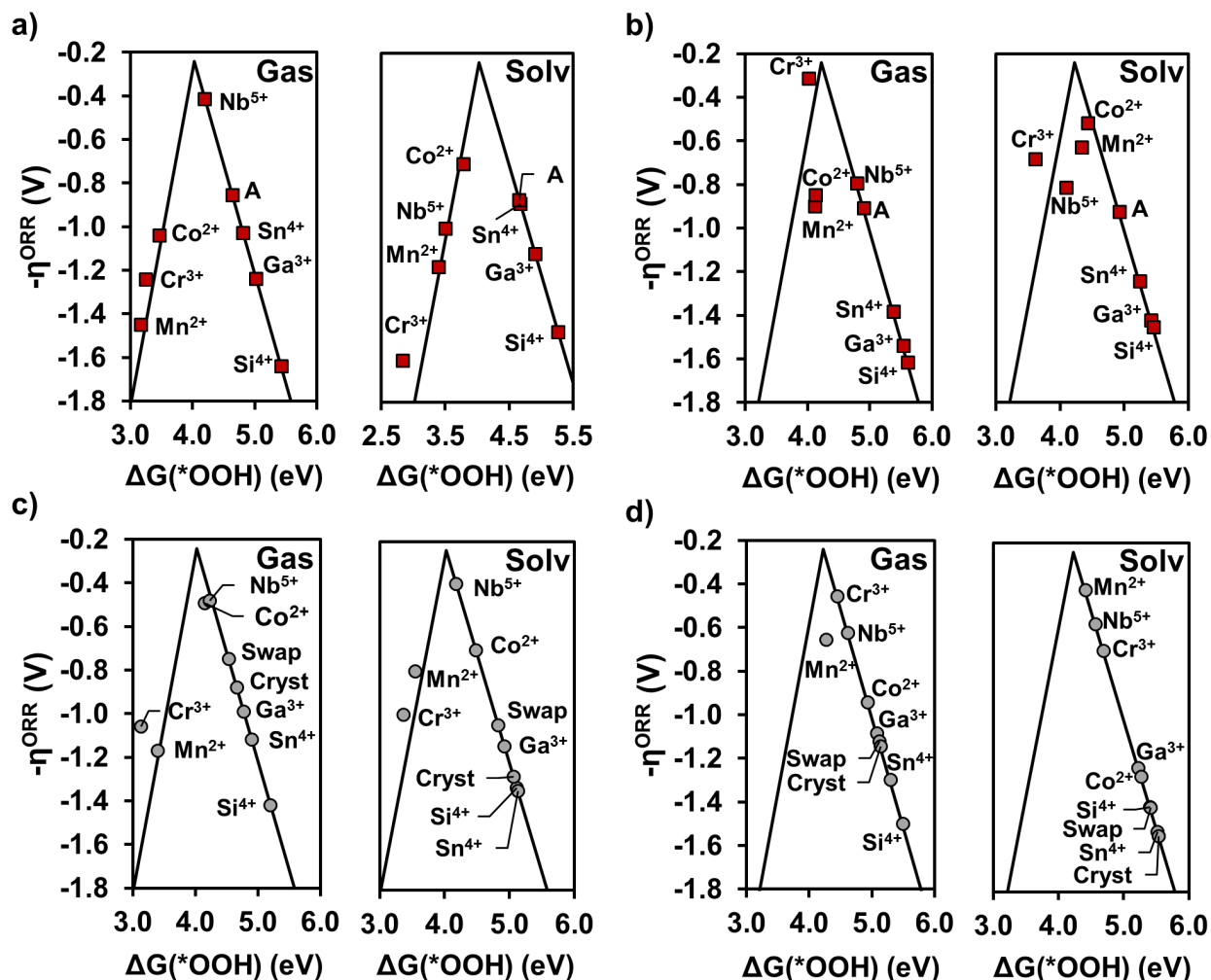


Figure 6.5: The gas and solvent phase ORR overpotentials for dopants embedded in an amorphous surface calculated with a) PBE and b) HSE06 as well as a crystalline surface calculated with c) PBE and d) HSE06. "A" = the most active amorphous surface site, "Swap" = the most active crystalline surface site when a surface Ti and Al are swapped, and "Cryst" = the most active crystalline surface site.

While we did not test the effect of dopants on the other defective or amorphous surface models, the trends in Figure 6.5 suggest that similar effects would be observed on the defective surfaces with intermediate activities. Higher energy amorphous surfaces would likely

have even smaller ORR overpotentials. This would cause dopants like Si^{4+} and Sn^{4+} to be more effective ORR inhibitors for these types of surface sites. This is consistent with conventional catalysis wisdom that suggests that high energy surface facets are often the most catalytically relevant sites. The ability to access less stable surface facets offers a potential explanation for why the activity of oxide based catalysts could change at higher temperatures. The additional energy that is present at higher temperatures can increase the diversity of reaction sites on the surfaces and may change how dopants impact catalytic reaction rates.

6.4 CONCLUSIONS

We have shown that we can train neural networks to the energies and forces of multi-component oxide structures (TiAl_2O_5). These potentials are accurate for structures similar to those in their training sets, but often have large errors when attempting to model structures that are not represented in the training data. The accuracy of such neural networks can be dramatically improved by the addition of training data for poorly represented structures.

Structures that are annealed and quenched with neural networks closely match their final DFT optimized geometries. This offers a potential gateway to creating amorphous and defective surface models that is significantly less computationally expensive than DFT, but offers better accuracy than most forcefield based approaches. The relative ORR activity of our TiAl_2O_5 surface models appeared to increase as the surfaces became less stable, but we were still able to predict dopants that consistently inhibited ORR activity (Sn^{4+} and Si^{4+}) and dopants that consistently promoted ORR activity (Co^{2+} , Mn^{2+} , Cr^{3+} , Nb^{5+}) for multiple TiAl_2O_5 surfaces.

7.0 SUMMARY AND FUTURE WORK

7.1 AROMATIC N-HETEROCYCLE CO-CATALYZED CARBON DIOXIDE REDUCTION

Chapter 2 showed that we could calculate the redox properties of small organic ANH molecules, and that those properties could be tuned by changing the structural characteristics of the molecules. While the one electron redox properties were significantly uphill in energy, processes involving more simultaneous proton and electron transfers could occur near CO₂ reduction conditions. By using a molecular screening procedure that we created to automatically calculate redox properties and molecular Pourbaix diagrams, we can rapidly screen through ANH molecules to identify viable electrocatalysts.

Chapters 3 and 4 highlighted tools that can be used to characterize redox reaction pathways in homogeneous solutions. Chapter 3 showed that we can locate hydride transfer reaction pathways with gSS-NEB optimizations and determine how those pathways are affected by interactions with nearby solvent molecules. Chapter 4 obtained free energy barriers for those reaction pathways from potentials of mean force derived from umbrella sampling simulations. These simulations showed that reaction free energies evaluated at realistic temperatures can be dramatically different from those evaluated at 0 K with DFT. This procedure enables us to characterize reaction energies and barrier heights that are more accurate than those determined with DFT calculations on stationary molecular clusters.

Molecular Pourbaix diagrams are useful tools for visualizing redox properties. However, Pourbaix diagrams do not contain any kinetic information, and it is difficult to assess the feasibility of redox reactions. Future work should be addressed towards evaluating the feasibility of different reaction processes by incorporating kinetic information into Pourbaix diagrams.

This would make Pourbaix diagrams even more useful tools for evaluating electrocatalysts. This could involve characterizing transition states, or training machine learned potentials to predict barriers for electrochemical reactions. Predicting the barriers for redox reactions involving the transfer of electrons is very challenging and developing a standard approach would be highly beneficial to the field of computational catalysis.

7.2 INHIBITING SURFACE OXYGEN REDUCTION REACTIVITY

Chapter 5 described an *in silico* procedure for predicting how dopants affect the ORR overpotentials of amorphous TiO_2 . Our methodology successfully predicted ORR overpotential trends for seven different dopants, and our top three predicted dopants (Mn, Al, and V) were experimentally shown to inhibit ORR currents by up to 77%. Chapter 6 attempted to utilize the methodology developed in Chapter 5 to perform an analogous study on TiAl_2O_5 (a native oxide of Ti-6Al-4V, a commonly used Ti alloy). By using neural networks trained to TiAl_2O_5 structures, we generated a large number of unique defective and amorphous surface models. Characterizing the ORR overpotentials of these surfaces showed that the more stable surfaces were less reactive. We were able to identify a set of dopants that inhibited ORR activity on both TiO_2 and TiAl_2O_5 (the two native oxides of Ti-6Al-4V). These insights shed light on the atomic scale factors that influence corrosion reactions and may help design materials that better resist corrosion.

Our TiAl_2O_5 predictions have not yet been experimentally verified. If our predictions differ from experimental results, there would be an opportunity to refine and improve the model. Our current approach does not account for any type of atomic segregation within the oxide surface. Modeling the segregation of dopants within an oxide structure could help explain how different dopants contribute to ORR reactivity trends. These processes are too computationally expensive to model with DFT, but machine learned potentials (such as neural networks) could be trained to model doped oxide structures and used to model the long term distribution of metal dopants within an oxide surface. These simulations could help create more realistic oxide surface models.

If successful, our approach could be extended to other metals/metal alloys. Many other metals, such as stainless steels and nickel alloys, can serve as the cathode of a galvanic corrosion process. Studying these materials could help identify the material-property relationships that promote/inhibit galvanic corrosion mechanisms across different types of materials. The ability of neural networks to generate accurate metal or metal oxide surface models could also be further explored. Neural networks and other machine learned potentials can facilitate the discovery of surface models that contain new surface morphologies or defects by decreasing the computational cost associated with Monte-Carlo modeling or molecular dynamics simulations. While neural networks have facilitated Monte-Carlo modeling of materials,^[281] there have been relatively few studies that use neural networks to perform molecular dynamics simulations (either for annealing simulations or obtaining other material properties). Machine learned potentials could obtain DFT caliber energies and properties at a fraction of the computational cost. Further studying how to train reliable potentials could greatly decrease the time required to perform in-depth computational quantum chemistry studies.

APPENDIX A

SUPPORTING INFORMATION FOR STRUCTURAL AND SUBSTITUENT GROUP EFFECTS ON MULTIELECTRON STANDARD REDUCTION POTENTIALS OF AROMATIC N-HETEROCYCLES

As seen in Table [A.1](#), the differences between B3LYP/ACCD energies on B3LYP/6-31+G* or B3LYP/ACCD optimized structures are minimal.

Table [A.2](#) shows the substituent group effects that are summarized by Figure [2.3](#). Molecules with electron withdrawing groups are easier to reduce, while molecules with electron donating groups are harder to reduce.

Figures [A.1](#) through [A.27](#) show the full Pourbaix diagrams for all of the ANH molecules studied in Chapter [2](#).

Table A.1: Energy differences between B3LYP/ACCD//B3LYP/6-31+G* and B3LYP/ACCD//B3LYP/ACCD

	dE (kcal/mol) = E(B3LYP/6-31+G*)- E(B3LYP/aug-cc-pVDZ)
quinoline	0.00
Hquinoline ⁺	0.04
Hquinoline radical	0.04
dihydroquinoline radical	0.05
dihydroquinoline	0.04
naphthyridine	0.04
naphthyridine radical	0.03
Hnaphthyridine radical	0.04
dihydronaphthyridine radical	0.02
quadhydronaphthyridine	0.06

Table A.2: Substituent group effects on absolute pK_a s and redox potentials

		pK_a (calc)	1e	1e1h	2e2h	2e1h to prot
	quinoline	4.6	-2.40	-0.89	-0.42	-0.55
Electron	4-chloroquinoline	2.4	-2.19	-0.81	-0.17	-0.24
Withdrawing	4-CN-quinoline	-0.3	-1.59	-0.43	-0.37	-0.36
Groups	4-NH ₃ -quinoline	-1.2	-1.96	-0.67	0.02	0.05
Electron	4-methylquinoline	6.0	-2.47	-0.95	-0.47	-0.65
Donating	4-OH-quinoline	6.6	-2.51	-1.05	-0.47	-0.67
Groups	4-NH ₂ -quinoline	10.5	-2.65	-1.11	-0.62	0.93
	1,8-naphthyridine	3.1	-2.06	-0.72	-0.34	-0.44
	4-chloro-1,8-naphthyridine	1.0	-1.84	-0.62	-0.12	-0.15

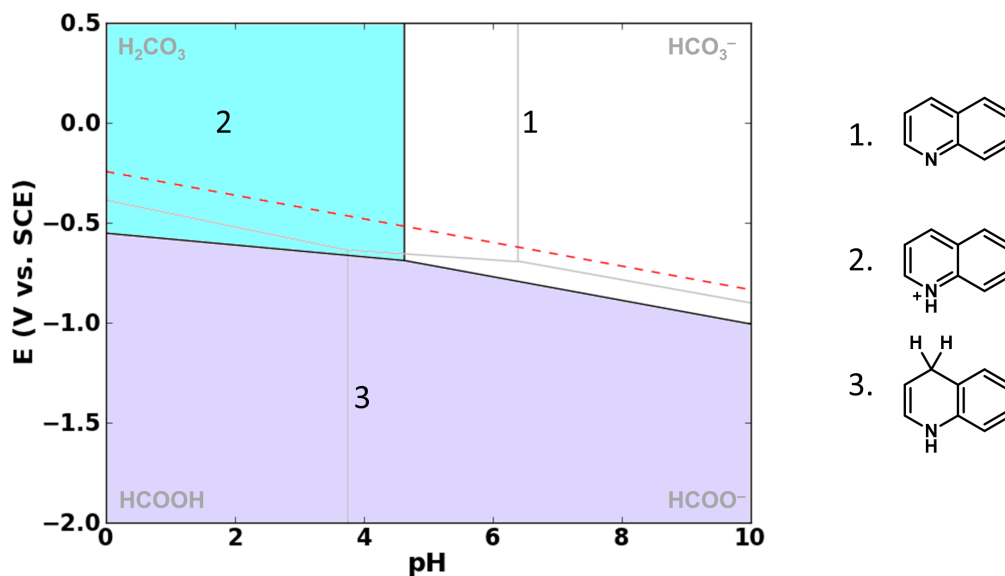


Figure A.1: Quinoline Pourbaix diagram

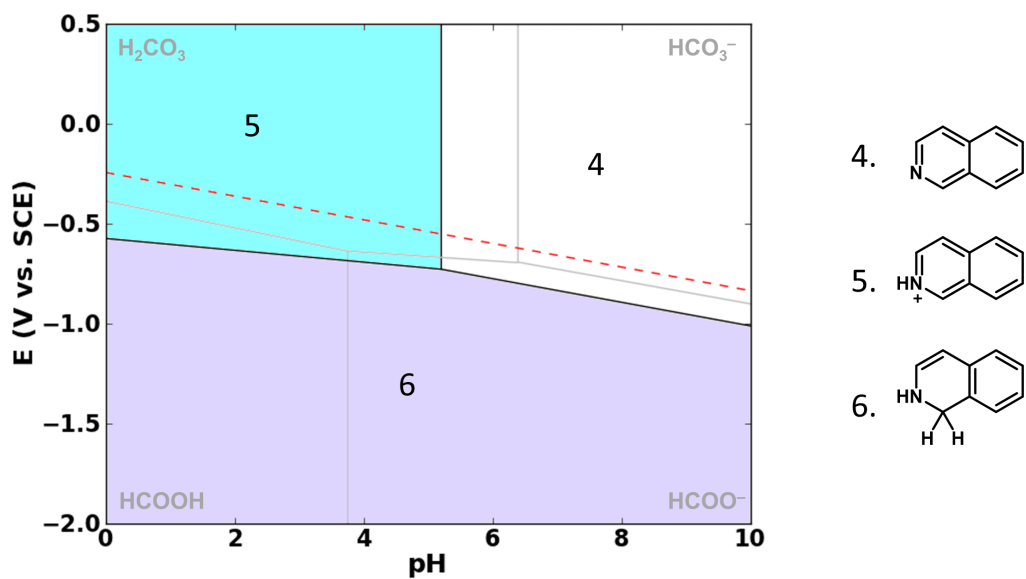


Figure A.2: 2-quinoline Pourbaix diagram

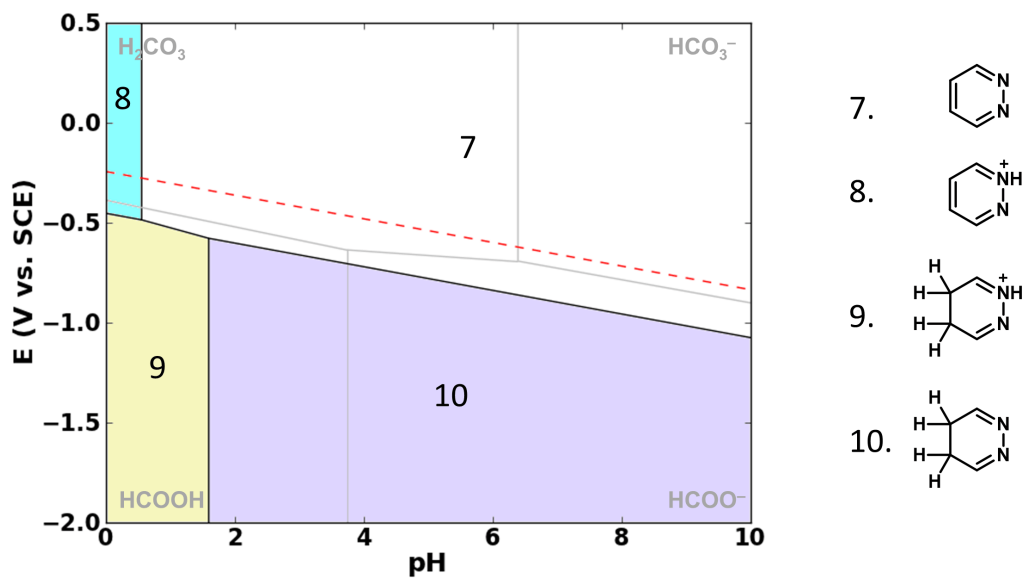


Figure A.3: 1,2-diazine Pourbaix diagram

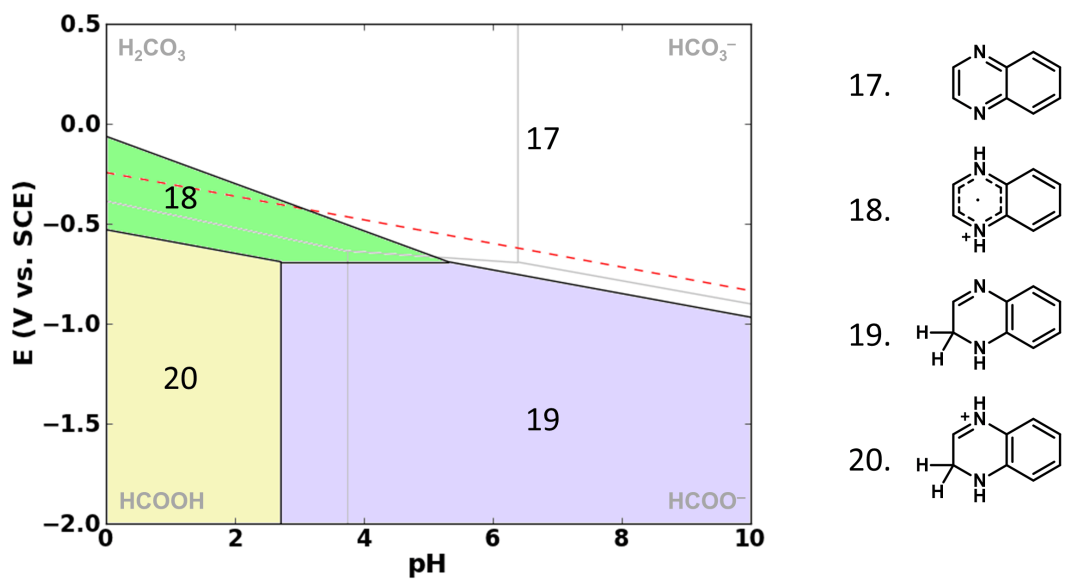


Figure A.6: 1,4-naphthyridine Pourbaix diagram

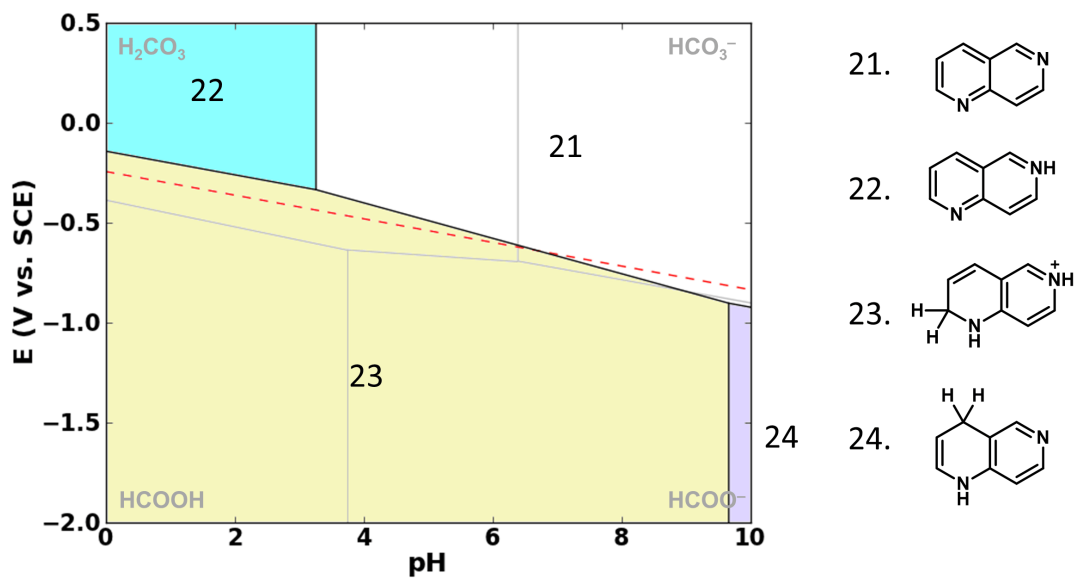


Figure A.7: 1,6-naphthyridine Pourbaix diagram

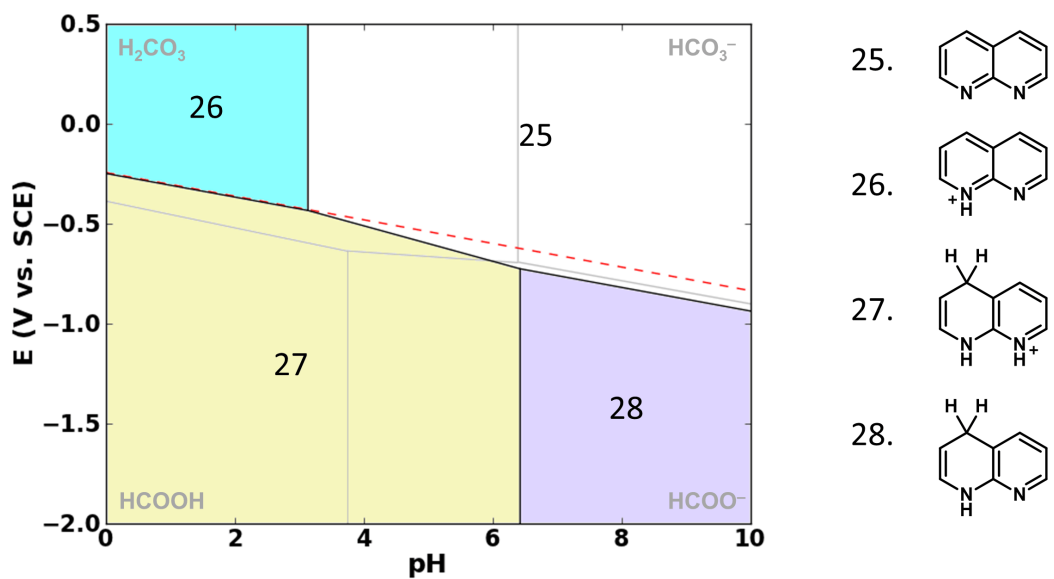


Figure A.8: 1,8-naphthyridine Pourbaix diagram

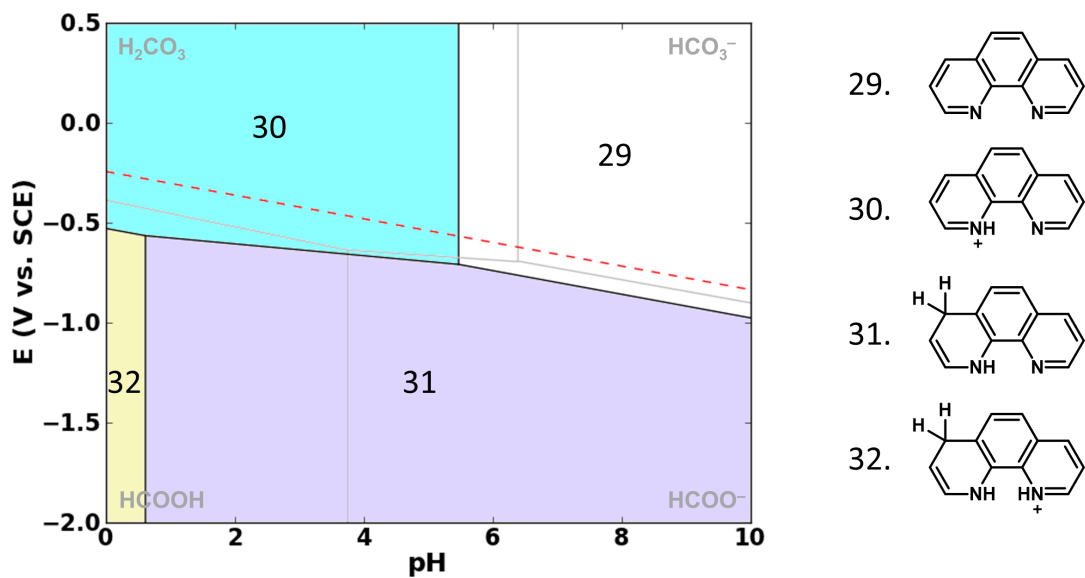


Figure A.9: Phenanthroline Pourbaix diagram

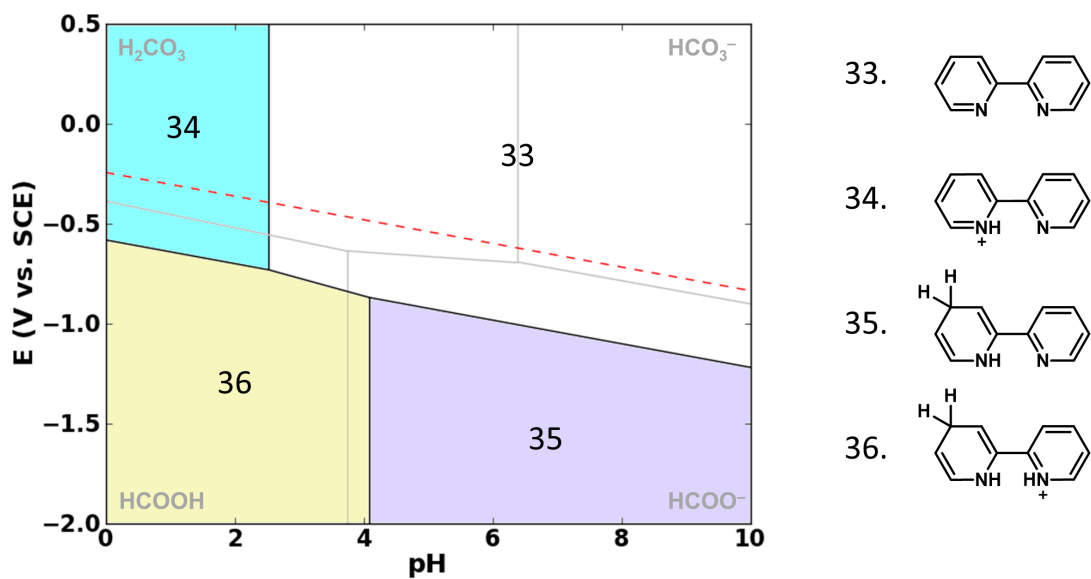


Figure A.10: 2,2'-bipyridine Pourbaix diagram

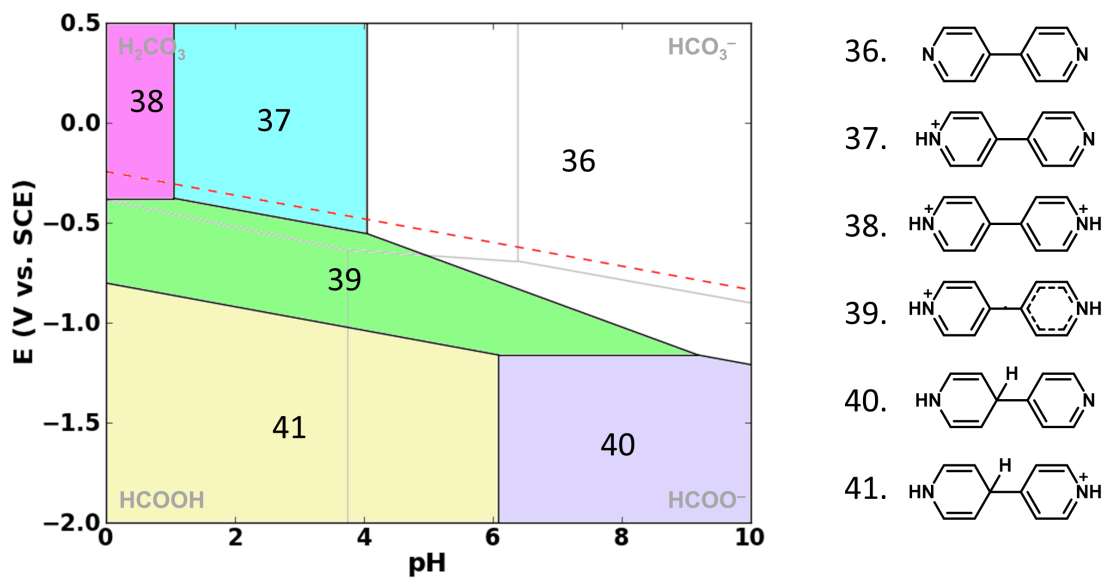


Figure A.11: 4,4'-bipyridine Pourbaix diagram

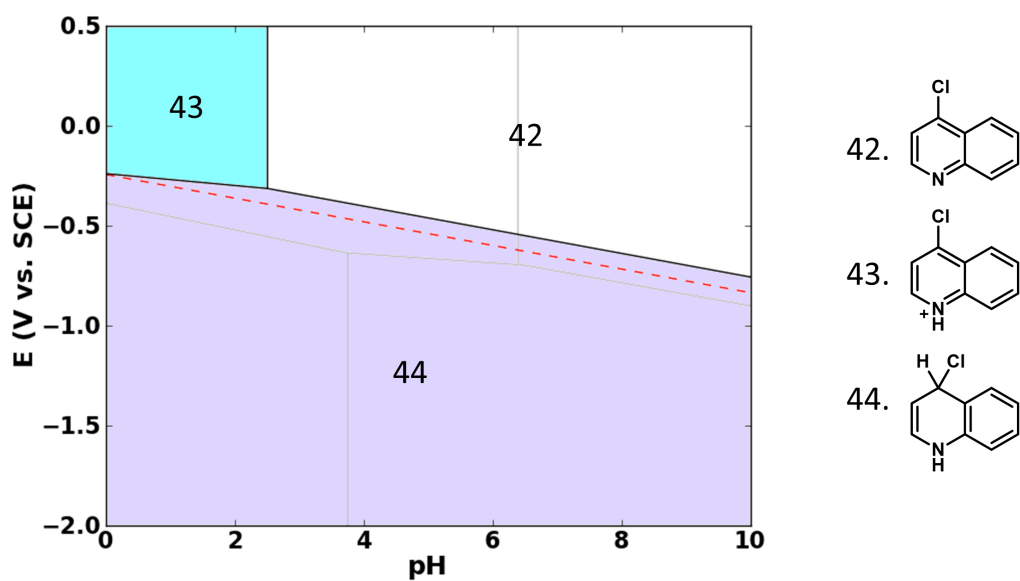


Figure A.12: 4-Cl-quinoline Pourbaix diagram

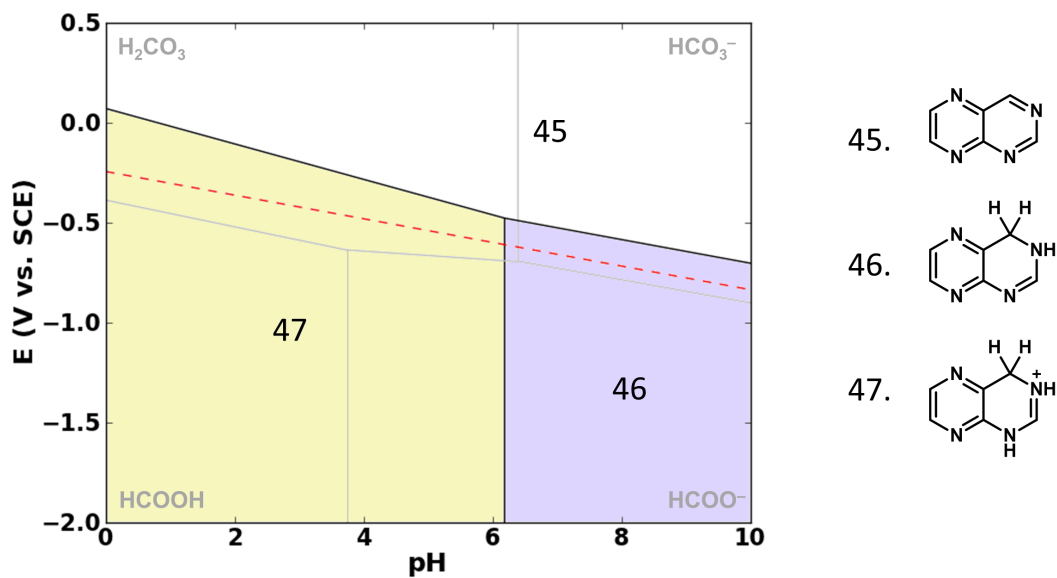


Figure A.13: Pteridine Pourbaix diagram

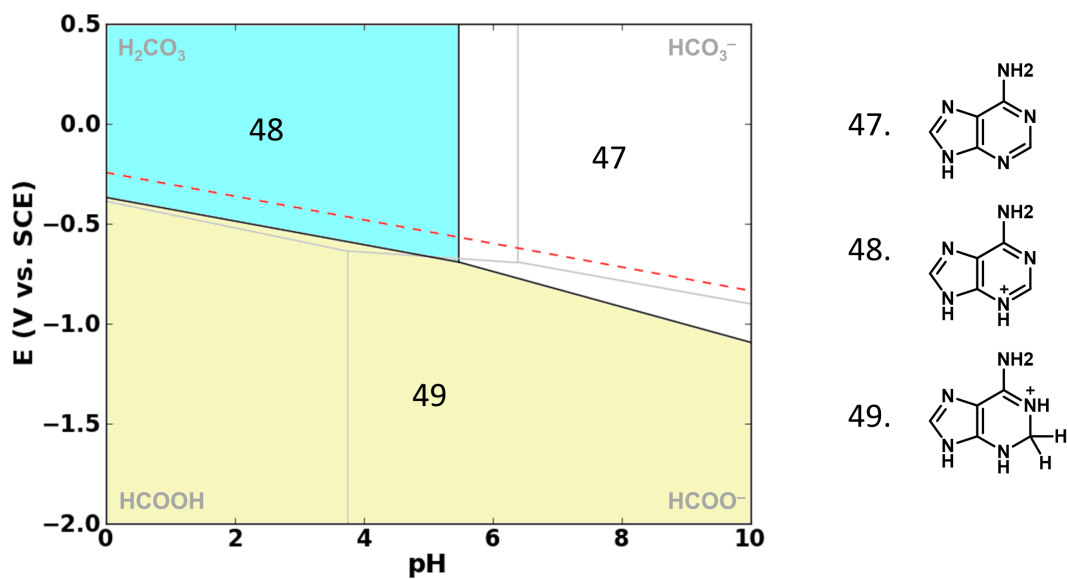


Figure A.14: Adenine Pourbaix diagram

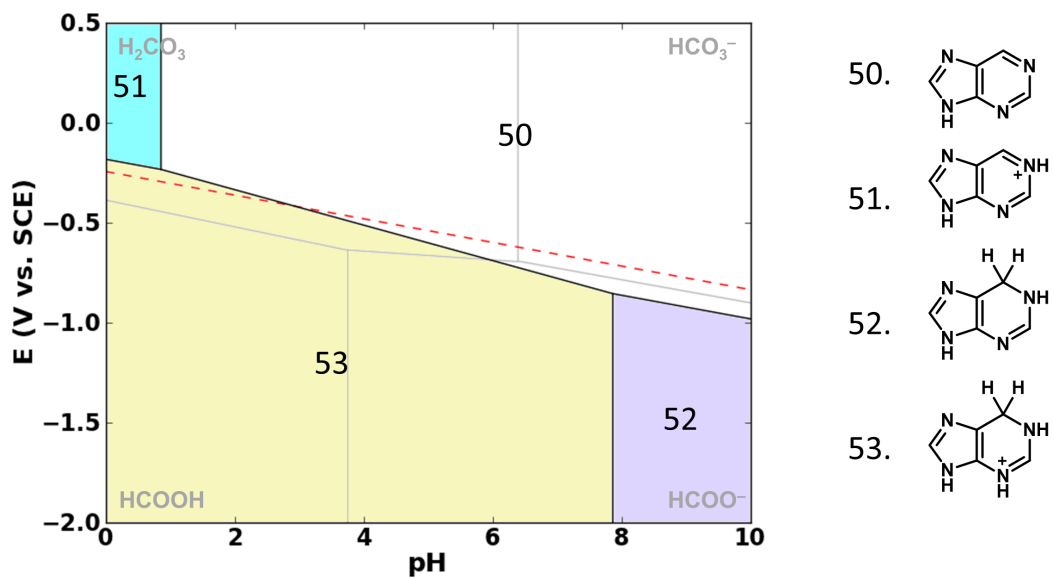


Figure A.15: Purine Pourbaix diagram

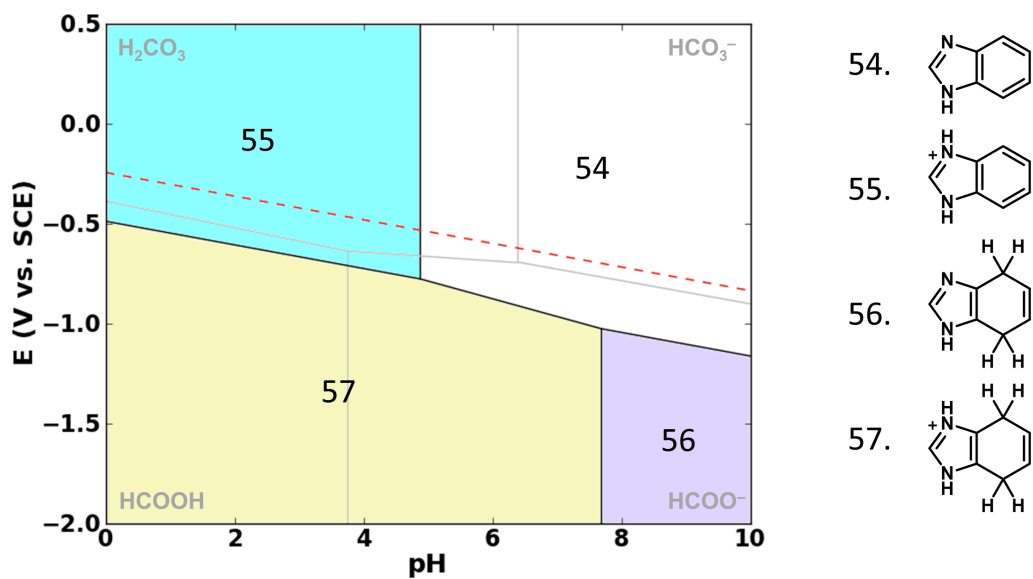


Figure A.16: Benzimidazole Pourbaix diagram

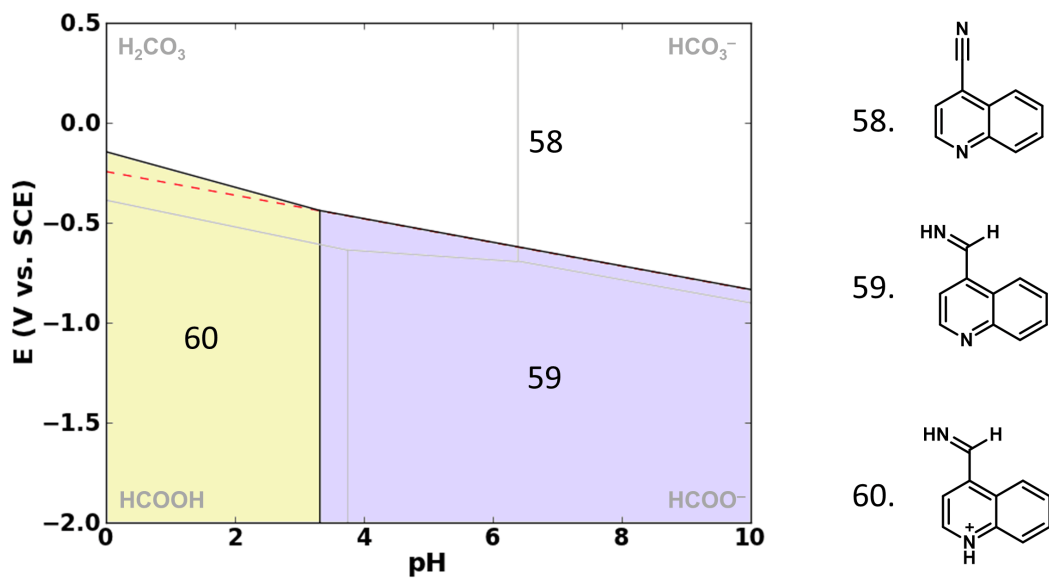


Figure A.17: 4-CN-quinoline Pourbaix diagram

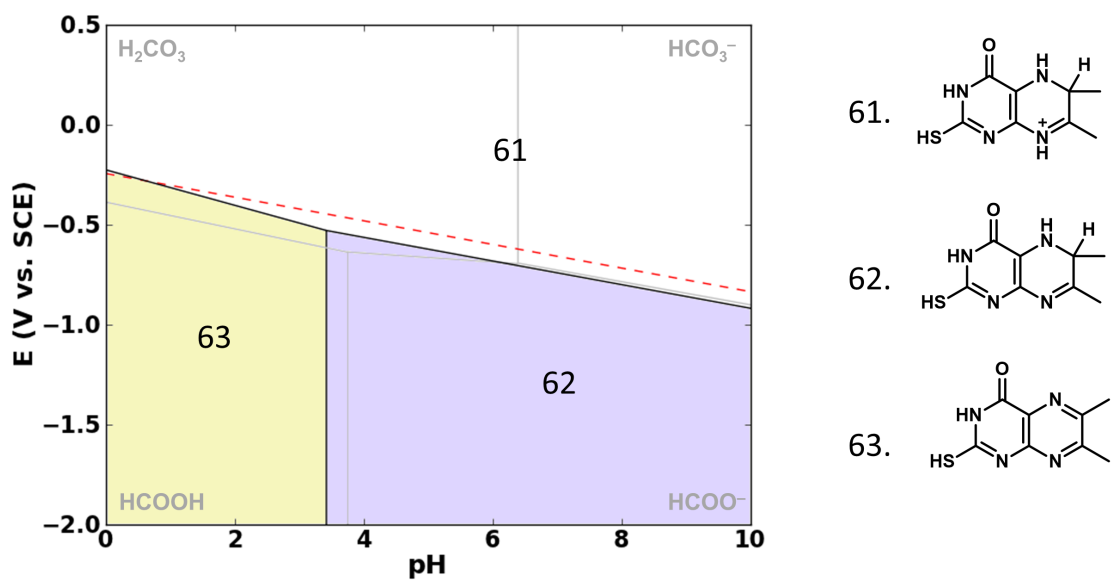


Figure A.18: Mercaptopteridine Pourbaix diagram

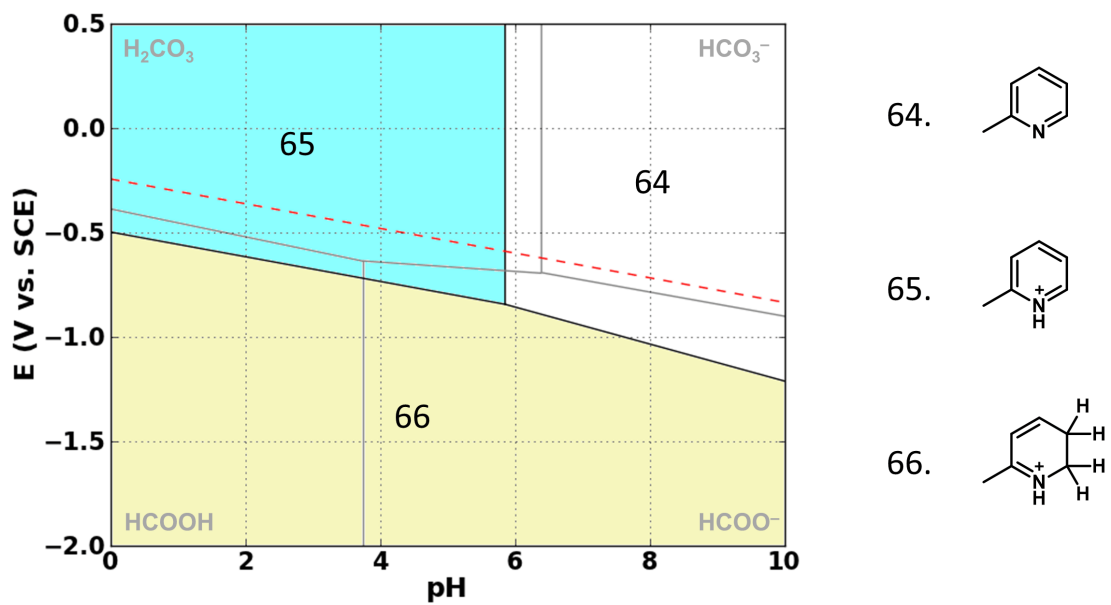


Figure A.19: 2-picoline Pourbaix diagram

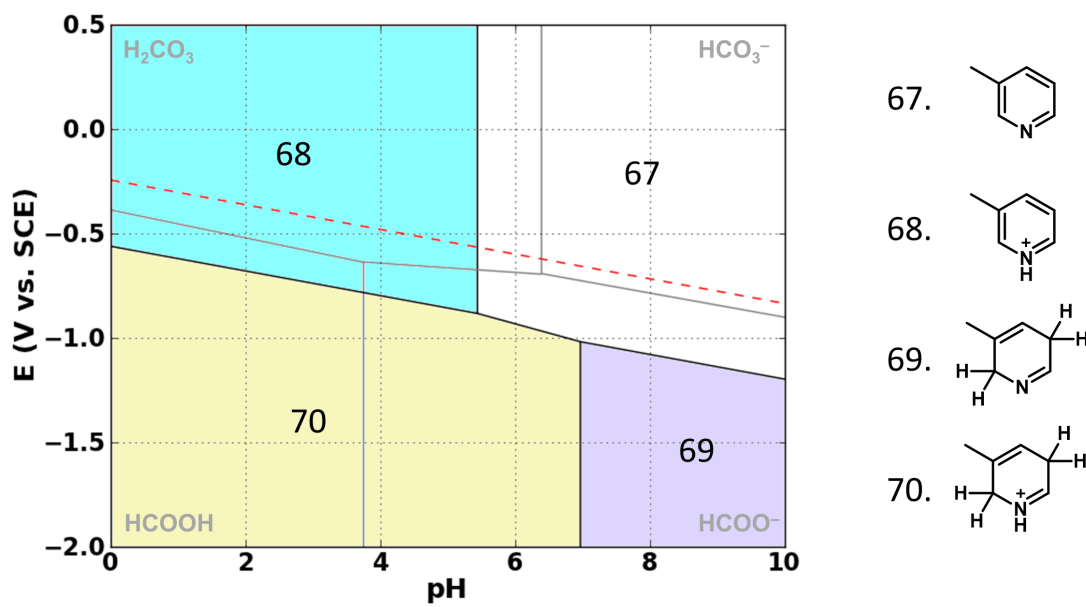


Figure A.20: 3-picoline Pourbaix diagram

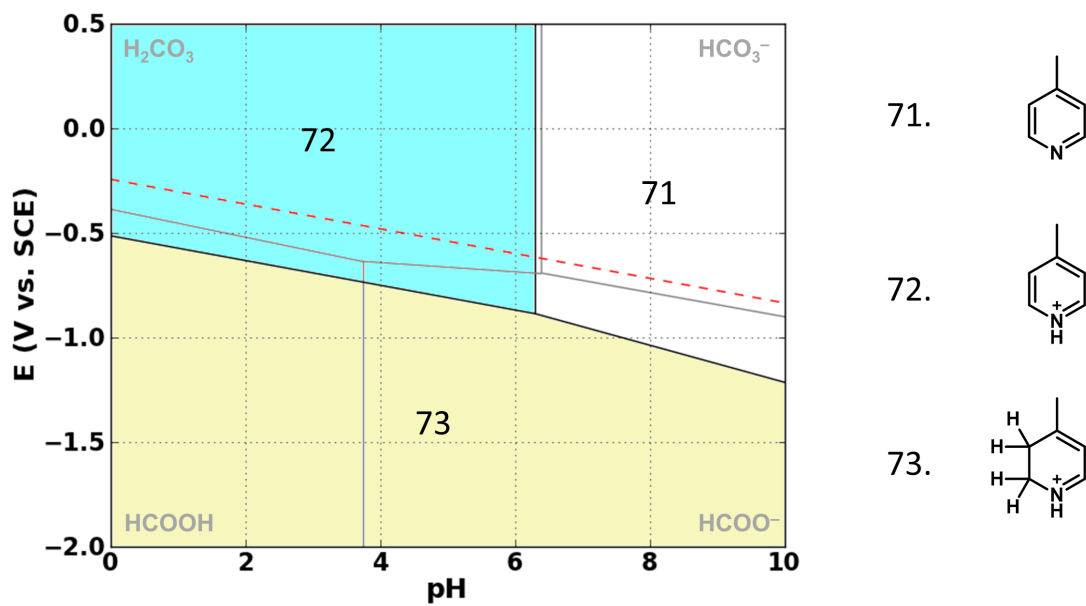


Figure A.21: 4-picoline Pourbaix diagram

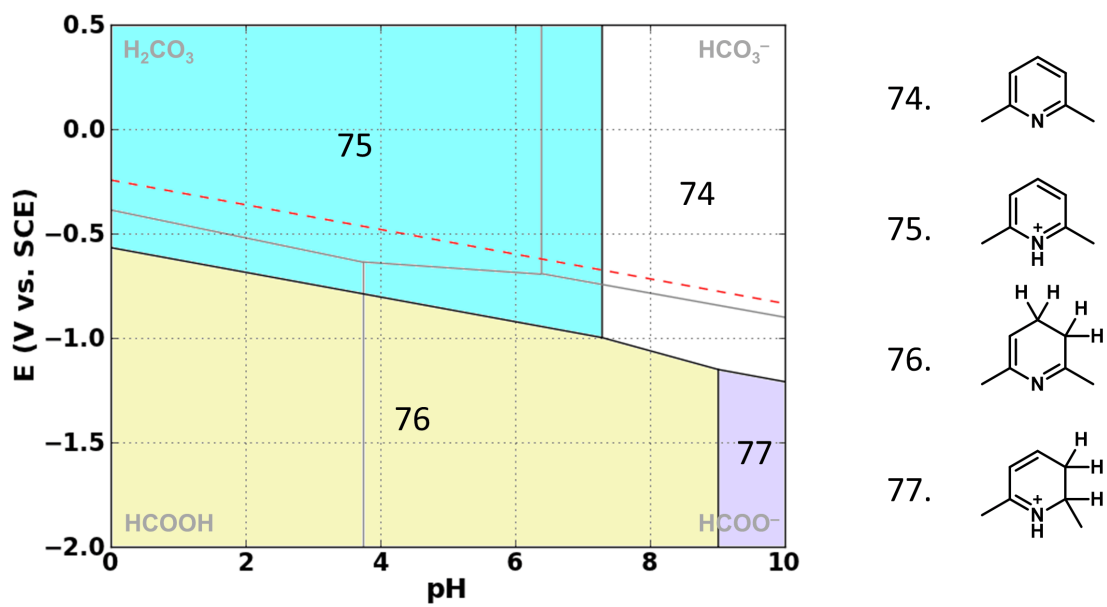


Figure A.22: 2,6-lutidine Pourbaix diagram

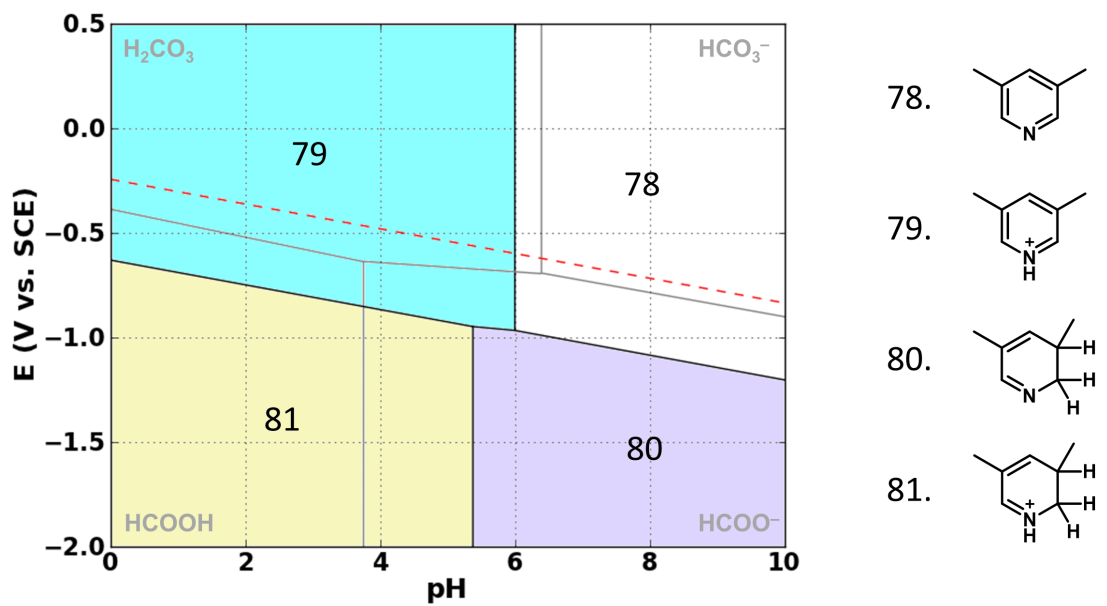


Figure A.23: 2,5-lutidine Pourbaix diagram

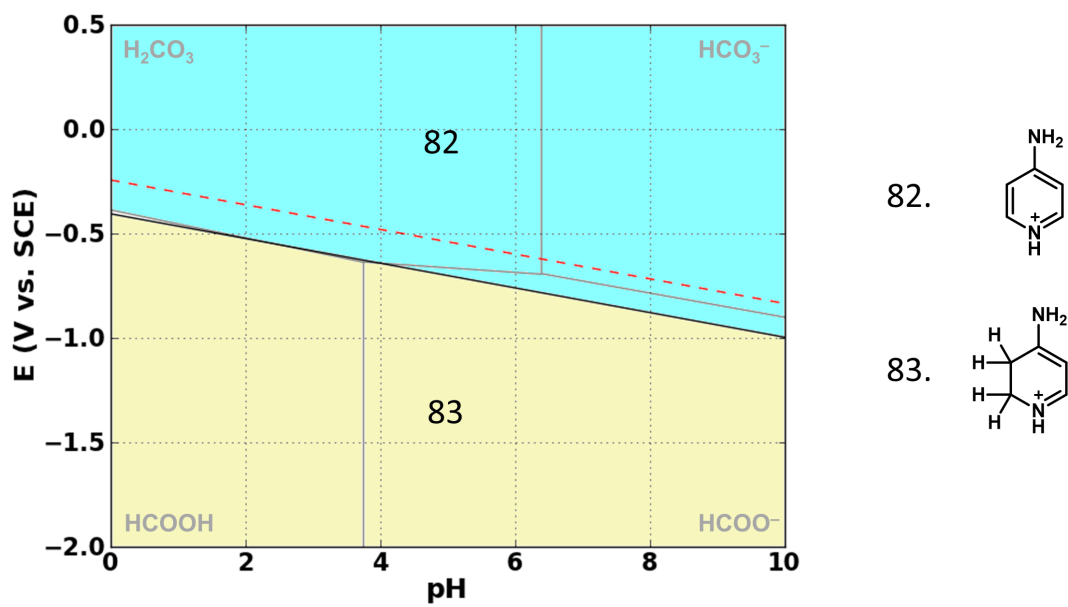


Figure A.24: 4-aminopyridine Pourbaix diagram

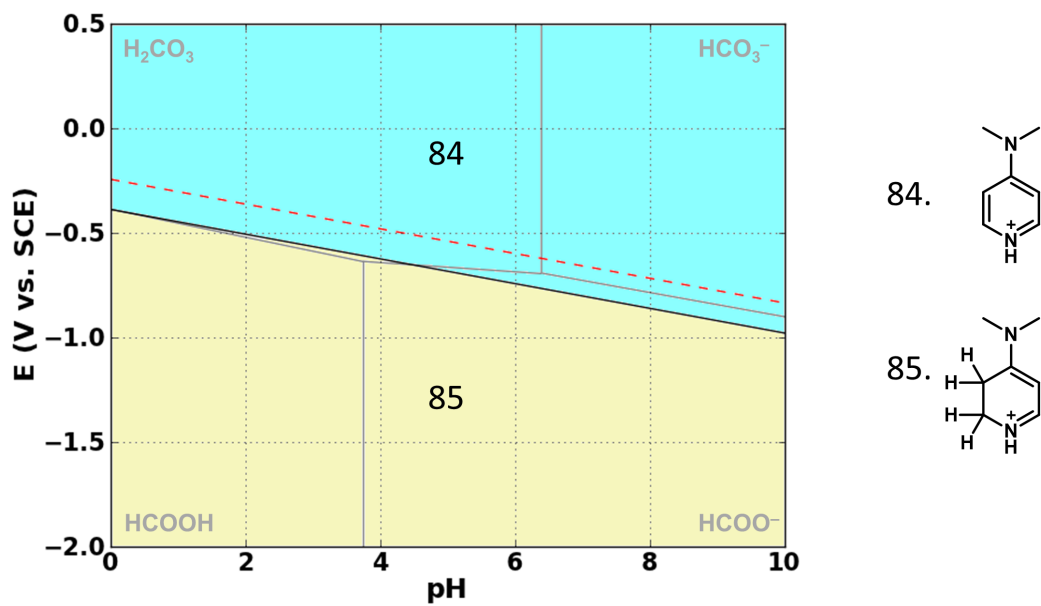


Figure A.25: N,N-dimethyl-4-aminopyridine Pourbaix diagram

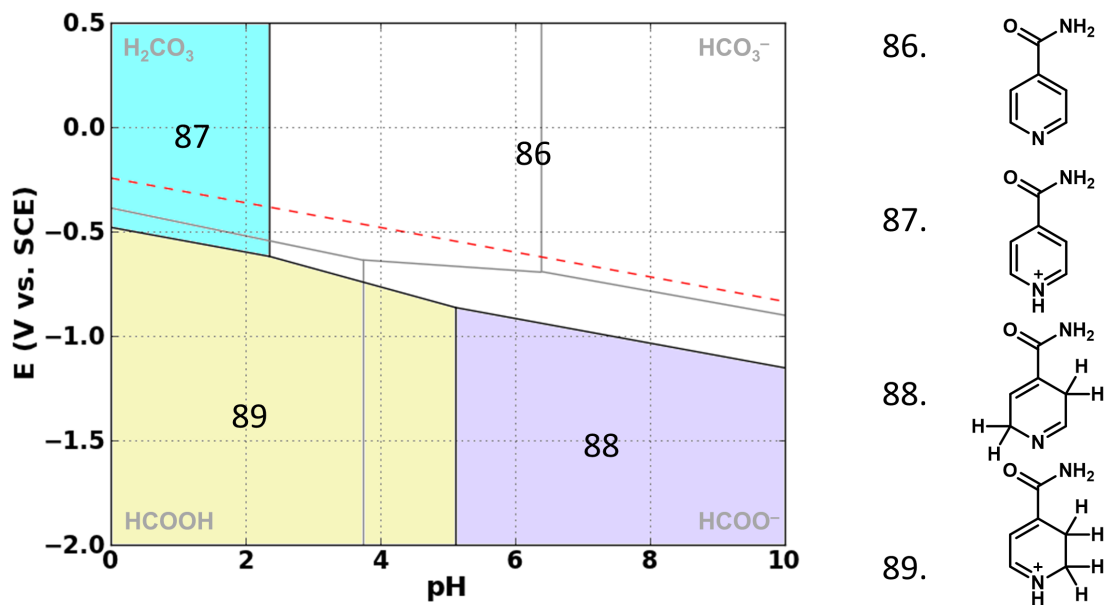


Figure A.26: Nicotinamide Pourbaix diagram

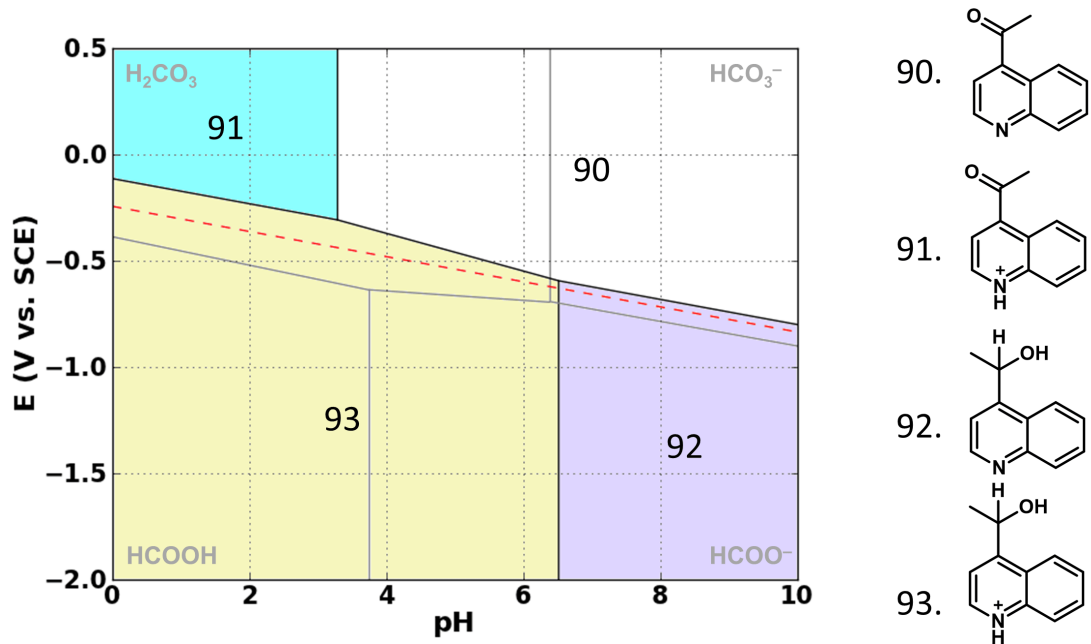


Figure A.27: 4-acetylquinoline Pourbaix diagram

APPENDIX B

POURBAIX DIAGRAM GENERATION PROCEDURE

This appendix briefly explains the Pourbaix diagram generation procedure used by Chapter 2. The procedure is currently implemented with the python library for automating molecular simulations (PLAMS) in the ADF modeling suite. Our Pourbaix diagram calculator use a screening procedure to reduce the number of total required quantum chemical calculations, and automates the quantum chemical calculations that are required to generate molecular Pourbaix diagrams.

B.1 POURBAIX DIAGRAM SCREENING PROCEDURE

One must consider all possible combinations of proton and electron combinations to a molecule to generate accurate molecular Pourbaix diagrams. One proton, one electron processes such as proton coupled electron transfers (PCET) are frequently reported in the literature. In theory, many simultaneous proton and electron transfers could occur, but these processes are typically limited to up to 2 simultaneous proton and electron transfers (corresponding to a proton coupled hydride transfer). The number of additional structures that must be considered to model these processes can increase exponentially with the size of the original molecule as demonstrated in Figure B.1.

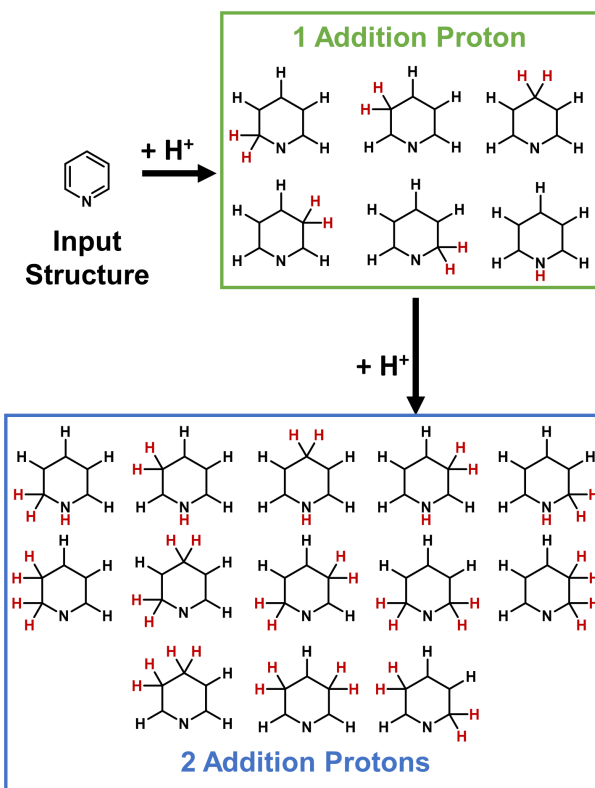


Figure B.1: The basic connectivity for the molecules produced by adding protons to pyridine. This demonstrates the exponential growth of unique molecular structures with additional protons.

To reduce the number of molecular structures that must be considered, we utilized the five step screening procedure described by Figure B.2. Starting from a user defined molecule, the procedure generates all of the unique combinations of proton additions to the original molecule by bonding additional H atoms to under-coordinated atoms. The procedure then optimizes the molecules with a range of charges (defined by the user, default = -1, 0, +1 relative to the original molecule) using DFTB or PM7 in mopac. These methods require significantly less computational resources than full DFT optimizations. The procedure then calculates the energies of the DFTB/PM7 optimized structures using small basis set DFT calculations, and the molecules that are above a user-defined cutoff from the lowest energy molecules are removed from the screening process. The remaining molecules are fully opti-

mized with DFT, and the molecules that are still not within a smaller energy cutoff of the lowest energy molecules are removed. The energies and vibrational frequencies of the final molecules are then calculated with DFT and used to generate molecular Pourbaix diagrams.

This procedure automatically eliminates a large number of irrational structures while using methods that are computationally inexpensive. This could be done with chemical intuition, but more complex molecules are difficult to differentiate without insight from semi-empirical or quantum chemical data. Each stage of the screening process is fully customizable. The user can change the maximum number of protons/electrons, the maximum allowed charges, the type of PM7, DFTB, or DFT used at any point in the procedure, or even the criteria used to define where protons are added. The python script that generates the quantum chemical data is shown in section B.4. That data can then be easily converted into a molecular Pourbaix diagram by the python script shown in section B.5. Both of these segments of code rely on functions defined in the "pourbaixlibrary" module. This module has been omitted for the sake of space. A full explanation of all possible keywords is listed below.

B.2 POURBAIX DIAGRAM GENERATOR KEYWORDS

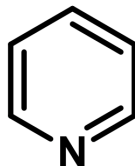
-f: This flag must be followed by the path to an xyz coordinate file. This is the only mandatory keyword. For example, "-f test.xyz" creates a molecular Pourbaix diagram for the molecule in "test.xyz"

-c: This flag is followed by the charge of the molecule. For example, "-c 1" for a molecule with a 1+ charge (Default = 0).

-skip: This flag is followed by a list of atomic indices of atoms that will not be protonated during the procedure. For example, "-skip 1,2,3" would exclude the first, second, and third atom listed in the coordinate file (Default = skip nothing).

-only: Only add protons to the atomic indices listed behind this flag. For example, "-only 1,2,3" would ignore all atoms except for atoms 1, 2, and 3 when generating molecular structures with additional Hs (Default = protonate all non-H atoms).

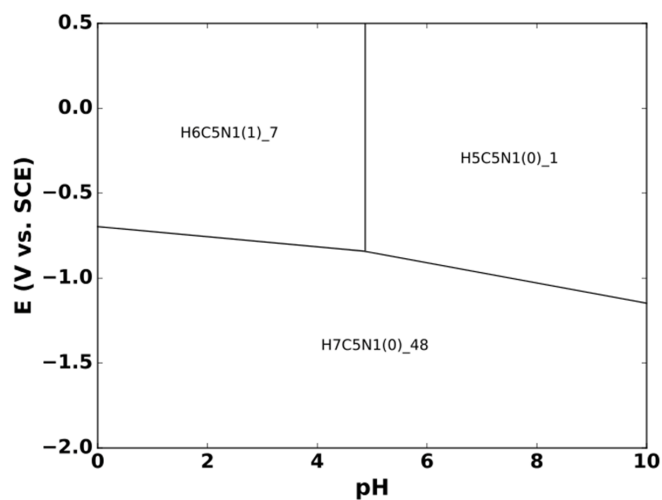
Input: Molecular Coordinates



1. Generate all relevant molecular structures
2. Optimize all molecules using DFTB, MOPAC, or ADF
3. (Optional) Calculate DFT energies for all molecules

4. Select low energy molecules and optimize their geometries using ADF

5. Final energy calculations



Output: Molecular Pourbaix Diagrams

Figure B.2: The screening procedure used to calculate molecular Pourbaix diagrams.

-ignore_dft_warning: If this flag is included, calculations that finished with warnings are included in the final analysis. Be sure to check the warnings if you include this keyword. For example, "-ignore_warning" (default = exclude calculations with warnings from the final analysis)

-ignore_structure_warning: Including this flag will cause molecules that form/break bonds during the DFTB or MOPAC preoptimization to not be excluded from the screening process (this is not recommended in most cases...).

-screening_type: Specifies the types of calculations performed for the initial screening procedure. "1" = All molecules are sorted based on their DFTB (or MOPAC) energies/structures. "2" = Neutral molecules are treated the same as in type 1. Charged molecules sorted by DFT energies calculated on DFTB (or MOPAC) optimized structures. "3" = All molecules are sorted based on DFT energies calculated on DFTB (or MOPAC) optimized molecules. This is the default mode. "4" = Molecules sorted by their energy at the end of a DFT optimization. This method does not require DFTB (or MOPAC) parameters. All DFT calculations are controlled by the "-screen" keyword.

-maxH: The maximum number of protons that will be added to the molecule. For example, "-maxH 3" creates structures with up to 3 additional protons (Default = 2).

-maxe: The maximum number of electrons that will be added to each molecule. For example, "-maxe 3" creates structures with up to 3 additional electrons (Default = 2).

-maxchar: The maximum +/- charge that is allowed during the screening process. The script will not create a molecule with a charge larger than defined here. For example, "-maxchar 2" allows structures with a +/- 2 charge to be included in the analysis (Default = 1).

-maxmult: The maximum multiplicity tested. For example, "-maxmult 5" would test multiplicities of 1, 3, and 5 for molecules with an even number of electrons, and 2, for molecules with unpaired electrons. The default analysis includes only doublets (default = 2).

-unintended_bond_detection: This constant proportionally effects the detection radius for atoms that are too close to the added proton (default = 1.0). Larger values are more restrictive when adding protons to highly coordinated atoms, and decrease the likelihood that

a proton will be added. Smaller values may add protons too close to atoms other than the intended protonation site. The cutoff for detecting neighbors that are too close is defined by the larger of either $((\text{radius}(\text{atom1}) + \text{radius}(\text{H})) * 0.92) * (\text{constant})$ or $((\text{radius}(\text{atom1}) + \text{radius}(\text{H})) * 0.8) ** 1.66) * (\text{constant})$. If atoms neighboring atoms are closer than this distance, that structure is excluded from the screening procedure.

-altermaxbond: Overrides the maximum default coordination of specified elements. For example, `"-altermaxbond C,5.N,6"` would change the maximum coordination of carbon from 4 to 5 and nitrogen from 4 to 6.

-sort: Determines the number of structures that are kept during the screening (Default = "bottom 3"). For example, `"-sort "Bottom n""` keeps the lowest n structures for each combination of protons and electrons. `"-sort "m kcal/mol""` keeps the minimum energy structure for each combination of protons and electrons as well as molecules within m kcal/mol.

-numfreq: If included, the final dft calculations are performed with numerical frequencies instead of analytical frequencies.

-serial: If present, the calculations will run serially (instead of in parallel).

-ppj: The number of processors per calculation (default = 1). This is ignored if the calculations are run in serial.

-procs: The total number of processors (default = 1). This is ignored if the calculations are run in serial.

-mopac: MOPAC is used for screening instead of DFTB if this flag is included.

`Screen/opt/sp/solv/freq` define the types of DFT performed at each subsequent screening stage. Any additional ADF/DFTB/MOPAC keywords can be added to these strings. The DFT type, Basis set, and Numerical quality must ALWAYS be defined.

-mopa_key: default = `LBFGS=True PM7=True INT=True`

-dftb: default = `'Task.RunType="Go" dftb.ResourcesDir = "QUASINANO2015" dftb.model= "dftb0"'`

-screen: default = `'XC.GGA="PBE" Basis.Type="DZP" Basis.Core="Large" NumericalQuality="Basic" Dependency=True'`

-opt: default = `'XC.GGA="PBE" Basis.Type="DZP" Basis.Core="Large" NumericalQuality="Basic" Dependency=True'`

-sp: default = 'XC.HYBRID="B3LYP" Basis.Type="AUG/ATZP" Basis.Core="Large" NumericalQuality="good" Dependency=True'

-solv: default = 'SOLVATION.SOLV="EPS=78.4"', help='COSMO keywords for solvation calculation (default: EPS=78.4)'

-freq: default = 'XC.GGA="PBE" Basis.Type="DZP" Basis.Core="Large" NumericalQuality="Basic" Dependency=True'

-test: Overrides all default settings to use small basis sets and less expensive DFT calculations. This should only be used for testing.

Command Line Example: "\$ADFBIN/startpython pourbaix_data_generator.py -f pyr.xyz -procs 8 -skip 1,2,4,5 -sort "1 kcal/mol" -ignore_warning"

B.3 POURBAIX DIAGRAM GENERATOR KEYWORDS

-f: The Pourbaix diagram input file generated by the pourbaix_data_generator script. Default = 'Pourbaix_Input'.

-fout: The name of the Pourbaix diagram plot created by this script. Default = 'plot_pourbaix'.

-ph_max (default = 10.000001), **-ph_min** (default = 0), **-v_max** (default = 0.5000001), and **-v_min** (default = -2) control the pH and applied potential ranges for the Pourbaix diagram. Change the pH/potential range of the final Pourbaix diagram plot

-tol: Controls the grid spacing for locating species on the Pourbaix diagram. Smaller tolerances will yield a higher quality Pourbaix diagram. Default = 0.1.

-line_tol: Controls the accuracy used when searching for boundaries between Pourbaix diagram regions. Smaller tolerances will yield a higher quality plot. Default = 0.005

Command Line Example: \$ADFBIN/startpython pourbaix_diagram_generator.py -f Pourbaix_Input -ph_max 14

B.4 POURBAIX DIAGRAM DATA GENERATION

```
import argparse
import os
import sys
import numpy as np
from pourbaixlibrary import *
from scm.plams import *
import time

init()

#Input options that vary from test to test
parser = argparse.ArgumentParser(prog='PourbaixDiagramGenerator', description =
    'Automatically generates Pourbaix diagram data')

parser.add_argument('-f', type=str, help='The filepath to the xyz-coordinate
    file used for the calculation', required=True)
parser.add_argument('-c', type=int, default=0, help='The original molecular
    charge (default = 0)')
parser.add_argument('-skip', type=str, default='', help='Atomic indices of atoms
    that should be ignored (i.e. 1,2,3,... default=ignore nothing)')
parser.add_argument('-only', type=str, default='', help='Indices of atoms that
    should protonated (all others will be ignored. i.e. 1,2,3,...
    default=protonate everything)')
parser.add_argument('-ignore_dft_warning', action='store_true', default=False,
    help='Include the data from calculations with warnings. Be sure you know what
    you are doing. The warnings may be reduced/eliminated with the dependency
    keyword (default = False)')
parser.add_argument('-ignore_structure_warning', action='store_true',
    default=False, help='Including this flag will cause molecules that have
    different final connectivity to not be removed from the screening process
    (Not recommended for organic molecules).')
parser.add_argument('-screening_type', type=int, default=3, help='The method
    used for the initial screening procedure. Possible options: DFTB only, 2.
    DFTB + some DFT, 3. DFTB + DFT, or 4. DFT optimizaitons(default: 3 (DFTB +
    DFT)). DFT parameters are controlled by -screen.' )

#These input options can be changed, but the defaults should usually suffice
parser.add_argument('-maxH', type=int, default=2, help='The maximum number of
    protons added to the molecule (default=2)')
parser.add_argument('-maxe', type=int, default=2, help='The maximum number of
    electrons added to the molecule (default=2)')
parser.add_argument('-maxchar', type=int, default=1, help='The maximum allowed
    charge change from the original molecular charge')
```

```

parser.add_argument('-maxmult', type=int, default=2, help='The maximum allowed
multiplicity, must be greater than 1. Using mult=1 ignores all radicals
(default = 1)')
parser.add_argument('-unintended_bond_detection', type=float, default=1.0,
help='Effects the detection radius for neighboring atoms when protons are
added to high coordinate atoms (default = 1). Larger values will be more
restrictive, smaller values can result in poor initial structures.')
parser.add_argument('-altermaxbond', type=str, default = ' ', help='overrides the
default maximum coordination of the specified atom type(s) (ex. C,5.N,5...)')
parser.add_argument('-sort', type=str, default='Bottom 3', help='Select the
"Bottom X" or select all molecules within "Y kcal/mol"')
parser.add_argument('-numfreq', action='store_false', default=True,
help='perform numerical frequency calculations instead of analytical (only
recommended if using hybrid DFT for frequency calculations)')

parser.add_argument('-serial', action='store_true', default=False, help='If this
flag is present the calculations will run serially')
parser.add_argument('-ppj', type=int, default=1, help='The number of processors
used per calculation. This is ignored if calculations are run serially')
parser.add_argument('-procs', type=int, default=1, help='The number of
simultaneous calculations (this x ppj = total number of processors). This is
ignored if calculations are run serially')

parser.add_argument('-mopac', action='store_true', default=False, help='perform
mopac optimizations for the screening process')
parser.add_argument('-mopac_key', type=str, default='LBFGS=True PM7=True
INT=True', help='mopac keywords')
parser.add_argument('-dftb', type=str, default='Task.RunType="Go"
dftb.ResourcesDir="QUASINAN02015" dftb.model="dftb0"', help='DFTB keywords
for the screening phase')
parser.add_argument('-screen', type=str, default = 'XC.GGA="PBE"
Basis.Type="DZP" Basis.Core="Large" NumericalQuality="Basic"
Dependency=True', help='DFT keywords for screening procedure')
parser.add_argument('-opt', type=str, default = 'XC.GGA="PBE" Basis.Type="DZP"
Basis.Core="Large" NumericalQuality="Basic" Dependency=True', help='DFT
keywords for DFT optimizations')
parser.add_argument('-sp', type=str, default = 'XC.HYBRID="B3LYP"
Basis.Type="AUG/ATZP" Basis.Core="Large" NumericalQuality="good"
Dependency=True', help='DFT keywords for final energy calculations')
parser.add_argument('-solv', type=str, default = 'SOLVATION.SOLV="EPS=78.4"',
help='COSMO keywords for solvation calculation (default: EPS=78.4)')
parser.add_argument('-freq', type=str, default = 'XC.GGA="PBE" Basis.Type="DZP"
Basis.Core="Large" NumericalQuality="Basic" Dependency=True', help='DFT
keywords for frequency calculations')

parser.add_argument('-test', action='store_true', default=False, help='overrides
defaults to perform quick calculations...')

```

```

args = parser.parse_args()

#Determine if DFT is used during the screening process
if args.screening_type == 1:
    dftb_only = "YES"
    screening_method = 'DFTB only'
elif args.screening_type == 2:
    dftb_only = 'PARTIAL'
    screening_method = 'DFTB for neutral molecules and DFT for charged species'
elif args.screening_type == 3:
    dftb_only = 'NO'
    screening_method = 'DFTB and DFT for all species'
elif args.screening_type == 4:
    screening_method = 'DFT only'

#only multiplicities greater than two can be tested.
if args.maxmult < 2:
    args.maxmult = 2

#a list of atomic indices to not protonate
skip = [int(i) for i in args.skip.split(',') if i]
only = [int(i) for i in args.only.split(',') if i]

#'-test' overrides the default parameters for faster calculations
if args.test:
    args.maxH = 2
    args.maxe = 2
    args.screening_type = 1
    args.screen = 'XC.GGA="PBE" Basis.Type="SZ" Basis.Core="None"
        NumericalQuality="Basic"'
    args.opt = 'XC.GGA="PBE" Basis.Type="SZ" Basis.Core="None"
        NumericalQuality="Basic"'
    args.sp = 'XC.GGA="PBE" Basis.Type="SZ" Basis.Core="None"
        NumericalQuality="Basic"'
    args.freq = 'XC.GGA="PBE" Basis.Type="SZ" Basis.Core="None"
        NumericalQuality="Basic"'
    args.solv = 'SOLVATION.SOLV="EPS=78.4"'
    dftb_only = 'YES'
    args.sort='Bottom 1'

if ('geometry' not in args.screen) and (args.screening_type == 4):
    args.screen += ' geometry.Iterations="50"'
elif 'geometry' not in args.screen:
    args.screen += ' geometry.sp=True'
if 'geometry' not in args.sp:
    args.sp += ' geometry.sp=True'

```



```

if 'geometry' not in args.opt:
    args.opt += ' geometry.Iterations="50"'

if not args.serial:
    str = ('\nCalculation is running in parallel, '
          '{0} jobs running simultaneously using {1} processor per
          job\n'.format(args.procs, args.ppj))
    job_log(str, print2screen=True)
    config.default_jobrunner = JobRunner(parallel=True, maxjobs=abs(args.procs))
config.log.stdout = 0

#-----PROCESSING-----
#Open a log file in the plams working directory
job_log('\nKeywords\n' + \
        'maxH = {0}\n'.format(args.maxH) + \
        'maxe = {0}\n'.format(args.maxe) + \
        'maxchar = {0}\n\n'.format(args.maxchar) + \
        'maxmult = {0}\n\n'.format(args.maxmult) + \
        'file = {0}\n'.format(args.f) + \
        'Initial charge = {0}\n'.format(args.c) + \
        'skipped atoms # {0}\n'.format(args.skip if args.skip else 'N/A') + \
        'only atoms # {0}\n\n'.format(args.only if args.only else 'N/A') + \
        'Screening method: {0}\n'.format(screening_method) + \
        'Sort method = {0}\nEnd keywords\n\n'.format(args.sort) + \
        'Ignoring warnings: {0}\n'.format(args.ignore_dft_warning) + \
        '\nWARNING... THESE CALCULATIONS CAN BE VERY EXPENSIVE FOR LARGE
        MOLECULES...\n' + \
        'To limit the computational cost of these calculations you can:\n' + \
        ' 1. Use smaller basis sets\n' + \
        ' 2. Restrict the number of protons/electrons to be added
        (-maxH/-maxe/-maxchar)\n' + \
        ' 3. Choose to not protonate selected atoms (-skip)', print2screen=True)

#create a plams molecule from a xyz coordinate file
mol = MoleculeData(args.f)
mol.guess_bonds()
num_e = sum((PeriodicTable.get_atomic_number(atom.symbol) for atom in mol)) -
          args.c

#generates large list of MoleculeData objects containing molecules with added
protons/electrons:
job_log('Generating input structures... this may take a few seconds.',
        print2screen=True)
molecule_list = [mol]
t00 = int(time.time())
for num_H in range(args.maxH): molecule_list = add_proton(num_H+1,
        molecule_list, skip, only, args.altermaxbond, args.unintended_bond_detection)

```

```

molecule_list = add_electron(args.maxe, molecule_list, args.maxchar,
    -args.maxchar, args.c, num_e, args.maxmult)
t01 = int(time.time())
job_log('Generating structures required {0}s'.format(t01-t00), print2screen=True)

#Screen the molecules using only DFTB, DFTB/DFT, or only DFT
t1 = int(time.time())
if args.screening_type != 4:
    screened_molecule_list = run_screen(molecule_list, dftb_only, args.screen,
        args.dftb, args.ignore_dft_warning, args.ignore_structure_warning,
        args.serial, args.ppj, args.mopac, args.mopac_key)
else:
    screened_molecule_list = run_dft_opt(molecule_list, args.screen,
        args.ignore_dft_warning, args.serial, args.ppj, screening=True)
    job_log('Skipping step 2...', print2screen=True)

molecules_screened = sort_energy(screened_molecule_list, args.sort)

t2 = int(time.time())
job_log('\n***Initial screening procedure completed after
    {0}s***\n'.format(t2-t1), print2screen=True)

#Optimize the molecules with DFT, write the final molecular structures to a
    directory
dft_opt_molecules = run_dft_opt(molecules_screened, args.opt,
    args.ignore_dft_warning, args.serial, args.ppj)
dft_opt_molecules = sort_energy_final(dft_opt_molecules, 'Bottom 2')
write_final_structures(dft_opt_molecules)

t3 = int(time.time())
job_log('\n***Geometry optimizations completed after {0}s***\n'.format(t3-t2),
    print2screen=True)

#Run the final DFT energy calculations
data = run_dft_final(dft_opt_molecules, args.sp, args.solv, args.freq,
    args.numfreq, args.ignore_dft_warning, args.serial, args.ppj)

t4 = int(time.time())
job_log('***Final energy calculations completed after {0}s***'.format(t4-t3),
    print2screen=True)
job_log('***Screening procedure completed after {0}s***'.format(t4-t1),
    print2screen=True)

#Open a Pourbaix diagram input file in the plams working directory
log_file = open(config.jm.workdir + '/Pourbaix_Input', 'w')
log_file.write('#Formula(charge)_id, Gas phase energy, Solvation energy, ')

```

```

log_file.write('Gibbs free energy correction, # protons, # electrons (all
energies in kcal/mol)\n')
for d in data:
    gas_kcal = Units.convert(d.dft_gas, 'hartree', 'kcal/mol')
    solv_kcal = Units.convert(d.dft_solv, 'hartree', 'kcal/mol')
    dG_kcal = Units.convert(d.dft_dG, 'hartree', 'kcal/mol')
    log_file.write('{6}({7})_{5}, {0}, {1}, {2}, {3}, {4}\n'.format(gas_kcal,
        solv_kcal, dG_kcal, d.num_H, d.num_e, d.id_number, d.get_formula(),
        d.charge))

finish()

```

B.5 GENERATING POURBAIX DIAGRAMS

```

import sys
import numpy as np
import argparse
from pourbaixlibrary import *

#The purpose of this script is to generate a Pourbaix diagram based on energies
    stored in an input file
#This script is build to use the "Pourbaix_Input" style file produced by the
    pourbaix_data_generator.py script
#Each line should contain: <molecule id number>, <Escf>, <SCF to G298>,
    <Solvation energy>, <#protons added>, <#electrons added>

parser = argparse.ArgumentParser(prog = 'PourbaixDiagramGenerator', description
    = 'Creates a Pourbaix diagram from QM data')
#The user can define the input/output filenames
parser.add_argument('-f', type=str, default='Pourbaix_Input', help = 'The file
    path to the QM data file (default = Pourbaix_Input)')
parser.add_argument('-fout', type=str, default='plot_pourbaix', help = 'The file
    name for the generated Pourbaix diagram (default = plot_pourbaix)')

#Change the pH/potential range of the final Pourbaix diagram plot
parser.add_argument('-ph_max', type=float, default=10.000001, help = 'The
    maximum pH considered (default = 10.000001)')
parser.add_argument('-ph_min', type=float, default=0, help = 'The minimum pH
    considered (default = 0)')
parser.add_argument('-v_max', type=float, default=0.5000001, help = 'The maximum
    considered applied potential vs SCE (default = 0.5000001)')
parser.add_argument('-v_min', type=float, default=-2, help = 'The minimum
    considered applied potential vs SCE (default = -2)')

```

```

#These parameters control the creation of the Pourbaix diagram, smaller values
  will produce better plots, but take much longer to create
parser.add_argument('-tol', type=float, default=0.1, help = 'Use smaller values
  to improve the quality of the plot. The default value is sufficient in most
  cases. (default = 0.1)')
parser.add_argument('-line_tol', type=float, default=0.005, help = 'Use smaller
  values to improve the quality of the plot. The default value is sufficient in
  most cases. (default = 0.005)')

args = parser.parse_args()

#Read the data from the Pourbaix diagram data file, and identify the relevant
  molecules
data, names = extract_data(args.f)
relevant_molecules, reference_molecule = simplify(data)

#Print the data to the screen so the user can check the numbers
#print('\n')
#print('Lowest energy species for each e/H addition are:')
#print('Name, G(298,Solvent), H+ added, e- added')
#for molecule in relevant_molecules:
#  print(molecule.name, molecule.energy, molecule.num_H, molecule.num_e)
#print('\n{0} {1} {2} {3} is the original
  molecule'.format(reference_molecule.name, reference_molecule.energy,
    reference_molecule.num_H, reference_molecule.num_e))

#Generate a pH and potential range to search over
ph_range      = np.arange(args.ph_min, args.ph_max + args.tol, args.tol)
potential_range = np.arange(args.v_max, args.v_min - args.tol, -args.tol)

#Find the molecules that are the lowest in energy at the pH/potentials created
  above
minimal_energy_species, region_boundaries = Gmin(reference_molecule,
  relevant_molecules, ph_range, potential_range)

#identify the molecules that are equally stable at some conditions (identifying
  isochemical potential lines)
species_change = specieschange(minimal_energy_species, ph_range, potential_range)

#Find the line coefficients for the isochemical potential lines
line_coefficients = coefficients(species_change, relevant_molecules,
  reference_molecule)

#Generate a higher precision pH/potential range
ph_range = np.arange(args.ph_min, args.ph_max + args.line_tol, args.line_tol)

```

```
potential_range = np.arange(args.v_max, args.v_min - args.line_tol,
                             -args.line_tol)

#Use the new pH/potential range to determine the domains/ranges of each line on
the Pourbaix diagram
new_line_coefficients = intersections(line_coefficients, relevant_molecules,
                                     reference_molecule, potential_range, ph_range)

#plot Pourbaix diagrams. One is plotted with molecule id labels, and one without
pourbaix_plot(relevant_molecules, args.fout, new_line_coefficients, args.ph_min,
              args.ph_max, args.v_min, args.v_max, names, True, region_boundaries)
```

APPENDIX C

SUPPORTING INFORMATION FOR EXPLICITLY UNRAVELING THE ROLES OF COUNTER IONS, SOLVENT MOLECULES, AND ELECTRON CORRELATION IN SOLUTION PHASE REACTION PATHWAYS

Figure C.2 shows the relative energetics vary by up to 0.26 eV when using different levels of theory. This difference is significant and about as large as the differences presented in the main text. The structures had the following energies.

Transition state energies with 1 H₂O range from 0.66 to 0.87 eV.

Transition state energies with 2 H₂O_s range from 0.65 to 0.83 eV.

Transition state energies with 4 H₂O_s range from 0.71 to 0.87 eV.

Reaction energies with 1 H₂O range from 0.14 to 0.23 eV.

Reaction energies with 2 H₂O_s range from -0.49 to -0.63 eV.

Reaction energies with 4 H₂O_s range from -0.58 to -0.69 eV.

Table C.1 shows that the counter ion also moves closer to the oxygen in CO₂ as it is converted into formate. The distance traveled by the Na⁺ is much smaller in this case (~ 0.3 Å here vs. ~ 1.7 Å for scheme 3.2) but this movement suggests that the counter ion plays a similar (but lesser) role in this reaction pathway.

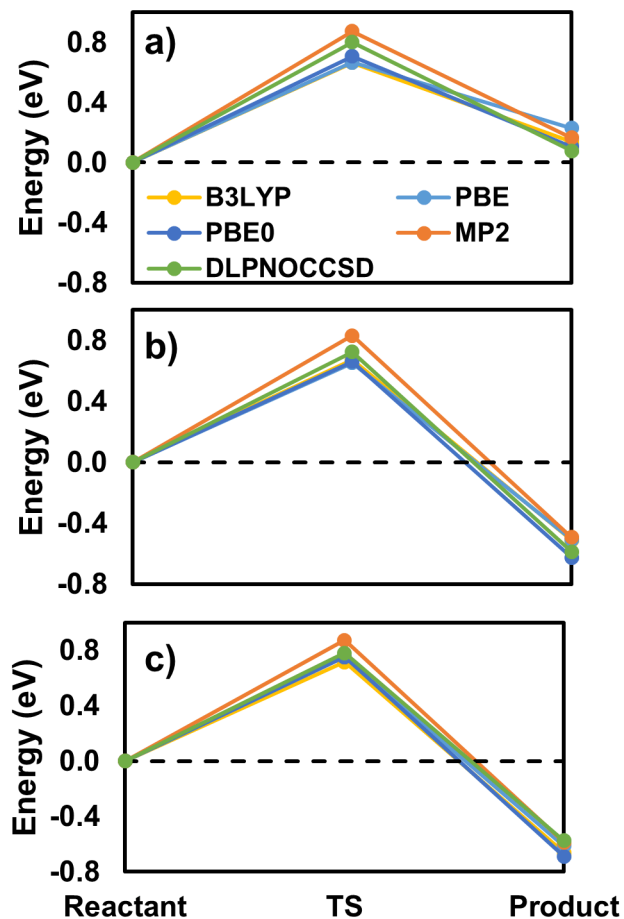


Figure C.1: Additional energetics for Model 1 at the B3LYP/PBE/PBE0/MP2/DLPNO-CCSD (def2-TZVP) level. The energetics correspond to the coordinates shown in a) Figure 3.3a (1 H₂O molecule) in the main text, b) figure 3.3b (2 H₂O molecules) in the main text, and c) figure 3.3c (4 H₂O molecules) in the main text. The transition state and product energies vary by up to 0.2 eV, but the overall trend is the same for every level of theory considered.

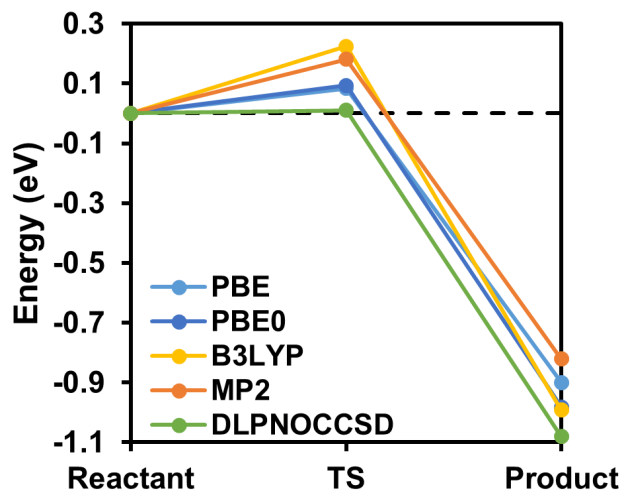


Figure C.2: Additional energetics for Figure 3.10 using Model 1 at the B3LYP, PBE, PBE0, MP2, DLPNO-CCSD (def2-TZVP) level. The energetics correspond to the coordinates shown in Figure 3.11a.

Table C.1: Bond lengths for Figure 3.10

	Bond Distance in Å		
	R_{C-H}	R_{B-H}	R_{O-Na}
R	2.51	1.25	2.53
TS	1.66	1.30	2.38
P	1.13	3.04	2.23

APPENDIX D

SUPPORTING INFORMATION FOR QUANTUM CHEMICAL ANALYSES OF BH_4^- AND BH_3OH^- HYDRIDE TRANSFERS TO CO_2 IN AQUEOUS SOLUTION WITH POTENTIALS OF MEAN FORCE

D.1 UMBRELLA SAMPLING CONSTRAINTS FOR REACTION 1 (BH_4^- $+ \text{CO}_2 \rightleftharpoons [\text{BH}_3\text{-H-CO}_2]^-$)

Table D.1 contains the sets of bond lengths and harmonic bond restraints used for our umbrella sampling simulations for reaction 1. The bond pairs labeled in black were obtained directly from our generalized solid-state nudged elastic band (G-SSNEB) calculations in previous work[216] while those in red, bold, italic were interpolated between G-SSNEB images. Interpolated images were selected to produce the best overlap between umbrella sampling simulation windows without needlessly increasing the number of required simulations.

D.2 UMBRELLA SAMPLING SIMULATION OVERLAP FOR REACTION 1 ($\text{BH}_4^- + \text{CO}_2 \rightleftharpoons [\text{BH}_3\text{-H-CO}_2]^-$)

Figure D.1 shows the overlap between umbrella sampling windows for the reported reaction pathways and reaction energetics for reaction 1. The overlap between neighboring umbrella sampling windows corresponds to adequate sampling along the reaction pathway.

Table D.1: The bond lengths and force constants used to harmonically restrain bonds for Reaction 1.

C-H (Å)	Restraint (eV/Å ²)	B-H (Å)	Restraint (eV/Å ²)
2.80	10.71	1.24	14.28
2.66	10.71	1.24	14.28
2.54	10.71	1.24	14.28
2.43	10.71	1.23	14.28
2.30	7.14	1.23	14.28
2.19	7.14	1.23	14.28
2.02	7.14	1.23	14.28
1.90	7.14	1.24	14.28
1.74	7.14	1.26	14.28
1.62	7.14	1.28	14.28
1.50	7.14	1.31	14.28
1.31	10.71	1.37	14.28
1.24	14.28	1.43	14.28

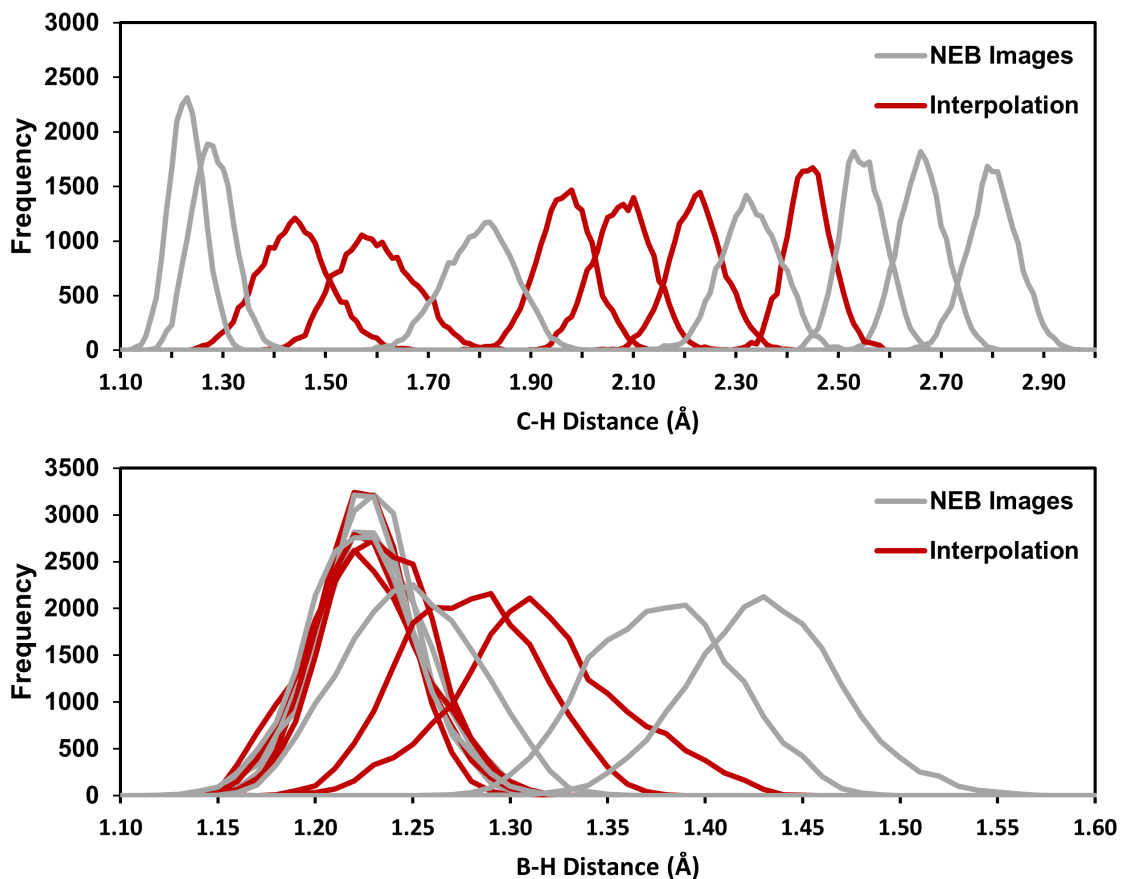


Figure D.1: The umbrella sampling simulation overlap between umbrella sampling windows. Gray B-H and C-H bond length distributions correspond to reaction coordinates from G-SSNEB calculations, while red B-H and C-H bond distributions correspond to reaction coordinates interpolated between G-SSNEB images.

D.3 UMBRELLA SAMPLING CONSTRAINTS FOR REACTION 2 ($\text{H}_2\text{O} + [\text{BH}_3\text{-H-CO}_2]^- \rightleftharpoons \text{BH}_3\text{OH}^- + \text{HCOOH}$)

Table D.2 contains the sets of bond lengths and harmonic bond restraints used for our umbrella sampling simulations for reaction 2. The bond pairs labeled in black were obtained directly from our generalized solid-state nudged elastic band (G-SSNEB) calculations in previous work[216] while those in labeled in red, bold, italic were interpolated between G-SSNEB images. Interpolated images were selected to produce the best overlap between umbrella sampling simulation windows without needlessly increasing the number of required simulations.

D.4 UMBRELLA SAMPLING SIMULATION OVERLAP FOR REACTION 2 ($\text{H}_2\text{O} + [\text{BH}_3\text{-H-CO}_2]^- \rightleftharpoons \text{BH}_3\text{OH}^- + \text{HCOOH}$)

Figure D.2 shows the overlap between umbrella sampling windows for the reported reaction pathways and reaction energetics for reaction 2. The overlap between neighboring umbrella sampling windows corresponds to adequate sampling along the reaction pathway.

D.5 UMBRELLA SAMPLING CONSTRAINTS FOR REACTION 3 ($\text{BH}_3\text{OH}^- + \text{CO}_2 \rightleftharpoons \text{BH}_2\text{OH} + \text{HCOO}^-$)

Table D.3 contains the sets of bond lengths and harmonic bond restraints used for our umbrella sampling simulations for reaction 3. The bond pairs labeled in black were obtained directly from our generalized solid-state nudged elastic band (G-SSNEB) calculations in previous work[216] while those in labeled in red, bold, italic were interpolated between G-SSNEB images. Interpolated images were selected to produce the best overlap between umbrella sampling simulation windows without needlessly increasing the number of required simulations.

Table D.2: The bond lengths and force constants used to harmonically restrain bonds for Reaction 2.

B-H (Å)	Restraint (eV/Å²)	B-O (Å)	Restraint (eV/Å²)
1.43	7.14	3.34	7.14
1.49	7.14	3.15	7.14
1.61	7.14	2.98	7.14
1.75	7.14	2.82	7.14
1.90	7.14	2.63	7.14
2.06	7.14	2.44	7.14
2.15	7.14	2.24	7.14
2.30	7.14	2.01	7.14
2.45	7.14	1.78	7.14
2.70	7.14	1.70	7.14
2.92	7.14	1.62	7.14
3.10	7.14	1.61	7.14
3.25	7.14	1.60	14.28
3.49	7.14	1.59	14.28
3.70	7.14	1.59	14.28
3.85	10.71	1.58	14.28
3.98	14.28	1.58	14.28
4.19	14.28	1.57	14.28

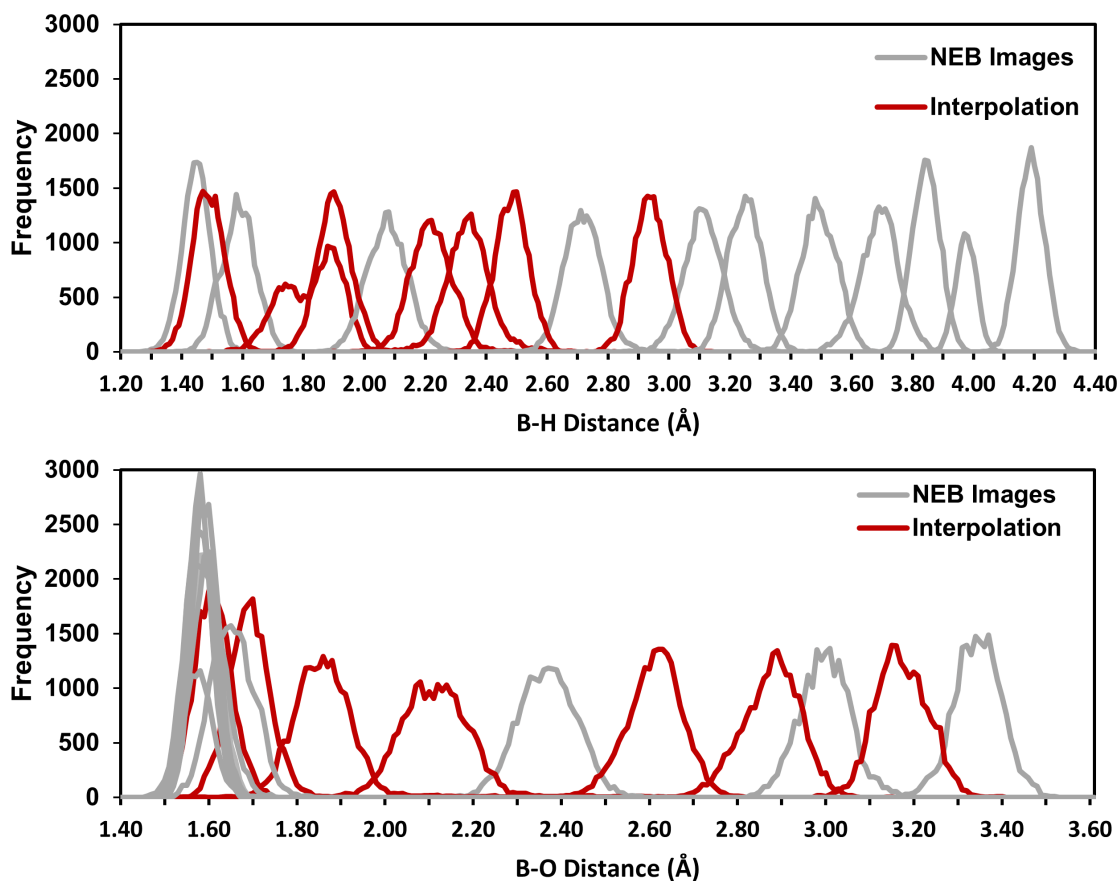


Figure D.2: The umbrella sampling simulation overlap between umbrella sampling windows. Gray B-H and C-H bond length distributions correspond to reaction coordinates from G-SSNEB calculations, while red B-H and C-H bond distributions correspond to reaction coordinates interpolated between G-SSNEB images.

Table D.3: The bond lengths and force constants used to harmonically restrain bonds for Reaction 3.

C-H (Å)	Restraint (eV/Å ²)	B-H (Å)	Restraint (eV/Å ²)
2.51	14.28	1.25	14.28
2.39	14.28	1.25	14.28
2.28	14.28	1.25	14.28
2.11	14.28	1.24	14.28
2.00	14.28	1.26	14.28
1.85	14.28	1.28	14.28
1.67	14.28	1.30	14.28
1.54	14.28	1.36	14.28
1.45	14.28	1.43	14.28
1.32	14.28	1.50	14.28
1.26	14.28	1.54	14.28
1.23	14.28	1.65	14.28
1.19	14.28	1.78	14.28
1.17	14.28	1.96	14.28
1.16	14.28	2.07	14.28
1.15	14.28	2.20	14.28
1.14	14.28	2.38	14.28
1.14	14.28	2.55	14.28
1.14	14.28	2.69	14.28
1.14	14.28	2.85	14.28
1.13	14.28	3.04	14.28
1.13	14.28	3.16	14.28
1.13	14.28	3.30	14.28

D.6 UMBRELLA SAMPLING SIMULATION OVERLAP FOR REACTION 3 ($\text{BH}_3\text{OH}^- + \text{CO}_2 \rightleftharpoons \text{BH}_2\text{OH} + \text{HCOO}^-$)

Figure D.3 shows the overlap between umbrella sampling windows for the reported reaction pathways and reaction energetics for reaction 3. The overlap between neighboring umbrella sampling windows corresponds to adequate sampling along the reaction pathway.

D.7 COMPARING REACTION ENERGIES AGAINST AVERAGE POTENTIAL ENERGIES

Figure D.4 shows that the relative average potential energies from the umbrella sampling windows yield reaction energies that agree with the PMF free energy profile. The reaction barrier from the average potential energies is significantly larger (0.78 eV) than those predicted by either the PMF free energy profile or the NEB energy profile. The difference between these barrier heights suggest that the potential energy of the umbrella sampling window requires longer simulation times to completely converge relative to the reactant and product windows or that other thermodynamic factors are responsible for the smaller barrier height in the PMF free energy profile.

D.8 UMBRELLA SAMPLING SIMULATION TIMESTEP COMPARISON

Figure D.5 compares reaction energetics calculated with different umbrella sampling simulation timesteps. The similarity between reaction energy profiles for Reaction 1 show that a 0.5 fs timestep is sufficient for the reactions reported in this work.

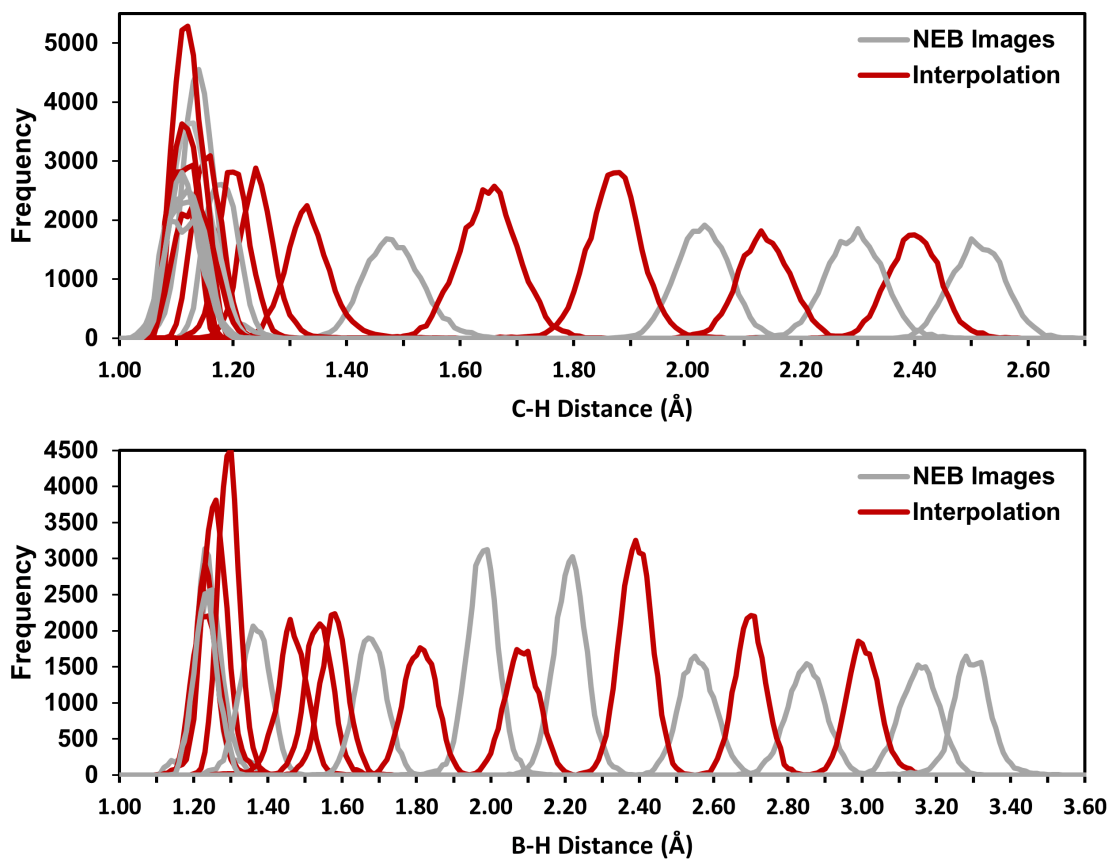


Figure D.3: The umbrella sampling simulation overlap between umbrella sampling windows. Gray B-H and C-H bond length distributions correspond to reaction coordinates from G-SSNEB calculations, while red B-H and C-H bond distributions correspond to reaction coordinates interpolated between G-SSNEB images.

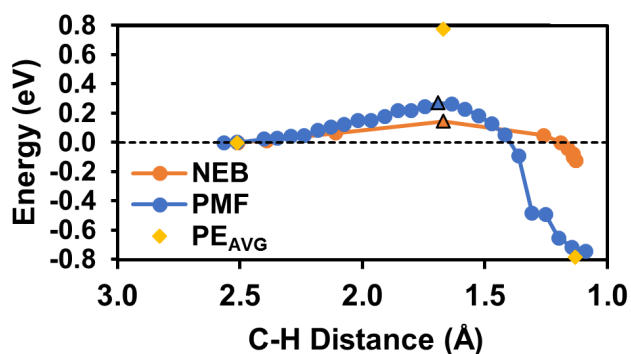


Figure D.4: The NEB energy profile, PMF free energy profile, and average unbiased potential energies from umbrella sampling windows containing the reactant, transition state, and product for reaction three.

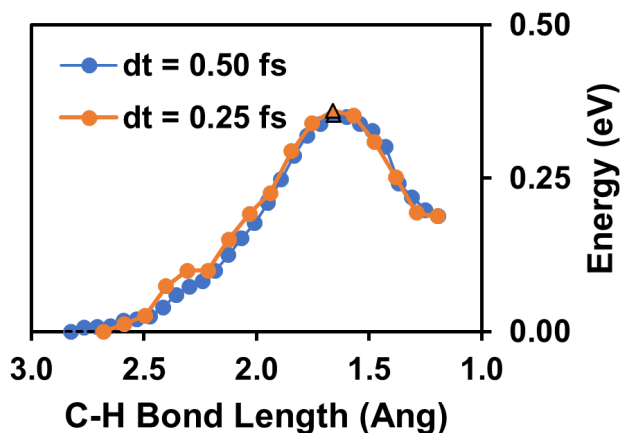


Figure D.5: Umbrella sampling energetics for Reaction 1 using an 0.5 and 0.25 fs timestep

APPENDIX E

SUPPORTING INFORMATION FOR DOPED TI OXIDES TO DEOPTIMIZE OXYGEN REDUCTION REACTION CATALYSIS

E.1 CREATING DOPED TI ALLOYS

XRD of the alloys after casting and processing is shown in Figure E.1 . For all of the cast alloys except Ti-Mn₁, the diffraction patterns indicate a single HCP phase. Shifts from the as-cast Ti HCP lattice peaks are likely due to lattice expansion or contraction due presence of the alloying additions in solid solution. In the case of Ti-Mn₁, a secondary peak is observed at 57° which indicates that there is a secondary, likely BCC phase present. In this case, the BCC phase is also a solid solution, but would have an approximately 15x higher ratio of Mn to Ti than the HCP phase.[282] There is also some texture differences between the different alloys. In particular, Ti-Sn shows a significant prevalence of the {103} orientation that is not seen in the other alloys.

E.2 METAL OXIDE X-RAY PHOTOELECTRON SPECTROSCOPY DATA

X-ray photoelectron spectroscopy (XPS) scans were performed on each of the alloys to determine composition of metal oxides natively formed on the alloy surface using the K-alpha XPS system. An Al X-ray source was used for monochromatic radiation and was focused to a 400 micron diameter spot size. Twenty high-resolution scans of the pure Ti were examined

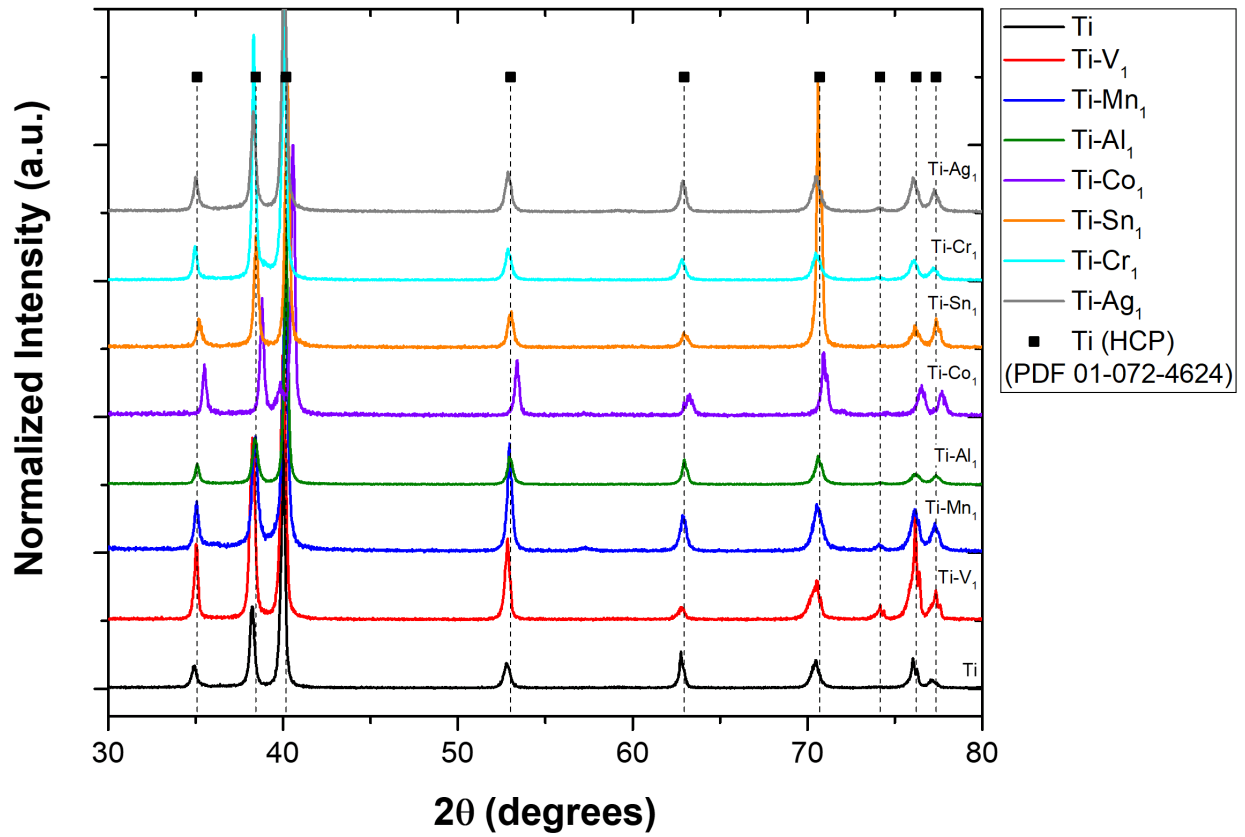


Figure E.1: X-ray diffraction spectra for each alloy after casting and machining processing.

Table E.1: Alloy and Oxide Compositions

Nominal Alloy Composition	Composition of Dopant in Oxide (at %)
Ti ₉₉ Cr ₁	6.2
Ti ₉₉ Sn ₁	2.1
Ti ₉₉ Co ₁	0.6
Ti ₉₉ V ₁	0.6
Ti ₉₉ Mn ₁	0.5
Ti ₉₉ Al ₁	1.0
Ti ₉₉ Ag ₁	1.1

to provide baseline oxide information on the native Ti oxide and 50 high-resolution scans of each alloying element were performed to maximize signal capture to aid in determining values of the dopant concentrations. Data analysis was performed using the CasaXPS software system and standard XPS references.[283, 284] All XPS data is referenced to the Au 4f_{7/2} peak at 84.0 eV. The scans of the minor component of these alloys generally yielded low signal to noise spectra due to the low dopant concentrations.

E.3 XPS CHARACTERIZATION OF SN DOPED TI OXIDE

E.4 REAXFF ANNEALING SIMULATIONS

We created amorphous TiO₂ surfaces by annealing crystalline TiO₂ slabs using the reax/c[237] implementation of ReaxFF[238] in LAMMPS.[239] All annealing simulations used the force-field parameterized by Kim and Kubicki[240] and a timestep of 1 fs. Rutile TiO₂ slabs were heated from 0 K to 1100 K at a rate of 0.06 K/fs. After 300 ps at 1100 K, we quenched the structures to 0 K at a rate of 0.05 K/fs. Increasing the initial surface size from a 1x1

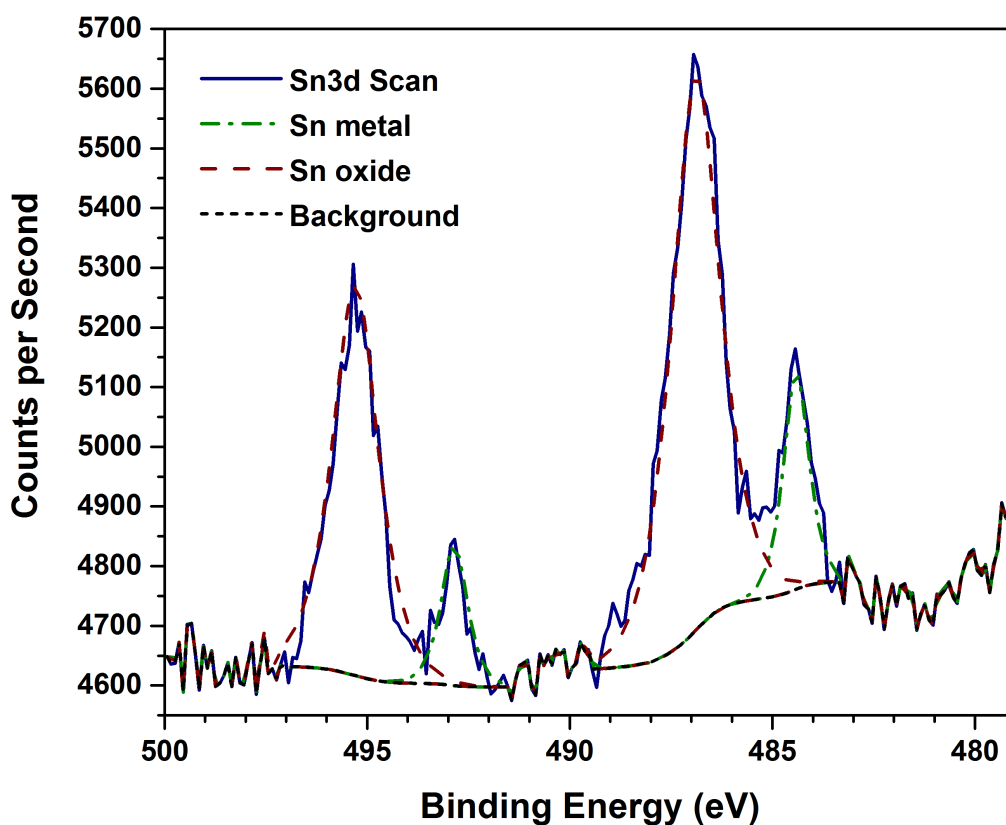


Figure E.2: Representative sample of chemical characterization of the oxides by XPS. Plot of counts per second as a function of binding energy for the oxide formed from the $\text{Ti}_{99}\text{Sn}_1$ alloy after 96 hours exposure to air.

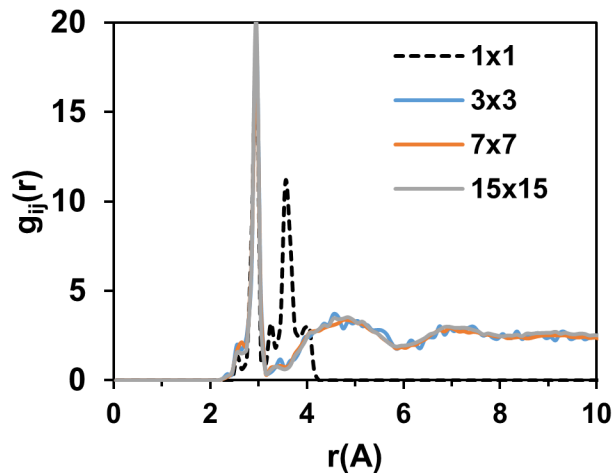
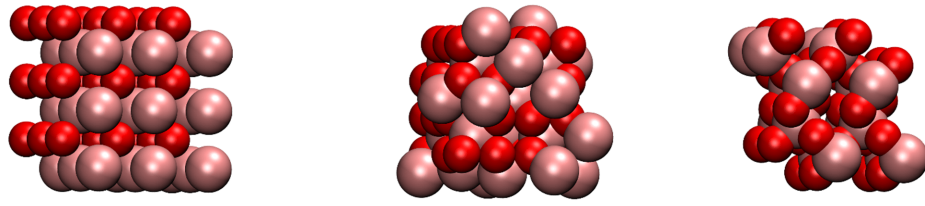


Figure E.3: The Ti-Ti pair radial distribution function for rutile TiO₂ annealed with ReaxFF in LAMMPS. The initial surfaces were supercells composed of 1x1, 3x3, 7x7, and 15x15 rutile TiO₂ unit cells. The average features of the material converge by the 3x3 simulation cell.

rutile unit cell to 3x3, 7x7, or 15x15 rutile unit cells (all three trilayers thick) shows that the features of the Ti-Ti radial distribution function (RDF) converge by the 3x3 simulation cell (Figure E.3). We use the 3x3 surface for subsequent calculations.



	MnO	Mn₂O₃	MnO₂
Mn Oxidation State	II	III	IV
Mn Charge	1.29	1.48	1.58

Figure E.4: Comparing Mn Bader charges in materials where Mn's oxidation state is well known. Benchmarking Bader charges helps determine the oxidation state of Mn in our amorphous surface.

E.5 DETERMINING DOPANT OXIDATION STATES

Determining the oxidation states of the metal dopants embedded in our model amorphous surface is an integral part to creating an accurate predictive model. Although Bader charges will not be equivalent to oxidation states, they will correlate with oxidation state.^[285, 286] We compared Bader charges of metal oxides with known oxidation states against the charges of the metal dopants embedded in our surface model to determine their oxidation states. The metal oxides and resulting Bader charges are different for each dopant, but Figure E.4 shows the structure of MnO, Mn₂O₃, and MnO₂ as well as the Mn oxidation state and Bader charge as an example.

After compiling the Bader charges for all considered dopants in Table E.2, we determined the oxidation states of the dopants in the amorphous surface as discussed previously. Originally, we incorporated metal dopants into the surface by directly replacing a Ti atom with a dopant atom. Table E.2 shows that this direct substitution results in higher dopant oxidation states than would be preferred for many dopants at the experimental conditions reported in our study (-0.8 V_{SHE}, pH 10). We modified the surface by reducing the number

of dopant-oxygen bonds to achieve lower oxidation states. For dopants that had their favored oxidation state in the unmodified surface (Al, Ga, Ge, Nb, Sc, Si, Sn, and Zn), the same charge and oxidation state are listed in both columns.

E.6 ORR INTERMEDIATE SCALING RELATIONSHIPS

Creating an activity volcano (shown in the main text) requires a relationship between the binding energies of the intermediates that limit the reaction rates. Figure E.5 shows the scaling relationship between *OOH and *OH when adsorbed to the different dopants included in this study. We attribute the relatively low R^2 to irregularities in the binding energies caused by the amorphous surface.

E.7 EFFECT OF SOLVATION ON ORR OVERPOTENTIALS

Figure E.6 shows that VASPsol solvation energies generally shifts data points to lower intermediate energies. Some dopants (such as Ti, Ag^+ , and Sn^{4+}) are shifted by 0.2-0.5 eV, while other dopants (such as V^{3+} , V^{5+} , Al^{3+} and Cr^{3+}) are much less effected. Comparing Figure E.6a and E.6b shows that this can yield larger overpotentials for dopants on the left side of the volcano plot, smaller overpotentials for dopants on the right (Si^{4+} and Sn^{4+}), or similar overpotentials for dopants near the peak (Ti and Ag^+). These comparisons show that, with the exception of Co^{2+} and Cr^{3+} , the ordering of the overpotentials calculated with PBE are in good agreement with those calculated with HSE06 and VASPsol. While solvation energies are not negligible in most cases, PBE gas phase energies appear to be a good approximation for higher level energies calculated with HSE06 and VASPsol.

Table E.2: Determining the oxidation state of metal dopants embedded in our amorphous TiO₂ surface by comparing their Bader charges to those of the dopants in metal oxides where the oxidation state is known.

	M ₂ O	MO	M ₂ O ₃	MO ₂	M ₂ O ₅	Original Surface		Modified Surface	
Oxidation State	I	II	III	IV	V	Bader Charge	Oxidation State	Bader Charge	Oxidation State
Ag	0.46	0.84	1.13	-	-	1.24	4+	0.66	1+
Al	-	2.27	2.47	2.57	-	2.45	3+	2.45	3+
Co	-	1.21	-	1.38	-	1.43	4+	1.21	2+
Cr	-	1.39	1.6	1.77	-	1.77	4+	1.59	3+
Cu	-	0.95	-	1.21	-	1.13	4+	0.96	2+
Ga	-	-	1.53	-	-	1.68	3+	1.68	3+
Ge	-	-	-	2.28	-	2.16	4+	2.16	4+
Mn	-	1.29	1.48	1.58	-	1.64	4+	1.4	2+
Nb	-	1.36	-	2.3	2.67	2.63	5+	2.63	5+
Ni	-	1.17	-	1.3	-	1.28	4+	1.09	2+
Sc	-	-	1.77	-	-	1.8	3+	1.8	3+
Si	-	-	-	1.15	-	1.06	4+	1.06	4+
Sn	-	1.10	-	2.47	-	2.34	4+	2.34	4+
V	-	1.47	-	1.86	1.91	1.91	5+	1.59	3+
Zn	-	1.18	-	-	-	1.27	2+	1.27	2+

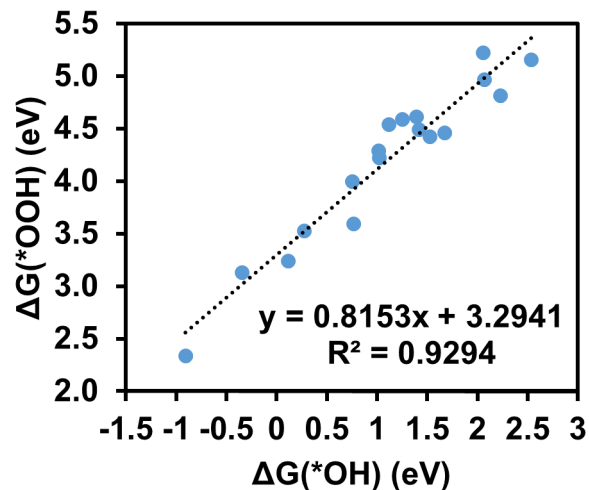


Figure E.5: The scaling relationship between the energy of OH and OOH adsorbed to dopant atoms in the amorphous surface. This correlation is used to create the volcano in the Sabatier activity volcano plots in the main text.

E.8 ORR INTERMEDIATES ADSORBED TO DOPANTS

Figure [E.7](#), [E.8](#), [E.9](#), [E.10](#), and [E.11](#) on the following pages depict the ORR intermediates ($*OOH$, $*O$, $*OH$) adsorbed to each of the studied dopants embedded in the amorphous surface.

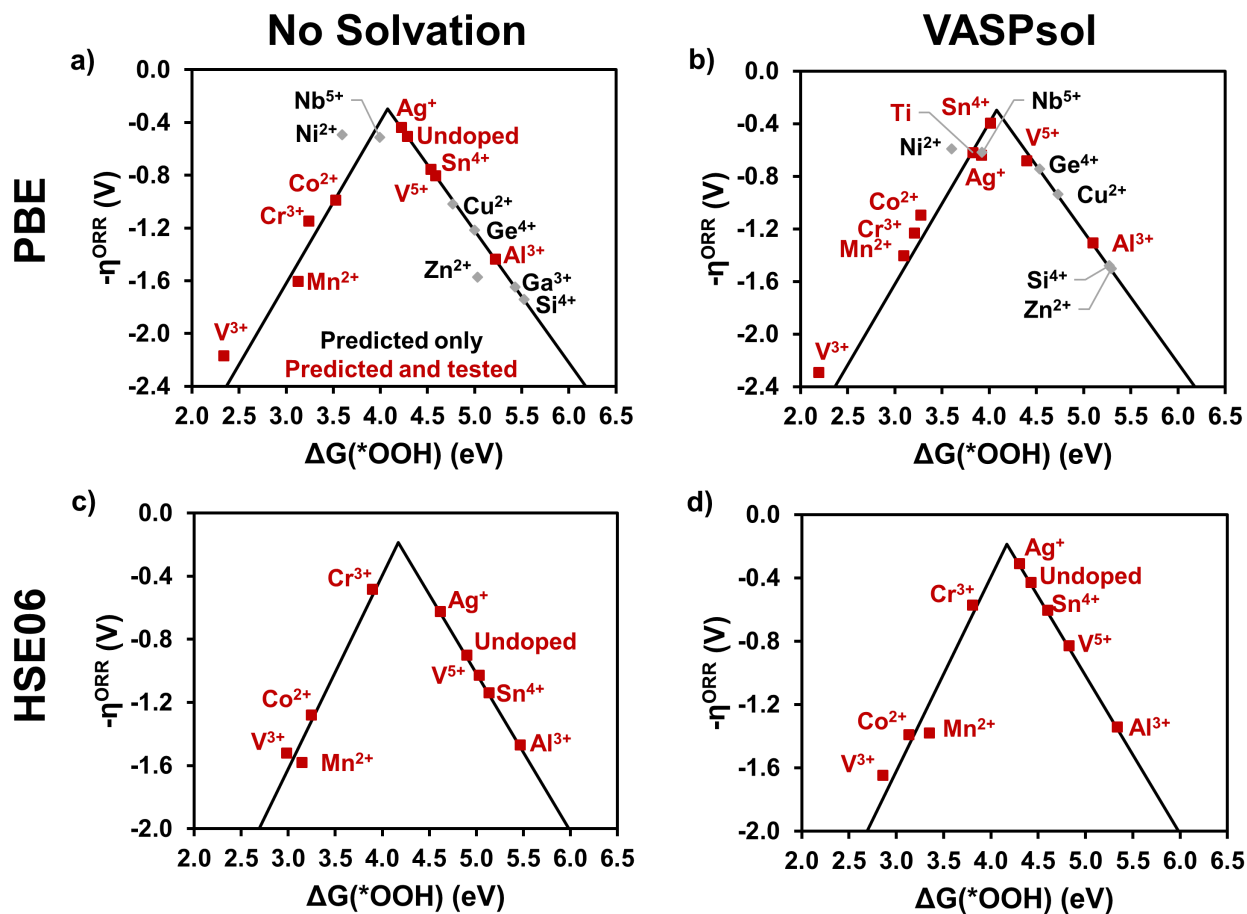


Figure E.6: Sabatier volcano plots of computationally predicted dopant overpotentials. Dopants that were predicted and tested in this work are labeled in red, and dopants not yet experimentally verified are labeled in black. Overpotentials calculated with a) PBE, b) PBE + VASPsol solvation, c) HSE06, and d) HSE06 + VASPsol solvation. Although already shown in the main text, a) and d) are shown here as a comparison.

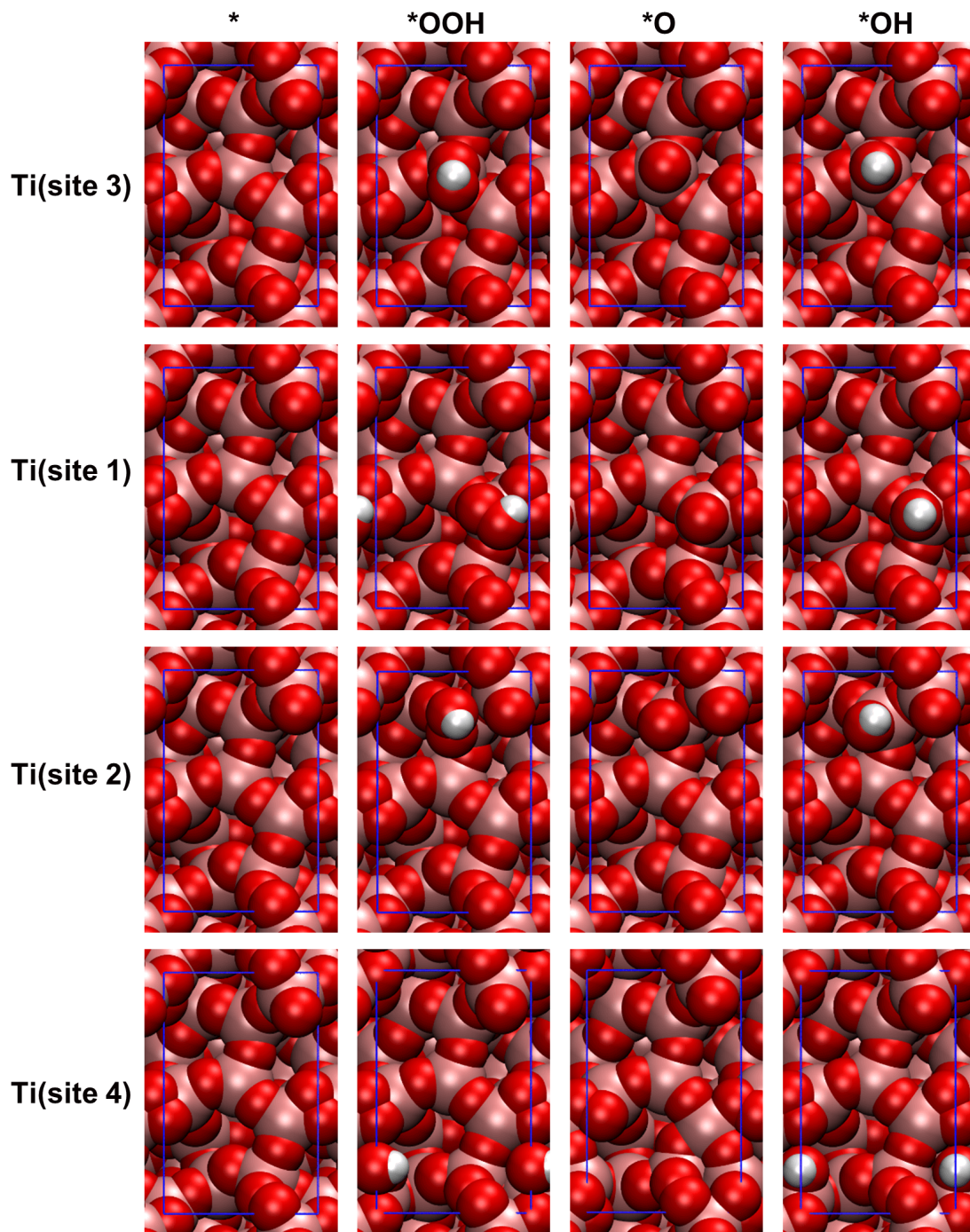


Figure E.7: Reaction intermediates adsorbed to the 4 different sites on the undoped surface. Pink spheres denote Ti atoms, red spheres atoms denote O atoms, and white spheres denote H atoms.

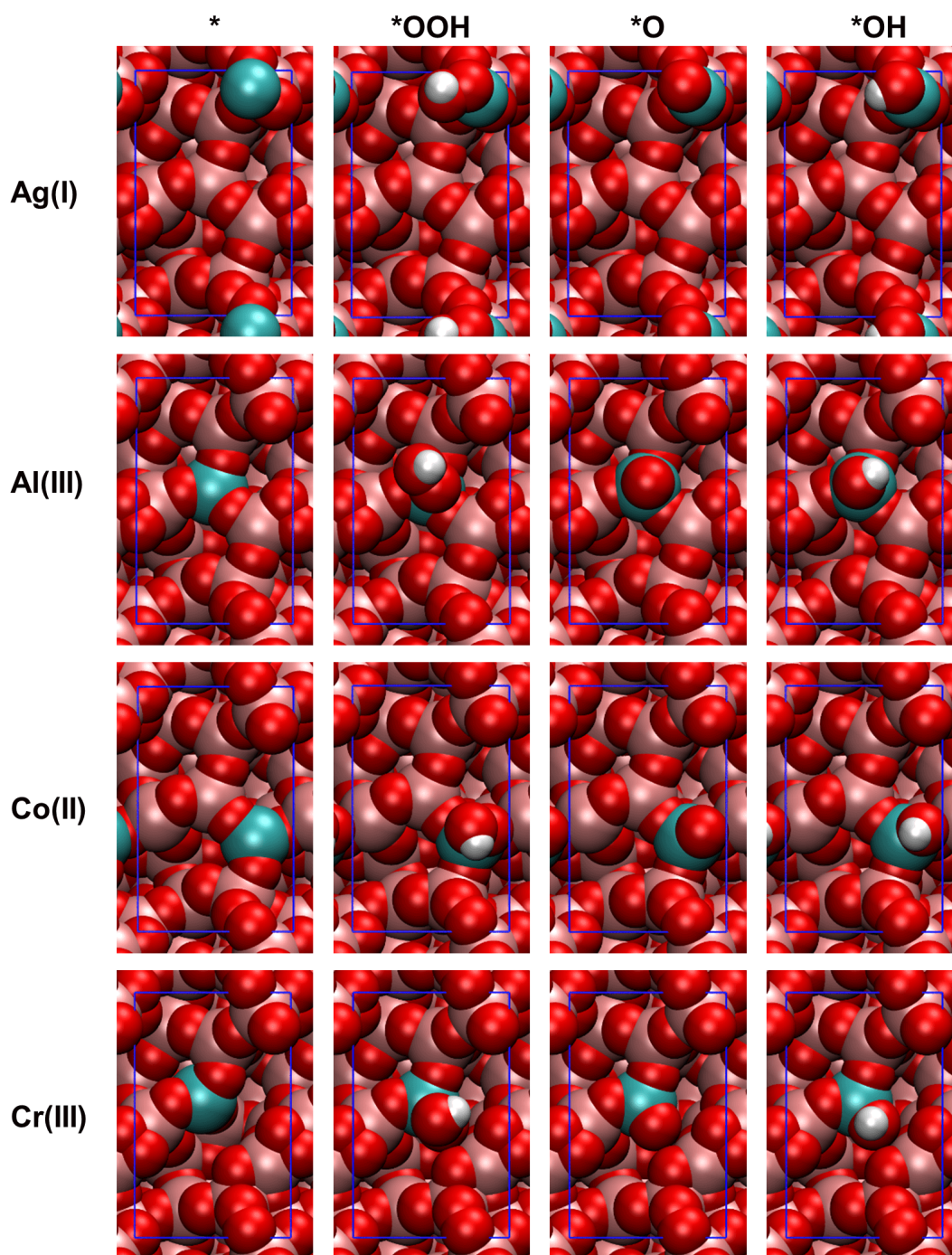


Figure E.8: ORR intermediates adsorbed to Ag^+ , Al^{3+} , Co^{2+} , and Cr^{3+} . Pink spheres denote Ti atoms, red spheres atoms denote O atoms, white spheres denote H atoms, and other colored spheres denote dopant atoms.

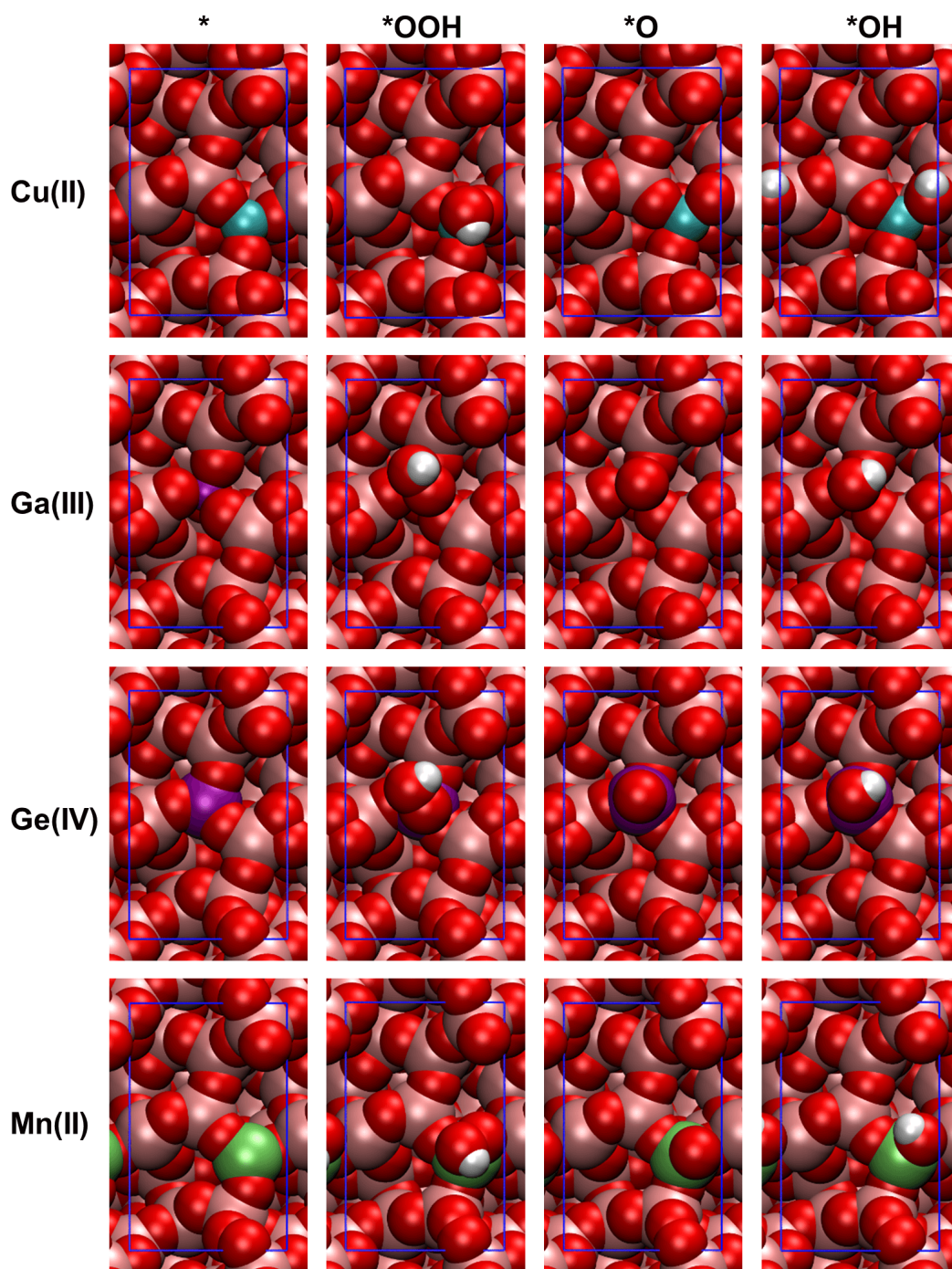


Figure E.9: ORR intermediates adsorbed to Cu^{2+} , Ga^{3+} , Ge^{4+} , and Mn^{2+} . Pink spheres denote Ti atoms, red spheres atoms denote O atoms, white spheres denote H atoms, and other colored spheres denote dopants atoms.

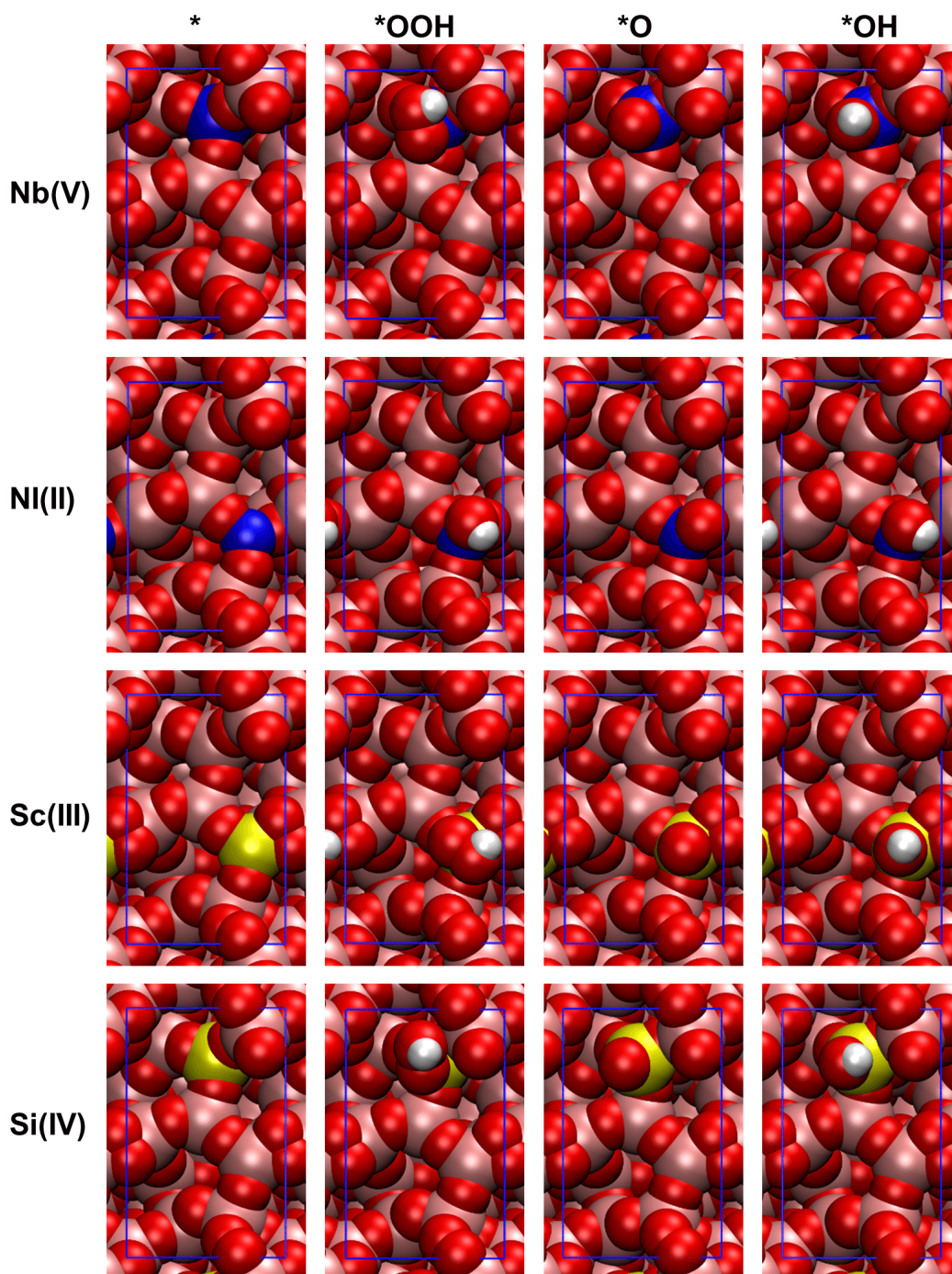


Figure E.10: ORR intermediates adsorbed to Nb^{5+} , Ni^{2+} , Sc^{3+} , and Si^{4+} . Pink spheres denote Ti atoms, red spheres atoms denote O atoms, white spheres denote H atoms, and other colored spheres denote dopant atoms.

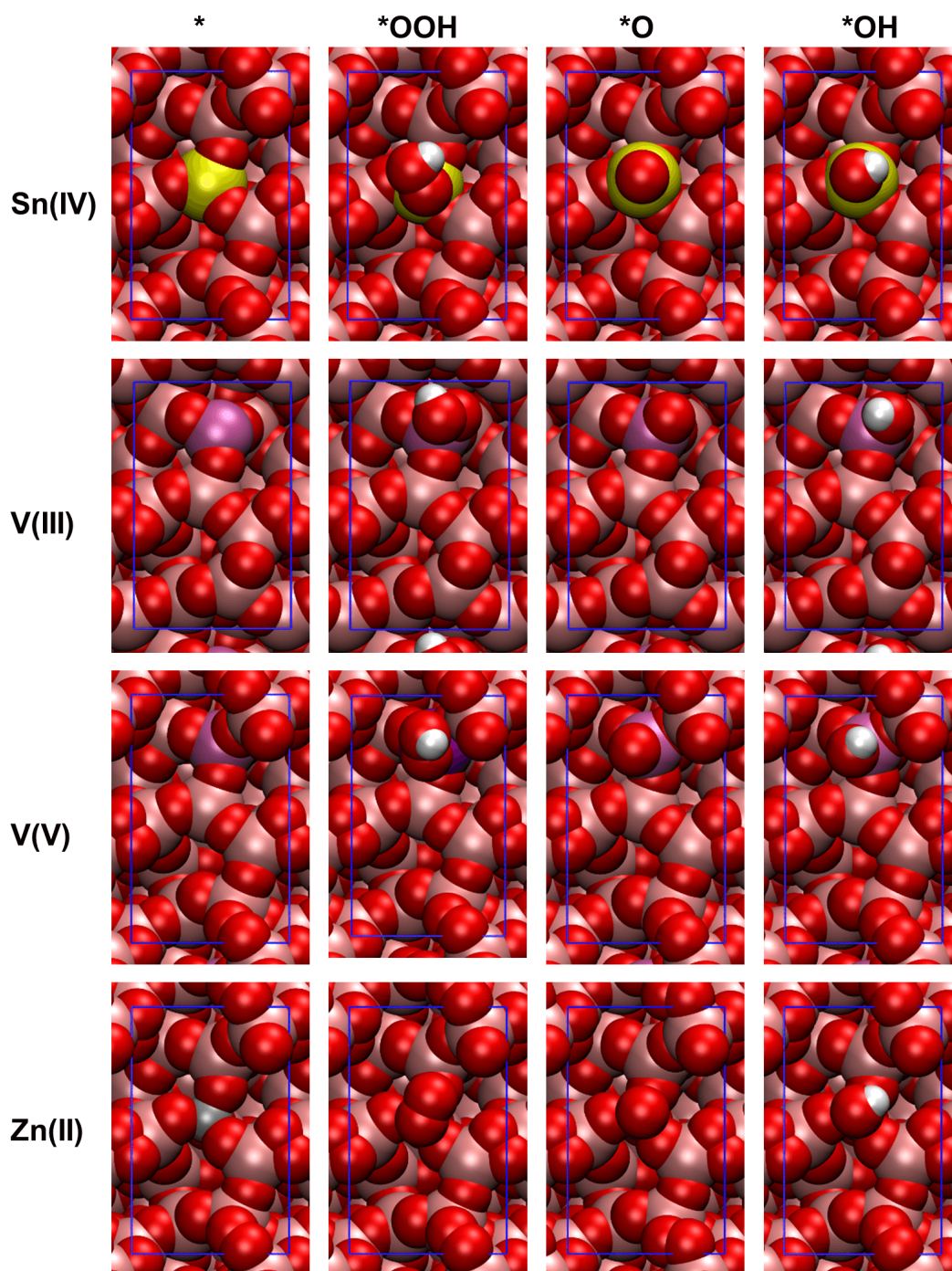


Figure E.11: ORR intermediates adsorbed to Sn^{4+} , V^{3+} , V^{5+} , and Zn^{2+} . Pink spheres denote Ti atoms, red spheres atoms denote O atoms, white spheres denote H atoms, and other colored spheres denote dopant atoms.

APPENDIX F

SUPPLEMENTARY ANALYSIS OF AVERAGE OXYGEN REDUCTION REACTION OVERPOTENTIALS

The material in this Appendix was not included in M. C. Groenenboom, R. M. Anderson, D. J. Horton, Y. Basdogan, D. F. Roeper, S. A. Policastro, and J. A. Keith, "Doped Amorphous Ti Oxides to Deoptimize Oxygen Reduction Reaction Catalysis" *J. Phys. Chem. C* 121 (2017) 16825-16830. The data presented in Figure F.1 and Table F.1 help justify several assumptions made in Chapter 5.

F.1 CALCULATING ORR OVERPOTENTIALS OF THE TWO ELECTRON ORR MECHANISM

Chapter 5 used ORR overpotentials calculated on an amorphous TiO₂ surface model to describe the reactivity trends of doped Ti oxides. The two electron ORR mechanism shown in Figure F.1a is a competing ORR mechanism that should be considered. The ORR overpotentials for the four electron ORR mechanism are determined by the *OOH binding energy, or the *OH desorption energy. The two electron ORR reaction only has a single reaction intermediate. As a result, two electron ORR overpotentials are always determined by the adsorption or desorption of *OOH.

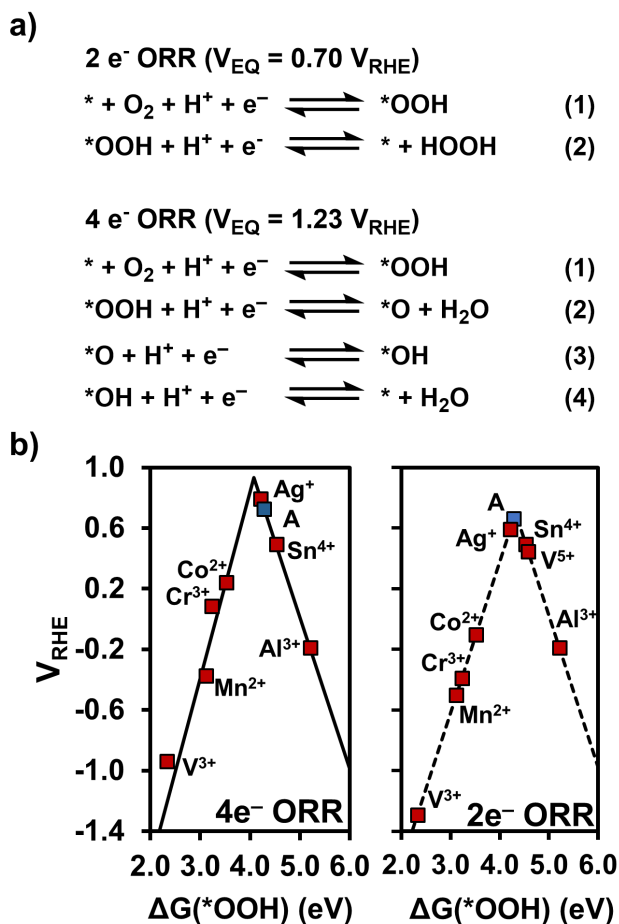


Figure F.1: a) The two electron ORR mechanism and four electron ORR mechanism. b) Comparing the four electron (left) and two electron ORR (right) mechanism thermodynamic onset potentials. "A" = the most active amorphous surface site. All energetics computed with PBE.

Figure F.1b compares the thermodynamic onset potentials of the two and four electron ORR mechanisms. The dopants that fall on the right side of the volcano plot (Sn^{4+} and Al^{3+}) have identical onset potentials. These processes are limited by the adsorption of $*\text{OOH}$ (reaction 1 in both mechanisms). The amorphous surface site occurs near the peak of the two electron ORR volcano plot. The thermodynamic onset potentials of dopants that bind $*\text{OOH}$ weaker than amorphous TiO_2 become more negative when calculated with the two

electron ORR mechanism. Although the thermodynamic onset potentials of the two electron ORR mechanism predict that V, Mn, Cr, Co, and Ag will be more effective ORR inhibitors, the majority of the ORR trends are consistent between the two mechanisms. The activity volcano plots predict that the four electron ORR mechanism would be exponentially more active (for V, Mn, Cr, Co, and Ag) or have equivalent thermodynamic onset potentials (Al, Sn, Al) compared to the two electron ORR mechanism. Because we seek to limit the maximum reactivity of the surface, we consider the trends from the four electron ORR mechanism to be more relevant.

F.2 COMPUTING AVERAGE OVERPOTENTIAL INCREASE FROM A METAL DOPANT

Chapter 5 assumed that the ability of metal dopants to inhibit the ORR activity of neighboring Ti sites would correlate with the ORR overpotential of the dopant. We showed that when amorphous TiO_2 was doped with Al^{3+} , the ORR overpotentials of the 1st and 2nd neighboring Ti sites increased from 0.50 V to 0.65 and 0.60 V, respectively. Our unit cell was not large enough to model an Al^{3+} dopant three sites away from any Ti adsorption site, so we assumed that the 3rd nearest neighboring Ti site would have an increased overpotential of approximately 0.55 V. All of these overpotential increases are significantly smaller than the 1.4 V overpotential of the Al^{3+} reaction site. Al was experimentally measured to decrease ORR activity of amorphous TiO_2 by approximately 60%. We have yet to determine if overpotential increases of 0.15, 0.10, and 0.05 V can account for an overall ORR activity decrease of 60%.

Table F.1 shows two test cases for evaluating the average ORR current decrease of an amorphous TiO_2 surface doped with Al^{3+} . The first case considers a 1% dopant concentration in the surface and subsurface of the oxide. The number of surface sites that are 1st, 2nd, and 3rd neighbors to the dopant atom were obtained by visually inspecting the surface. These calculations assume that the dopants are uniformly distributed and provide the maximum possible inhibition. We calculated the ORR current decrease relative to the undoped

material with the Butler-Volmer equation (Eq 1.6) for each type of surface atom. The maximum predicted ORR current decrease was obtained by weighting the current decrease of each surface type relative to their concentration. In this best case scenario, the maximum predicted ORR current decrease is 46%. If we assume an enrichment of Al^{3+} in the surface (up to 2%), the ORR current decrease improves from 46% to 73%. These predictions make several favorable assumptions and represent the maximum possible ORR inhibition, but they suggest that the experimentally measured ORR activity decrease caused by the presence of dopants is feasible based on our predicted ORR energetics.

Table F.1: Computing average surface ORR inhibition for an Al^{3+} dopant in amorphous TiO_2

1% Dopant in the Surface and 1% Dopant in the Subsurface			
	% of Surface Sites	Effective Overpotential (V)	ORR Current Decrease
Dopant	1	1.40	99%
1st Neighbor	6	0.65	95%
2nd Neighbor	20	0.60	86%
3rd Neighbor	35	0.55	62%
Rest	38	0.50	0%
Total	100		46%

2% Dopant in the Surface and 1% Dopant in the Subsurface			
	% of Surface Sites	Effective Overpotential (V)	ORR Current Decrease
Dopant	2	1.40	99%
1st Neighbor	10	0.65	95%
2nd Neighbor	30	0.60	86%
3rd Neighbor	58	0.55	62%
Rest	0	0.50	0%
Total	100		73%

APPENDIX G

SUPPORTING INFORMATION FOR INHIBITING THE OXYGEN REDUCTION REACTION ACTIVITY ON THE OXIDES OF TI-6AL-4V

G.1 TRAINING AND VALIDATION OF NEURAL NETWORKS

We created a dataset of 1077 TiAl_2O_5 structures from which 850 structures were selected as an initial training set. The dataset contained the coordinates, energies, and forces of 307 equation of state structures, 352 structures with stressed and strained unit cells, 124 crystalline structures with individual Ti/Al/O atoms moved within the crystalline lattice, 127 annealed surface structures, 50 annealed bulk structures, and 117 structures from surface vacancy diffusion pathways. We later added 100 amorphous surface structures to the training set. These structures were produced from crystalline surface structures that were annealed with our initial neural network. We calculated the energies of all structures using VASP and PBE as described in the computational methods section. Geometry optimizations were only performed on crystalline surface structures and the fully amorphous surfaces. Vacancy diffusion pathways were optimized with gSS-NEB optimizations.

All equation of state and unit cell stress and strain structures consisted of a single TiAl_2O_5 unit cell containing two Ti atoms, four Al atoms, and ten O atoms. All 124 structures with moved Ti, Al, or O atoms consisted of a $2 \times 2 \times 1$ supercell of TiAl_2O_5 unit cells. Annealed surfaces were periodic in the x and y directions and consisted of a $3 \times 2 \times 2$ slab of TiAl_2O_5 unit cells with 20 Å of vacuum space. Annealed bulk structures consisted of a $3 \times 2 \times 1$ supercell of TiAl_2O_5 unit cells. Vacancy diffusion pathways were located using

gSS-NEB optimizations on a 2x3 supercell of the (010) crystalline surface that was two layers thick, and a 3x2 supercell of the (001) crystalline surface that was two layers thick. All of the surface structures produced from neural network annealing simulations originated from a 3x2 supercell of a (010) crystalline surface that was two layers thick, consisted of 144 atoms, 30 Å of vacuum space, and had 9.77 x 10.85 Å surface. All of the structures, energies, and forces are provided in a json database file.

We used ~80% of the dataset to train neural networks and saved the remaining datapoints as a validation set. A uniform percentage of structures were selected from each type of data. The accuracy of a neural network can depend on number and combination of nodes and hidden layers. We trained four neural networks with different combinations of nodes and hidden layers (shown in Table G.1) to find the neural network architecture that provided the best fit to our DFT data. For the systems reported here, the neural network with four hidden layers composed of six, five, five, and three nodes (Type three in Table G.1) always provided the best fit to the training and validation sets. Table G.2 shows the error per formula unit for neural network one (NN1) and neural network two (NN2) for the training and validation sets. The average error, mean unsigned error, and standard deviation for the validation set is always similar or smaller than those of the training set. This indicated that our neural networks are not overfit for these types of structures. NN1 and NN2 were both composed of four hidden layers with six, five, five, and three nodes. NN1 is the best neural network that was trained to only crystalline TiAl_2O_5 structures, and NN2 is the best neural network that was trained to crystalline and amorphous TiAl_2O_5 structures.

The error for amorphous surfaces is significantly larger than the error of the bulk crystalline structures and structures annealed with DFT (2-3x larger for NN2 and 13-14x larger for NN1). This is expected because our initial training set contained no amorphous surface structures. Fortunately, the addition of amorphous structures to the dataset significantly improved the ability of NN2 to model these structures (decreasing the error by more than 50%). This suggests that we could approach the same level of accuracy that was achieved for the other types of TiAl_2O_5 structures if we incorporated more amorphous structures into the training set.

Table G.1: The combinations nodes in each hidden layer that were used to train neural networks

Hidden Layer	Nodes			
	Type 1	Type 2	Type 3	Type 4
1	6	6	6	7
2	5	5	5	4
3	3	5	5	4
4		3	5	3
5			3	

Figures G.1 and G.2 show the errors between the neural network energies and DFT energies for different types of bulk crystalline TiAl_2O_5 structures computed with neural network one and two. Although the exact fit is different for each neural network, there is a similar overall distribution of data. This is in agreement with the statistics shown in Table G.2. The accuracy of NN1 and NN2 for these types of surface structures could not be reduced without increasing the cutoff radius of the symmetry functions that describe the local atomic environments. Increasing the cutoff radius corresponded to dramatic increases in computational cost, especially when calculating atomic forces.

Figure G.3 shows the error distribution of annealed surfaces and bulk structures for neural network one and two. Again, the error and distribution of each neural network is similar, but the addition of amorphous structures into the training set of neural network two slightly improves the ability of the neural network to represent some annealed surfaces. No vacancy diffusion pathways are compared in Figures G.1, G.2, or G.3. Our dataset contained more than 100 data points from 13 different surface vacancy diffusion pathways. Nine images from each pathway were not sufficient for NN1 to recreate the diffusion energetics, so we excluded the diffusion structures from the training set of NN2. The absence of diffusion pathway structures did not negatively affect the fit of any other structures with NN2.

Table G.2: The average error, mean unsigned error (mue), and standard deviation for portions of the training and validation sets.

Error (meV/atom)				
Amorphous Surfaces				
	NN2	NN2	NN1	NN1
	Training	Validation	Training	Validation
Average	-12.8	-21.3	NA	-70.0
MUE	14.8	21.3	NA	70.0
St. Dev.	15.1	12.6	NA	32.3
Annealed Surface and Bulk Structures				
	NN2	NN2	NN1	NN1
	Training	Validation	Training	Validation
Average	5.4	0.3	6.6	4.7
MUE	5.7	2.9	6.7	4.9
St. Dev.	6.7	3.5	7.5	5.9
Bulk Crystalline Structures				
	NN2	NN2	NN1	NN1
	Training	Validation	Training	Validation
Average	-0.1	-1.6	0.1	0.3
MUE	10.7	9.2	12.9	10.9
St. Dev.	16.6	16.0	19.9	17.4

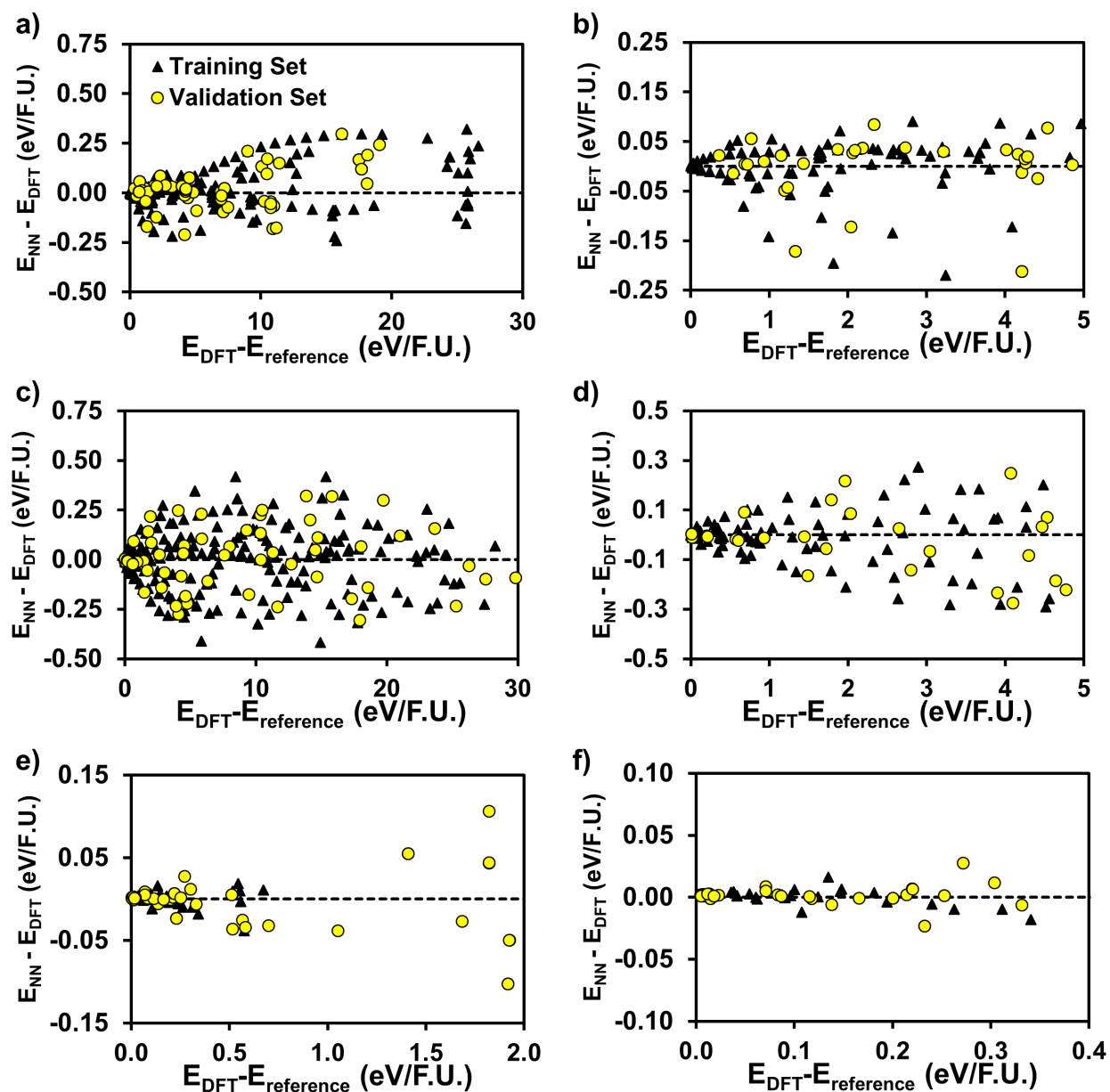


Figure G.1: The error in the training and validation set for neural network one for a) and b) all equation of state data, c) and d) independent stresses on each unit cell vector, and e) and f) moving individual Ti, Al, and O atoms in the x, y, and z directions within a crystalline supercell. All energies are referenced against that of the crystalline material.

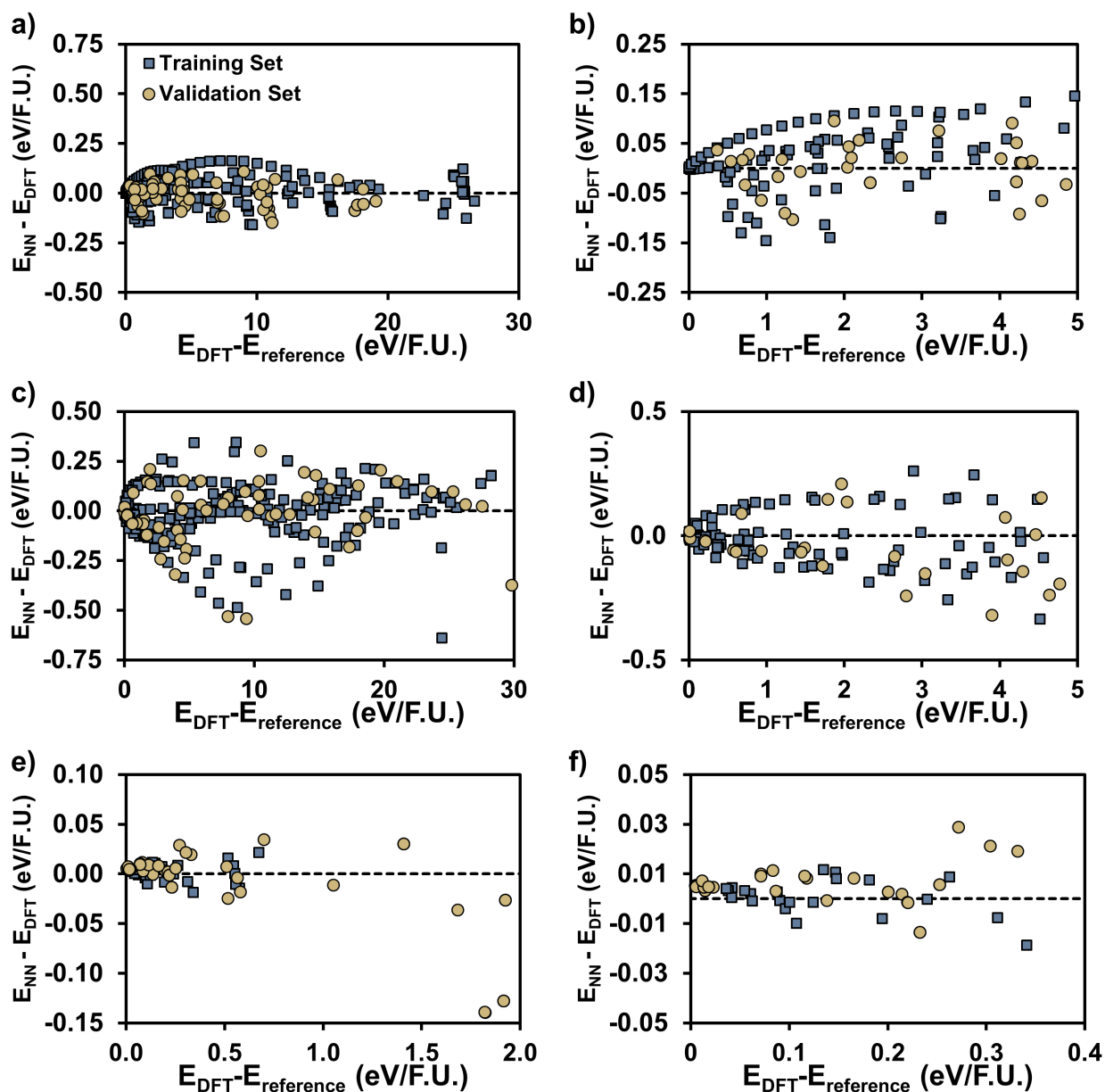


Figure G.2: The error in the training and validation set for neural network two for a) and b) all equation of state data, c) and d) independent stresses on each unit cell vector, and e) and f) moving individual Ti, Al, and O atoms in the x, y, and z directions within a crystalline supercell. All energies are referenced against that of the crystalline material.

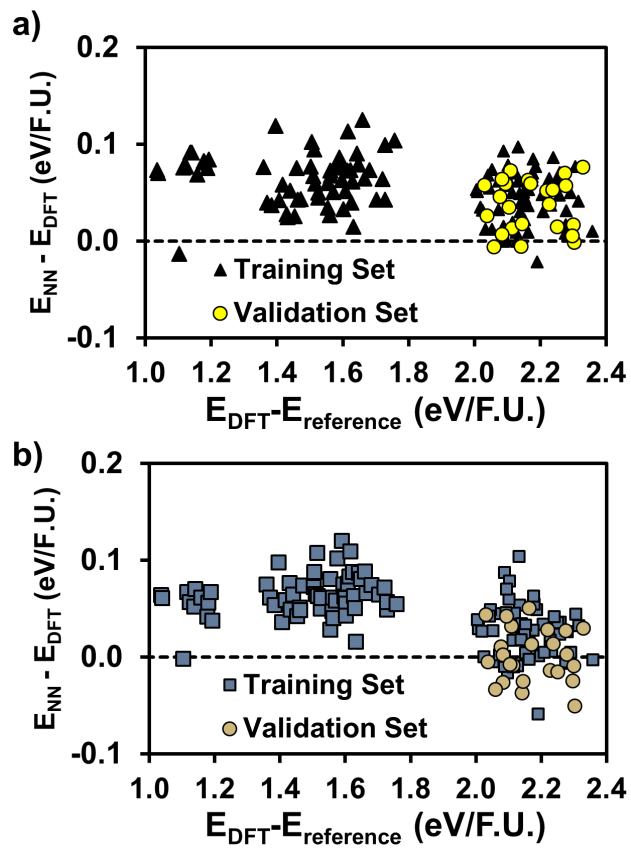


Figure G.3: The error in the training and validation set for annealed bulk structures computed with a) neural network one and b) neural network two. All energies are referenced against that of the crystalline material.

G.2 CREATING ACCURATE SURFACE MODELS

Figure G.4 compares the energies of crystalline surfaces, defective crystalline surfaces, and amorphous surfaces computed with NN1 and DFT. The defective and amorphous surfaces were obtained from annealing simulations with NN1. While NN1 matches the relative trend of the crystalline and defective surfaces (zones I and II), NN1 has large errors for the amorphous surface structures. NN1 was not trained to any amorphous structural data, so this is not surprising. The DFT energetics suggest that the amorphous surfaces found by these annealing simulations are too unstable to form at temperatures near 300 K.

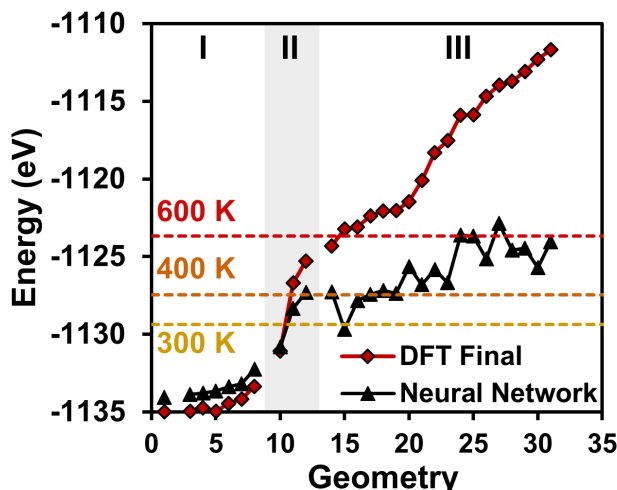


Figure G.4: A comparison of neural network and DFT energies for surface structures annealed and quenched with NN1. Zone I = crystalline surfaces with swapped Ti/Al atoms, II = surface defects, III = amorphous surface structures. The 300, 400, and 600 K lines correspond to the kinetic energy present at each temperature added to the energy of the relaxed (010) crystalline surface ($E = -1134.97$ eV).

Figure G.5 shows the Ti/Al/O-Ti/Al/O and Ti-Ti/Al radial distribution functions (RDFs) of 4 different amorphous structures that were annealed and quenched with NN1. The RDFs show that the structures produced by NN1 do not significantly change after being fully relaxed with DFT. While the exact height and location of the peaks shift, the general structure

is preserved. These changes are most noticeable in the Ti-Ti/Al RDF. The agreement between the peaks at $r < 4 \text{ \AA}$ shows that structures obtained with NN1 are highly similar to those that would be predicted by DFT. The total RDFs (Ti/Al/O-Ti/Al/O) appear similar, while the Ti-Ti/Al RDFs can be used to differentiate the amorphous surface structures. A real amorphous TiAl_2O_5 surface would likely have a Ti-Ti/Al RDF that is an average of many small amorphous surface segments that are contained in our amorphous surface models.

Neural networks can be continuously refined with the addition of more training data. Figure G.6 shows the energies of surfaces annealed (G.6a and G.6c) and quenched (G.6b and G.6d) from two separate annealing simulations compared against energies calculated with DFT. Although there is not perfect agreement between the NN2 and DFT energies, the addition of 100 additional amorphous structures to the training set significantly improved the relative energy trends over what was observed with NN1 (see Figure G.4). In theory, structures created with NN2 could be incorporated into the training set, and a third neural network would be even more accurate when modeling amorphous surfaces. This feedback loop could be used to create neural networks that can accurately model complex surfaces at a much lower computational cost than currently possible with DFT alone.

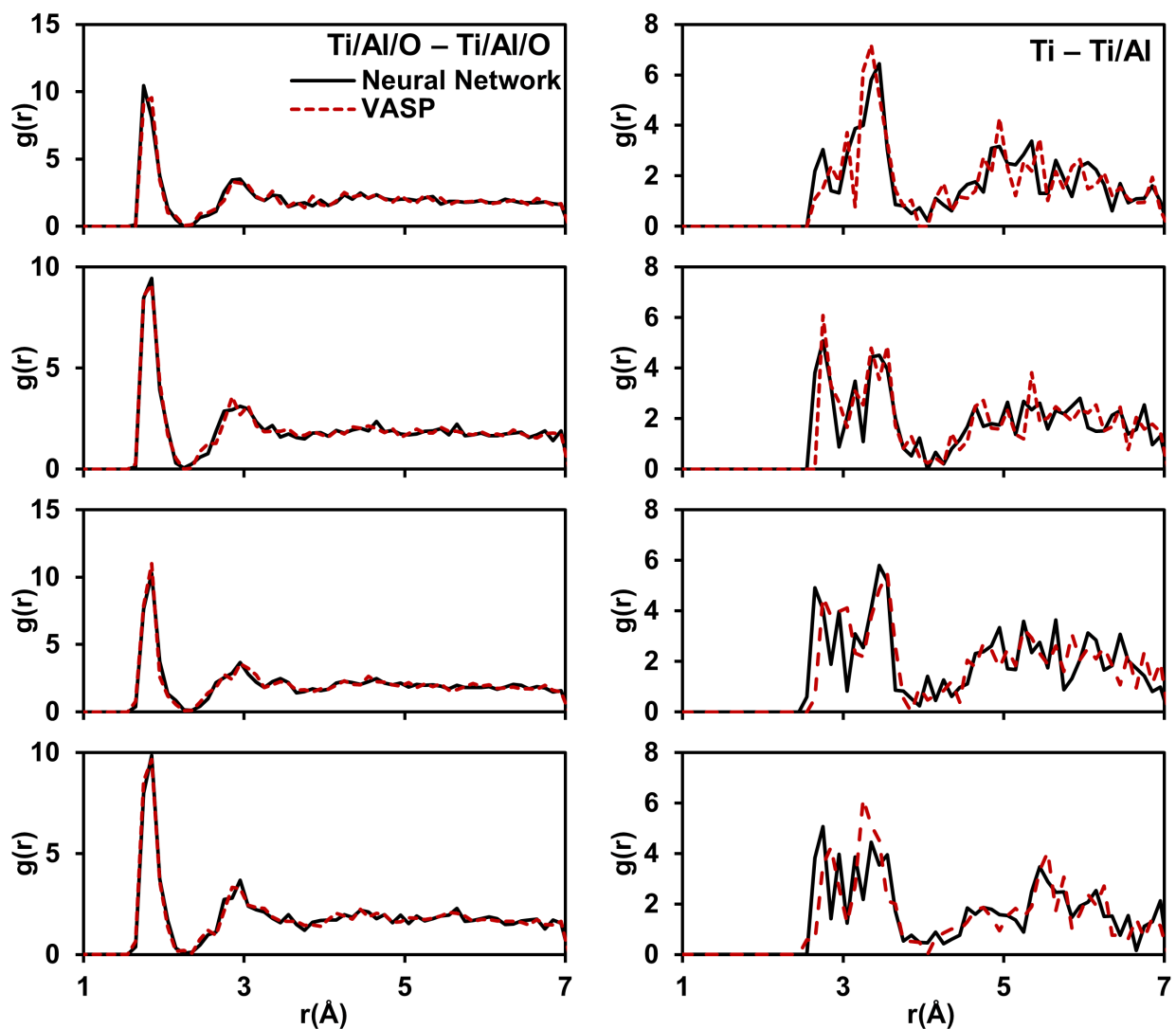


Figure G.5: The Ti/Al/O-Ti/Al/O and Ti-Al/Ti RDFs for four different annealed structures. Each structure was fully relaxed with DFT (PBE) after being annealed and quenched using a neural network. The Ti-Ti/Al radial distribution function shows the variety of different structures that can be observed with annealing simulations.

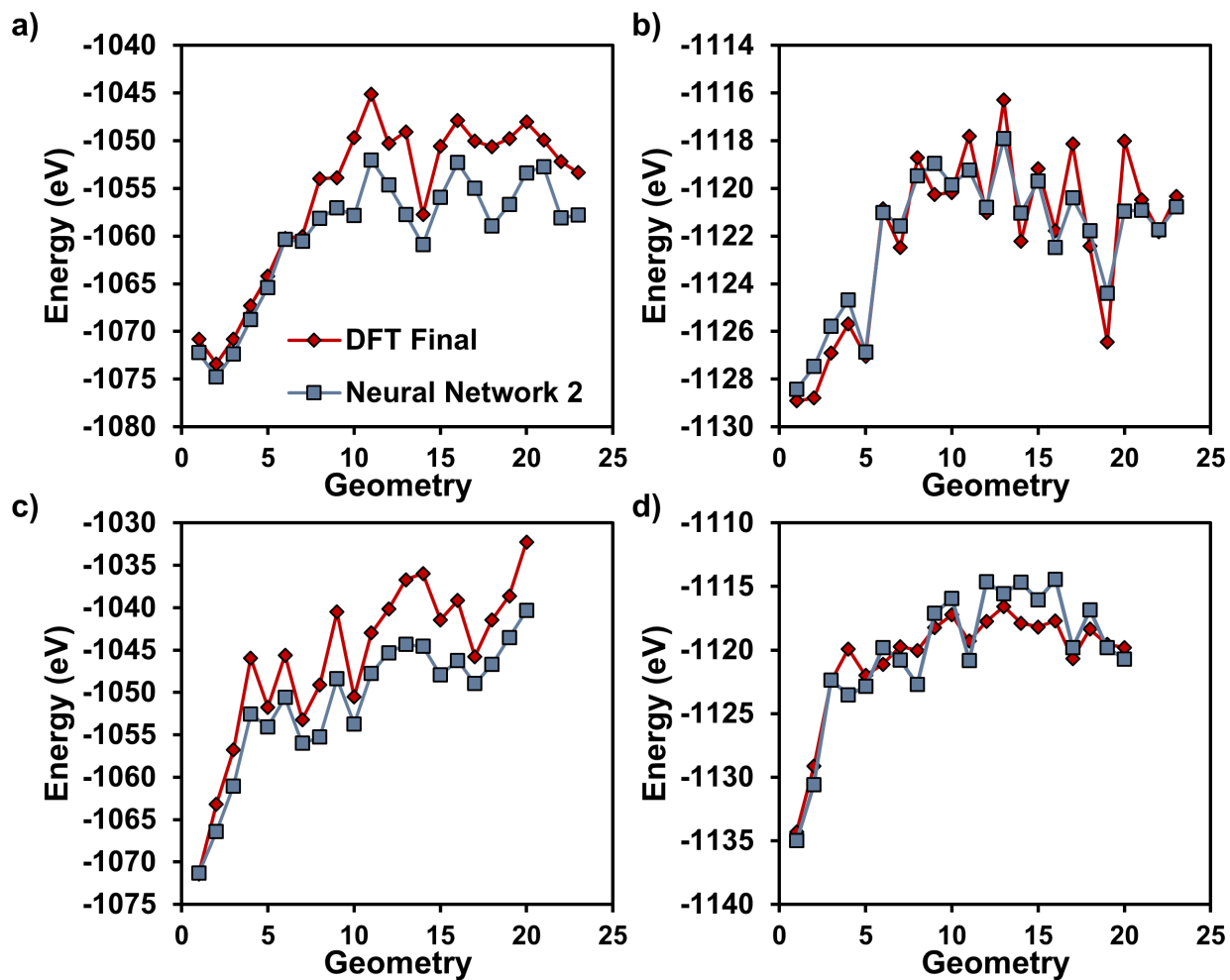


Figure G.6: a) and c) The neural network and DFT energies computed during on structures obtained from MD simulations using neural network two. b) and d) The neural network and DFT energies computed on fully quenched structures obtained from MD simulations using neural network two.

G.3 CALCULATING ORR OVERPOTENTIALS

We selected the 6 surface models shown in Figure G.7 to characterize the atomic scale factors that affect the ORR activity of TiAl_2O_5 surfaces. These surfaces were selected to compare how surfaces with increasing concentrations of structural defects could affect the ORR activity of an oxide catalyst. We hypothesized that minor defects (such as the crystalline surfaces with swapped Ti/Al atoms) would have similar reactivity to the crystalline surface, while larger defects would result in activities that converged to those of the fully amorphous oxide surface.

Many multi-step electrochemical reactions can have their maximum activity limited by scaling relationships between the binding energies of reaction intermediates adsorbed to the catalyst surface. Figure G.8 shows the scaling relationship between $^*\text{OOH}$ and $^*\text{OH}$ bound to doped and undoped surface sites in our crystalline and amorphous TiAl_2O_5 surfaces. This correlation is responsible for estimating the left side of the activity volcano when ORR overpotentials are plotted as a function of the binding energy of $^*\text{OOH}$ to the surface. The imperfect correlation causes certain surface sites to not fall directly on the predicted activity volcano.

While crystalline surface models may only have one or two unique reaction sites, defective and amorphous surface models have a larger number of unique adsorption sites. The surfaces shown in Figure G.7 have a number of unique reaction sites, and it is important to understand how ORR activity can vary on a site-by-site basis. Figure G.9 shows the distributions of ORR overpotentials for each surface shown in Figure G.7 as computed with HSE06. The amorphous surface (Figure G.9a) and defect B (Figure G.9b) have a much wider variance of activity than surfaces with fewer defects. These surfaces are predicted to have relatively similar gas and solvent phase ORR activity, while solvation corrections significantly affect the reactivity of the crystalline materials. As discussed in the main text, the more stable surfaces are less effective ORR catalysts. These trends are mirrored by the overpotentials of each surface predicted with PBE (see Figure G.10).

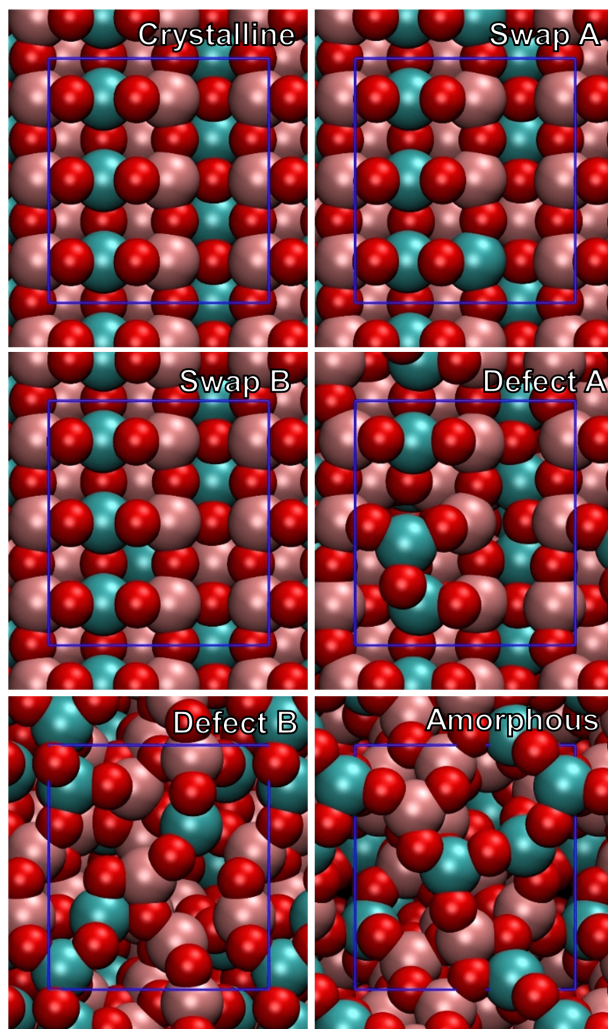


Figure G.7: The low energy (010) crystalline surface, two (010) crystalline surfaces with swapped Ti/Al atoms, two defective surfaces produced by annealing simulations, and the lowest energy amorphous surface located from an annealing simulation.

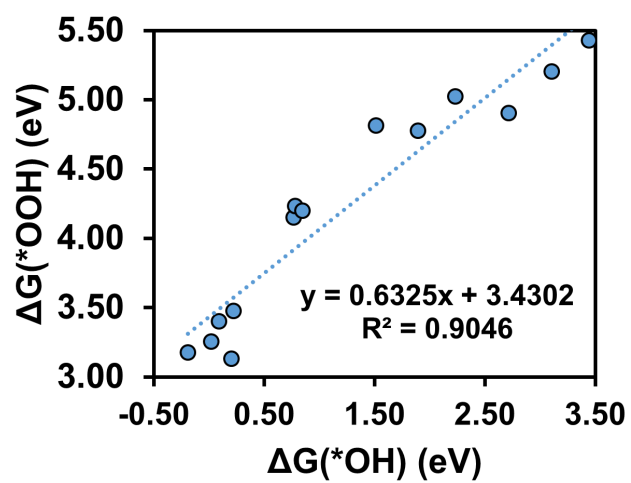


Figure G.8: The scaling relationship between *OOH and *OH on the doped TiAl_2O_5 surfaces.

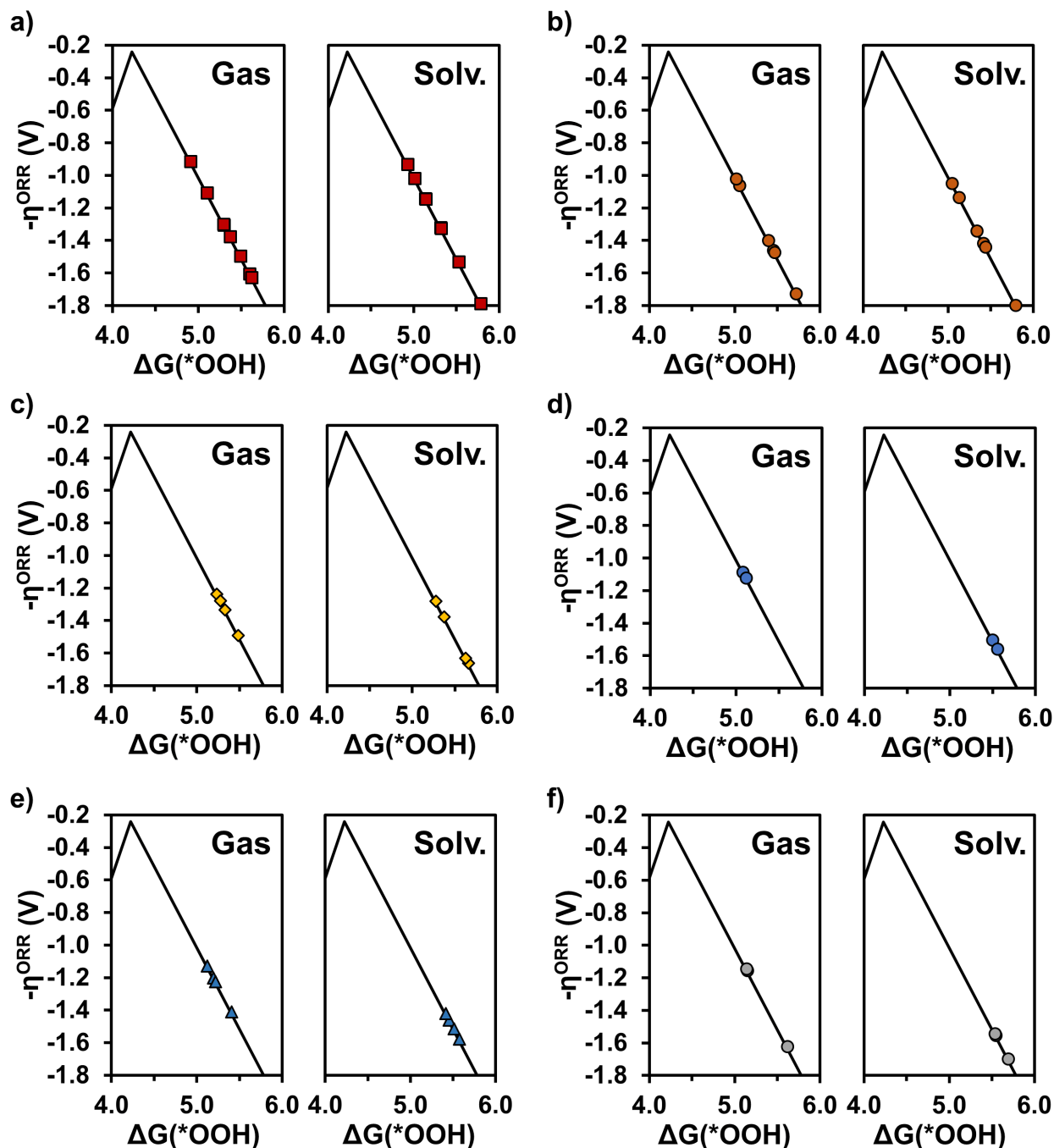


Figure G.9: The ORR overpotentials for all potential reaction sites on the a) Amorphous, b) Defect B, c) Defect A, d) Swap B, e) Swap A, and f) Crystalline TiAl_2O_5 surfaces. All overpotentials are computed from HSE06 energy calculations on structures optimized with PBE.

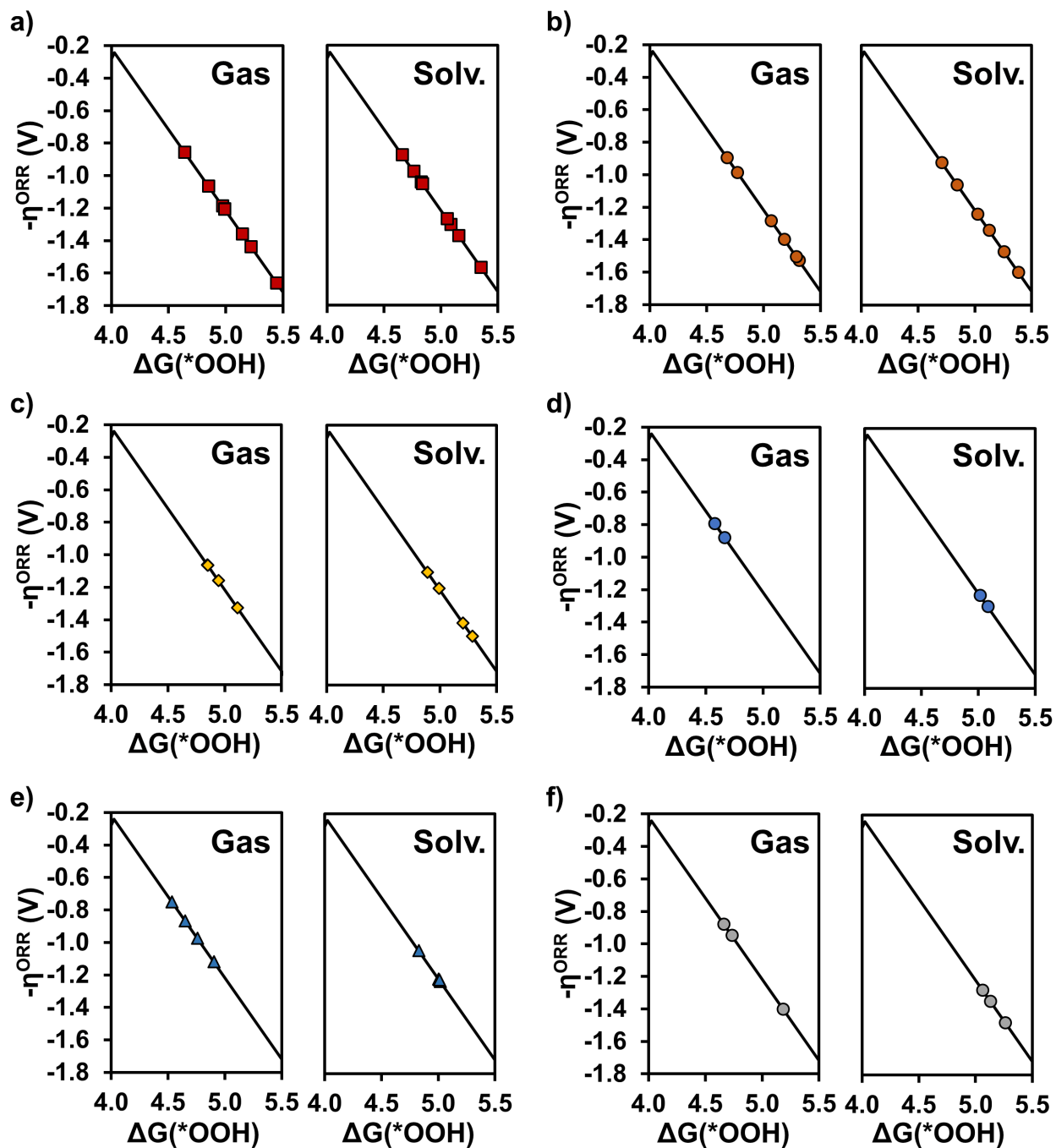


Figure G.10: The ORR overpotentials for all potential reaction sites on the a) Amorphous, b) Defect B, c) Defect A, d) Swap B, e) Swap A, and f) Crystalline TiAl_2O_5 surfaces. All overpotentials are computed from PBE energies.

G.4 DETERMINING DOPANT OXIDATION STATES

Accurately modeling dopants in the TiAl_2O_5 surface requires modeling the correct dopant oxidation state. Replacing a Ti^{4+} or Al^{3+} in the surface biases the dopant toward the oxidation state of the atom that it replaced. This is not always the correct oxidation state for the dopant at experimentally relevant conditions. To estimate the oxidation states of each dopant, we performed a bader charge analysis. We estimated the oxidation state of each dopant by comparing the bader charges of metal dopants against bader charges of each dopant in a material where their oxidation states were known. In many cases, we replaced Ti^{4+} or Al^{3+} with dopants that should be either 4+ or 3+ to easily achieve the desired oxidation state. Other dopants, like Mn^{2+} and CO^{2+} , required surface modifications to reach their desired oxidation states. Table G.3 shows the bader charges of each dopant in the crystalline and amorphous surfaces. We previously used this approach to successfully model the effect of dopants incorporated into TiO_2 .

Table G.3: Determining the oxidation states of metal dopants by comparing Bader charges.

	MO	M₂O₃	MO₂	M₂O₅
Co	1.21	-	1.38	-
Cr	1.39	1.60	1.77	-
Ga	-	1.58	-	-
Mn	1.29	1.48	1.58	-
Nb	1.36	-	2.30	2.67
Si	-	-	3.22	-
Sn	1.10	-	2.34	-
Crystalline Surface			Modified Crystalline Surface	
	Charge	Ox. State	Charge	Ox. State
Co	1.50	4+	1.09	2+
Cr	1.60	3+	-	-
Ga	1.70	3+	-	-
Mn	1.65	4+	1.31	2+
Nb	2.64	5+	-	-
Si	3.08	4+	-	-
Sn	2.16	4+	-	-
Amorphous Surface			Modified Amorphous Surface	
	Charge	Ox State.	Charge	Ox. State
Co	1.54	4+	1.09	2+
Cr	1.72	3+	-	-
Ga	1.66	3+	-	-
Mn	1.68	4+	1.36	2+
Nb	2.64	5+	-	-
Si	3.15	4+	-	-
Sn	2.18	4+	-	-

BIBLIOGRAPHY

- [1] G. A. Olah, A. Goepfert, and G. K. S. Prakash, “Fossil Fuels and Climate Change,” in *Beyond Oil and Gas: The Methanol Economy*, pp. 77–89, Wiley-VCH Verlag GmbH & Co. KGaA, 2009.
- [2] M. Aresta, “Carbon Dioxide: Utilization Options to Reduce its Accumulation in the Atmosphere,” in *Carbon Dioxide as Chemical Feedstock*, pp. 1–13, Weinheim, Germany: Wiley-VCH Verlag GmbH & Co. KGaA, 2010.
- [3] E. A. Quadrelli, G. Centi, J.-L. Duplan, and S. Perathoner, “Carbon Dioxide Recycling: Emerging Large-Scale Technologies with Industrial Potential,” *ChemSusChem*, vol. 4, no. 9, pp. 1194–1215, 2011.
- [4] M. A. Bender, T. R. Knutson, R. E. Tuleya, J. J. Sirutis, G. A. Vecchi, S. T. Garner, and I. M. Held, “Modeled Impact of Anthropogenic Warming on the Frequency of Intense Atlantic Hurricanes,” *Science*, vol. 327, no. 5964, pp. 454–458, 2010.
- [5] H. Le Treut, R. Somerville, U. Cubasch, Y. Ding, C. Mauritzen, A. Mokssit, T. Peterson, and M. Prather, “Historical Overview of Climate Change,” in *Climate Change 2007: The Physical Science Basis. Contribution of Working Group I to the Fourth Assessment Report of the Intergovernmental Panel on Climate Change* (S. Solomon, D. Qin, M. Manning, Z. Chen, M. Marquis, K. Averyt, M. Tignor, and H. Miller, eds.), Cambridge, United Kingdom and New York, NY, USA: Cambridge University Press, 2007.
- [6] U.S. Energy Information Administration, “Annual Energy Outlook 2017 with projections to 2050,” tech. rep., EIA, 2017.
- [7] G. A. Olah, G. K. S. Prakash, and A. Goepfert, “Anthropogenic Chemical Carbon Cycle for a Sustainable Future,” *J. Am. Chem. Soc.*, vol. 133, no. 33, pp. 12881–12898, 2011.
- [8] K. Z. House, A. C. Baclig, M. Ranjan, E. A. van Nierop, J. Wilcox, and H. J. Herzog, “Economic and energetic analysis of capturing CO₂ from ambient air,” *Proc. Natl. Acad. Sci. USA*, vol. 108, no. 51, pp. 20428–20433, 2011.

- [9] Y. Izumi, "Recent advances in the photocatalytic conversion of carbon dioxide to fuels with water and/or hydrogen using solar energy and beyond," *Coord. Chem. Rev.*, vol. 257, no. 1, pp. 171 – 186, 2013.
- [10] N. S. Lewis and D. G. Nocera, "Powering the planet: chemical challenges in solar energy utilization.," *Proc. Natl. Acad. Sci. USA*, vol. 103, pp. 15729–35, 10 2006.
- [11] M. W. Keller, G. J. Schut, G. L. Lipscomb, A. L. Menon, I. J. Iwuchukwu, T. T. Leuko, M. P. Thorgersen, W. J. Nixon, A. S. Hawkins, R. M. Kelly, and M. W. W. Adams, "Exploiting microbial hyperthermophilicity to produce an industrial chemical, using hydrogen and carbon dioxide," *Proc. Natl. Acad. Sci. USA*, vol. 110, no. 15, pp. 5840–5845, 2013.
- [12] S. Licht, B. Wang, and H. Wu, "STEPA Solar Chemical Process to End Anthropogenic Global Warming. II: Experimental Results," *J. Phys. Chem. C*, vol. 115, no. 23, pp. 11803–11821, 2011.
- [13] H. Yin, X. Mao, D. Tang, W. Xiao, L. Xing, H. Zhu, D. Wang, and D. R. Sadoway, "Capture and electrochemical conversion of CO₂ to value-added carbon and oxygen by molten salt electrolysis," *Energy Environ. Sci.*, vol. 6, no. 5, pp. 1538–1545, 2013.
- [14] T. W. Woolerton, S. Sheard, Y. S. Chaudhary, and F. A. Armstrong, "Enzymes and bio-inspired electrocatalysts in solar fuel devices," *Energy Environ. Sci.*, vol. 5, no. 6, pp. 7470–7490, 2012.
- [15] A. M. Appel, J. E. Bercaw, A. B. Bocarsly, H. Dobbek, D. L. DuBois, M. Dupuis, J. G. Ferry, E. Fujita, R. Hille, P. J. A. Kenis, C. A. Kerfeld, R. H. Morris, C. H. F. Peden, A. R. Portis, S. W. Ragsdale, T. B. Rauchfuss, J. N. H. Reek, L. C. Seefeldt, R. K. Thauer, and G. L. Waldrop, "Frontiers, Opportunities, and Challenges in Biochemical and Chemical Catalysis of CO₂ Fixation," *Chem. Rev.*, vol. 113, pp. 6621–6658, 8 2013.
- [16] J.-H. Jeoung and H. Dobbek, "Carbon Dioxide Activation at the Ni₂Fe-Cluster of Anaerobic Carbon Monoxide Dehydrogenase," *Science*, vol. 318, no. 5855, pp. 1461–1464, 2007.
- [17] T. Spatzal, M. Aksoyoglu, L. Zhang, S. L. A. Andrade, E. Schleicher, S. Weber, D. C. Rees, and O. Einsle, "Evidence for Interstitial Carbon in Nitrogenase FeMo Cofactor," *Science*, vol. 334, no. 6058, p. 940, 2011.
- [18] Y. Oh and X. Hu, "Organic molecules as mediators and catalysts for photocatalytic and electrocatalytic CO₂ reduction," *Chem. Soc. Rev.*, vol. 42, no. 6, pp. 2253–2261, 2013.
- [19] C. Costentin, M. Robert, and J.-M. Savéant, "Catalysis of the electrochemical reduction of carbon dioxide," *Chem. Soc. Rev.*, vol. 42, pp. 2423–2436, 2 2013.

- [20] E. E. Benson, C. P. Kubiak, A. J. Sathrum, and J. M. Smieja, "Electrocatalytic and homogeneous approaches to conversion of CO₂ to liquid fuels," *Chem. Soc. Rev.*, vol. 38, no. 1, pp. 89–99, 2009.
- [21] A. J. Morris, G. J. Meyer, and E. Fujita, "Molecular Approaches to the Photocatalytic Reduction of Carbon Dioxide for Solar Fuels," *Acc. Chem. Res.*, vol. 42, no. 12, pp. 1983–1994, 2009.
- [22] Y. Tamaki, T. Morimoto, K. Koike, and O. Ishitani, "Photocatalytic CO₂ reduction with high turnover frequency and selectivity of formic acid formation using Ru(II) multinuclear complexes," *Proc. Natl. Acad. Sci. USA*, vol. 109, no. 39, pp. 15673–15678, 2012.
- [23] J.-M. Savéant, "Molecular Catalysis of Electrochemical Reactions. Mechanistic Aspects," *Chem. Rev.*, vol. 108, no. 7, pp. 2348–2378, 2008.
- [24] S. Wang, G. Q. Lu, and G. J. Millar, "Carbon Dioxide Reforming of Methane To Produce Synthesis Gas over Metal-Supported Catalysts: State of the Art," *Energy Fuels*, vol. 10, no. 4, pp. 896–904, 1996.
- [25] G. P. Smestad and A. Steinfeld, "Review: Photochemical and Thermochemical Production of Solar Fuels from H₂O and CO₂ Using Metal Oxide Catalysts," *Ind. Eng. Chem. Res.*, vol. 51, no. 37, pp. 11828–11840, 2012.
- [26] Y. Hori, "Electrochemical CO₂ Reduction on Metal Electrodes," in *Modern Aspects of Electrochemistry* (C. G. Vayenas, R. E. White, and M. E. Gamboa-Aldeco, eds.), pp. 89–189, New York, NY: Springer New York, 2008.
- [27] Z. Zhan, W. Kobsiriphat, J. R. Wilson, M. Pillai, I. Kim, and S. A. Barnett, "Syngas Production By Coelectrolysis of CO₂/H₂O: The Basis for a Renewable Energy Cycle," *Energy Fuels*, vol. 23, no. 6, pp. 3089–3096, 2009.
- [28] B. Kim, S. Ma, H.-R. M. Jhong, and P. J. A. Kenis, "Influence of dilute feed and pH on electrochemical reduction of CO₂ to CO on Ag in a continuous flow electrolyzer," *Electrochim. Acta*, vol. 166, pp. 271 – 276, 2015.
- [29] K. Branker, M. J. M. Pathak, and J. M. Pearce, "A review of solar photovoltaic levelized cost of electricity," *Renew. Sust. Energy Rev.*, vol. 15, no. 9, pp. 4470 – 4482, 2011.
- [30] J. K. Nørskov, J. Rossmeisl, A. Logadottir, L. Lindqvist, J. R. Kitchin, T. Bligaard, and H. Jónsson, "Origin of the Overpotential for Oxygen Reduction at a Fuel-Cell Cathode," *J. Phys. Chem. B*, vol. 108, no. 46, pp. 17886–17892, 2004.
- [31] J. Greeley and J. K. Nørskov, "Large-scale, density functional theory-based screening of alloys for hydrogen evolution," *Surf. Sci.*, vol. 601, no. 6, pp. 1590 – 1598, 2007.

- [32] J. Greeley and J. K. Nørskov, “Combinatorial Density Functional Theory-Based Screening of Surface Alloys for the Oxygen Reduction Reaction,” *J. Phys. Chem. C*, vol. 113, no. 12, pp. 4932–4939, 2009.
- [33] A. A. Peterson, F. Abild-Pedersen, F. Studt, J. Rossmeisl, and J. K. Nørskov, “How copper catalyzes the electroreduction of carbon dioxide into hydrocarbon fuels,” *Energy Environ. Sci.*, vol. 3, no. 9, pp. 1311–1315, 2010.
- [34] J. M. Mayer, “Proton-Coupled Electron Transfer: A Reaction Chemist’s View,” *Annu. Rev. Phys. Chem.*, vol. 55, no. 1, pp. 363–390, 2004.
- [35] D. R. Weinberg, C. J. Gagliardi, J. F. Hull, C. F. Murphy, C. A. Kent, B. C. Westlake, A. Paul, D. H. Ess, D. G. McCafferty, and T. J. Meyer, “Proton-Coupled Electron Transfer,” *Chem. Rev.*, vol. 112, no. 7, pp. 4016–4093, 2012.
- [36] S. Hammes-Schiffer, “Proton-coupled electron transfer: classification scheme and guide to theoretical methods,” *Energy Environ. Sci.*, vol. 5, no. 7, pp. 7696–7703, 2012.
- [37] A. B. Bocarsly, Q. D. Gibson, A. J. Morris, R. P. L’Esperance, Z. M. Detweiler, P. S. Lakkaraju, E. L. Zeitler, and T. W. Shaw, “Comparative Study of Imidazole and Pyridine Catalyzed Reduction of Carbon Dioxide at Illuminated Iron Pyrite Electrodes,” *ACS Catal.*, vol. 2, no. 8, pp. 1684–1692, 2012.
- [38] E. B. Cole, P. S. Lakkaraju, D. M. Rampulla, A. J. Morris, E. Abelev, and A. B. Bocarsly, “Using a One-Electron Shuttle for the Multielectron Reduction of CO₂ to Methanol: Kinetic, Mechanistic, and Structural Insights,” *J. Am. Chem. Soc.*, vol. 132, no. 33, pp. 11539–11551, 2010.
- [39] E. E. Barton, D. M. Rampulla, and A. B. Bocarsly, “Selective Solar-Driven Reduction of CO₂ to Methanol Using a Catalyzed p-GaP Based Photoelectrochemical Cell,” *J. Am. Chem. Soc.*, vol. 130, pp. 6342–6344, 5 2008.
- [40] J.-M. Saveant, C. Tard, J.-M. Savéant, and C. Tard, “Attempts To Catalyze the Electrochemical CO₂-to-Methanol Conversion by Biomimetic 2e⁻ + 2H⁺ Transferring Molecules,” *J. Am. Chem. Soc.*, vol. 138, no. 3, pp. 1017–1021, 2016.
- [41] A. J. Lucio and S. K. Shaw, “Pyridine and Pyridinium Electrochemistry on Polycrystalline Gold Electrodes and Implications for CO₂ Reduction,” *J. Phys. Chem. C*, vol. 119, pp. 12523–12530, 6 2015.
- [42] E. Portenkirchner, C. Enengl, S. Enengl, G. Hinterberger, S. Schlager, D. Apaydin, H. Neugebauer, G. Knör, and N. S. Sariciftci, “A Comparison of Pyridazine and Pyridine as Electrocatalysts for the Reduction of Carbon Dioxide to Methanol,” *Chem-ElectroChem*, vol. 1, no. 9, pp. 1543–1548, 2014.

- [43] S. I. Rybchenko, D. Touhami, J. D. Wadhawan, and S. K. Haywood, "Study of Pyridine-Mediated Electrochemical Reduction of CO₂ to Methanol at High CO₂ Pressure," *ChemSusChem*, vol. 9, no. 13, pp. 1660–1669, 2016.
- [44] C. Costentin, J. C. Canales, B. Haddou, J.-M. Savéant, J. M. Saveant, and J.-M. Savéant, "Electrochemistry of Acids on Platinum. Application to the Reduction of Carbon Dioxide in the Presence of Pyridinium Ion in Water," *J. Am. Chem. Soc.*, vol. 135, no. 47, pp. 17671–17674, 2013.
- [45] D. J. Boston, C. Xu, D. W. Armstrong, and F. M. MacDonnell, "Photochemical Reduction of Carbon Dioxide to Methanol and Formate in a Homogeneous System with Pyridinium Catalysts," *J. Am. Chem. Soc.*, vol. 135, no. 44, pp. 16252–16255, 2013.
- [46] D. Xiang, D. Magana, and R. B. Dyer, "CO₂ Reduction Catalyzed by Mercaptopteridine on Glassy Carbon," *J. Am. Chem. Soc.*, vol. 136, pp. 14007–14010, 10 2014.
- [47] H.-P. Yang, S. Qin, H. Wang, and J.-X. Lu, "Organically doped palladium: a highly efficient catalyst for electroreduction of CO₂ to methanol," *Green Chem.*, vol. 17, no. 12, pp. 5144–5148, 2015.
- [48] S. Ponnuram, C. M. Yun, and I. V. Chernyshova, "Robust Electroreduction of CO₂ at a Poly(4-vinylpyridine)-Copper Electrode," *ChemElectroChem*, vol. 3, no. 1, pp. 74–82, 2016.
- [49] J. H. Q. Lee, S. J. L. Lauw, and R. D. Webster, "The electrochemical reduction of carbon dioxide (CO₂) to methanol in the presence of pyridoxine (vitamin B6) ," *Electrochem. Commun.*, vol. 64, pp. 69 – 73, 2016.
- [50] A. G. Peroff, E. Weitz, and R. P. Van Duyne, "Mechanistic studies of pyridinium electrochemistry: alternative chemical pathways in the presence of CO₂," *Phys. Chem. Chem. Phys.*, vol. 18, no. 3, pp. 1578–1586, 2016.
- [51] J. A. Tossell, "Calculation of the properties of molecules in the pyridine catalyst system for the photochemical conversion of CO₂ to methanol ," *Comput. Theor. Chem.*, vol. 977, no. 1-3, pp. 123 – 127, 2011.
- [52] J. A. Keith and E. A. Carter, "Theoretical Insights into Pyridinium-Based Photoelectrocatalytic Reduction of CO₂," *J. Am. Chem. Soc.*, vol. 134, no. 18, pp. 7580–7583, 2012.
- [53] F. Riboni, E. Selli, M. R. Hoffmann, and A. J. Colussi, "Homogeneous Reduction of CO₂ by Photogenerated Pyridinyl Radicals," *J. Phys. Chem. A*, vol. 119, no. 19, pp. 4433–4438, 2015.
- [54] J. A. Keith and E. A. Carter, "Electrochemical reactivities of pyridinium in solution: consequences for CO₂ reduction mechanisms," *Chem. Sci.*, vol. 4, no. 4, pp. 1490–1496, 2013.

- [55] A. Marjolin and J. A. Keith, "Thermodynamic Descriptors for Molecules That Catalyze Efficient CO₂ Electroreductions," *ACS Catal.*, vol. 5, no. 2, pp. 1123–1130, 2015.
- [56] C.-H. Lim, A. M. Holder, and C. B. Musgrave, "Mechanism of Homogeneous Reduction of CO₂ by Pyridine: Proton Relay in Aqueous Solvent and Aromatic Stabilization," *J. Am. Chem. Soc.*, vol. 135, no. 1, pp. 142–154, 2013.
- [57] J. A. Keith and E. A. Carter, "Quantum Chemical Benchmarking, Validation, and Prediction of Acidity Constants for Substituted Pyridinium Ions and Pyridinyl Radicals," *J. Chem. Theory Comput.*, vol. 8, no. 9, pp. 3187–3206, 2012.
- [58] P. E. M. Siegbahn, "Two, Three, and Four Water Chain Models for the Nucleophilic Addition Step in the Wacker Process," *J. Phys. Chem.*, 1996.
- [59] C.-H. Lim, A. M. Holder, J. T. Hynes, and C. B. Musgrave, "Reduction of CO₂ to Methanol Catalyzed by a Biomimetic Organo-Hydride Produced from Pyridine," *J. Am. Chem. Soc.*, vol. 136, pp. 16081–16095, 11 2014.
- [60] M. Z. Ertem, S. J. Konezny, C. M. Araujo, and V. S. Batista, "Functional Role of Pyridinium during Aqueous Electrochemical Reduction of CO₂ on Pt(111)," *J. Phys. Chem. Lett.*, vol. 4, pp. 745–748, 3 2013.
- [61] K. Liao, M. Askerka, E. L. Zeitler, A. B. Bocarsly, and V. S. Batista, "Electrochemical Reduction of Aqueous Imidazolium on Pt(111) by Proton Coupled Electron Transfer," *Top. Catal.*, vol. 58, no. 1, pp. 23–29, 2015.
- [62] E. L. Zeitler, M. Z. Ertem, J. E. Pander, Y. Yan, V. S. Batista, and A. B. Bocarsly, "Isotopic Probe Illuminates the Role of the Electrode Surface in Proton Coupled Hydride Transfer Electrochemical Reduction of Pyridinium on Pt(111)," *J. Electrochem. Soc.*, vol. 162, no. 14, pp. H938–H944, 2015.
- [63] E. Lebègue, J. Agullo, M. Morin, and D. Bélanger, "The Role of Surface Hydrogen Atoms in the Electrochemical Reduction of Pyridine and CO₂ in Aqueous Electrolyte," *ChemElectroChem*, vol. 1, pp. 1013–1017, 6 2014.
- [64] J. A. Keith, A. B. Muñoz-García, M. Lessio, and E. A. Carter, "Cluster Models for Studying CO₂ Reduction on Semiconductor Photoelectrodes," *Top. Catal.*, vol. 58, no. 1, pp. 46–56, 2015.
- [65] J. A. Keith and E. A. Carter, "Theoretical Insights into Electrochemical CO₂ Reduction Mechanisms Catalyzed by Surface-Bound Nitrogen Heterocycles," *J. Phys. Chem. Lett.*, vol. 4, no. 23, pp. 4058–4063, 2013.
- [66] M. Lessio and E. A. Carter, "What Is the Role of Pyridinium in Pyridine-Catalyzed CO₂ Reduction on p-GaP Photocathodes?," *J. Am. Chem. Soc.*, vol. 137, no. 41, pp. 13248–13251, 2015.

- [67] T. P. Senftle, M. Lessio, and E. A. Carter, “The Role of Surface-Bound Dihydropyridine Analogues in Pyridine-Catalyzed CO₂ Reduction over Semiconductor Photoelectrodes,” *ACS Cent. Sci.*, vol. 3, no. 9, pp. 968–974, 2017.
- [68] C. X. Kronawitter, Z. Chen, P. Zhao, X. Yang, and B. E. Koel, “Electrocatalytic hydrogenation of pyridinium enabled by surface proton transfer reactions,” *Catal. Sci. Technol.*, vol. 7, no. 4, pp. 831–837, 2017.
- [69] J. A. Joule and K. Mills, “Pyridines,” in *Heterocyclic Chemistry at a Glance*, pp. 33–47, John Wiley and Sons, Ltd, 2012.
- [70] C. X. Kronawitter, M. Lessio, P. Zahl, A. B. Muñoz-García, P. Sutter, E. A. Carter, and B. E. Koel, “Orbital-Resolved Imaging of the Adsorbed State of Pyridine on GaP(110) Identifies Sites Susceptible to Nucleophilic Attack,” *J. Phys. Chem. C*, vol. 119, no. 52, pp. 28917–28924, 2015.
- [71] P. E. Philip A. Schweitzer, *Fundamentals of Corrosion: Mechanisms, Causes, and Preventative Methods*. CRC Press, 2009.
- [72] O. of Prevention, T. Substances;, O. of Information Analysis, and P. Access, “Report on the Corrosion of Certain Alloys,” tech. rep., United States Environmental Protection Agency, Washington, D.C., 2001.
- [73] P. Roberge, *Handbook of Corrosion Engineering*. Mcgraw-hill, 1999.
- [74] U. Donatus, G. E. Thompson, and X. Zhou, “Effect of Near-Ambient Temperature Changes on the Galvanic Corrosion of an AA2024-T3 and Mild Steel Couple,” *J. Electrochem. Soc.*, vol. 162, pp. C42–C46, 11 2014.
- [75] F. Andreatta, H. Terryn, and J. de Wit, “Effect of solution heat treatment on galvanic coupling between intermetallics and matrix in AA7075-T6,” *Corros. Sci.*, vol. 45, pp. 1733–1746, 8 2003.
- [76] W. J. Clark, J. D. Ramsey, R. L. McCreery, and G. S. Frankel, “A Galvanic Corrosion Approach to Investigating Chromate Effects on Aluminum Alloy 2024-T3,” *J. Electrochem. Soc.*, vol. 149, p. B179, 5 2002.
- [77] W. Zhang and G. Frankel, “Transitions between pitting and intergranular corrosion in AA2024,” *Electrochim. Acta*, vol. 48, pp. 1193–1210, 4 2003.
- [78] H. Gräfen, E.-M. Horn, H. Schlecker, and H. Schindler, “Corrosion,” in *Ullmann’s Encyclopedia of Industrial Chemistry*, Wiley-VCH Verlag GmbH & Co. KGaA, 2000.
- [79] F. Mansfeld and E. Parry, “Galvanic corrosion of bare and coated Al alloys coupled to stainless steel 304 or Ti-6Al-4V,” *Corros. Sci.*, vol. 13, pp. 605–621, 1 1973.

- [80] X. Zhou, C. Luo, T. Hashimoto, A. Hughes, and G. Thompson, "Study of localized corrosion in AA2024 aluminium alloy using electron tomography," *Corros. Sci.*, vol. 58, pp. 299–306, 5 2012.
- [81] C. M. Hangarter and S. A. Policastro, "Electrochemical Characterization of Galvanic Couples Under Saline Droplets in a Simulated Atmospheric Environment," *Corrosion*, vol. 73, pp. 268–280, 3 2017.
- [82] S. Sathiyarayanan, S. Muthukrishnan, G. Venkatachari, and D. Trivedi, "Corrosion protection of steel by polyaniline (PANI) pigmented paint coating," *Prog. Org. Coat.*, vol. 53, pp. 297–301, 8 2005.
- [83] A. Samui, A. Patankar, J. Rangarajan, and P. Deb, "Study of polyaniline containing paint for corrosion prevention," *Prog. Org. Coat.*, vol. 47, pp. 1–7, 7 2003.
- [84] J. H. Braun, A. Baidins, and R. E. Marganski, "TiO₂ pigment technology: a review," *Prog. Org. Coat.*, vol. 20, pp. 105–138, 5 1992.
- [85] E. J. Mittemeijer and M. A. J. Somers, *Thermochemical Surface Engineering of Steels: Improving Materials Performance*. Elsevier Science, 2014.
- [86] W. von Baeckmann, W. Schwenk, and W. Prinz, *Handbook of Cathodic Corrosion Protection*. Elsevier Science, 1997.
- [87] A. W. Peabody, *Control of pipeline corrosion*. National Association of Corrosion Engineers, 1967.
- [88] K. De Baere, H. Verstraelen, L. Lemmens, S. Lenaerts, R. Dewil, Y. Van Ingelgem, and G. Potters, "A field study of the effectiveness of sacrificial anodes in ballast tanks of merchant ships," *J. Mar. Sci. Technol.*, vol. 19, pp. 116–123, 3 2014.
- [89] H. Li, X. Wang, Q. Wei, and B. Hou, "Photocathodic Protection of 304 Stainless Steel by Bi(2)S(3)/TiO(2) Nanotube Films Under Visible Light," *Nanoscale Res. Lett.*, vol. 12, p. 80, 2017.
- [90] . Hyunwoong Park, . Kyoo Young Kim, , and . Wonyong Choi, "Photoelectrochemical Approach for Metal Corrosion Prevention Using a Semiconductor Photoanode," *J. Phys. Chem. B*, 2002.
- [91] E. Fabbri, A. Habereder, K. Waltar, R. Kötz, and T. J. Schmidt, "Developments and perspectives of oxide-based catalysts for the oxygen evolution reaction," *Catal. Sci. Technol.*, vol. 4, pp. 3800–3821, 10 2014.
- [92] P. Liao, J. A. Keith, and E. A. Carter, "Water Oxidation on Pure and Doped Hematite (0001) Surfaces: Prediction of Co and Ni as Effective Dopants for Electrocatalysis," *J. Am. Chem. Soc.*, vol. 134, pp. 13296–13309, 8 2012.

- [93] J. Greeley and N. M. Markovic, “The road from animal electricity to green energy: combining experiment and theory in electrocatalysis,” *Energy Environ. Sci.*, vol. 5, p. 9246, 10 2012.
- [94] C. G. Morales-Guio, L.-A. Stern, and X. Hu, “Nanostructured hydrotreating catalysts for electrochemical hydrogen evolution,” *Chem. Soc. Rev.*, vol. 43, p. 6555, 3 2014.
- [95] J. D. Goodpaster, A. T. Bell, and M. Head-Gordon, “Identification of Possible Pathways for C-C Bond Formation during Electrochemical Reduction of CO₂: New Theoretical Insights from an Improved Electrochemical Model,” *J. Phys. Chem. Lett.*, vol. 7, no. 8, pp. 1471–1477, 2016.
- [96] J. Cheng, X. D. Liu, J. VandeVondele, M. Sulpizi, and M. Sprik, “Redox Potentials and Acidity Constants from Density Functional Theory Based Molecular Dynamics,” *Acc. Chem. Res.*, vol. 47, no. 12, pp. 3522–3529, 2014.
- [97] S. P. Lin, K. W. Wang, C. W. Liu, H. S. Chen, and J. H. Wang, “Trends of Oxygen Reduction Reaction on Platinum Alloys: A Computational and Experimental Study,” *J. Phys. Chem. C*, vol. 119, no. 27, pp. 15224–15231, 2015.
- [98] M. Russo, *Titanium Oxide Hydrates: Optical Properties and Applications*. PhD thesis, London, 2009.
- [99] H. H. Pham and L.-W. Wang, “Oxygen vacancy and hole conduction in amorphous TiO₂,” *Phys. Chem. Chem. Phys.*, vol. 17, no. 1, pp. 541–550, 2015.
- [100] X. Zhang and M. H. F. Sluiter, “Cluster Expansions for Thermodynamics and Kinetics of Multicomponent Alloys,” *J. Phase Equilibria Diffus.*, 2015.
- [101] F. Gesmundo and B. Gleeson, “Oxidation of multicomponent two-phase alloys,” *Oxid. Met.*, vol. 44, no. 1, pp. 211–237, 1995.
- [102] S. Sankaranarayanan and S. Ramanathan, “Molecular dynamics simulation study of nanoscale passive oxide growth on Ni-Al alloy surfaces at low temperatures,” *Phys. Rev. B*, vol. 78, no. 8, p. 17, 2008.
- [103] J. Qiao, Y. Liu, F. Hong, and J. Zhang, “A Review of Catalysts for the Electroreduction of Carbon Dioxide to Produce Low-Carbon Fuels,” *Chem. Soc. Rev.*, vol. 43, no. 2, pp. 631–675, 2014.
- [104] B. Kumar, M. Llorente, J. Froehlich, T. Dang, A. Sathrum, and C. P. Kubiak, “Photochemical and Photoelectrochemical Reduction of CO₂,” *Annu. Rev. Phys. Chem.*, vol. 63, no. 1, pp. 541–569, 2012.
- [105] D. K. Bediako, C. Costentin, E. C. Jones, D. G. Nocera, and J.-M. Savéant, “Proton-Electron Transport and Transfer in Electrocatalytic Films. Application to a Cobalt-Based O₂-Evolution Catalyst,” *J. Am. Chem. Soc.*, vol. 135, no. 28, pp. 10492–10502, 2013.

- [106] Y. Gorlin and T. F. Jaramillo, "A Bifunctional Nonprecious Metal Catalyst for Oxygen Reduction and Water Oxidation," *J. Am. Chem. Soc.*, vol. 132, no. 39, pp. 13612–13614, 2010.
- [107] J. K. Norskov, T. Bligaard, A. Logadottir, J. R. Kitchin, J. G. Chen, S. Pandalov, and J. K. Norskov, "Trends in the Exchange Current for Hydrogen Evolution," *J. Electrochem. Soc.*, vol. 152, no. 3, pp. J23–J26, 2005.
- [108] Y. Yan, E. L. Zeitler, J. Gu, Y. Hu, and A. B. Bocarsly, "Electrochemistry of Aqueous Pyridinium: Exploration of a Key Aspect of Electrocatalytic Reduction of CO₂ to Methanol," *J. Am. Chem. Soc.*, vol. 135, no. 38, pp. 14020–14023, 2013.
- [109] B. A. Rosen, A. Salehi-Khojin, M. R. Thorson, W. Zhu, D. T. Whipple, P. J. A. Kenis, and R. I. Masel, "Ionic Liquid-Mediated Selective Conversion of CO₂ to CO at Low Overpotentials," *Science*, vol. 334, no. 6056, pp. 643–644, 2011.
- [110] D. J. Boston, Y. M. F. Pachón, R. O. Lezna, N. R. de Tacconi, and F. M. MacDonnell, "Electrocatalytic and Photocatalytic Conversion of CO₂ to Methanol using Ruthenium Complexes with Internal Pyridyl Cocatalysts," *Inorg. Chem.*, vol. 53, no. 13, pp. 6544–6553, 2014.
- [111] J. J. Teesdale, A. J. Pistner, G. P. A. Yap, Y.-Z. Ma, D. A. Lutterman, and J. Rosenthal, "Reduction of CO₂ using a rhenium bipyridine complex containing ancillary BOD-IPY moieties," *Catal. Today*, vol. 225, no. 0, pp. 149–157, 2014.
- [112] J. Bezençon, M. B. Wittwer, B. Cutting, M. Smieško, B. Wagner, M. Kansy, and B. Ernst, "pK_a Determination by ¹H NMR Spectroscopy - An Old Methodology Revisited," *J. Pharm. Biomed. Anal.*, vol. 93, pp. 147–155, 2014.
- [113] A. D. Gift, S. M. Stewart, and P. Kwete Bokashanga, "Experimental Determination of pK_a Values by Use of NMR Chemical Shifts, Revisited," *J. Chem. Educ.*, vol. 89, no. 11, pp. 1458–1460, 2012.
- [114] A. Búcsi, J. Karlovská, M. Chovan, F. Devínsky, and D. Uhríková, "Determination of pK_a of N-alkyl-N,N-dimethylamine-N-oxides using ¹H NMR and ¹³C NMR spectroscopy," *Chem. Pap.*, vol. 68, no. 6, pp. 842–846, 2014.
- [115] M. S. Gordon, M. W. Schmidt, C. E. Dykstra, G. Frenking, K. S. Kim, and G. E. Scuseria, "Advances in electronic structure theory: GAMESS a decade later," 2005.
- [116] M. W. Schmidt, K. K. Baldrige, J. A. Boatz, S. T. Elbert, M. S. Gordon, J. H. Jensen, S. Koseki, N. Matsunaga, K. A. Nguyen, S. Su, T. L. Windus, M. Dupuis, and J. A. Montgomery, "General atomic and molecular electronic structure system," *J. Comput. Chem.*, vol. 14, pp. 1347–1363, 11 1993.
- [117] C. J. Cramer, *Essentials of Computational Chemistry : Theories and Models*. West Sussex, England ; New York : J. Wiley, 2002. Print., 2002.

- [118] R. D. Johnson, "III NIST Computational Chemistry Comparison and Benchmark Database NIST Standard Reference Database Number 101 Release 15b," 2011.
- [119] V. Barone and M. Cossi, "Quantum Calculation of Molecular Energies and Energy Gradients in Solution by a Conductor Solvent Model," *J. Phys. Chem. A*, 1998.
- [120] M. Cossi, N. Rega, G. Scalmani, and V. Barone, "Energies, structures, and electronic properties of molecules in solution with the C-PCM solvation model," *J. Comput. Chem.*, vol. 24, pp. 669–681, 4 2003.
- [121] J. J. P. Stewart, "Optimization of Parameters for Semiempirical Methods VI: More Modifications to the NDDO Approximations and Re-optimization of Parameters," *J. Mol. Model.*, vol. 19, no. 1, pp. 1–32, 2013.
- [122] J. Szegezdi and F. Csizmadia, "A Method for Calculating the pK_a Values of Small and Large Molecules," in *233rd ACS National Meeting*, (Chicago, USA), 2007.
- [123] J. Ho and M. Coote, "A Universal Approach for Continuum Solvent pK_a Calculations: Are We There Yet?," *Theor. Chem. Acc.*, vol. 125, no. 1-2, pp. 3–21, 2010.
- [124] J. T. Muckerman, J. H. Skone, M. Ning, and Y. Wasada-Tsutsui, "Toward the accurate calculation of pK_a values in water and acetonitrile," *Biochim. Biophys. Acta.*, vol. 1827, pp. 882–891, 8 2013.
- [125] J. A. Keith, K. A. Grice, C. P. Kubiak, and E. A. Carter, "Elucidation of the Selectivity of Proton-Dependent Electrocatalytic CO_2 Reduction by fac-Re(bpy)(CO)₃Cl," *J. Am. Chem. Soc.*, vol. 135, pp. 15823–15829, 10 2013.
- [126] Y. Fu, L. Liu, H.-Z. Yu, Y.-M. Wang, and Q.-X. Guo, "Quantum-chemical predictions of absolute standard redox potentials of diverse organic molecules and free radicals in acetonitrile," *J. Am. Chem. Soc.*, vol. 127, no. 19, pp. 7227–7234, 2005. PMID: 15884964.
- [127] S. C. Doney, V. J. Fabry, R. A. Feely, and J. A. Kleypas, "Ocean Acidification: The Other CO_2 Problem," *Annu. Rev. Mar. Sci.*, vol. 1, pp. 169–192, 1 2009.
- [128] P. M. Vitousek, "Beyond Global Warming: Ecology and Global Change," *Ecology*, vol. 75, pp. 1861–1876, 10 1994.
- [129] J. R. McKone, N. S. Lewis, and H. B. Gray, "Will Solar-Driven Water-Splitting Devices See the Light of Day?," *Chem. Mater.*, vol. 26, pp. 407–414, 1 2014.
- [130] A. J. Esswein and D. G. Nocera, "Hydrogen Production by Molecular Photocatalysis," *Chem. Rev.*, 2007.
- [131] S. C. Roy, O. K. Varghese, M. Paulose, and C. A. Grimes, "Toward Solar Fuels: Photocatalytic Conversion of Carbon Dioxide to Hydrocarbons," *ACS Nano*, vol. 4, pp. 1259–1278, 3 2010.

- [132] G. Kovács, A. Stirling, A. Lledós, and G. Ujaque, “The Nature of $[\text{PdCl}_2(\text{C}_2\text{H}_4)(\text{H}_2\text{O})]$ as an Active Species in the Wacker Process: New Insights from Ab Initio Molecular Dynamics Simulations,” *Chem. Eur. J.*, vol. 18, pp. 5612–5619, 4 2012.
- [133] M. Salvalaglio, P. Tiwary, and M. Parrinello, “Assessing the Reliability of the Dynamics Reconstructed from Metadynamics,” *J. Chem. Theory Comput.*, vol. 10, pp. 1420–1425, 4 2014.
- [134] A. Comas-Vives, A. Stirling, A. Lledós, and G. Ujaque, “The Wacker Process: Inner- or Outer-Sphere Nucleophilic Addition? New Insights from Ab Initio Molecular Dynamics,” *Chem. Eur. J.*, vol. 16, pp. 8738–8747, 8 2010.
- [135] K. L. Fleming, P. Tiwary, and J. Pfaendtner, “New Approach for Investigating Reaction Dynamics and Rates with Ab Initio Calculations,” *J. Phys. Chem. A*, vol. 120, pp. 299–305, 1 2016.
- [136] V. Agarwal, P. J. Dauenhauer, G. W. Huber, and S. M. Auerbach, “Ab Initio Dynamics of Cellulose Pyrolysis: Nascent Decomposition Pathways at 327 and 600 °C,” *J. Am. Chem. Soc.*, vol. 134, pp. 14958–14972, 9 2012.
- [137] R. Tripathi and N. N. Nair, “Mechanism of Meropenem Hydrolysis by New Delhi Metallo β -Lactamase,” *ACS Catal.*, vol. 5, pp. 2577–2586, 4 2015.
- [138] S. Zheng and J. Pfaendtner, “Car-Parrinello Molecular Dynamics + Metadynamics Study of High-Temperature Methanol Oxidation Reactions Using Generic Collective Variables,” *J. Phys. Chem. C*, vol. 118, pp. 10764–10770, 5 2014.
- [139] J. F. Dama, G. Rotskoff, M. Parrinello, and G. A. Voth, “Transition-Tempered Metadynamics: Robust, Convergent Metadynamics via On-the-Fly Transition Barrier Estimation,” *J. Chem. Theory Comput.*, vol. 10, pp. 3626–3633, 9 2014.
- [140] P. G. Bolhuis, D. Chandler, C. Dellago, and P. L. Geissler, “Transition path sampling: Throwing ropes over rough mountain passes, in the dark,” *Annu. Rev. Phys. Chem.*, vol. 53, pp. 291–318, 2002.
- [141] J. P. Perdew, K. Burke, and M. Ernzerhof, “Generalized Gradient Approximation Made Simple,” *Phys. Rev. Lett.*, vol. 77, pp. 3865–3868, 10 1996.
- [142] J. P. Perdew, K. Burke, and M. Ernzerhof, “Generalized Gradient Approximation Made Simple [Phys. Rev. Lett. 77, 3865 (1996)],” *Phys. Rev. Lett.*, vol. 78, no. 7, p. 1396, 1997.
- [143] J. P. Perdew and A. Zunger, “Self-interaction correction to density-functional approximations for many-electron systems,” *Phys. Rev. B*, vol. 23, no. 10, pp. 5048–5079, 1981.
- [144] H. M. Senn and W. Thiel, “QM/MM Methods for Biomolecular Systems,” *Angew. Chem. Int. Ed.*, vol. 48, no. 7, pp. 1198–1229, 2009.

- [145] J. Kästner, H. M. Senn, S. Thiel, N. Otte, and W. Thiel, "QM/MM Free-Energy Perturbation Compared to Thermodynamic Integration and Umbrella Sampling: Application to an Enzymatic Reaction," *J. Chem. Theory Comput.*, vol. 2, no. 2, pp. 452–461, 2006.
- [146] T. D. Poulsen, M. Garcia-Viloca, J. Gao, and D. G. Truhlar, "Free Energy Surface, Reaction Paths, and Kinetic Isotope Effect of Short-Chain Acyl-CoA Dehydrogenase," *J. Phys. Chem. B*, vol. 107, no. 35, pp. 9567–9578, 2003.
- [147] J. Gao, K.-Y. Wong, and D. T. Major, "Combined QM/MM and path integral simulations of kinetic isotope effects in the proton transfer reaction between nitroethane and acetate ion in water," *J. Comput. Chem.*, vol. 29, no. 4, pp. 514–522, 2008.
- [148] D. G. Fedorov, Y. Sugita, and C. H. Choi, "Efficient Parallel Implementations of QM/MM-REMD (Quantum Mechanical/Molecular Mechanics-Replica-Exchange MD) and Umbrella Sampling: Isomerization of H₂O₂ in Aqueous Solution," *J. Phys. Chem. B*, vol. 117, no. 26, pp. 7996–8002, 2013.
- [149] R. Rajamani, K. J. Naidoo, and J. Gao, "Implementation of an adaptive umbrella sampling method for the calculation of multidimensional potential of mean force of chemical reactions in solution," *J. Comput. Chem.*, vol. 24, no. 14, pp. 1775–1781, 2003.
- [150] J. M. Parks, H. Hu, J. Rudolph, and W. Yang, "Mechanism of Cdc25B Phosphatase with the Small Molecule Substrate p-Nitrophenyl Phosphate from QM/MM-MFEP Calculations," *J. Phys. Chem. B*, vol. 113, no. 15, pp. 5217–5224, 2009.
- [151] D. Rinaldo, D. M. Philipp, S. J. Lippard, and R. A. Friesner, "Intermediates in Dioxygen Activation by Methane Monooxygenase: A QM/MM Study," *J. Am. Chem. Soc.*, vol. 129, no. 11, pp. 3135–3147, 2007.
- [152] L. Tian and R. A. Friesner, "QM/MM Simulation on P450 BM3 Enzyme Catalysis Mechanism," *J. Chem. Theory Comput.*, vol. 5, no. 5, pp. 1421–1431, 2009.
- [153] H. Hu and W. Yang, "Elucidating Solvent Contributions to Solution Reactions with Ab Initio QM/MM Methods," *J. Phys. Chem. B*, vol. 114, no. 8, pp. 2755–2759, 2010.
- [154] H. Lin and D. G. Truhlar, "QM/MM: what have we learned, where are we, and where do we go from here?," *Theor. Chem. Acc.*, vol. 117, no. 2, pp. 185–199, 2006.
- [155] K. Park, A. W. Götz, R. C. Walker, and F. Paesani, "Application of Adaptive QM/MM Methods to Molecular Dynamics Simulations of Aqueous Systems," *J. Chem. Theory Comput.*, vol. 8, no. 8, pp. 2868–2877, 2012.
- [156] M. Arnó, L. R. Domingo, M. Arno, and L. R. Domingo, "Density functional theory study of the mechanism of the proline-catalyzed intermolecular aldol reaction," *Theor. Chem. Acc.*, vol. 108, no. 4, pp. 232–239, 2002.

- [157] L. C. Dias, E. C. de Lucca, M. A. B. Ferreira, D. C. Garcia, and C. F. Tormena, "The Role of β -Bulky Substituents in Aldol Reactions of Boron Enolates of Methylketones with Aldehydes: Experimental and Theoretical Studies by DFT Analysis," *J. Org. Chem.*, vol. 77, pp. 1765–1788, 2 2012.
- [158] C. B. Shinisha and R. B. Sunoj, "Bicyclic proline analogues as organocatalysts for stereoselective aldol reactions: an in silico DFT study," *Org. Biomol. Chem.*, vol. 5, no. 8, pp. 1287–1294, 2007.
- [159] F. Bernardi, A. Bottoni, and G. P. Miscione, "A Theoretical Study of Homogeneous ZieglerNatta Catalysis," *Organometallics*, vol. 17, no. 1, pp. 16–24, 1998.
- [160] R. E. Plata and D. A. Singleton, "A Case Study of the Mechanism of Alcohol-Mediated Morita Baylis-Hillman Reactions. The Importance of Experimental Observations," *J. Am. Chem. Soc.*, vol. 137, pp. 3811–3826, 3 2015.
- [161] D. K. Malick, G. A. Petersson, and J. A. Montgomery, "Transition states for chemical reactions I. Geometry and classical barrier height," *J. Chem. Phys.*, vol. 108, no. 14, pp. 5704–5713, 1998.
- [162] P. Li, G. Henkelman, J. A. Keith, and J. K. Johnson, "Elucidation of Aqueous Solvent-Mediated Hydrogen-Transfer Reactions by ab Initio Molecular Dynamics and Nudged Elastic-Band Studies of NaBH₄ Hydrolysis," *J. Phys. Chem. C*, vol. 118, pp. 21385–21399, 9 2014.
- [163] S. J. Benkovic and S. Hammes-Schiffer, "A perspective on enzyme catalysis," *Science*, vol. 301, no. 5637, pp. 1196–1202, 2003.
- [164] S. Kumar, D. Bouzida, R. H. Swendsen, P. A. Kollman, and J. M. Rosenberg, "The Weighted Histogram Analysis Method for Free-energy Calculations on Biomolecules 1: The Method," *J. Comput. Chem.*, vol. 13, no. 8, pp. 1011–1021, 1992.
- [165] G. M. Torrie and J. P. Valleau, "Non-Physical Sampling Distributions in Monte-Carlo Free-energy Estimation - Umbrella Sampling," *J. Comput. Phys.*, vol. 23, no. 2, pp. 187–199, 1977.
- [166] B. Roux, "The Calculation of the Potential of Mean Force using Computer-simulations," *Comput. Phys. Commun.*, vol. 91, no. 1-3, pp. 275–282, 1995.
- [167] J. R. Pliego and J. M. Riveros, "The cluster-continuum model for the calculation of the solvation free energy of ionic species," *J. Phys. Chem. A*, vol. 105, no. 30, pp. 7241–7247, 2001.
- [168] V. S. Bryantsev, M. S. Diallo, and W. A. Goddard, "Calculation of solvation free energies of charged solutes using mixed cluster/continuum models," *J. Phys. Chem. B*, vol. 112, no. 32, pp. 9709–9719, 2008.

- [169] D. Riccardi, H. B. Guo, J. M. Parks, B. H. Gu, L. Y. Liang, and J. C. Smith, “Cluster-Continuum Calculations of Hydration Free Energies of Anions and Group 12 Divalent Cations,” *J. Chem. Theory Comput.*, vol. 9, no. 1, pp. 555–569, 2013.
- [170] K. A. Grice, M. C. Groenenboom, J. D. A. Manuel, M. A. Sovereign, and J. A. Keith, “Examining the selectivity of borohydride for carbon dioxide and bicarbonate reduction in protic conditions,” *Fuel*, vol. 150, pp. 139–145, 2015.
- [171] F. Neese, “The ORCA program system,” *Wiley Interdisciplinary Reviews-Computational Molecular Science*, vol. 2, no. 1, pp. 73–78, 2012.
- [172] C. Adamo and V. Barone, “Toward reliable density functional methods without adjustable parameters: The PBE0 model,” *J. Chem. Phys.*, vol. 110, no. 13, pp. 6158–6170, 1999.
- [173] A. D. Becke, “Densityfunctional thermochemistry. III. The role of exact exchange,” *J. Chem. Phys.*, vol. 98, no. 7, pp. 5648–5652, 1993.
- [174] M. Headgordon, J. A. Pople, and M. J. Frisch, “MP2 Energy Evaluation by Direct Methods,” *Chem. Phys. Lett.*, vol. 153, no. 6, pp. 503–506, 1988.
- [175] C. Møller and M. S. Plesset, “Note on an approximation treatment for many-electron systems,” *Phys. Rev.*, vol. 46, no. 7, pp. 618–622, 1934.
- [176] R. Izsak and F. Neese, “An overlap fitted chain of spheres exchange method,” *J. Chem. Phys.*, vol. 135, no. 14, pp. 144105/1–11, 2011.
- [177] S. Kossmann and F. Neese, “Efficient Structure Optimization with Second-Order Many-Body Perturbation Theory: The RIJCOSX-MP2 Method,” *J. Chem. Theory Comput.*, vol. 6, pp. 2325–2338, 8 2010.
- [178] S. Kossmann and F. Neese, “Comparison of two efficient approximate Hartree-Fock approaches,” *Chem. Phys. Lett.*, vol. 481, no. 4-6, pp. 240–243, 2009.
- [179] F. Neese, F. Wennmohs, A. Hansen, and U. Becker, “Efficient, approximate and parallel Hartree-Fock and hybrid DFT calculations. A ‘chain-of-spheres’ algorithm for the Hartree-Fock exchange,” *Chem. Phys.*, vol. 356, no. 1-3, pp. 98–109, 2009.
- [180] F. Neese, “An improvement of the resolution of the identity approximation for the formation of the Coulomb matrix,” *J. Comput. Chem.*, vol. 24, no. 14, pp. 1740–1747, 2003.
- [181] C. Riplinger and F. Neese, “An efficient and near linear scaling pair natural orbital based local coupled cluster method,” *J. Chem. Phys.*, vol. 138, no. 3, 2013.
- [182] S. Sinnecker, A. Rajendran, A. Klamt, M. Diedenhofen, and F. Neese, “Calculation of solvent shifts on electronic g-tensors with the conductor-like screening model (COSMO)

- and its self-consistent generalization to real solvents (Direct COSMO-RS),” *J. Phys. Chem. A*, vol. 110, no. 6, pp. 2235–2245, 2006.
- [183] S. Grimme, S. Ehrlich, and L. Goerigk, “Effect of the damping function in dispersion corrected density functional theory,” *J. Comput. Chem.*, vol. 32, no. 7, pp. 1456–1465, 2011.
- [184] G. Kresse and J. Furthmüller, “Efficient iterative schemes for *ab initio* total-energy calculations using a plane-wave basis set,” *Phys. Rev. B*, vol. 54, pp. 11169–11186, 10 1996.
- [185] G. Kresse, J. Furthmüller, J. Furthmüller, and J. Furthmüller, “Efficiency of *ab-initio* total energy calculations for metals and semiconductors using a plane-wave basis set,” *Comput. Mater. Sci. Science*, vol. 6, pp. 15–50, 7 1996.
- [186] G. Kresse and J. Hafner, “*Ab initio* molecular-dynamics simulation of the liquid-metal-amorphous-semiconductor transition in germanium,” *Phys. Rev. B*, vol. 49, pp. 14251–14269, 5 1994.
- [187] G. Kresse and J. Hafner, “*Ab initio* molecular dynamics for liquid metals,” *Phys. Rev. B*, vol. 47, pp. 558–561, 1 1993.
- [188] P. E. Blöchl, “Projector augmented-wave method,” *Phys. Rev. B*, vol. 50, no. 24, pp. 17953–17979, 1994.
- [189] G. Kresse and D. Joubert, “From ultrasoft pseudopotentials to the projector augmented-wave method,” *Phys. Rev. B*, vol. 59, pp. 1758–1775, 1 1999.
- [190] D. Sheppard, P. H. Xiao, W. Chemelewski, D. D. Johnson, and G. Henkelman, “A generalized solid-state nudged elastic band method,” *J. Chem. Phys.*, vol. 136, no. 7, pp. 074103/1–8, 2012.
- [191] G. Henkelman, B. P. Uberuaga, and H. Jonsson, “A climbing image nudged elastic band method for finding saddle points and minimum energy paths,” *J. Chem. Phys.*, vol. 113, no. 22, pp. 9901–9904, 2000.
- [192] D. Sheppard, R. Terrell, and G. Henkelman, “Optimization methods for finding minimum energy paths,” *J. Chem. Phys.*, vol. 128, p. 134106, 4 2008.
- [193] H. Jonsson, G. Mills, and K. W. Jacobsen, *Classical and quantum dynamics in condensed phase simulations*. Singapore: World Scientific, 1998.
- [194] W. Humphrey, A. Dalke, and K. Schulten, “VMD: Visual molecular dynamics,” *J. Mol. Graph. Model.*, vol. 14, no. 1, pp. 33–38, 1996.
- [195] M. F. Hawthorne and E. S. Lewis, “Amine Boranes. III. Hydrolysis of Pyridine Diphenylborane and the Mechanism of Hydride Transfer Reactions,” *J. Am. Chem. Soc.*, vol. 80, pp. 4296–4299, 8 1958.

- [196] B. Bartocha, W. Graham, and F. Stone, "Hydride-transfer reactions of borineI: Synthesis of boron-carbon bonds from the fluoroethylenes," *J. Inorg. Nucl. Chem.*, vol. 6, pp. 119–129, 4 1958.
- [197] A. Kohen and J. P. Klinman, "Enzyme catalysis: Beyond classical paradigms," *Acc. Chem. Res.*, vol. 31, no. 7, pp. 397–404, 1998.
- [198] C. P. Casey, S. W. Singer, D. R. Powell, R. K. Hayashi, and M. Kavana, "Hydrogen transfer to carbonyls and imines from a hydroxycyclopentadienyl ruthenium hydride: Evidence for concerted hydride and proton transfer," *J. Am. Chem. Soc.*, vol. 123, no. 6, pp. 1090–1100, 2001.
- [199] S. E. Clapham, A. Hadzovic, and R. H. Morris, "Mechanisms of the H₂-hydrogenation and transfer hydrogenation of polar bonds catalyzed by ruthenium hydride complexes," *Coord. Chem. Rev.*, vol. 248, no. 21-24, pp. 2201–2237, 2004.
- [200] S. Hammes-Schiffer, "Comparison of hydride, hydrogen atom, and proton-coupled electron transfer reactions," *Chemphyschem*, vol. 3, no. 1, pp. 33–42, 2002.
- [201] M. W. Dzierlenga, D. Antoniou, and S. D. Schwartz, "Another Look at the Mechanisms of Hydride Transfer Enzymes with Quantum and Classical Transition Path Sampling," *J. Phys. Chem. Lett.*, vol. 6, pp. 1177–1181, 4 2015.
- [202] I. Mayer, "Bond orders in three-centre bonds: an analytical investigation into the electronic structure of diborane and the three-centre four-electron bonds of hypervalent sulphur," *J. Mol. Struct.*, vol. 186, pp. 43–52, 1989.
- [203] M. Yu and D. R. Trinkle, "Accurate and efficient algorithm for Bader charge integration," *J. Chem. Phys.*, vol. 134, no. 6, pp. 064111/1–8, 2011.
- [204] F. Neese, T. Petrenko, D. Ganyushin, and G. Olbrich, "Advanced aspects of ab initio theoretical optical spectroscopy of transition metal complexes: Multiplets, spin-orbit coupling and resonance Raman intensities," *Coord. Chem. Rev.*, vol. 251, no. 3-4, pp. 288–327, 2007.
- [205] C. Angeli, R. Cimiraglia, S. Evangelisti, T. Leininger, and J.-P. Malrieu, "Introduction of n-electron valence states for multireference perturbation theory," *J. Chem. Phys.*, vol. 114, no. 23, pp. 10252–10264, 2001.
- [206] C. Angeli, R. Cimiraglia, and J.-P. Malrieu, "N-electron valence state perturbation theory: a fast implementation of the strongly contracted variant," *Chem. Phys. Lett.*, vol. 350, no. 3, pp. 297–305, 2001.
- [207] C. Angeli, R. Cimiraglia, and J.-P. Malrieu, "N-electron valence state perturbation theory: A spinless formulation and an efficient implementation of the strongly contracted and of the partially contracted variants," *J. Chem. Phys.*, vol. 117, no. 20, pp. 9138–9153, 2002.

- [208] A. V. Marenich, C. J. Cramer, and D. G. Truhlar, "Universal Solvation Model Based on Solute Electron Density and on a Continuum Model of the Solvent Defined by the Bulk Dielectric Constant and Atomic Surface Tensions," *J. Phys. Chem. B*, vol. 113, pp. 6378–6396, 5 2009.
- [209] S. Verma, B. Kim, H. Jhong, S. C. Ma, and P. J. A. Kenis, "A Gross-Margin Model for Defining Technoeconomic Benchmarks in the Electroreduction of CO₂," *ChemSusChem*, vol. 9, no. 15, pp. 1972–1979, 2016.
- [210] W. H. Wang, Y. Himeda, J. T. Muckerman, G. F. Manbeck, and E. Fujita, "CO₂ Hydrogenation to Formate and Methanol as an Alternative to Photo- and Electrochemical CO₂ Reduction," *Chem. Rev.*, vol. 115, no. 23, pp. 12936–12973, 2015.
- [211] M. D. Doherty, D. C. Grills, J. T. Muckerman, D. E. Polyansky, and E. Fujita, "Toward more efficient photochemical CO₂ reduction: Use of scCO₂ or photogenerated hydrides," *Coord. Chem. Rev.*, vol. 254, no. 21-22, pp. 2472–2482, 2010.
- [212] U. Rusching, U. Müller, P. Willnow, and T. Höpner, "CO₂ Reduction to Formate by NADH Catalysed by Formate Dehydrogenase from *Pseudomonas oxalaticus*," *Europ. J. Biochem.*, vol. 70, no. 2, pp. 325–330, 1976.
- [213] T. P. Senftle, M. Lessio, and E. A. Carter, "Interaction of Pyridine and Water with the Reconstructed Surfaces of GaP(111) and CdTe(111) Photoelectrodes: Implications for CO₂ Reduction," *Chem. Mater.*, vol. 28, no. 16, pp. 5799–5810, 2016.
- [214] C. H. Lim, A. M. Holder, J. T. Hynes, and C. B. Musgrave, "Dihydropteridine/Pteridine as a 2H⁺/2e⁻ Redox Mediator for the Reduction of CO₂ to Methanol: A Computational Study," *J. Phys. Chem. B*, vol. 121, no. 16, pp. 4158–4167, 2017.
- [215] P. K. Giesbrecht and D. E. Herbert, "Electrochemical Reduction of Carbon Dioxide to Methanol in the Presence of Benzannulated Dihydropyridine Additives," *ACS Energy Lett.*, vol. 2, no. 3, pp. 549–555, 2017.
- [216] M. C. Groenenboom and J. A. Keith, "Explicitly Unraveling the Roles of Counterions, Solvent Molecules, and Electron Correlation in Solution Phase Reaction Pathways," *J. Phys. Chem. B*, vol. 120, no. 41, pp. 10797–10807, 2016.
- [217] G. König, Y. Mei, F. C. Pickard, A. C. Simmonett, B. T. Miller, J. M. Herbert, H. L. Woodcock, B. R. Brooks, and Y. H. Shao, "Computation of Hydration Free Energies Using the Multiple Environment Single System Quantum Mechanical/Molecular Mechanical Method," *J. Chem. Theory Comput.*, vol. 12, no. 1, pp. 332–344, 2016.
- [218] B. Ensing, A. Laio, M. Parrinello, and M. L. Klein, "A recipe for the computation of the free energy barrier and the lowest free energy path of concerted reactions," *J. Phys. Chem. B*, vol. 109, no. 14, pp. 6676–6687, 2005.

- [219] K. Leung, I. M. B. Nielsen, and I. Kurtz, “Ab Initio molecular dynamics study of carbon dioxide and bicarbonate hydration and the nucleophilic attack of hydroxide on CO₂,” *J. Phys. Chem. B*, vol. 111, no. 17, pp. 4453–4459, 2007.
- [220] K. Leung, I. M. B. Nielsen, N. Sai, C. Medforth, and J. A. Shelnutt, “Cobalt-Porphyrin Catalyzed Electrochemical Reduction of Carbon Dioxide in Water. 2. Mechanism from First Principles,” *J. Phys. Chem. A*, vol. 114, no. 37, pp. 10174–10184, 2010.
- [221] M. J. Yang, L. J. Yang, Y. Q. Gao, and H. Hu, “Combine umbrella sampling with integrated tempering method for efficient and accurate calculation of free energy changes of complex energy surface,” *J. Chem. Phys.*, vol. 141, no. 4, pp. 044108/1–9, 2014.
- [222] O. Ivchenko, P. Bachert, and P. Imhof, “Umbrella sampling of proton transfer in a creatine-water system,” *Chem. Phys. Lett.*, vol. 600, pp. 51–55, 2014.
- [223] J. Hutter, M. Iannuzzi, F. Schiffmann, and J. VandeVondele, “CP2K: atomistic simulations of condensed matter systems,” *Wiley Interdisciplinary Reviews-Computational Molecular Science*, vol. 4, no. 1, pp. 15–25, 2014.
- [224] S. Goedecker, M. Teter, and J. Hutter, “Separable dual-space Gaussian pseudopotentials,” *Phys. Rev. B*, vol. 54, no. 3, pp. 1703–1710, 1996.
- [225] C. Hartwigsen, S. Goedecker, and J. Hutter, “Relativistic separable dual-space Gaussian pseudopotentials from H to Rn,” *Phys. Rev. B*, vol. 58, no. 7, pp. 3641–3662, 1998.
- [226] M. Krack, “Pseudopotentials for H to Kr optimized for gradient-corrected exchange-correlation functionals,” *Theor. Chem. Acc.*, vol. 114, no. 1-3, pp. 145–152, 2005.
- [227] J. VandeVondele and J. Hutter, “Gaussian basis sets for accurate calculations on molecular systems in gas and condensed phases,” *J. Chem. Phys.*, vol. 127, no. 11, pp. 114105/1–9, 2007.
- [228] G. Bussi, D. Donadio, and M. Parrinello, “Canonical sampling through velocity rescaling,” *J. Chem. Phys.*, vol. 126, no. 1, pp. 014101/1–7, 2007.
- [229] A. Grossfield, *WHAM: the weighted histogram analysis method*. <http://membrane.urmc.rochester.edu/content/wham: version 2.0.9>.
- [230] G. Koch, N. Thompson, O. Moghissi, M. Gould, J. Payer, and G. Jacobson, “International Measures of Prevention, Application, and Economics of Corrosion Technologies Study,” tech. rep., NACE International, Houston, Texas, USA, NACE International, 2016.
- [231] K. Lo, C. Shek, and J. Lai, “Mater. Sci. Eng. R Rep. in stainless steels,” *Materials Science and Engineering: R: Reports*, vol. 65, pp. 39–104, 5 2009.

- [232] G. Song, “Recent Progress in Corrosion and Protection of Magnesium Alloys,” *Adv. Eng. Mater.*, vol. 7, pp. 563–586, 7 2005.
- [233] . Valdés, Z.-W. Qu, G.-J. Kroes, J. Rossmeisl, and J. K. Nørskov, “Oxidation and Photo-Oxidation of Water on TiO₂ Surface,” *J. Phys. Chem. C*, vol. 112, pp. 9872–9879, 7 2008.
- [234] K. Mathew, R. Sundararaman, K. Letchworth-Weaver, T. A. Arias, and R. G. Hennig, “Implicit solvation model for density-functional study of nanocrystal surfaces and reaction pathways,” *J. Chem. Phys.*, vol. 140, p. 084106, 2 2014.
- [235] K. Mathew and R. G. Hennig, “Implicit self-consistent description of electrolyte in plane-wave density-functional theory,” 1 2016.
- [236] A. V. Krukau, O. A. Vydrov, A. F. Izmaylov, and G. E. Scuseria, “Influence of the exchange screening parameter on the performance of screened hybrid functionals,” *J. Chem. Phys.*, vol. 125, p. 224106, 12 2006.
- [237] H. Aktulga, J. Fogarty, S. Pandit, and A. Grama, “Parallel reactive molecular dynamics: Numerical methods and algorithmic techniques,” *Parallel Comput.*, vol. 38, pp. 245–259, 4 2012.
- [238] A. C. T. van Duin, S. Dasgupta, F. Lorant, and W. A. Goddard III, “ReaxFF: A Reactive Force Field for Hydrocarbons,” *J. Phys. Chem. A*, vol. 105, no. 41, pp. 9396–9409, 2001.
- [239] S. Plimpton, “Fast Parallel Algorithms for Short-Range Molecular Dynamics,” *J. Comput. Phys.*, vol. 117, no. 1, pp. 1–19, 1995.
- [240] S.-Y. Kim, N. Kumar, P. Persson, J. Sofo, A. C. T. van Duin, and J. D. Kubicki, “Development of a ReaxFF Reactive Force Field for Titanium Dioxide/Water Systems,” *Langmuir*, vol. 29, pp. 7838–7846, 6 2013.
- [241] S. A. Policastro, C. M. Hangarter, D. J. Horton, J. A. Wollmershauser, and D. F. Roeper, “Effect of Low-Concentration Alloying in Titanium on Reduction Reaction Kinetics in Alkaline Environments,” *J. Electrochem. Soc.*, vol. 163, pp. C269–C274, 3 2016.
- [242] C. S. Ewing, S. Bhavsar, G. Veser, J. J. McCarthy, and J. K. Johnson, “Accurate Amorphous Silica Surface Models from First-Principles Thermodynamics of Surface Dehydroxylation,” *Langmuir*, vol. 30, pp. 5133–5141, 5 2014.
- [243] V. Petkov, G. Holzrüter, U. Tröge, T. Gerber, and B. Himmel, “Atomic-scale structure of amorphous TiO₂ by electron, X-ray diffraction and reverse Monte Carlo simulations,” *J. Non-Cryst. Solids*, vol. 231, pp. 17–30, 7 1998.

- [244] Y. Wang and H.-P. Cheng, “Oxygen Reduction Activity on Perovskite Oxide Surfaces: A Comparative First-Principles Study of LaMnO_3 , LaFeO_3 , and LaCrO_3 ,” *J. Phys. Chem. C*, vol. 117, pp. 2106–2112, 2 2013.
- [245] H.-Y. Su, Y. Gorlin, I. C. Man, F. Calle-Vallejo, J. K. Nørskov, T. F. Jaramillo, and J. Rossmeisl, “Identifying active surface phases for metal oxide electrocatalysts: a study of manganese oxide bi-functional catalysts for oxygen reduction and water oxidation catalysis,” *Phys. Chem. Chem. Phys.*, vol. 14, p. 14010, 9 2012.
- [246] T. Arashi, J. Seo, K. Takanabe, J. Kubota, and K. Domen, “Nb-doped TiO_2 cathode catalysts for oxygen reduction reaction of polymer electrolyte fuel cells,” *Catal. Today*, vol. 233, pp. 181–186, 9 2014.
- [247] F. Calle-Vallejo, D. Loffreda, M. T. M. Koper, and P. Sautet, “Introducing structural sensitivity into adsorption-energy scaling relations by means of coordination numbers,” *Nat. Chem.*, vol. 7, pp. 403–410, 4 2015.
- [248] V. Fung, F. F. Tao, and D.-e. Jiang, “General Structure-Reactivity Relationship for Oxygen on Transition-Metal Oxides,” *J. Phys. Chem. Lett.*, vol. 8, pp. 2206–2211, 5 2017.
- [249] N. Takeno, “Atlas of Eh-pH Diagrams: Intercomparison of Thermodynamic Databases, Geological Survey of Japan Open File Report No.419,” tech. rep., National Institute of Advanced Industrial Science and Technology, 2005.
- [250] P. Mehta, J. Greeley, W. N. Delgass, and W. F. Schneider, “Adsorption Energy Correlations at the Metal-Support Boundary,” *ACS Catal.*, vol. 7, pp. 4707–4715, 7 2017.
- [251] W. Lee, J. W. Han, Y. Chen, Z. Cai, and B. Yildiz, “Cation Size Mismatch and Charge Interactions Drive Dopant Segregation at the Surfaces of Manganite Perovskites,” *J. Am. Chem. Soc.*, vol. 135, pp. 7909–7925, 5 2013.
- [252] H. Hu, B. Dong, H. Hu, F. Chen, M. Kong, Q. Zhang, T. Luo, L. Zhao, Z. Guo, J. Li, Z. Xu, S. Wang, D. Eder, and L. Wan, “Atomic Layer Deposition of TiO_2 for a High-Efficiency Hole-Blocking Layer in Hole-Conductor-Free Perovskite Solar Cells Processed in Ambient Air,” *ACS Appl. Mater. Interfaces*, vol. 8, pp. 17999–18007, 7 2016.
- [253] S. J. Durand, “Attaining a 30-year photovoltaic system lifetime: The BOS issues,” *Prog. Photovoltaics*, vol. 2, pp. 107–113, 4 1994.
- [254] Y. Shi, B. Yang, and P. Liaw, “Corrosion-Resistant High-Entropy Alloys: A Review,” *Metals*, vol. 7, p. 43, 2 2017.
- [255] P. Refait, M. Jeannin, R. Sabot, H. Antony, and S. Pineau, “Corrosion and cathodic protection of carbon steel in the tidal zone: Products, mechanisms and kinetics,” *Corros. Sci.*, vol. 90, pp. 375–382, 1 2015.

- [256] I. M. Gadala, M. Abdel Wahab, and A. Alfantazi, “Numerical simulations of soil physicochemistry and aeration influences on the external corrosion and cathodic protection design of buried pipeline steels,” *Mater. Des.*, vol. 97, pp. 287–299, 5 2016.
- [257] Y. Zhao, Z. Zhang, L. Yu, and Q. Tang, “Electrospinning of polyaniline microfibers for anticorrosion coatings: An avenue of enhancing anticorrosion behaviors,” *Synth. Met.*, vol. 212, pp. 84–90, 2 2016.
- [258] R. Yuan, S. Wu, P. Yu, B. Wang, L. Mu, X. Zhang, Y. Zhu, B. Wang, H. Wang, and J. Zhu, “Superamphiphobic and Electroactive Nanocomposite toward Self-Cleaning, Antiwear, and Anticorrosion Coatings,” *ACS Appl. Mater. Interfaces*, vol. 8, pp. 12481–12493, 5 2016.
- [259] L. Gu, S. Liu, H. Zhao, and H. Yu, “Facile Preparation of Water-Dispersible Graphene Sheets Stabilized by Carboxylated Oligoanilines and Their Anticorrosion Coatings,” *ACS Appl. Mater. Interfaces*, vol. 7, pp. 17641–17648, 8 2015.
- [260] H. Wei, Y. Wang, J. Guo, N. Z. Shen, D. Jiang, X. Zhang, X. Yan, J. Zhu, Q. Wang, L. Shao, H. Lin, S. Wei, and Z. Guo, “Advanced micro/nanocapsules for self-healing smart anticorrosion coatings,” *J. Mater. Chem. A*, vol. 3, pp. 469–480, 12 2015.
- [261] B. W. Whitman, L. Li, and G. M. Swain, “Anti-Corrosion Properties of a TCP Pretreatment Conversion Coating on Aluminum Alloy 2024-T3 during Moist SO₂ Atmospheric Testing: Effects of Galvanic Coupling,” *J. Electrochem. Soc.*, vol. 164, pp. C135–C147, 2 2017.
- [262] L. Chen, J. Hu, X. Zhong, S. Yu, Z. Zhang, D. Zeng, and T. Shi, “The Corrosion Behavior of 17-4 Stainless Steel in a Stainless Steel-Carbon Steel Galvanic Couple,” *Int. J. Electrochem. Sci.*, vol. 1210, no. 10, pp. 9445–945540, 2017.
- [263] A. Astarita, M. Curioni, A. Squillace, X. Zhou, F. Bellucci, G. E. Thompson, and K. A. Beamish, “Corrosion behaviour of stainless steel-titanium alloy linear friction welded joints: Galvanic coupling,” *Mater. Corros.*, vol. 66, pp. 111–117, 2 2015.
- [264] A. Pardo, M. Merino, A. Coy, R. Arrabal, F. Viejo, and E. Matykina, “Corrosion behaviour of magnesium/aluminium alloys in 3.5 wt.% NaCl,” *Corros. Sci.*, vol. 50, pp. 823–834, 3 2008.
- [265] F. Mansfeld and J. V. Kenkel, “Laboratory Studies of Galvanic Corrosion of Aluminum Alloys,” in *Galvanic and Pitting Corrosion Field and Laboratory Studies*, pp. 20–20, 100 Barr Harbor Drive, PO Box C700, West Conshohocken, PA 19428-2959: ASTM International, 1976.
- [266] J. H. Montoya, M. Garcia-Mota, J. K. Nørskov, and A. Vojvodic, “Theoretical evaluation of the surface electrochemistry of perovskites with promising photon absorption properties for solar water splitting,” *Phys. Chem. Chem. Phys.*, vol. 17, no. 17, pp. 2634–2640, 2634.

- [267] J. H. Montoya, L. C. Seitz, P. Chakthranont, A. Vojvodic, T. F. Jaramillo, and J. K. Nørskov, “Materials for solar fuels and chemicals,” *Nat. Mater.*, vol. 16, pp. 70–81, 1 2017.
- [268] Y. Zheng, Y. Jiao, M. Jaroniec, and S. Z. Qiao, “Advancing the Electrochemistry of the Hydrogen-Evolution Reaction through Combining Experiment and Theory,” *Angew. Chem. Int. Ed.*, vol. 54, pp. 52–65, 1 2015.
- [269] Y. Zheng, Y. Jiao, Y. Zhu, L. H. Li, Y. Han, Y. Chen, A. Du, M. Jaroniec, and S. Z. Qiao, “Hydrogen evolution by a metal-free electrocatalyst,” *Nat. Commun.*, vol. 5, p. 3783, 4 2014.
- [270] L. Zhang, J. Xiao, H. Wang, and M. Shao, “Carbon-Based Electrocatalysts for Hydrogen and Oxygen Evolution Reactions,” *ACS Catal.*, vol. 7, pp. 7855–7865, 11 2017.
- [271] M. C. Groenenboom, R. M. Anderson, D. J. Horton, Y. Basdogan, D. F. Roeper, S. A. Policastro, and J. A. Keith, “Doped Amorphous Ti Oxides To Deoptimize Oxygen Reduction Reaction Catalysis,” *J. Phys. Chem. C*, vol. 121, pp. 16825–16830, 8 2017.
- [272] O. Assowe, O. Politano, V. Vignal, P. Arnoux, B. Diawara, O. Verners, and A. C. T. van Duin, “Reactive Molecular Dynamics of the Initial Oxidation Stages of Ni(111) in Pure Water: Effect of an Applied Electric Field,” *J. Phys. Chem. A*, vol. 116, pp. 11796–11805, 12 2012.
- [273] T. Hanawa, S. Hiramoto, K. Asami, O. Okuno, and K. Asaoka, “Surface Oxide Films on Titanium Alloys Regenerated in Hanks’ Solution,” *Metall. Mater. Trans*, vol. 43, no. 12, 2002.
- [274] W. B. Xue, C. Wang, R. Y. Chen, and Z. W. Deng, “Structure and properties characterization of ceramic coatings produced on Ti-6Al-4V alloy by microarc oxidation in aluminate solution,” *Mater. Lett.*, vol. 52, no. 6, pp. 435–441, 2002.
- [275] A. L. Yerokhin, X. Nie, A. Leyland, and A. Matthews, “Characterisation of oxide films produced by plasma electrolytic oxidation of a Ti-6Al-4V alloy,” *Surf. Coat. Technol.*, vol. 130, no. 2-3, pp. 195–206, 2000.
- [276] A. Khorshidi and A. A. Peterson, “Amp: A modular approach to machine learning in atomistic simulations,” *Comput. Phys. Commun.*, vol. 207, pp. 310–324, 10 2016.
- [277] A. Hjorth Larsen, J. Jørgen Mortensen, J. Blomqvist, I. E. Castelli, R. Christensen, M. Dulak, J. Friis, M. N. Groves, B. Hammer, C. Hargus, E. D. Hermes, P. C. Jennings, P. Bjerre Jensen, J. Kermode, J. R. Kitchin, E. Leonhard Kolsbjerg, J. Kubal, K. Kaasbjerg, S. Lysgaard, J. Bergmann Maronsson, T. Maxson, T. Olsen, L. Pastewka, A. Peterson, C. Rostgaard, J. Schiøtz, O. Schütt, M. Strange, K. S. Thygesen, T. Vegge, L. Vilhelmsen, M. Walter, Z. Zeng, and K. W. Jacobsen, “The atomic simulation environment: A Python library for working with atoms,” *J. Phys. Condens. Matter*, vol. 29, p. 273002, 7 2017.

- [278] J. R. Boes, M. C. Groenenboom, J. A. Keith, and J. R. Kitchin, “Neural Network and ReaxFF Comparison for Au Properties,” *Int. J. Quantum Chem.*, vol. 116, no. 13, pp. 979–987, 2016.
- [279] Y. Hinuma, H. Hayashi, Y. Kumagai, I. Tanaka, and F. Oba, “Comparison of approximations in density functional theory calculations: Energetics and structure of binary oxides,” *Phys. Rev. B*, vol. 96, p. 094102, 9 2017.
- [280] K. Kwapien, S. Piccinin, and S. Fabris, “Energetics of Water Oxidation Catalyzed by Cobalt Oxide Nanoparticles: Assessing the Accuracy of DFT and DFT+U Approaches against Coupled Cluster Methods,” *J. Phys. Chem. Lett.*, vol. 2, no. 24, pp. 4223–4230, 2013.
- [281] J. R. Boes and J. R. Kitchin, “Modeling Segregation on AuPd(111) Surfaces with Density Functional Theory and Monte Carlo Simulations,” *J. Phys. Chem. C*, vol. 121, pp. 3479–3487, 2 2017.
- [282] A. U. Khan, P. Brož, M. Premović, J. Pavl, J. Vřešťál, X. Yan, D. Maccio, A. Saccone, G. Giester, and P. Rogl, “The Ti-Mn system revisited: experimental investigation and thermodynamic modelling,” *Phys. Chem. Chem. Phys.*, vol. 18, pp. 23326–23339, 8 2016.
- [283] J. F. Moulder and J. Chastain, *Handbook of x-ray photoelectron spectroscopy : a reference book of standard spectra for identification and interpretation of XPS data*. Physical Electronics Division, Perkin-Elmer Corp, 1992.
- [284] D. D. Briggs and M. P. Seah, *Practical surface analysis*. Wiley, 1990.
- [285] H. Raebiger, S. Lany, and A. Zunger, “Charge self-regulation upon changing the oxidation state of transition metals in insulators,” *Nature*, vol. 453, pp. 763–766, 6 2008.
- [286] M. Xu, P. Xiao, S. Stauffer, J. Song, G. Henkelman, and J. B. Goodenough, “Theoretical and Experimental Study of Vanadium-Based Fluorophosphate Cathodes for Rechargeable Batteries,” *Chem. Mater.*, vol. 26, pp. 3089–3097, 5 2014.